MAGNETOM Flash

Issue Number 69 · 3/2017
RSNA Edition

Not for distribution in the US

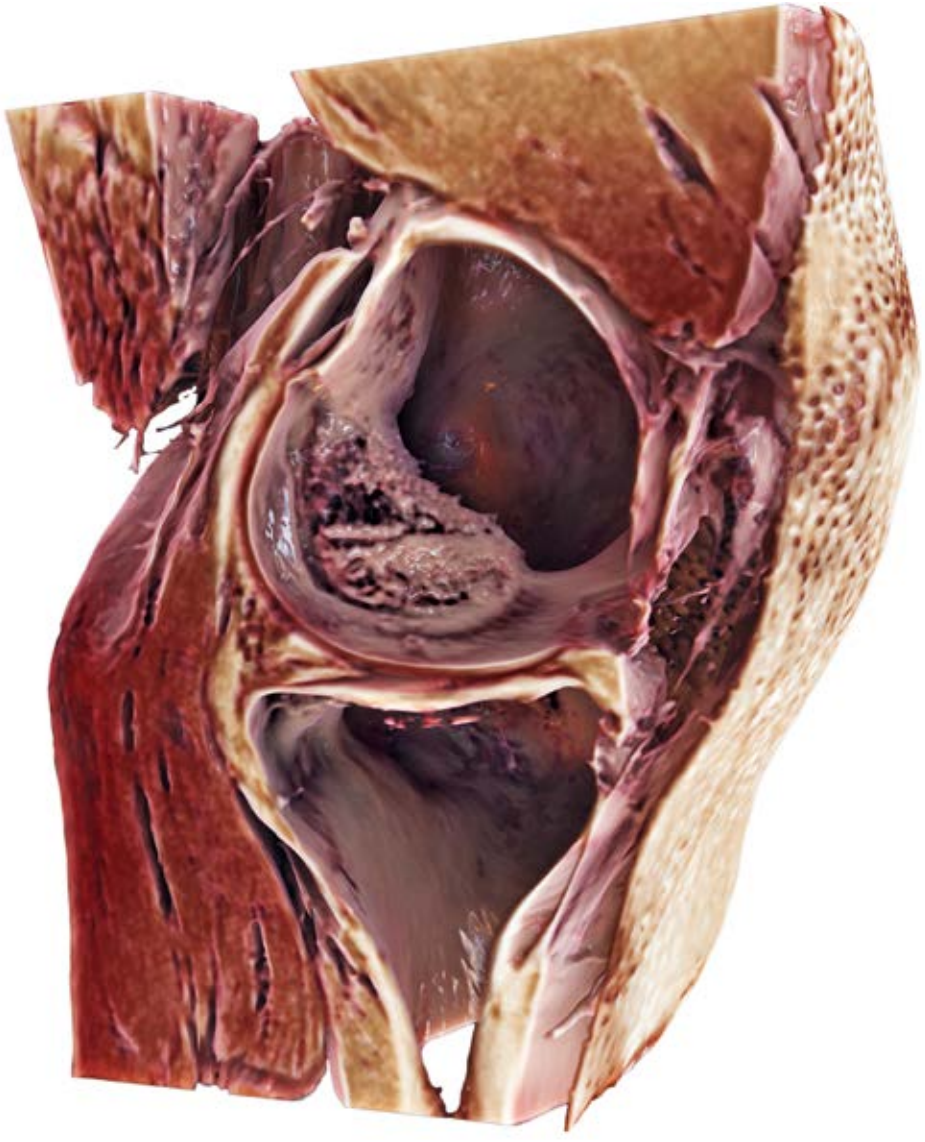

siemens.com/magnetom-world

SIEMENS Healthineers

Steven L. Mendelsohn, M.D., graduated from Jefferson Medical School in Philadelphia in 1979 shortly after his 23rd birthday. After completing his diagnostic radiology residency at North Shore University Hospital in 1983, he joined Zwanger-Pesiri Radiology as a staff radiologist. In 1992, he became managing partner of Zwanger-Pesiri Radiology – originally a small private practice group. Just five radiologists worked across two limited modality outpatient centers with a total office staff of 15 (including techs, receptionists, transcription, and billing).

From 1992 until 2002, Mendelsohn was chairman of radiology at Central General Hospital (renamed North Shore University Hospital at Plainview in 1995). At that time, Zwanger-Pesiri Radiology started to grow: Between 1992 and 2002, outpatient centers expanded from two to four, and later growing to eight between 2002 and 2011. Freed of the time pressure constraints of being the radiology chairman, Mendelsohn focused on expanding Zwanger-Pesiri Radiology even further. From 2012 until 2017, outpatient facilities increased to 24, each equipped with one or two MRIs, CT, mammography, X-ray, ultrasound, and DEXA systems. Five sites also have PET and nuclear radiology. All are located in New York, on Long Island and in Queens. Currently, six more facilities are under construction and several more are under architectural development.

Outside work, Mendelsohn enjoys skiing, snowboarding, hiking, biking, kayaking, sailing, and fitness. Of his six children, five already hold degrees from leading universities and have successful careers in various fields. The youngest is still at kindergarten – tracing letters and counting.

Zwanger-Pesiri Radiology snapshot

For over 60 years, Zwanger-Pesiri Radiology has focused on patient-centered care, research, education, and a strong commitment to the community. Led by Steven L. Mendelsohn, M.D., the team of 1,100 professionals with over 60 radiologists, 45 nurses, 300 receptionists, 75 MRI technologists, 15 nuclear technologists, 150 X-ray and CT technologists, 110 schedulers, 80 billers, and 30 IT staff members is dedicated to providing state-of-the-art radiology services. The radiologists specialize in areas such as neuroradiology, musculoskeletal imaging, body imaging, and breast imaging. They work closely with referring physicians to ensure optimal outcomes for patients. To support them in their clinical work, they use high-end imaging equipment including one Siemens Biograph mMR PET/MRI, 25 3T Siemens MRIs (22 MAGNETOM Skyra, one MAGNETOM Vida, and two MAGNETOM Verio), nine 1.5T Siemens MRIs (six MAGNETOM Aera, two MAGNETOM Espree, one MAGNETOM Amira), five Siemens PET/CTs, and a myriad of other units from 3D mammography, to open-sided MRIs as well as countless ultrasound, X-ray, DEXA and ABUS units.

Zwanger-Pesiri firsts:

- First outpatient Biograph mMR PET/MRI scanner in the USA
- First outpatient MAGNETOM Skyra 3T MRI scanner in the USA
- First outpatient Dual Source SOMATOM Definition 256 CT scanner in the USA
- First outpatient MAGNETOM Vida 3T MRI scanner in the USA
- First radiology practice to provide patient results online
- First radiology practice to provide imaging free of charge for the uninsured

New York, USA

Discover the Components of a Successful Radiology Practice

Dear colleagues, dear readers,

Not a high-powered academic, I may not be the right person to write this editorial comment. I am not the chairperson of a prestigious department, nor have I published any research articles – although our practice is involved in research.

The reason I was invited to write this editorial comment is because I grew a large, successful outpatient radiology practice while many others were downsizing, consolidating, selling or even closing. My comments are therefore drawn from my own personal experience, thoughts, and ideas over the past 35 years.

Before you read further, please consider what quality in radiology means to you:

- Is quality having the latest equipment?
- Is quality using the highest resolution MRI software?
- Is quality measured by the number of publications the radiologists have?
- Is quality creating an atmosphere of ease where patients can discuss openly with radiologists?
- Is quality having the friendliest, kindest, and most polite staff?
- Is quality having prominent locations?
- Is quality ensuring fast appointment availability?
- Is quality enabling patient access to reports via mobile devices?

And who defines, benchmarks, qualifies and quantifies quality: Legislators? Researchers? Facebook likes? Online reviews? In my opinion, everything outlined below shapes the overall patient experience and influences the level of quality at your institution. Decide which aspects you can best address and improve upon!

Good is not just good enough: Attitude sets the tone for the entire organization

Hospitality and customer service industries have already learned something that medicine is just beginning to grasp: There is only one chance to make a great first impression! What matters most here is kindness. It should be of #1 importance in corporate culture. For our staff, it may seem like merely another routine day but patients are often scared. This is why our entire corporate culture is driven by our motto: **Smile. Be Kind. Be Nice.** And start by being kind to each and every one or your coworkers! Most people work 40-plus hours a week and also spend time socializing in the evenings and at weekends. A happy work environment starts with the staff themselves. Kindness is catching: When staff are kind to each other, this spreads to patients, their families, referring physicians, and their staff. Naturally, managers must lead by example:

- Demonstrate a calm relaxed demeanor
- Focus on the patient in front of you – this person is your only priority
- Keep the patient informed
- Never say no; always go higher to find the person who can make it happen

Finally, walk through the facility in the shoes of a patient and consider how friendly you find the environment: Is there a clear sign on the building showing where the radiology practice is? Is it well illuminated at night? Then check the floors, walls, furnishing, ceilings, bathrooms, and the general office space. Look up from inside the CT gantry and the MRI bore. Remember, there is only one chance to make a great first impression – miss it and it's gone forever!

"In radiology, change is constant. Stop fighting it. Embrace it!"

Steven L. Mendelsohn

Strive to eliminate waiting

Patients' #1 complaint is about waiting times. In no other industry, would this level of customer service be even marginally acceptable! And radiology is even more of a service industry than other medical practices:

- We know how long each examination takes
- We know there sometimes will be emergencies and additional examinations
- We know some patients will arrive late, and a few early …

Nevertheless, waiting continues to be part of daily life. Any delay should be explained to the patient. We all have the right to be kept informed of how long a wait will be. Ideally, no one should wait any longer than five minutes. Anything beyond 15 minutes becomes annoying. But how can we actually control waiting times? Find the foot on the hose: Are you overscheduled? Too many patients? Too few radiologists? Are people distracted by other tasks or waiting on paperwork? So, fix the delay.

Moreover, we should not decide what the patient's priority is but rather:

- Offer to perform the examination whenever the patient wants it
- Enable appointments outside standard working hours
- Make exceptions the rule

Make contact easier

It should be possible to contact a radiology practice using various methods including: Walk-in visits in person or by phone, text, fax, or email. Try to make the path to the relevant contact person as direct as possible. Staff members should develop a rapport with every patient who visits the facility. Receptionists, aids, techs, nurses and even radiologists should explain the examination procedure and answer questions before the study is initiated. Technologists should guide the patient throughout the examination. Always tell the patient when the results will be available. Everyone wants to know, whether they ask or not! Once results are released, the reading radiologist should be available to the patient or the referring physician immediately.

Make simple and straightforward reports

A patient should not need to resort to Google or consult their own doctor when reading a report. Avoid abbreviations, drop the jargon, skip the flowery prose! Proofread anything that is created by articulation and voice recognition. The impressions and conclusions should be relevant, appropriate, and to the point. Stop equivocating and remove phrases such as: "Probably", "Consistent with", "Cannot rule out", "Could represent" or "Should be considered". Structured reporting may help to avoid errors.

Clarity and simplicity rule. Just a few seconds are needed for report clarity but it could:

- save a coder 5–10 minutes of time
- save a patient an anxiety filled weekend
- save unnecessary calls from the patient or referring physician

Complaints drive improvements

Feedback including complaints provides the best ingredients, ideas, and opportunities for improvement: Turn lemons into lemonade, and perhaps even a lemon meringue tarte. Listen closely to any complaints from patients, staff, referring doctors, management, and administrators. Respond to every single point. Thank them for taking their time to make the complaint (rather than simply go to another radiology facility …).

The statements by Siemens' customers presented here are based on results that were achieved in the customer's unique setting. Since there is no 'typical' hospital and many variables exist (e.g., hospital size, case mix, level of IT adoption), there can be no guarantee that other customers will achieve the same results.

Apologize openly, but never argue, defend or justify. Accept complaints as valid and act on the information. Finally, follow up by letting the person know what actions have been taken and thank them again for their valuable feedback.

Use marketing to educate the public

Develop personal relationships and educate physicians and their staff about the latest developments in radiology, about your most recent features, staff additions, new facilities or new equipment. Some people prefer educational information, articles, publications, whereas others prefer to know what is latest and greatest – some people will focus on the differentiators. Some people are on their computers, smartphones, some watch TV or listen to the radio, and others read newspapers or mailed brochures. Consider all media and methods to suit different tastes – each one is effective.

Stop fighting change. Embrace it!

Maintaining the status quo may be one of the strongest forces on earth but radiology must continually evolve with the times. If you are still doing things the same way as three years ago, then complacency may have set in. In my opinion, every single process should be re-evaluated and adapted every few years: Some changes may be major, others minor – but some sort of change nevertheless! Parse every minute the patient spends from the moment the physician tells the patient a radiological study is needed until the moment follow-up treatment is initiated. Direct or indirect activities or actions that benefit the patient are at the heart of absolutely everything we do. In radiology, change is constant. Stop fighting it. Embrace it!

Steven L. Mendelsohn, M.D.

Visit us at **www.siemens.com/magnetom-world** to read Steven L. Mendelsohn's comprehensive thoughts on numerous aspects that shape a large, successful outpatient radiology practice.

Content

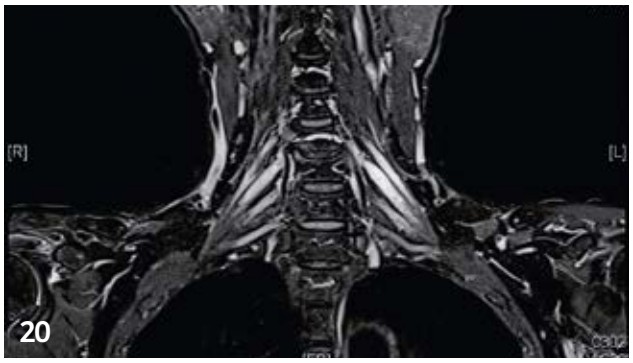

Enhancing the quality of MRI Services

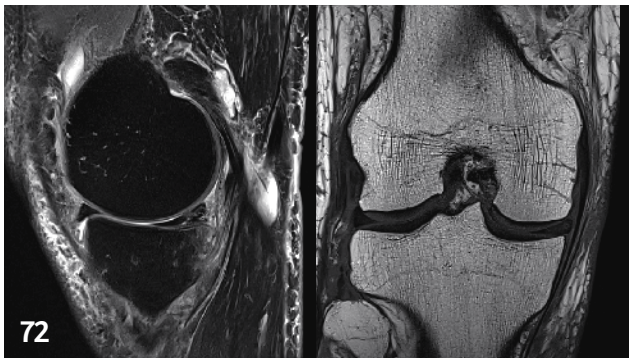

MAGNETOM Vida clinical case studies

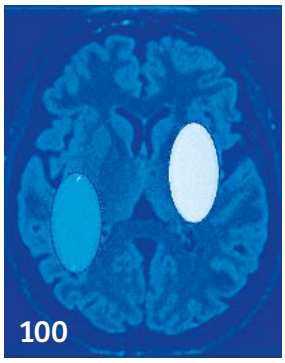

FLAIR Fusion in MS follow-up

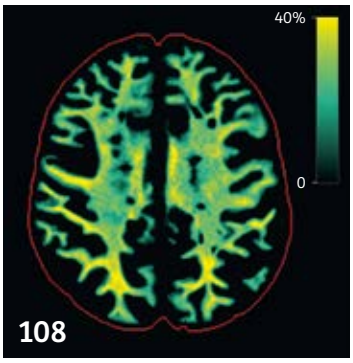

Myelin detection without additional scan time

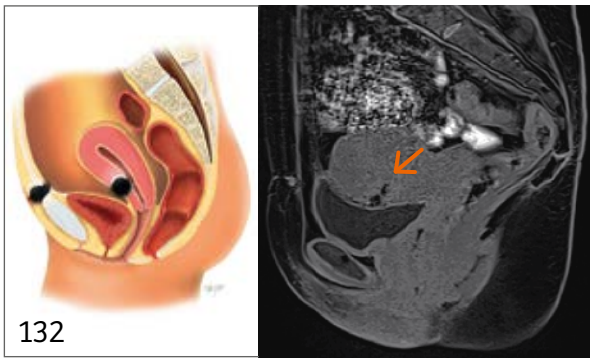

MRI after cesarean delivery

[1] WIP, the product is currently under development and is not for sale in the US and in other countries. Its future availability cannot be ensured.

[2] 510(k) pending. The product is not commercially available. Future availability cannot be guaranteed.

[3] The MRI restrictions (if any) of the metal implant must be considered prior to patient undergoing MRI exam. MR imaging of patients with metallic implants brings specific risks. However, certain implants are approved by the governing regulatory bodies to be MR conditionally safe. For such implants, the previously mentioned warning may not be applicable. Please contact the implant manufacturer for the specific conditional information. The conditions for MR safety are the responsibility of the implant manufacturer, not of Siemens.

[4] MR scanning has not been established as safe for imaging fetuses and infants less than two years of age. The responsible physician must evaluate the benefits of the MR examination compared to those of other imaging procedures.

Benefits of Accelerated MR Imaging in Daily Routine

Val M. Runge, M.D.; Johannes K. Richter, M.D.; Hendrik von Tengg-Kobligk, M.D.; Johannes T. Heverhagen, M.D., Ph.D.

Department of Diagnostic, Interventional and Pediatric Radiology, Inselspital, University Hospital, University of Bern, Bern, Switzerland

Introduction

Clinical development in magnetic resonance imaging in recent years has focused on decreasing scan time, an important topic because of the greater length of time required for and cost therein of an MR exam when compared to computed tomography and ultrasound. The two relevant major technical innovations in the current decade, simultaneous multi-slice imaging and compressed sensing are discussed in depth by organ system in the following article, focusing in particular on four top areas in terms of number of exams performed, the brain, upper abdomen, musculoskeletal system and breast [1]. Additional relevant new imaging approaches – which in general are specific to a single area of the body – that can lend speed to the clinical exam are also included.

Brain

In clinical brain imaging, simultaneous multi-slice (SMS) today has major impact [2]. Diffusion-weighted echoplanar and T2-weighted turbo spin echo scans are acquired in nearly every patient exam. Due to the large number of elements employed in state-of-the-art head coils, SMS is easily adapted, most commonly with an acceleration factor of two. With current technology, in limited situations, a factor of three can also be employed. In the brain, for routine clinical imaging, both single shot and readout segmented (RESOLVE) EPI DWI are widely employed, with the choice often site-specific. Single shot EPI is substantially faster, but as a screening exam with thicker sections is limited at 3T due to bulk susceptibility artifacts. Readout segmented EPI scans take substantially longer, but at many sites are favored even for screening exams. When SMS is applied to screening single shot EPI diffusion exams of the brain, the improvement is minimal due to the fact that scan time is already short. This is not the case however for readout segmented EPI[1], where a substantial savings in scan time is possible (Fig. 1). In certain situations, where thinner sections would potentially improve diagnostic yield, the use of SMS is advocated, as also illustrated, not to decrease scan time with readout segmented EPI but to enable a decrease in slice thickness to be obtained within a reasonable scan time.

An alternative approach in routine clinical brain imaging for diffusion-weighted scans is that of acquiring the entire brain with thin section (1 mm) sections. Prior to the advent of SMS, this was not practical from a scan time point of view. With state-of-the-art coils at 3T, such a scan is today possible in an acquisition time under five minutes if SMS is employed (Fig. 2). The specific diffusion technique used is single shot EPI, with the small voxel size limiting bulk

[1] SMS and RESOLVE are products. The combination of the two technologies, SMS RESOLVE is works in progress, currently under development and is not for sale in the US and in other countries. Its future availability cannot be ensured.

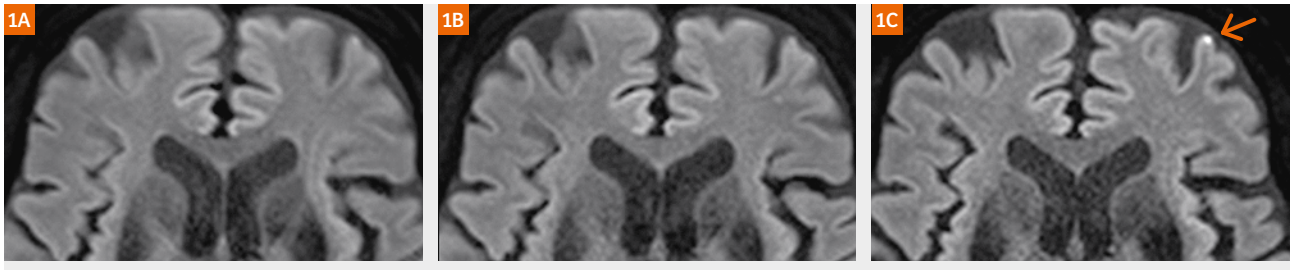

Figure 1:
The use of SMS with RESOLVE[1] for either reduced scan time or improved spatial resolution (specifically a reduction in slice thickness, while maintaining full brain coverage). A non-accelerated, 4 mm slice thickness, b 1000 RESOLVE image of the frontal lobes **(1A)** is compared to that with SMS2 (**1B**, 4 mm) and with SMS3 (**1C**, 2 mm). Scan times were 3:08 (min:sec) vs. 2:06 vs. 4:27. Image quality is equivalent between the conventional and SMS2 scans, however a small pinpoint cortical infarct (arrow) is visualized only with SMS3, due to the thinner slice thickness.

susceptibility artifact. Looking back at the history of the development of clinical MR, for brain screening exams, slice thickness decreased from 10 mm (initially) to 7 mm (with the advent of 1.5T) to 4 mm (with the advent of 3T). Given the possibilities offered by SMS, it is quite possible that high resolution thin section (1 mm) brain diffusion imaging will become routine in the future except for uncooperative patients.

TSE T2-weighted scans of the brain are typically fast, and thus at first glance not a likely candidate for the application of SMS. However, when thinner sections (< 4 mm) of the entire brain are desired, scan times often become substantial (over 4 minutes). This is due to the need to employ concatenations or other approaches such as extending TR in order to acquire the needed number of images to cover the entire brain. Although T2-weighted imaging is considered to be relatively robust to motion artifacts for brain imaging, this is generally a consequence of the relatively short scan time. With longer scan times, as well as with uncooperative patients, motion artifacts can be quite prominent and substantially degrade diagnostic image quality. Patients with acute ischemia are an important patient population in clinical brain MR imaging, with this population in particular benefiting by the use of SMS to achieve shorter scan times (Fig. 3).

Another approach to reducing overall exam time for a patient, specifically for brain imaging, involves the use of synthetic MRI [3]. If a specialized scan is acquired, then from this single acquisition, T1-, T2- and proton density-weighted images can be reconstructed (Fig. 4). Indeed, it is simply an issue of mathematics to calculate an image with any combination of TE and TR, or for example a FLAIR image that would for acquisition necessitate also the specification of an additional inversion pulse, and specifically TI. Likewise, parameter maps can be calculated, in the most simplistic approach

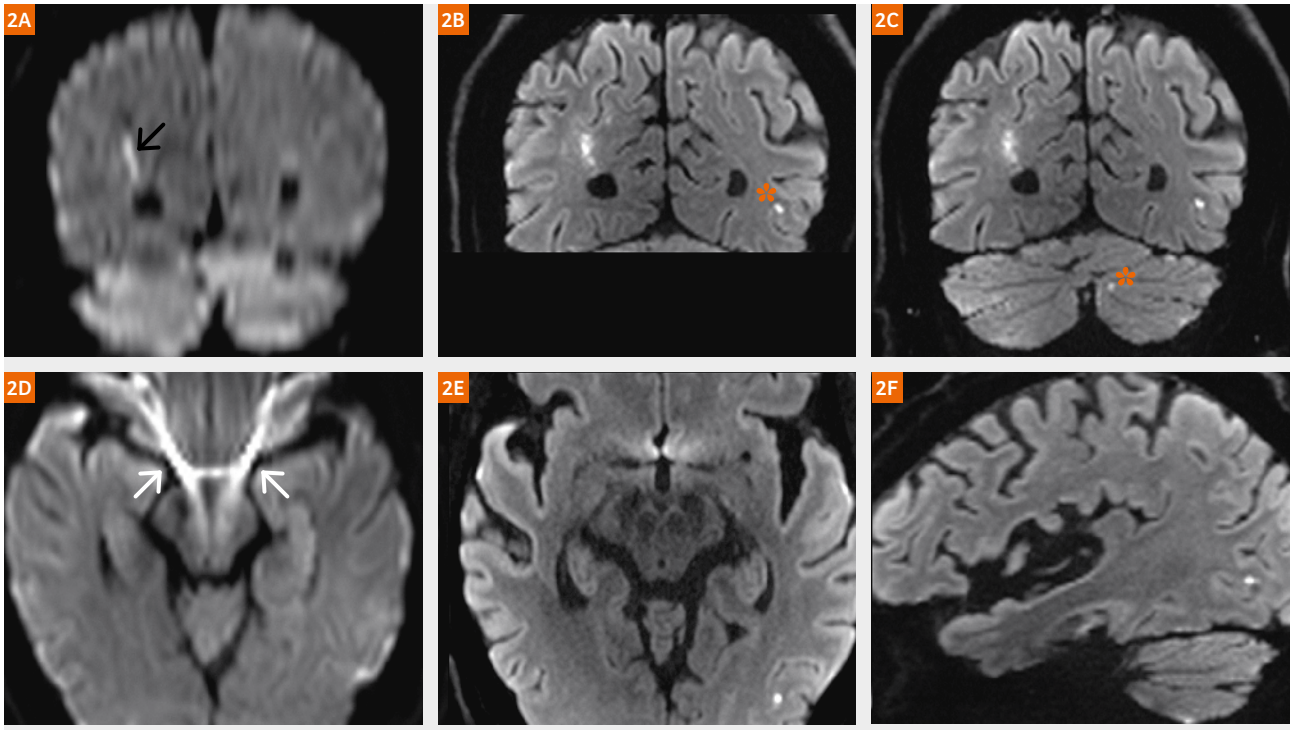

Figure 2:
Conventional 2D ss-EPI DWI (**2A, D** – 5 mm) vs. thin section (1 mm), high in plane resolution (0.6 x 0.6 mm²) scans without SMS **(2B)** and with SMS2 **(2C, E, F)**. At 3T, bulk susceptibility artifacts (white arrows) degrade substantially conventional 5 mm section ss-EPI DWI, as seen in the axial scan (2D). A coronal reformat (2A) in this patient depicts, although poorly due to the low resolution, a small watershed infarct (black arrow). By reducing slice thickness and improving in-plane spatial resolution, bulk susceptibility artifacts are reduced and the infarct is well visualized on a reformatted coronal scan (2B, from a 62 image, 1 mm slice thickness, 4:24 min:sec scan). However, the entire brain cannot be scanned thus in a reasonable acquisition time. Employing SMS2, the entire brain can be imaged, with the acquisition time in this instance 4:39 min:sec, with high-resolution images and reformats possible in all planes (2C, E, F). These images reveal a pinpoint cerebellar infarct (*, 2C) in addition to the previously noted pinpoint occipital infarct (*, 2B, also visualized in 2E and F). Note also the marked reduction in bulk susceptibility artifacts in the axial plane (2E). Full brain imaging in this instance revealed multiple pinpoint acute infarcts, none visualized on the conventional 5 mm scan, and only that in the cerebral hemispheres seen on the high-resolution scan without SMS.

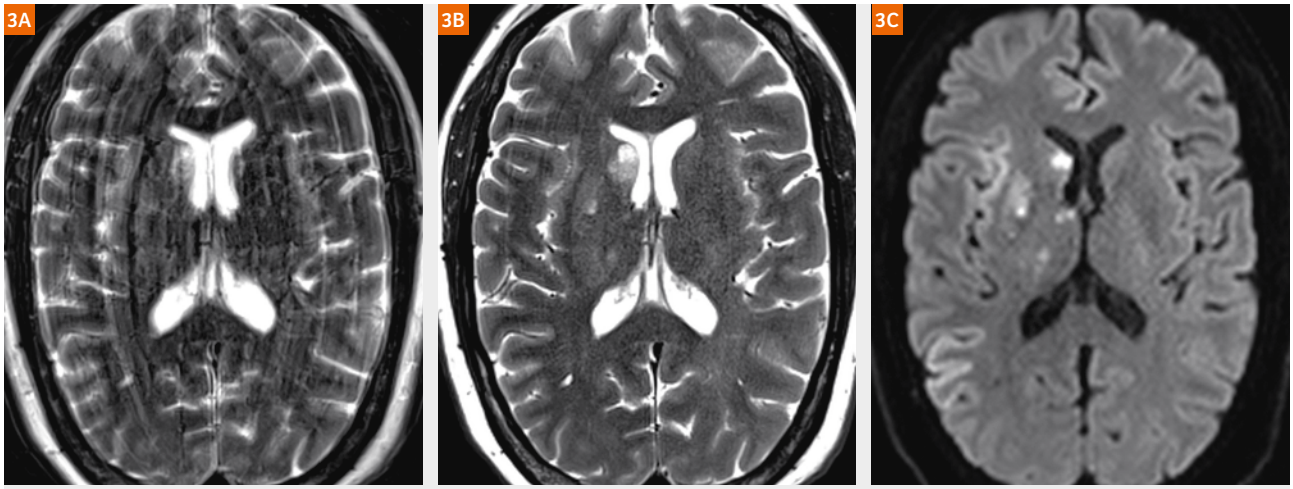

Figure 3:
Small infarcts of the caudate, putamen, and thalamus, **(3A, B)** T2-weighted TSE and **(3C)** diffusion-weighted ss-EPI scans. (3A) Conven-tional acquisition compared to (3B) SMS, using an acceleration factor of three. For the diffusion-weighted scan, (3C), SMS was also employed, with an acceleration factor of 2. Note the ghosting and image degradation on the conventional T2-weighted scan due tothe long acquisition time, with markedly improved image quality on the accelerated SMS T2-weighted scan. The SMS DWI scan was equivalent in terms of image quality to the scan acquired in a conventional fashion (not shown).

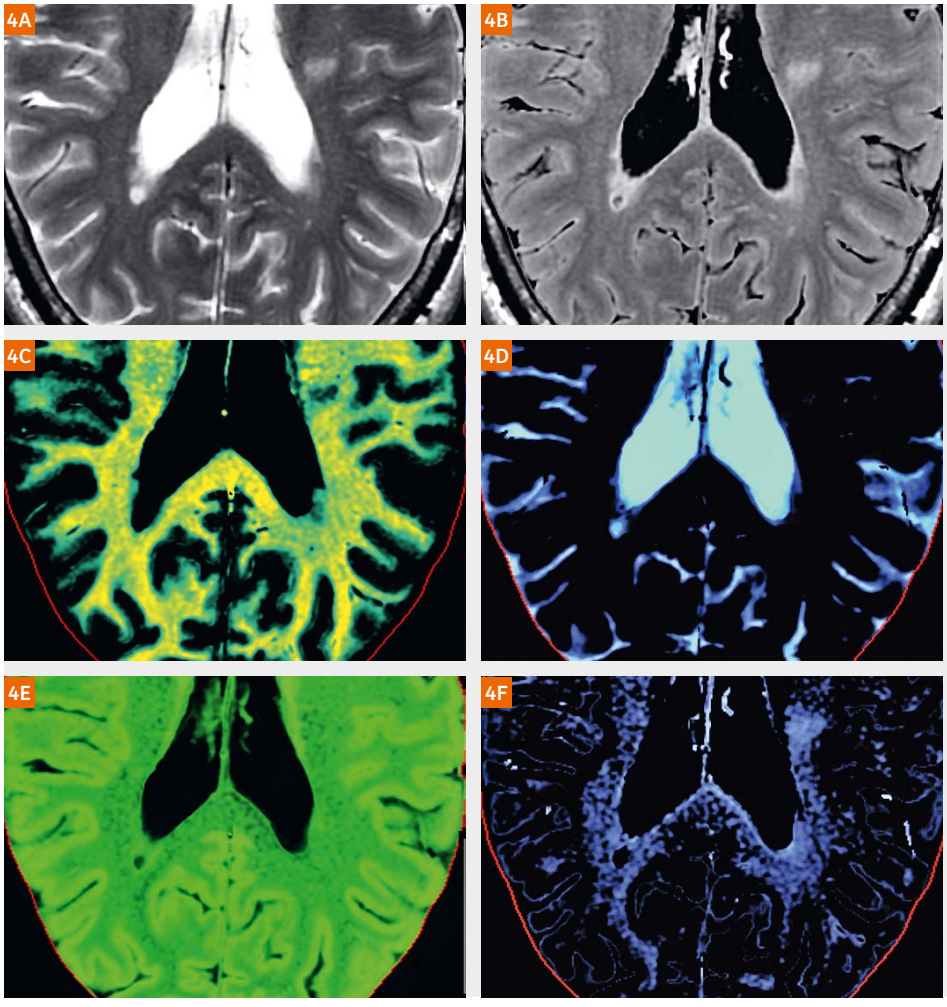

Figure 4:
Synthetic MRI, brain segmentation and myelin measurement in a patient with multiple sclerosis. From a scan requiring approximately six minutes for acquisition, R1, R2, and proton density maps are measured. This allows reconstruction of synthetic **(4A)** T2-weighted and **(4B)** FLAIR images. From the same data, myelin segmentation can be performed with calculation of **(4C)** myelin, **(4D)** free water, **(4E)** cellular, and **(4F)** excess parenchymal water partial volumes.
Reprinted with permission from Akifumi Hagiwara et al., Invest Radiol 2017;52 (10).

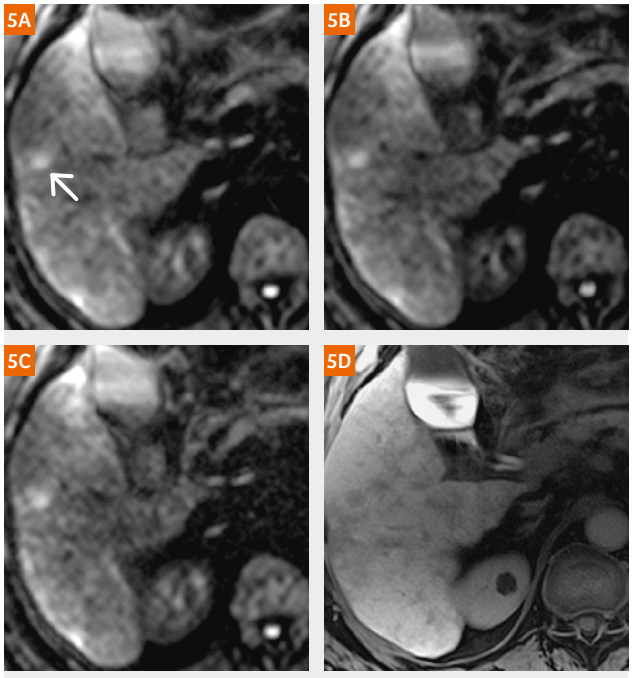

Figure 5:
SMS in liver imaging, in a patient with multifocal hepatocellular carcinoma (HCC), at 3T with 2D EPI DWI. SMS can be used, as illustrated, to either shorten scan time or acquire thinner sections without a substantial increase in scan time. Scan times were **(5A)** 2:41 (non-SMS), **(5B)** 1:38, and **(5C)** 2:54 min:sec (the latter both SMS with a 2-fold acceleration). The entire liver was covered in all scans, using a 5 mm slice thickness for **(5A, B)** and a 3 mm slice thickness for **(5C)**. A small HCC (arrow) with restricted diffusion is noted. For comparison, a delayed post-contrast scan after gadoxetic acid administration **(5D)** is also presented, using a non-breath-hold 2-minute acquisition radial VIBE scan. On the latter, the lesion is hypointense due to the lack of functioning hepatocytes.

T1, T2 and proton density maps. However, there is much more information available from such an acquisition, including volume estimations such as gray matter, white matter and ventricular volume. More sophisticated segmentation involves, as illustrated, evaluating myelin and the compartmentalization of water, which can be of value in the assessment of multiple sclerosis.

Image acquisition and reconstruction techniques that exploit data sparsity (compressed sensing) will also impact favorably brain imaging in the near future, and specifically contrast-enhanced MRA and time-of-flight (TOF) MRA – two common exams. Early clinical articles show the impact, with work in progress acquisition techniques readily available together with limited sequences for routine clinical use. Combining radial undersampling and sparse reconstruction, time resolved high-resolution contrast-enhanced MRA can be acquired, enabling improved characterization of arteriovenous malfor-mations, for example in determination of Spetzler-Martin grade as well as assessment of venous ectasia and deep venous drainage [4]. Data undersampling can also be combined with arterial spin labeling and 3D radial acquisition to improve the detection and characterization of intracranial arteriovenous shunts. 3D TOF MRA is employed clinically for brain aneurysm detection and evaluation, providing as well detection of intracranial stenoses and occlusions. This commonly used technique is also readily combined with data sparsity approaches in order to shorten scan time. Although development of specific techniques is still in its infancy, acceleration of the scan by a factor of five appears quite feasible [5].

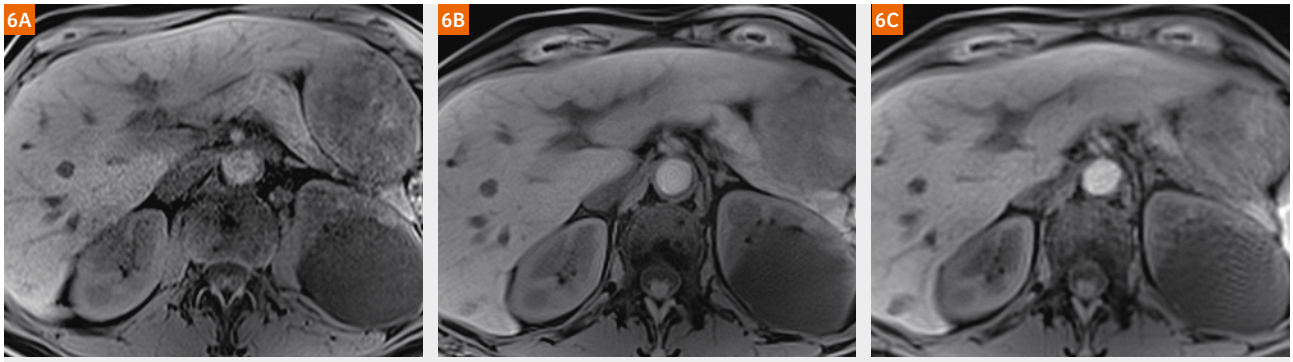

Figure 6:
Options for speed in liver T1-weighted imaging, comparison of ultrashort breath-hold and radial, free breathing, imaging. Images were acquired at 3T using a slice thickness of 3 mm without IV contrast administration. A large left renal cyst is noted. **(6A)** An ultrashort breath-hold Dixon VIBE sequence is compared to **(6B)** standard and **(6C)** scan time optimized (by restricting the number of radial views) radial VIBE scans. Scan times were 5 seconds, 2 minutes, and 21 seconds.

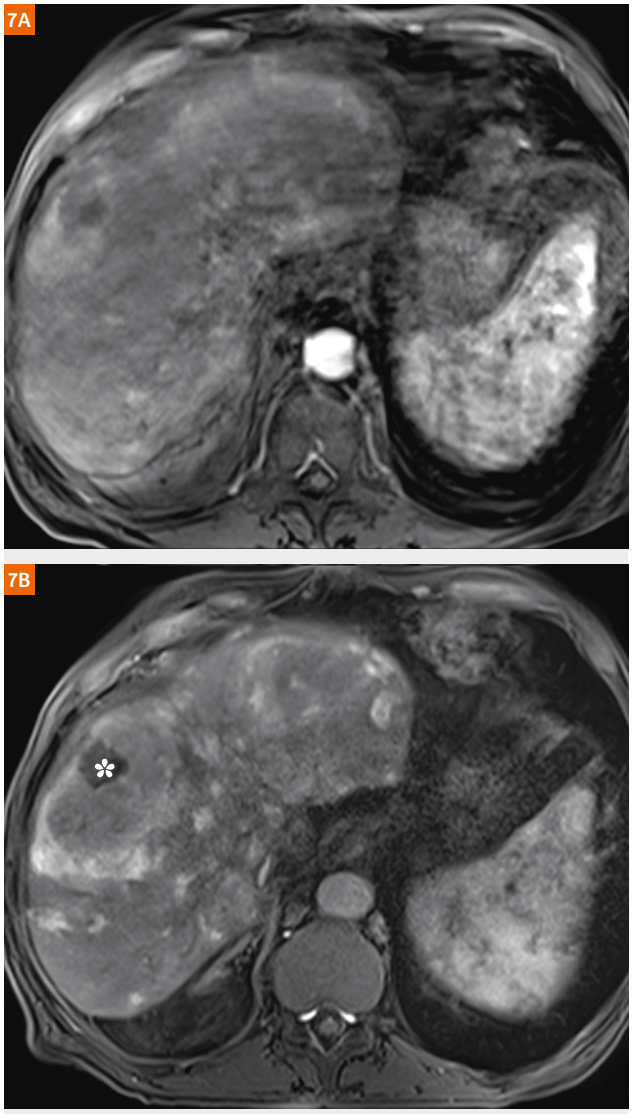

Figure 7:
Improved clinical liver imaging by utilization of ultrashort breath-hold T1-weighted imaging. Two early arterial phase T1-weighted exams in the same patient are compared. **(7A)** The first is a conventional CAIPIRINHA-VIBE sequence with fat saturation requiring an acquisition time of 16 seconds. **(7B)** The second is an accelerated Dixon VIBE sequence requiring a breath-hold time of only five seconds. A large partially necrotic hepatocellular carcinoma is noted in liver segment VIII (*) in this elderly male patient. The substantially reduced acquisition time for the latter scan (7B) enabled improved patient compliance, with the result being a marked increase in diagnostic image quality.

An important additional application of radial imaging with compressed sensing is for dynamic imaging of the pituitary (implemented with GRASP), providing both the high spatial and temporal resolution necessary for this evaluation. Very high image quality has been demonstrated in initial clinical implementation, providing improved recognition on the basis of differential contrast enhancement during the dynamic phase between the normal enhancing pituitary and microadenomas [1].

Upper abdomen

Diffusion-weighted imaging today is a vital sequence for routine abdominal MRI. Acquisition is normally during free breathing, using single shot EPI technique. SMS is easily applied, by using a shorter TR yet still enabling the desired anatomic coverage (Fig. 5) [6]. Although SMS could be used to achieve thinner sections or higher in-plane resolution, the focus for use of the technique in the upper abdomen has been to decrease scan time. Motion and the lower SNR in body imaging in general dictates the use in this manner.

Motion, primarily due to breathing, is likely the clinical factor with the greatest negative impact on the quality of MRI in the upper abdomen. Over the past 20 years, sequences have been optimized and new sequences have been developed allowing shorter and shorter breath-hold times. For example, on a state-of-the-art scanner today, the Dixon VIBE sequence can be acquired in as little as five seconds (Fig. 6). Many patients have difficulty holding their breath for even 20 seconds, with such a reduction in acquisition time improving greatly patient compliance and diagnostic image quality (Fig. 7). In patients unable to hold their breath at all, e.g. pediatric patients[2], radial imaging represents a further alternative direction for sequence development to combat breathing artifacts. As compared to a Cartesian acquisition, motion artifacts are reflected in the final image in a less prominent and more benign fashion (Fig. 6). This technique can be used to acquire high-resolution 3D post-contrast images in many regions where involuntary motion occurs, for example in the oral cavity. On the downside, however, the acquisition time for a high-resolution dataset is typically in the order of 2–3 minutes. If radial scans are optimized for scan time, the same SNR limitations as in all MR acquisitions apply. However, an additional consideration when shortening radial scans is the greater prominence of streak artifacts that reflect motion, if the approach used aims to decrease the number of phase-encoding steps.

Another consideration besides breath-hold capabilities is to gain more information in dynamic contrast-enhanced imaging with faster acquisition techniques. With CT, radiologists are largely limited by radiation dose considerations in terms of acquiring additional arterial phase images, while scan acquisition time has been the limitation in MRI.

[2] MR scanning has not been established as safe for imaging fetuses and infants less than two years of age. The responsible physician must evaluate the benefits of the MR examination compared to those of other imaging procedures.

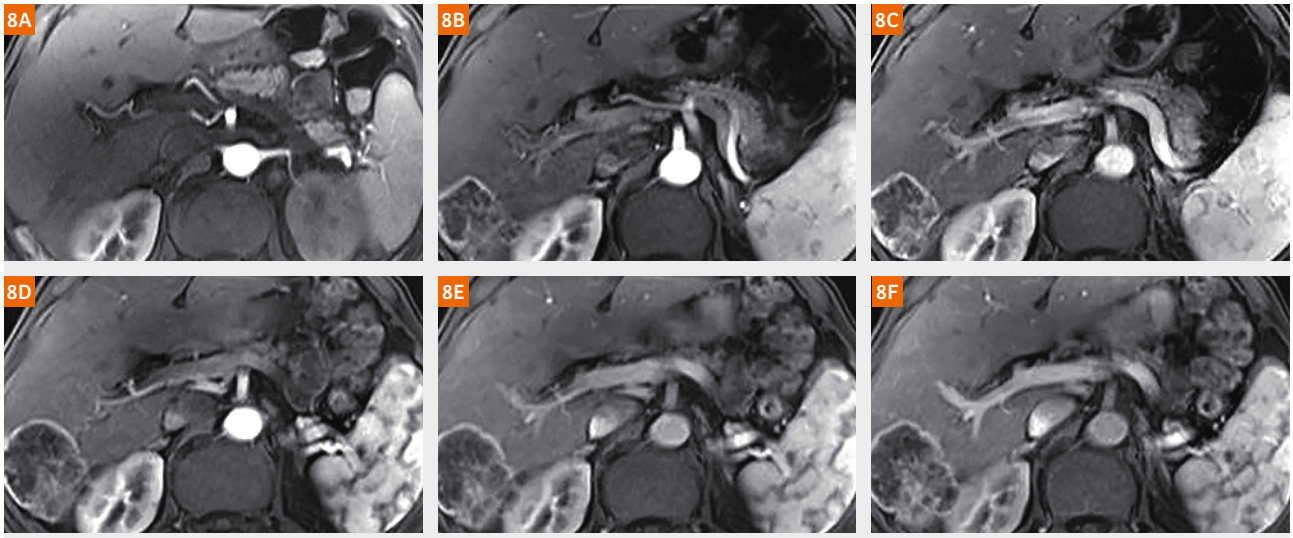

Figure 8:
Liver metastasis from rectal carcinoma, imaged with **(8A)** single phase, **(8B, C)** dual phase, and **(8D–F)** triple phase arterial acquisitions. The scans are separated in time by several months in each instance. CAIPIRINHA-VIBE with spectral fat saturation was employed for **(8A)**, CAIPIRINHA-VIBE, Dixon fat separation, and TWIST without view sharing for **(8B, C)**, and with view sharing for **(8D–F)**. Acquisition times for the three techniques per phase were 13 vs. 7.5 vs. 4.6 seconds. Use of the dual arterial phase acquisition led to well-timed arterial phase images with low respiratory motion artifact.
Adapted with permission from Yang Shin Park et al., Invest Radiol 2017;52 (10).

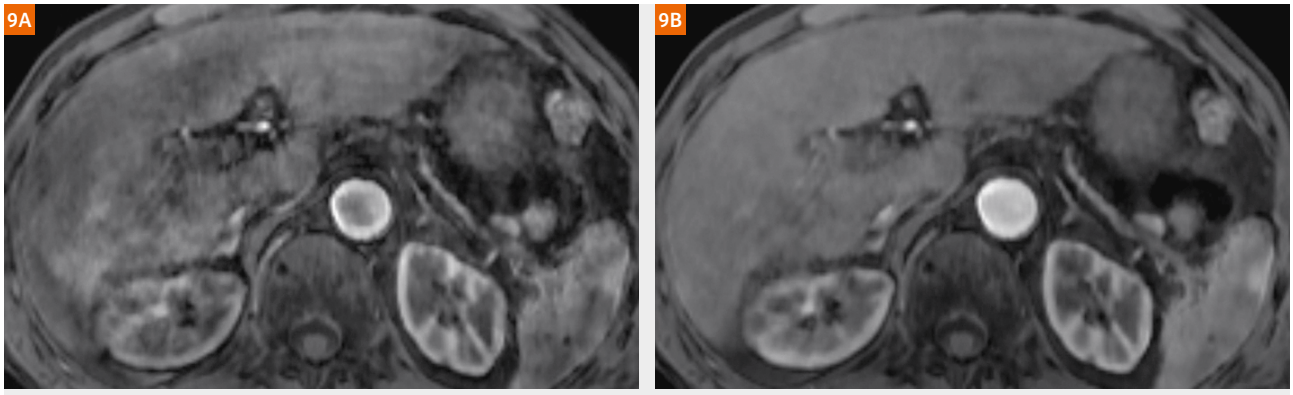

Figure 9:
Improved early arterial phase liver imaging using compressed sensing with respiratory-motion resolved reconstruction (XD-VIBE)[3].
The patient is an 81-year-old man with chronic hepatitis B and limited breath-holding capacity. The scans were acquired during free breathing. Pre-contrast, multi-arterial and portal venous phases were obtained with compressed sensing VIBE. Using a navigation signal acquired as part of the acquisition, two different image sets were reconstructed, **(9A)** the first using hard gating by either rejecting or accepting the echo train for reconstruction. For **(9B)** the second image set, with motion resolved reconstruction, the echo train was assigned to the motion state determined by the navigation signal. A substantial reduction in motion artifacts and improved image quality is achieved with (9B) XD-VIBE.
Reprinted with permission from Jeong Hee Yoon et al, Invest Radiol 2017;52 (10).

With the advent of new sequence types, however, multi-phase arterial acquisitions became possible, opening up a new diagnostic window for MRI of the upper abdomen (Fig. 8) [7]. By combining a view-sharing acquisition scheme with highly accelerated parallel imaging and fast T1-weighted 3D imaging (TWIST-VIBE), acquisition times of five seconds for imaging the entire upper abdomen are now possible. This allows for acquisition of early, mid and late arterial phase MR imagings in one 15-second breath-hold. In the past few years, many clinical studies have been published that advocate this approach and have shown the additional diagnostic information available in multi-arterial acquisitions.

[3] WIP, the product is currently under development and is not for sale in the US and in other countries. Its future availability cannot be ensured.

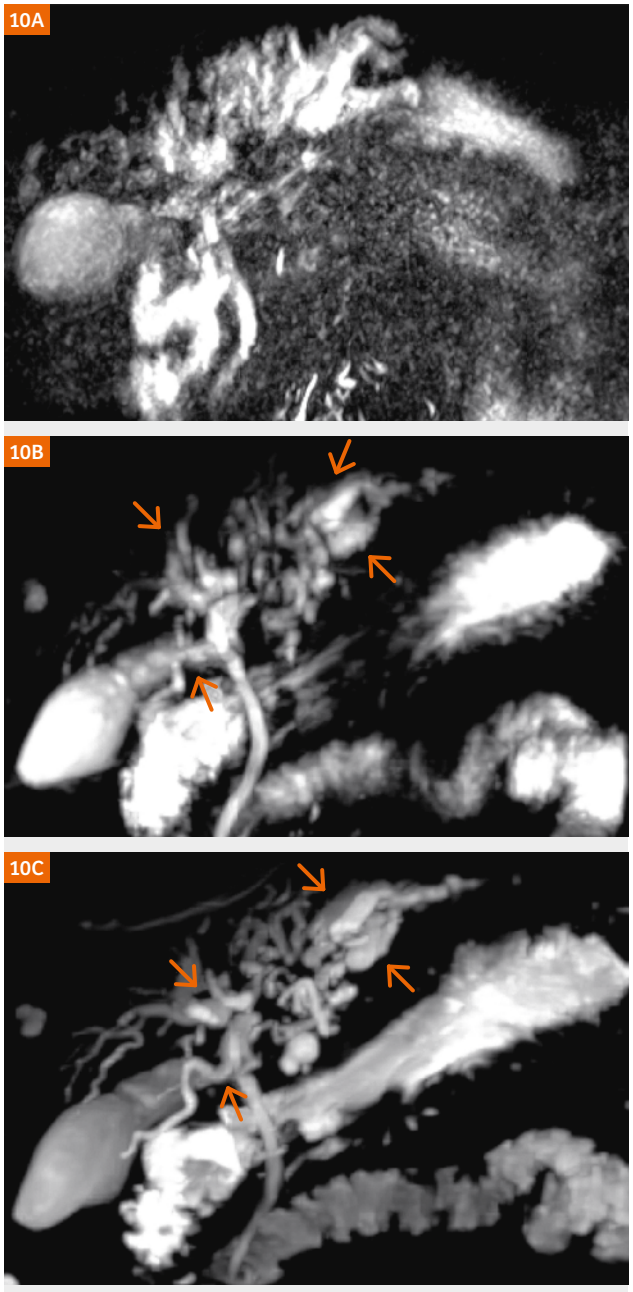

Figure 10:
3D MRCP exams of a patient with a hilar cholangiocarcinoma, comparing **(10A)** conventional and **(10B, C)** compressed sensing exams, with **(10C)** acquired during breath holding (16 sec). Conventional 3D MRCP exams require on the order of 5–10 minutes for acquisition, depending on the breathing pattern of the patient. On the conventional exam, dilatation of the intrahepatic ducts is evident, but the exam otherwise uninterpretable due to motion artifacts. Image quality with the non-breath hold compressed sensing exam is markedly improved. However, dilatation of the intrahepatic ducts and in particular second order branches (arrows) of the left hepatic duct are best visualized on the breath-hold compressed sensing exam. *Adapted with permission from Jeong Hee Yoon et al, Invest Radiol 2017;52 (10).*

While beath-holds are still required with the TWIST-VIBE approach, the combination of radial image acquisition with compressed sensing reconstruction (GRASP-VIBE) was a seminal development in abdominal MRI in this decade. The previously mentioned streaking artifacts can be significantly reduced by introducing iterative reconstruction, thereby enabling reconstruction of 3D datasets that cover time frames of 5–10 seconds. This enables the acquisition of dynamic, contrast-enhanced scans of the liver during free-breathing in one continuous run. Studies have shown that this overcomes the timing challenges in dynamic imaging as well as limiting respiratory artifacts, expanding substantially the patient population eligible for abdominal MRI. A further improvement of image quality is achieved by applying self-gating, which recognizes the end-expiratory phase and rejects all other data.

The integration of compressed sensing into sequences optimized for imaging of the upper abdomen has already had a major impact upon clinical imaging, with further major developments anticipated in this rapidly developing field. XD-VIBE[3] is one such approach, using compressed sensing and simultaneous acquisition of a navigator signal for motion resolved reconstruction (Fig. 9) [8]. With this approach, excellent image quality and lesion detectability, together with a relative lack of motion artifacts, has been demonstrated in oncologic patients with images acquired during free breathing [9].

Turning to the biliary system, compressed sensing has a major impact as well in MR cholangiopancreatography. An important scan clinically is the heavily T2-weighted 3D acquisition which is used to visualize the biliary ducts. Due to the number of breath-holds required and the long TR, acquisition time is typically in the order of 4–6 minutes. This exam, when acquired with SPACE, may also be combined with compressed sensing. Depending upon the desired result, a substantial reduction in scan time can be achieved with the exam still acquired during quiet breathing, or the scan can be further optimized to allow acquisition in a single breath-hold [10]. Initial results favor clinical use of the latter (Fig. 10), reflecting as well the historical development of upper abdominal MR imaging.

Musculoskeletal system

As in other areas of the body, simultaneous multi-slice and compressed sensing go hand-in-hand in terms of improving the clinical exam in musculoskeletal imaging. For the knee in particular, due to the cylindrical, high number of elements design of the receiver coil, SMS is

[3] WIP, the product is currently under development and is not for sale in the US and in other countries. Its future availability cannot be ensured.

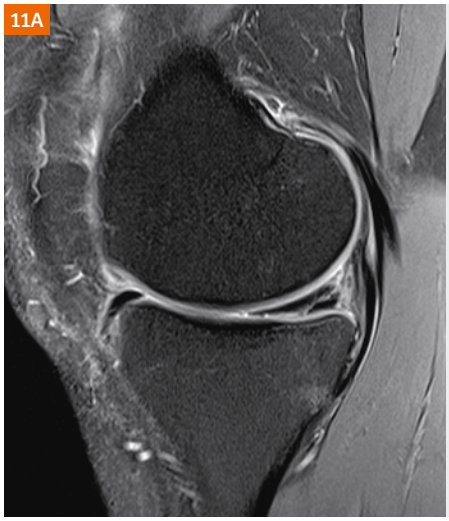

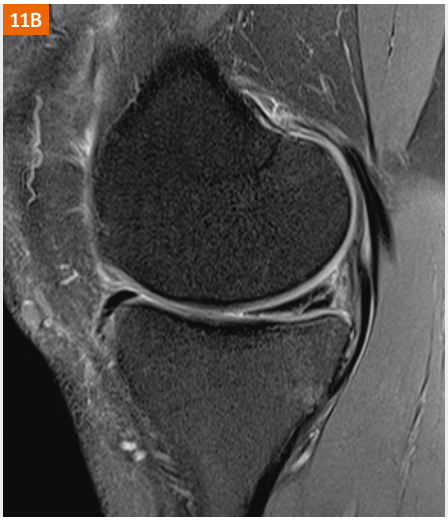

Figure 11:
High-resolution sagittal proton density-weighted images of a horizontal tear of the medial meniscus (posterior horn) demonstrating the value of SMS. Turbo spin echo exams acquired **(11A)** in a conventional fashion and **(11B)** using 2-fold SMS acceleration are compared. Voxel dimensions were 0.5 x 0.4 x 2.5 mm^3. Scan time was reduced from 6:36 to 3:27 min:sec by the use of SMS, with image quality and SNR maintained.

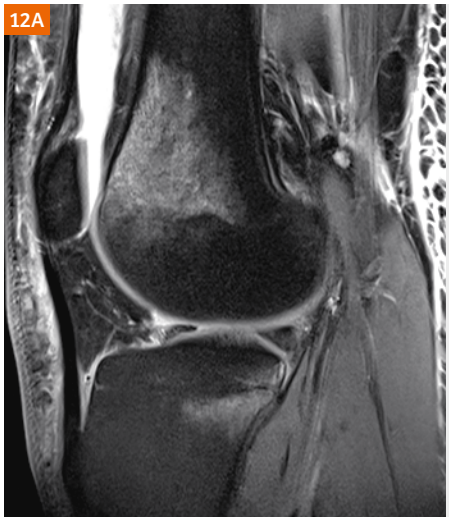

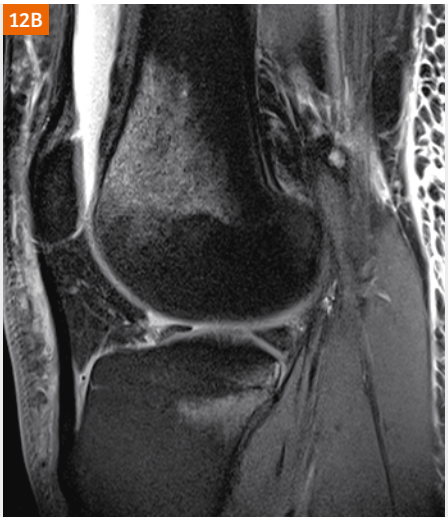

Figure 12:
SMS can be employed to markedly shorten scan time, which can be of high value either to increase patient throughput or as in the current example in the evaluation of a trauma patient. Extensive bone marrow edema (within the distal femur and proximal tibia) is seen, together with subcutaneous edema posteriorly and a large effusion within the suprapatellar bursa, on sagittal proton density-weighted images (with fat saturation) in this patient. As compared to **(12A)** the conventional scan, using **(12B)** an SMS factor of 2, the acquisition time was reduced by nearly a factor of two, to 1:34 min:sec.

highly applicable. The complex anatomy and numerous small critical components of the knee, all important for its proper function, have driven knee imaging clinically towards higher and higher resolution. The application of SMS enables a substantial reduction in scan time, making such desired high-resolution techniques viable (Fig. 11). Alternatively, if standard resolution scans will suffice for the clinical question and/or if possible patient movement limits the exam, for example in trauma patients, SMS can be critical to enable faster scans (Fig. 12). Both proton density and T2-weighted scans are commonly used in the musculoskeletal system, with SMS easily integrated in both instances. The use of two concatenations is often required, or a prolongation of TR, due to the number of slices needed to cover the structure anatomically using thin section imaging, with an SMS factor of 2 thus readily applicable.

The use of SEMAC for the reduction of metal[4] artifacts in orthopedic imaging is an ideal area for scan time reduction by the implementation of compressed sensing. Metal artifacts in many instances limit image interpretability, in particular at 3T. SEMAC corrects for metal artifacts by robust encoding of each excited slice. View angle tilting is incorporated to suppress most in-plane distortions, with *z*-phase encoding resolving the distorted excitation profiles which cause through-plane distortion. Unfortunately, the addition of *z*-phase encoding steps leads to longer scan times. To maintain feasible scan times, compressed sensing is incorporated into the SEMAC sequence. 8-fold acceleration through the implementation

[4] The MRI restrictions (if any) of the metal implant must be considered prior to patient undergoing MRI exam. MR imaging of patients with metallic implants brings specific risks. However, certain implants are approved by the governing regulatory bodies to be MR conditionally safe. For such implants, the previously mentioned warning may not be applicable. Please contact the implant manufacturer for the specific conditional information. The conditions for MR safety are the responsibility of the implant manufacturer, not of Siemens.

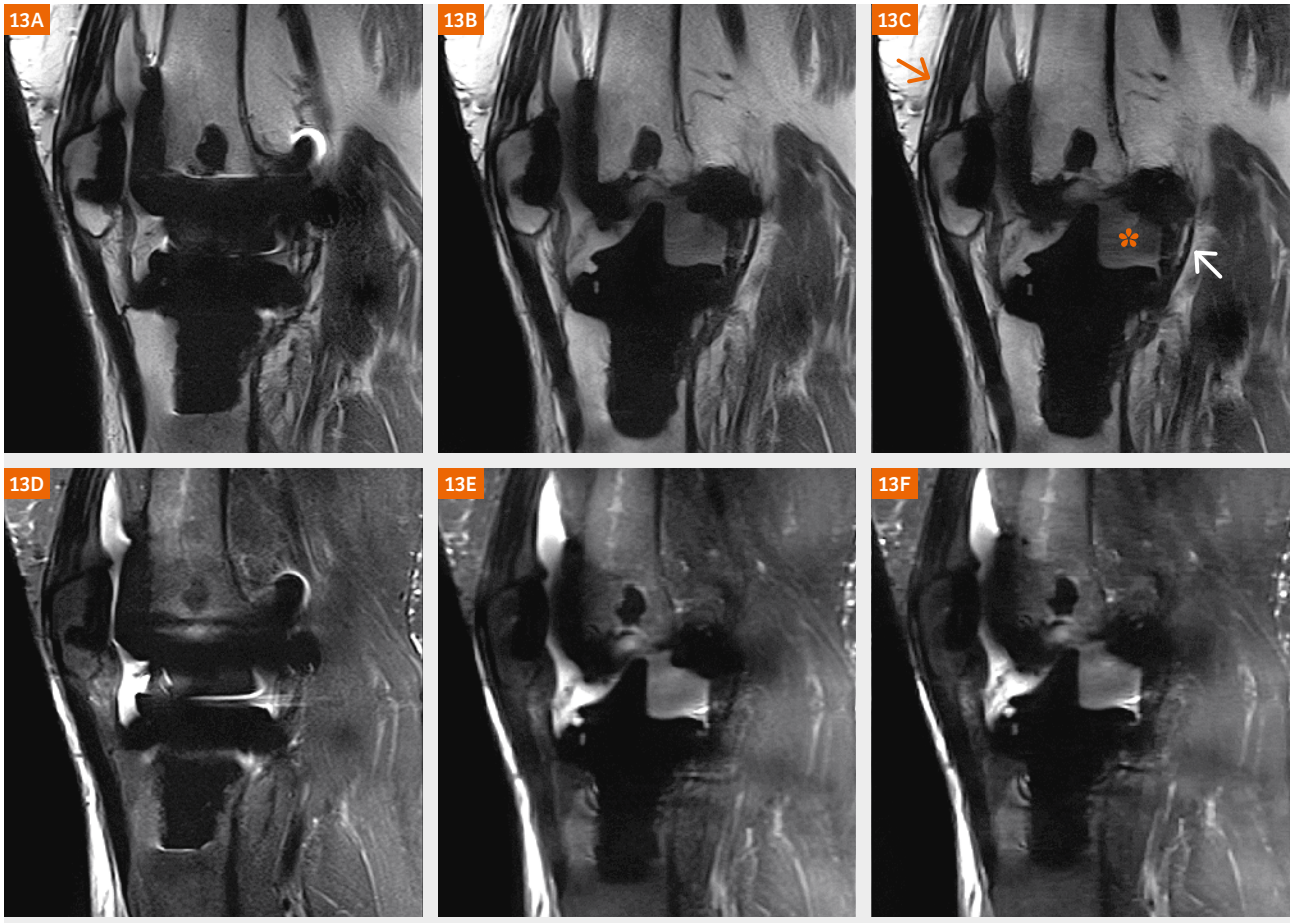

Figure 13:
Comparison of **(13A, D)** high-bandwidth TSE, **(13B, E**) SEMAC TSE, and **(13C, F)** compressed sensing SEMAC TSE[3] for metal artifact reduction. The (13A–C) upper row of images is with mild proton density-weighting and the (13D–F) lower row acquired with STIR. This older man had a cobalt-chromium knee arthroplasty implant. Scan times for the high-bandwidth sequences were five minutes, which with the application of SEMAC extended to 11 minutes in each instance. The application of compressed sensing allowed a reduction in scan time of the sequences with SEMAC to that of the high-bandwidth sequences. The extensor mechanism (orange arrow) is well seen on all scans, however the articular structures including specifically joint fluid (*) and the posterior capsule (white arrow) are best seen on the SEMAC images.
Adapted with permission from Jan Fritz et al., Invest Radiol 2016;51: 666–676.

of compressed sensing–based incoherent *k*-space undersampling has been demonstrated, yielding improved image quality relative to the use of high-bandwidth alone and equivalent image quality to the much longer conventional SEMAC acquisition (Fig. 13) [11]. This approach enables SEMAC to be extended in clinical application to the millions of patients with metallic implants.

Breast

Today breast MRI is an integral part of screening, diagnosis, and follow-up for breast cancer. For radiographic breast imaging, the direction of development has been towards increasingly complex and expensive methods [12]. Both SMS and compressed sensing offer an excellent way to move in the opposite direction, specifically in terms of shortening the exam. The application of SMS is simplistic, simply to decrease scan time for breast diffusion-weighted imaging, a crucial part of any breast evaluation (Fig. 14).

Dynamic contrast-enhanced (DCE) MR imaging is a vital tool in the diagnosis of breast cancer. To assess tumor morphology and contrast kinetics, ideally such an acquisition would have both high spatial and temporal resolution. The use of compressed sensing (CS), specifically in combination with VIBE, permits an increase in through-plane spatial resolution in dynamic exams with comparable visual assessment of lesions as with

[3] WIP, the product is currently under development and is not for sale in the US and in other countries. Its future availability cannot be ensured.

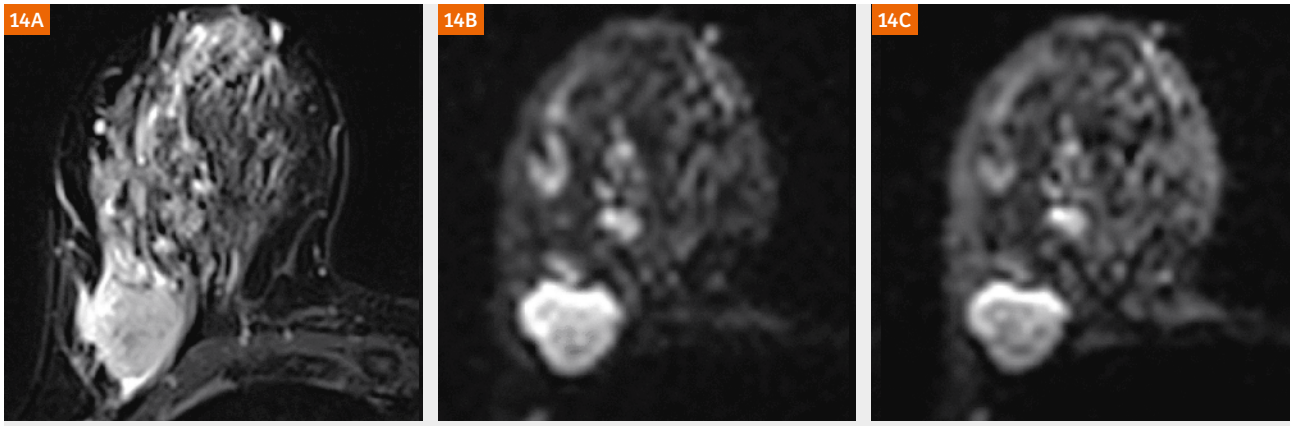

Figure 14:
The application of SMS to reduce scan time for readout segmented (rs, RESOLVE) EPI DWI in imaging of the breast. **(14A)** T2-weighted Dixon TSE and **(14B, C)** rs-EPI DWI scans of the right breast in a 45-year-old woman with invasive breast carcinoma are presented. The diffusion-weighted scans are 3 mm in slice thickness, with scan times of (14B) 7:28 and (14C) 3:17 min:sec. For (14C) an SMS factor of 2 was used.

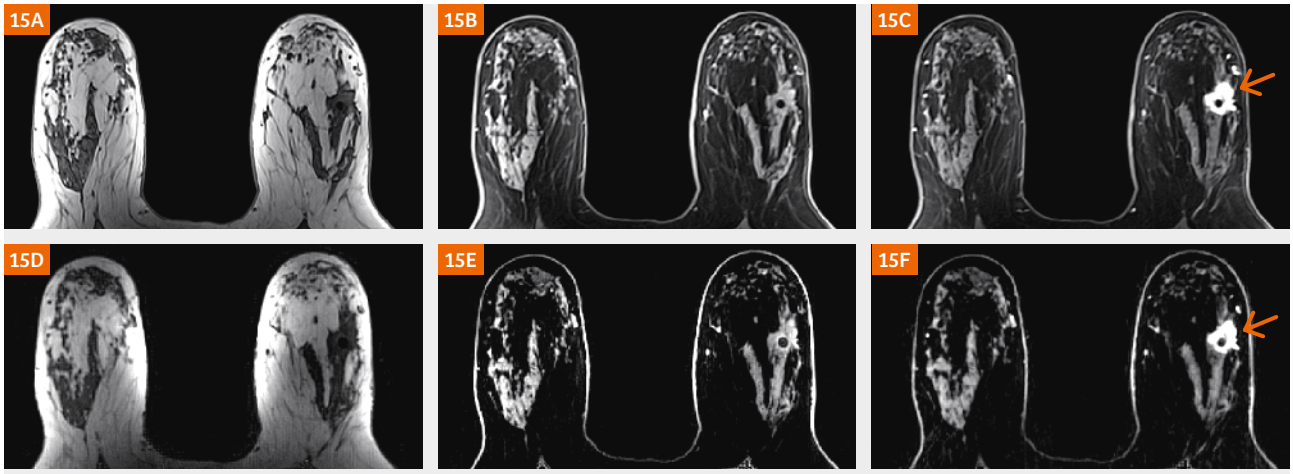

Figure 15:
Applicability of Dixon radial volumetric encoding (Dixon-RAVE[3]) for a comprehensive 3D dynamic contrast-enhanced MR exam of the breast. Conventional T1-weighted VIBE scans pre-contrast **(15A)** without and **(15B)** with fat suppression together with a **(15C)** post-contrast fat suppressed scan are illustrated on the top row. The images with equivalent tissue contrast on the bottom row **(15D–F)** are from a single continuous Dixon-RAVE scan performed during contrast injection, employing radial sampling and compressed sensing. This approach provides a diagnostic quality, comprehensive T1-weighted breast MR with high spatiotemporal resolution, reduced overall imaging time, and superior fat suppression. Illustrated are scans from a 61-year-old woman with invasive ductal carcinoma (arrow). *Reprinted with permission from Thomas Benkert et al, Invest Radiol 2017;52 (10).*

non-dynamic techniques such as VIBE-Dixon [13]. For example, in the clinical study just referenced, acquisition time was decreased by a factor of 18 in comparison to the T1-weighted Dixon sequence, yet with morphologic assessment not significantly different. CS-VIBE is a promising technique for ultrafast MR imaging, providing high spatial and temporal resolution, with image quality comparable to non-dynamic scans, providing in distinction to prior dynamic techniques reduced temporal blurring as well as the possibility of multiplanar lesion morphology assessment.

Another application of compressed sensing for dynamic contrast enhanced 3D breast imaging is with Dixon radial volumetric encoding (Dixon-RAVE)[3] [14]. Robust and uniform fat suppression improves the clinical applicability of DCE breast MRI. Dixon-RAVE combines compressed sensing, radial sampling and excellent fat suppression – providing scans with both high spatial and temporal resolution. In addition to contrast-enhanced images,

[3] WIP, the product is currently under development and is not for sale in the US and in other countries. Its future availability cannot be ensured.

from such an acquisition pre-contrast images with and without fat suppression can be extracted, enabling a comprehensive T1-weighted DCE exam with reduced overall scan time. Dixon-RAVE thus can serve as a one-stop-shop approach for comprehensive T1-weighted imaging of the breast (Fig. 15).

Conclusion

Improving the speed of MRI is important for its continued future widespread clinical use and success. Sparse imaging (compressed sensing, CS) and simultaneous multi-slice (SMS) are the two most important developments in the current decade to achieve this goal. These build upon the foundations laid by parallel imaging, VIBE, and radial imaging as well as many other innovations. CS and SMS have very general applications in routine clinical practice, together with improving several important subspecialty exams, covering the spectrum of what clinical MRI offers today, for example from pituitary imaging on the one hand to metal artifact reduction in musculoskeletal imaging on the other. Speed also improves the robustness of the technique, with these developments fundamentally impacting clinical utilization today and further developments extending at least into the next decade.

Contact

Val M. Runge, M.D.
Editor-in-Chief, Investigative Radiology
Department of Diagnostic, Interventional and Pediatric Radiology
University Hospital of Bern, Inselspital Bern
Switzerland
ValMurray.Runge@insel.ch

References

1 Runge VM, Richter JK, Heverhagen JT. Speed in Clinical Magnetic Resonance. Invest Radiol. 2017;52(1):1-17.
2 Barth M, Breuer F, Koopmans PJ, Norris DG, Poser BA. Simultaneous multislice (SMS) imaging techniques. Magn Reson Med. 2016;75(1):63-81.
3 Hagiwara A, Warntjes M, Hori M, et al. SyMRI of the Brain: Rapid Quantification of Relaxation Rates and Proton Density, With Synthetic MRI, Automatic Brain Segmentation, and Myelin Measurement. Invest Radiol. 2017;52(10):647-657.
4 Schubert T, Wu Y, Johnson KM, et al. Time-of-Arrival Parametric Maps and Virtual Bolus Images Derived From Contrast-Enhanced Time-Resolved Radial Magnetic Resonance Angiography Improve the Display of Brain Arteriovenous Malformation Vascular Anatomy. Invest Radiol. 2016;51(11):706-13.
5 Fushimi Y, Fujimoto K, Okada T, et al. Compressed Sensing 3-Dimensional Time-of-Flight Magnetic Resonance Angiography for Cerebral Aneurysms: Optimization and Evaluation. Invest Radiol. 2016;51(4):228-35.
6 Taron J, Weiss J, Martirosian P, et al. Clinical Robustness of Accelerated and Optimized Abdominal Diffusion-Weighted Imaging. Invest Radiol. 2017;52(10):590-595.
7 Park YS, Lee CH, Kim JW, Lee YS, Paek M, Kim KA. Application of High-Speed T1 Sequences for High-Quality Hepatic Arterial Phase Magnetic Resonance Imaging: Intraindividual Comparison of Single and Multiple Arterial Phases. Invest Radiol. 2017;52(10):605-611.
8 Yoon JH, Yu MH, Chang W, et al. Clinical Feasibility of Free-Breathing Dynamic T1-Weighted Imaging With Gadoxetic Acid-Enhanced Liver Magnetic Resonance Imaging Using a Combination of Variable Density Sampling and Compressed Sensing. Invest Radiol. 2017;52(10):596-604.
9 Kaltenbach B, Bucher AM, Wichmann JL, et al. Dynamic Liver Magnetic Resonance Imaging in Free-Breathing: Feasibility of a Cartesian T1-Weighted Acquisition Technique With Compressed Sensing and Additional Self-Navigation Signal for Hard-Gated and Motion-Resolved Reconstruction. Invest Radiol. 2017;(11).
10 Yoon JH, Lee SM, Kang HJ, et al. Clinical Feasibility of 3-Dimensional Magnetic Resonance Cholangiopancreatography Using Compressed Sensing: Comparison of Image Quality and Diagnostic Performance. Invest Radiol. 2017;52(10):612-619.
11 Fritz J, Ahlawat S, Demehri S, et al. Compressed Sensing SEMAC: 8-fold Accelerated High Resolution Metal Artifact Reduction MRI of Cobalt-Chromium Knee Arthroplasty Implants. Invest Radiol. 2016;51(10):666-76.
12 Kuhl CK. The Changing World of Breast Cancer: A Radiologist's Perspective. Invest Radiol. 2015;50(9):615-28.
13 Vreemann S, Rodriguez-Ruiz A, Nickel D, et al. Compressed Sensing for Breast MRI: Resolving the Trade-Off Between Spatial and Temporal Resolution. Invest Radiol. 2017;52(10):574-582.
14 Benkert T, Block KT, Heller S, et al. Comprehensive Dynamic Contrast-Enhanced 3D Magnetic Resonance Imaging of the Breast With Fat/Water Separation and High Spatiotemporal Resolution Using Radial Sampling, Compressed Sensing, and Parallel Imaging. Invest Radiol. 2017;52(10):583-589.

Try them on your system

Trial licenses for many of the applications featured in this issue of MAGNETOM Flash are available free of charge for a period of 90 days.

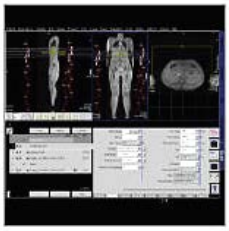

Tim Planning Suite
Allows planning of several stations at once, e.g. on composed localizer images. >

Tim Planning Suite

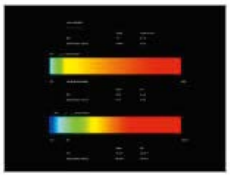

LiverLab
Evaluating the iron and fat content of the liver is an important step in monitoring early stages of liver diseases. >

LiverLab

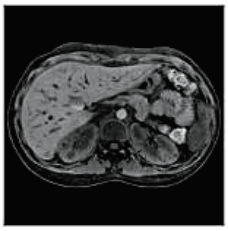

FREEZEit
Embrace motion in liver imaging. >

FREEZEit

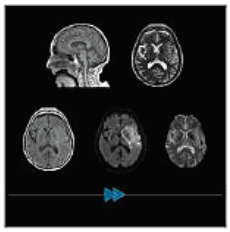

GOBrain
Push-button brain exam in 5 minutes.* >

GOBrain

Brain Dot Engine
The Brain Dot Engine increaes productivity and standardization with guided and automated workflows. >

Brain Dot Engine

Abdomen Dot Engine
The Abdomen Dot Engine is customized for dynamic liver examinations and cosistent contrast timing. >

Abdomen Dot Engine

Spine Dot Engine
The Spine Dot Engine optimizes cervical, thoracic, and lumbar spine imaging for a wide range of patients and conditions. >

Spine Dot Engine

Breast Dot Engine
The Breast Dot Engine supports consistent frequency selection for fat, water, saline or silicone. >

Breast Dot Engine

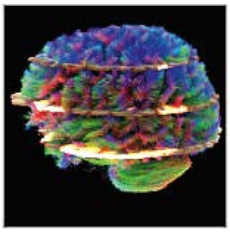

Simultaneous Multi-Slice
Accelerate advanced neuro applications for clinical routine. >

Simultaneous Multi-Slice

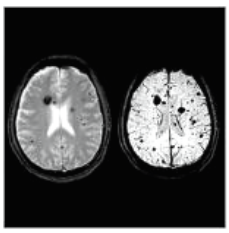

SWI
SWI is a new type of contrast technique in MRI that detects blood and iron deposits better than conventinal methods. >

Susceptibility-Weighted Imaging

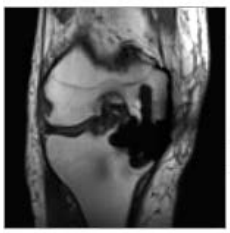

Advanced WARP
Advanced WARP corrects in- and through-plane distortions for more accurate diagnosis of tissue surrounding orthopedic implants. >

Advanced WARP

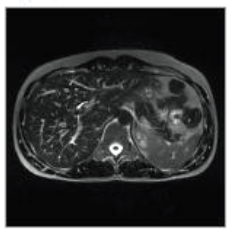

SPACE
SPACE enables the acquisition of high resolution 3D datasets. >

SPACE

For further details, product overviews, image galleries, step-by-step videos and general requirements visit us at:

www.siemens.com/mri-options-overview

Enhancing the Quality of MRI Services with a MAGNETOM Aera MRI System

Lawrance KC Yip[1]; Wendy WM Lam[2]

[1] Department Manager, Department of Radiology, Queen Mary Hospital, Hong Kong
[2] Consultant Radiologist / Chief of Service, Department of Radiology, Queen Mary Hospital, Hong Kong

Introduction

In view of the escalating demand for MRI services, one of the annual plan programs of the Hospital Authority in Hong Kong for the 2015/2016 fiscal year included installing a third MRI system in the Department of Radiology at Queen Mary Hospital. The decision to purchase a 1.5T MAGNETOM Aera MRI system was based on the results of an open bidding process. To accommodate an additional MRI system, the seminar room in the MRI Unit was converted into a control room, scanner room, and computer room. The new MRI suite has limited floor space, but MAGNETOM Aera's short bore design means that it fits in a smaller scanner room while still providing a field of view measuring 50 cm x 50 cm x 45 cm. The 70-cm magnet bore enhances patient comfort, reduces anxiety-related movement, and benefits claustrophobic patients. The MAGNETOM Aera system went into operation in January 2016. By June 2017, it had already provided MRI services to more than 4,000 patients.

With its cutting-edge hardware configuration and imaging applications, the MAGNETOM Aera system greatly enhances the quality of MRI examinations. It has also allowed us to expand the scope of MRI applications to accommodate our clinical needs. In what follows, we highlight a number of imaging applications and techniques to illustrate the expanded clinical capabilities of our new MRI system.

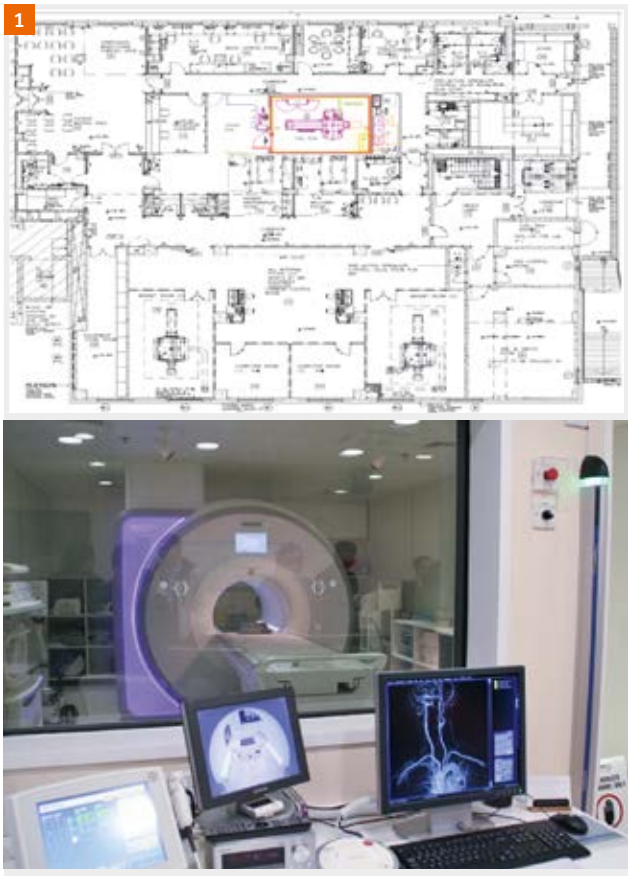

Figure 1:
MRI Unit, Department of Radiology, Queen Mary Hospital.

Dot (day optimizing throughput) engines

Our MAGNETOM Aera MRI system operates on the *syngo* MR E11 platform, where the Dot engines offer a customizable framework for patient personalization, user guidance, and examination automation to enhance clinical workflows and increase staff efficiency. The Brain Dot Engine features an AutoAlign function that automatically aligns e.g. transverse slices with the anterior and posterior commissures of the brain to ensure consistent slice positioning for different patients, and for follow-up scans of the same patient. The Spine Dot Engine has an automatic spine-labelling function that can label vertebral levels from the cervical to the lumbosacral region by acquiring dedicated multistation scout images. Once the system-generated vertebral levels have been checked and confirmed by radiographers, the labels will be indicated on the corresponding transverse images of the spine to facilitate radiology reporting. This can significantly enhance the efficiency of MRI workflows.

Dixon fat and water separation
Thanks to the excellent field homogeneity of the TrueForm magnet design in the MAGNETOM Aera system, the Dixon technique can be used for all anatomical regions to provide homogeneous fat and water images over a large field of view and thus enhance lesion conspicuity on T2-weighted or post-contrast images. It is particularly useful for musculoskeletal and head-and-neck imaging, as conventional spectral fat saturation can be problematic in these cases.

TWIST-VIBE, StarVIBE, and SPACE for abdominal MRI
TWIST-VIBE is a keyhole imaging and echo-sharing technique offering high temporal and spatial resolution in 3D T1-weighted gradient-echo images for multiple arterial phase MRI of the liver and abdominal organs. Three or four arterial phases can be acquired with a single breath-hold to catch the optimal point of the arterial phase for lesion characterization.

StarVIBE is a free-breathing, 3D T1-weighted gradient-echo sequence with radial *k*-space trajectories. It reduces motion artifacts caused by breathing, swallowing, bowel peristalsis, etc. It is useful for pediatric patients and patients who cannot comply with breath-hold instructions during body MRI examinations.

SPACE (sampling perfection with application-optimized contrast using different flip angle evolution) is a 3D turbo spin echo sequence offering high spatial resolution isotropic data for retrospective multiplanar reconstruction. It can be used in conjunction with navigator echo gating for MRCP examinations.

Quiescent-interval single-shot (QISS) non-contrast-enhanced MR angiography of the lower limbs
QISS imaging is a non-contrast-enhanced MR angiography technique for the lower limbs that uses a stack of cardiac-gated 2D TrueFISP images. The pulse sequence design includes a slice-selective saturation radiofrequency pulse, a spatial venous saturation pulse, a quiescent interval for inflow of fresh arterial spins, and a spectrally selective fat-saturation radiofrequency pulse to augment the arterial signal of the lower limbs. QISS benefits patients who have suspected peripheral vascular disease with renal dysfunction, and for whom gadolinium-based contrast media are contraindicated. Moreover, QISS images can act as a road map for subsequent contrast-enhanced MRA of the lower limbs to ensure sufficient anatomical coverage of the vasculatures of interest.

MyoMaps
MyoMaps sequences can provide pixel maps of myocardial T1 or T2 relaxation times. The related T1 or T2 maps can be acquired with a single breath-hold and include inline non-rigid motion correction and pixel-wise fitting. Additional parameters of T1 and T2 relaxation times are available for characterizing myocardial tissue, and in particular for assessing nonischemic cardiomyopathy.

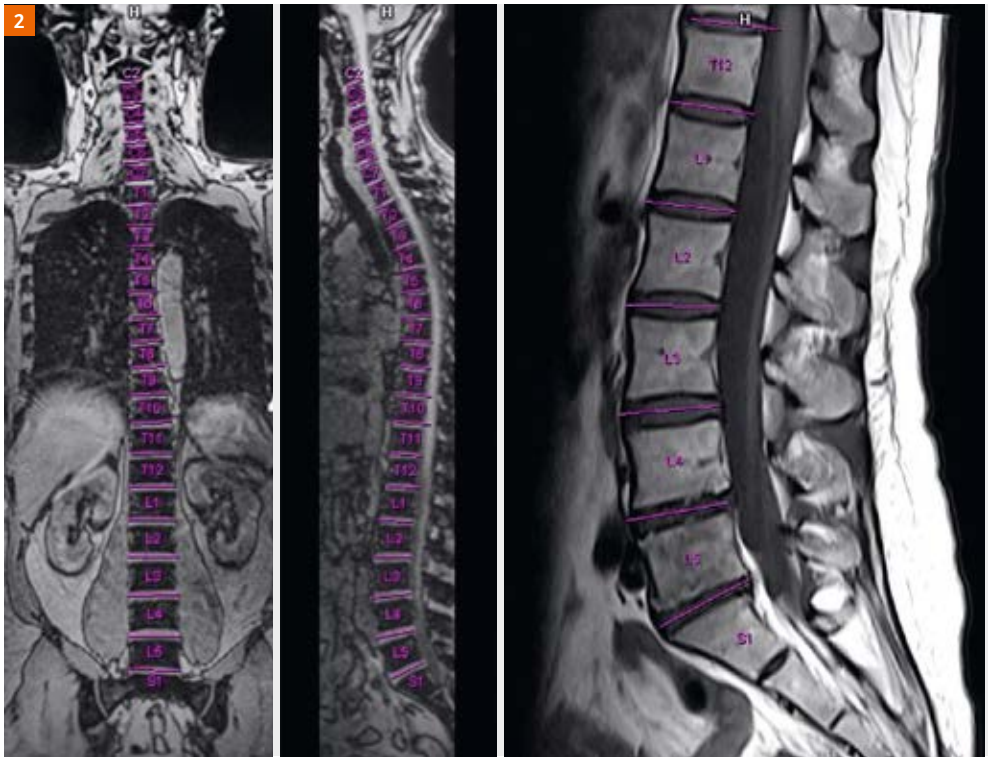

Figure 2:
Automatic spine labelling with the Spine Dot Engine.

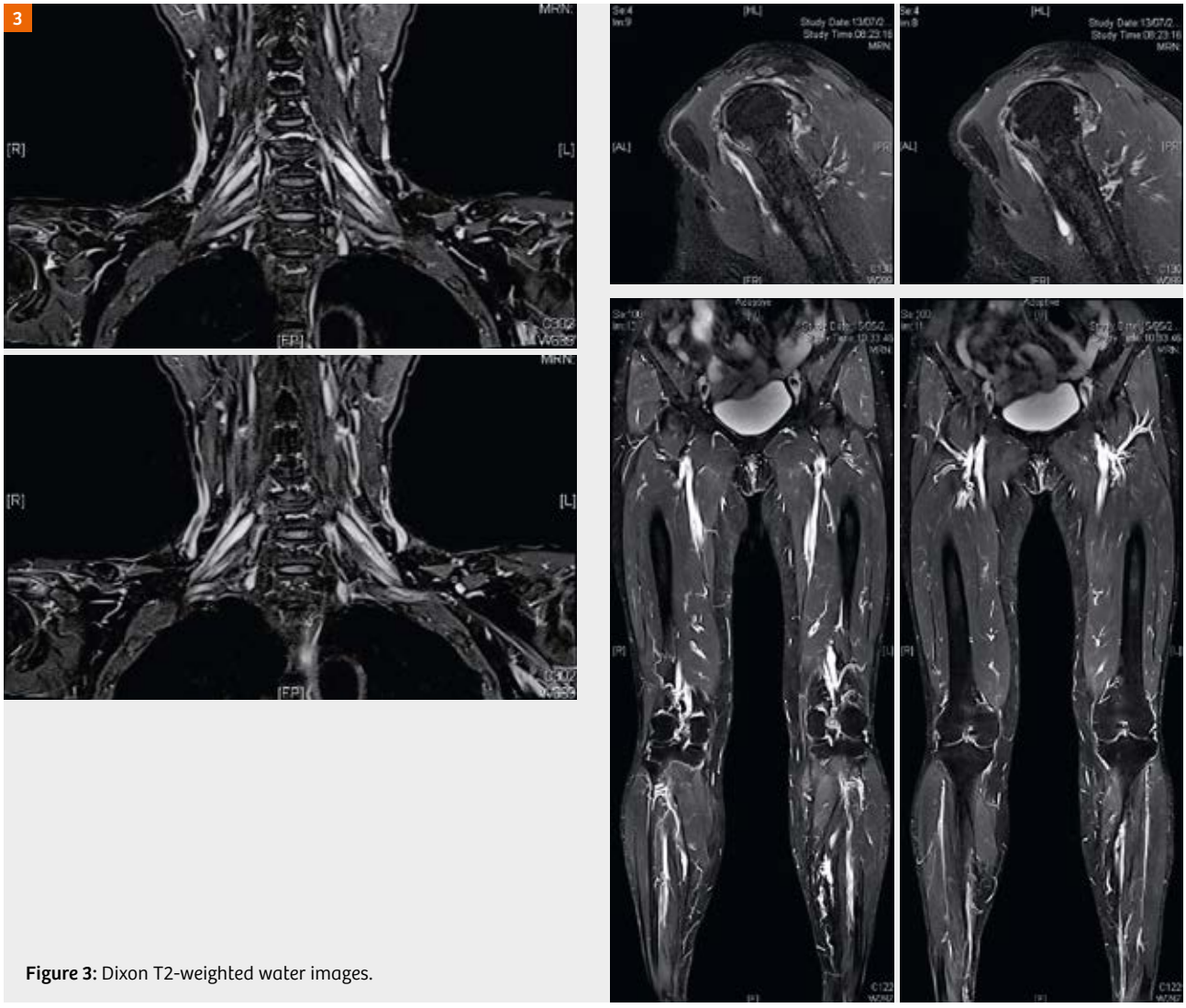

Figure 3: Dixon T2-weighted water images.

WARP metal artifact reduction[1]

Since metal and soft tissue differ significantly in terms of magnetic susceptibility, metal implants will distort the static magnetic field in their vicinity. This type of field disturbance leads to signal void, changes in tissue contrast, and in-plane and through-plane distortion of MR images. Incorporating the cutting-edge WARP application – which includes view-angle tilting (VAT) and slice-encoding for metal artifact correction (SEMAC) – into high-bandwidth turbo spin echo sequences significantly reduce metal artifacts and improve the evaluation of soft tissue in the vicinity of MR-conditional metal implants.

NATIVE TrueFISP non-contrast-enhanced MRA of renal arteries

Contrast-enhanced MRA is a non-invasive examination for diagnosing and assessing the location and extent of stenosis in patients with suspected vascular stenosis of native or graft renal arteries. However, it is not uncommon for these patients to have renal function impairment – a condition which, in view of concerns regarding nephrogenic systemic fibrosis (NSF), is a contraindication for gadolinium-based contrast media. NATIVE TrueFISP MRA is an alternative method of assessing vascular stenosis of native or graft renal arteries without contrast administration. It is a respiratory-triggered 3D TrueFISP sequence with a static-tissue and venous inversion pulse that enhances the contrast difference between flowing arterial blood and static tissue.

[1] The MRI restrictions (if any) of the metal implant must be considered prior to patient undergoing MRI exam. MR imaging of patients with metallic implants brings specific risks. However, certain implants are approved by the governing regulatory bodies to be MR conditionally safe. For such implants, the previously mentioned warning may not be applicable. Please contact the implant manufacturer for the specific conditional information. The conditions for MR safety are the responsibility of the implant manufacturer, not of Siemens.

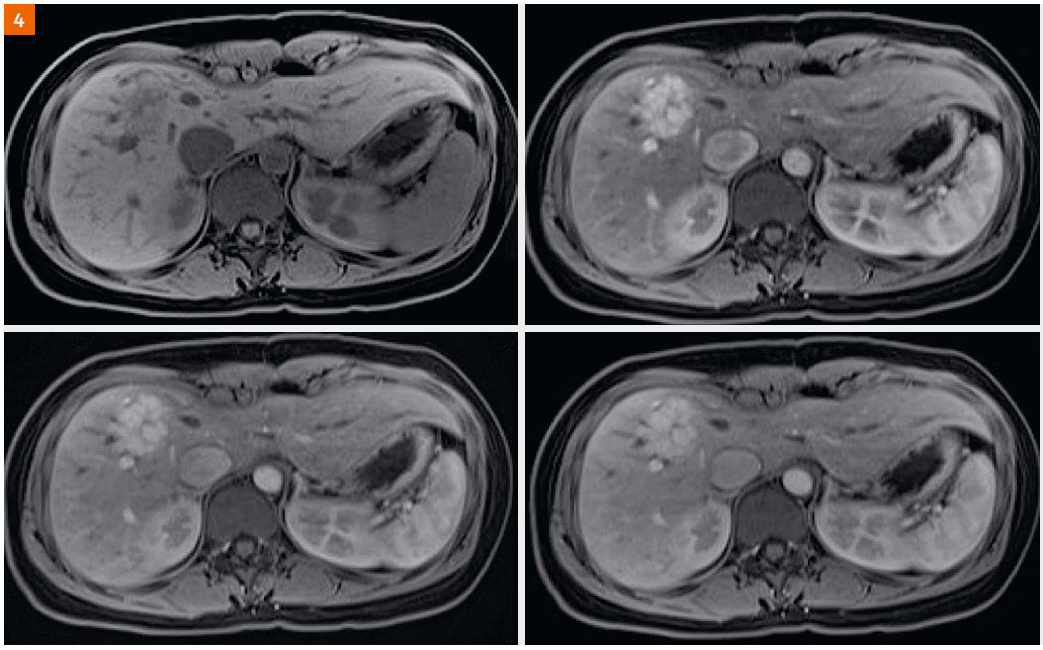

Figure 4:
TWIST-VIBE dynamic contrast-enhanced imaging of liver.

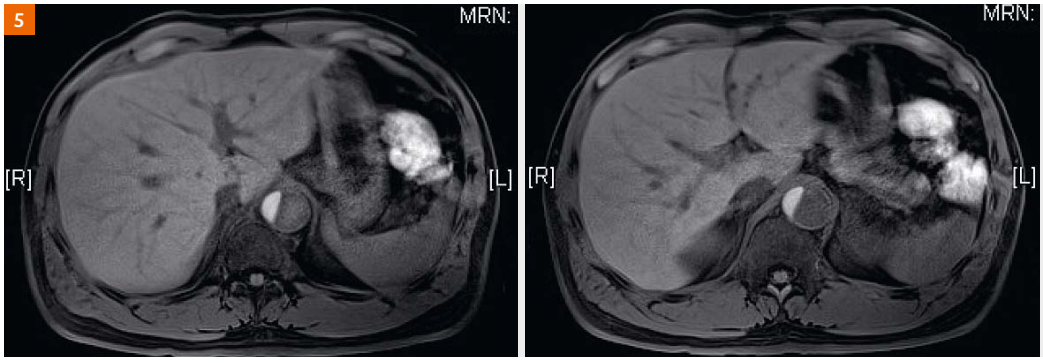

Figure 5:
StarVIBE free-breathing imaging of abdomen.

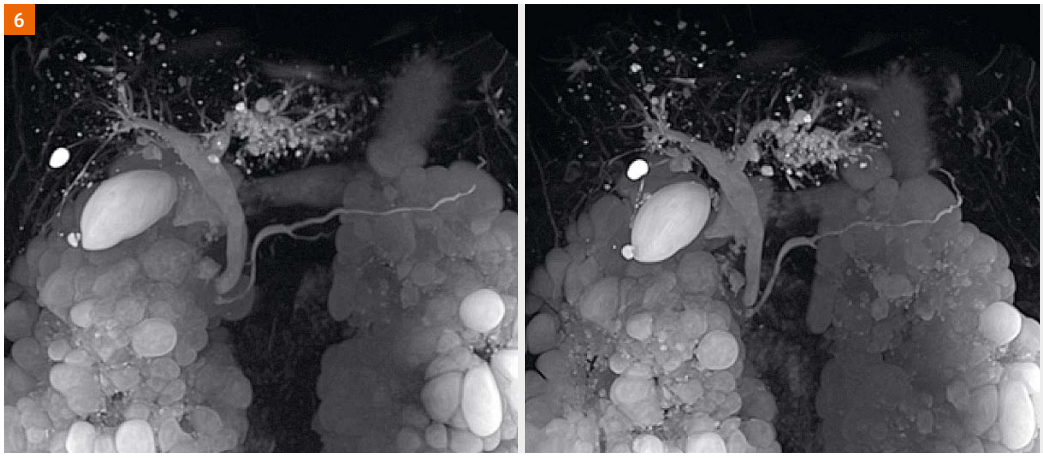

Figure 6:
3D SPACE magnetic resonance cholangio-pancreatography (MRCP).

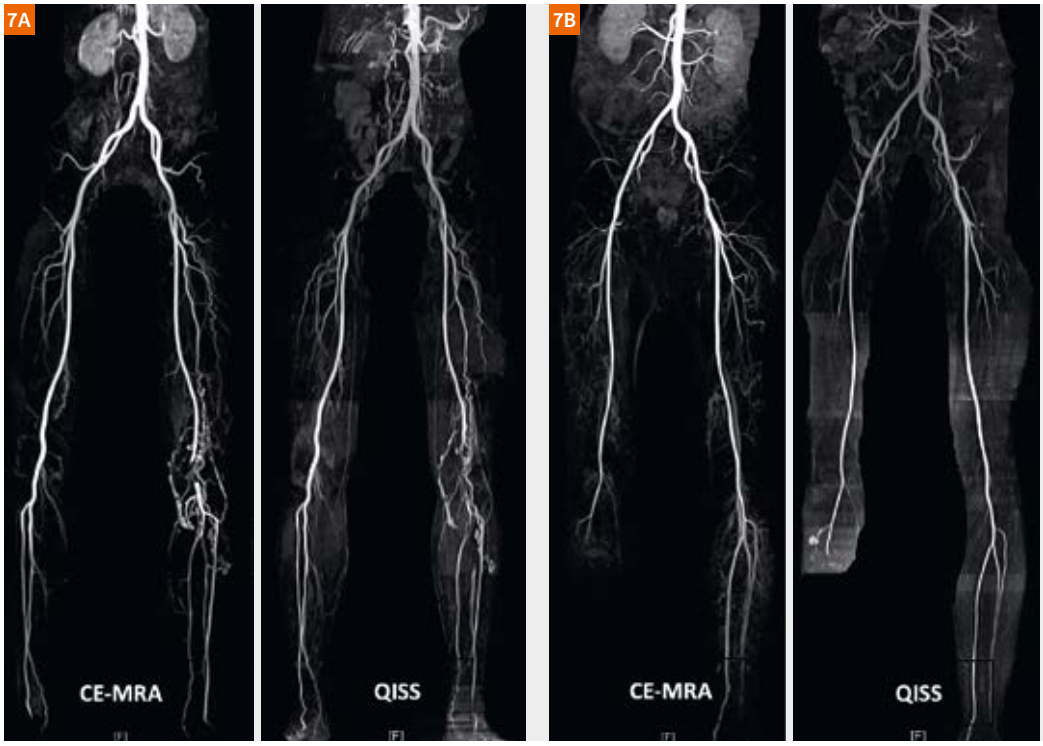

Figure 7:
7A: Peripheral vascular disease with occlusion of left popliteal artery.

7B: Peripheral vascular disease with right below-knee amputation.

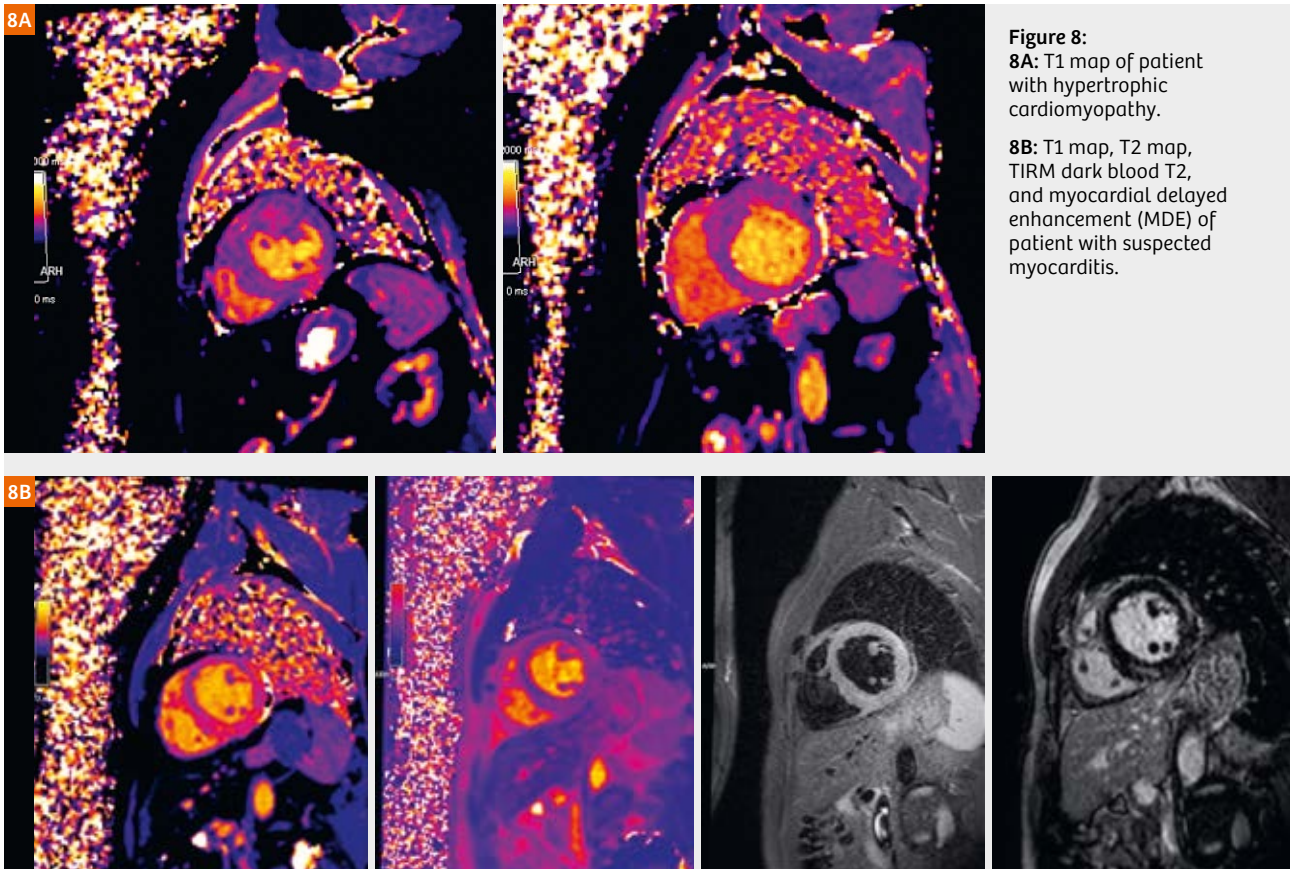

Figure 8:
8A: T1 map of patient with hypertrophic cardiomyopathy.

8B: T1 map, T2 map, TIRM dark blood T2, and myocardial delayed enhancement (MDE) of patient with suspected myocarditis.

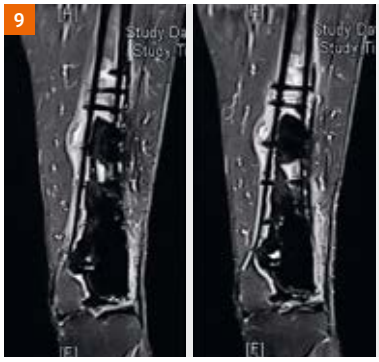

Figure 9:
WARP TSE-FSTIR.

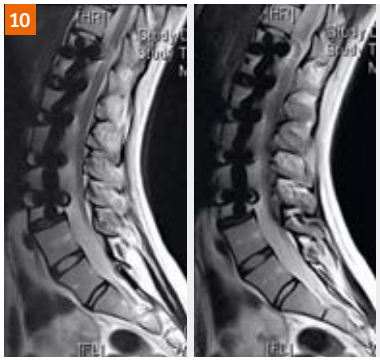

Figure 10:
WARP TSE T2.

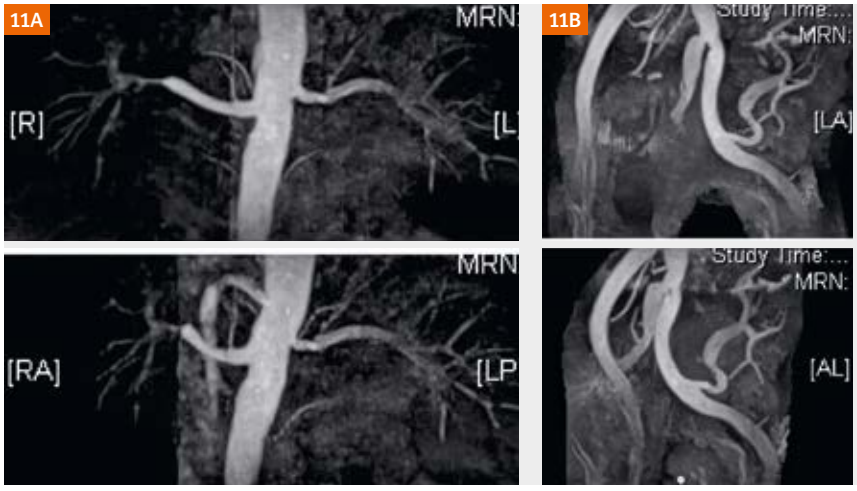

Figure 11:
11A: NATIVE TrueFISP non-contrast-enhanced MRA of native renal arteries.

11B: NATIVE TrueFISP non-contrast-enhanced MRA of graft renal arteries.

Summary

Our new MAGNETOM Aera MRI system has been in operation for about 18 months. It allows us to provide high-quality MRI services to different groups of patients. Thanks to the latest *syngo* MR E11 platform, we are looking forward to further expanding our MRI applications into more clinical fields in the future. This will include using T1 maps for extracellular volume (ECV) assessments of the myocardium, and using the LiverLab application to quantify hepatic lipid.

Contact

Dr. Lam Wai Man Wendy, M.D.
Department of Radiology
Queen Mary Hospital
Pokfulam Road
Hong Kong

Lawrance KC Yip, MSc.
Department of Radiology
Queen Mary Hospital
Pokfulam Road
Hong Kong

MAGNETOM Vida: the Freiburg Experience

Mathias Langer, M.D.

University Hospital Freiburg, Department for Diagnostic and Therapeutic Radiology, Freiburg, Germany

The Department of Radiology at the University Hospital of Freiburg was one of the first clinical and research facilities to install the new MAGNETOM Vida 3T MRI (Siemens Healthcare GmbH, Erlangen, Germany).

The primary rationale for our institution to invest in this new technology platform concerned the system specifications and the clinical capabilities of a state-of-the-art 3T platform in synergy with our installed base of MRI systems. Our facility is equipped with three Siemens 1.5T scanners (MAGNETOM Aera, Avanto, Espree) and one Esaote O-Scan system for musculoskeletal imaging of outpatients (Esaote SpA, Genoa, Italy). Each of these systems has its strengths for certain patients and indications. The MAGNETOM Avanto, for example, is characterized by its benchmark homogeneity and robustness, while the MAGNETOM Aera and Espree scanners provide excellent patient comfort due to the shorter magnet with a wide 70 cm bore opening.

One of the main reasons for installing a 3T system in our department was the clinical advantage of the higher field-strength for certain clinical questions. Over recent years, we have seen a substantial increase in prostate MRI referrals and other pelvic exams (rectal cancer, gynecological patients) which are now predominantly examined with the new 3T MRI system. Other key indications for the system are MR mammography, brain and head/neck exams.

Furthermore, it was important to have a system with a large field-of-view (FOV) and robust fat saturation for body examinations, a 70 cm bore opening for patient comfort and strong gradients with a slew rate of 200 T/m/s and a strength of 60 mT/m for uncompromised quality in functional imaging techniques such as diffusion-weighted imaging (DWI).

In order to meet the high standards of our institution in terms of spatial resolution, the system was fully equipped with 128 independent receive channels, and respective high element-density receive coils, e.g. two Body imaging coils with 30 channels each and a 72-channel spine coil.

Right from the beginning we saw substantial improvements in image quality and/or acquisition time for many sequences, e.g. PD fs, T2-weighted HASTE or T1-weighted VIBE fs post-contrast and improved robustness in DWI (Cases 1-4). Furthermore, novel techniques like ZOOMit 3D SPACE for imaging of the acoustic nerves (Case 5), GRASP-VIBE for dynamic contrast-enhanced imaging in the pelvis (Case 6) or RESOLVE for diffusion in regions with strong susceptibility effects (Case 1 and Case 7) are now our clinical standard. With ZOOMit 3D T2 SPACE, for example, we can improve the spatial resolution to 0.5 mm isotropic, whereas the CISS sequence was limited to 0.6 mm isotropic given the same acquisition time.

However, it took some weeks to transfer our institutional standards from 1.5T to the new 3T system and to optimize image quality for all routine protocols with the support of the local Siemens MR Application specialist, for example in breast imaging (Case 7). For our MR technologists the transition to the evolved software platform was easy, enabling them to work on all our MR systems with equal proficiency.

While some minor challenges remain to be solved, e.g. proper transfer and visualization of advanced breast MRI processing results in our PACS, we are very satisfied with the image quality and performance of our new flagship MR system. We intend to use the advanced capabilities of the new MR system to provide excellent diagnostic imaging to referring departments and for translational research.

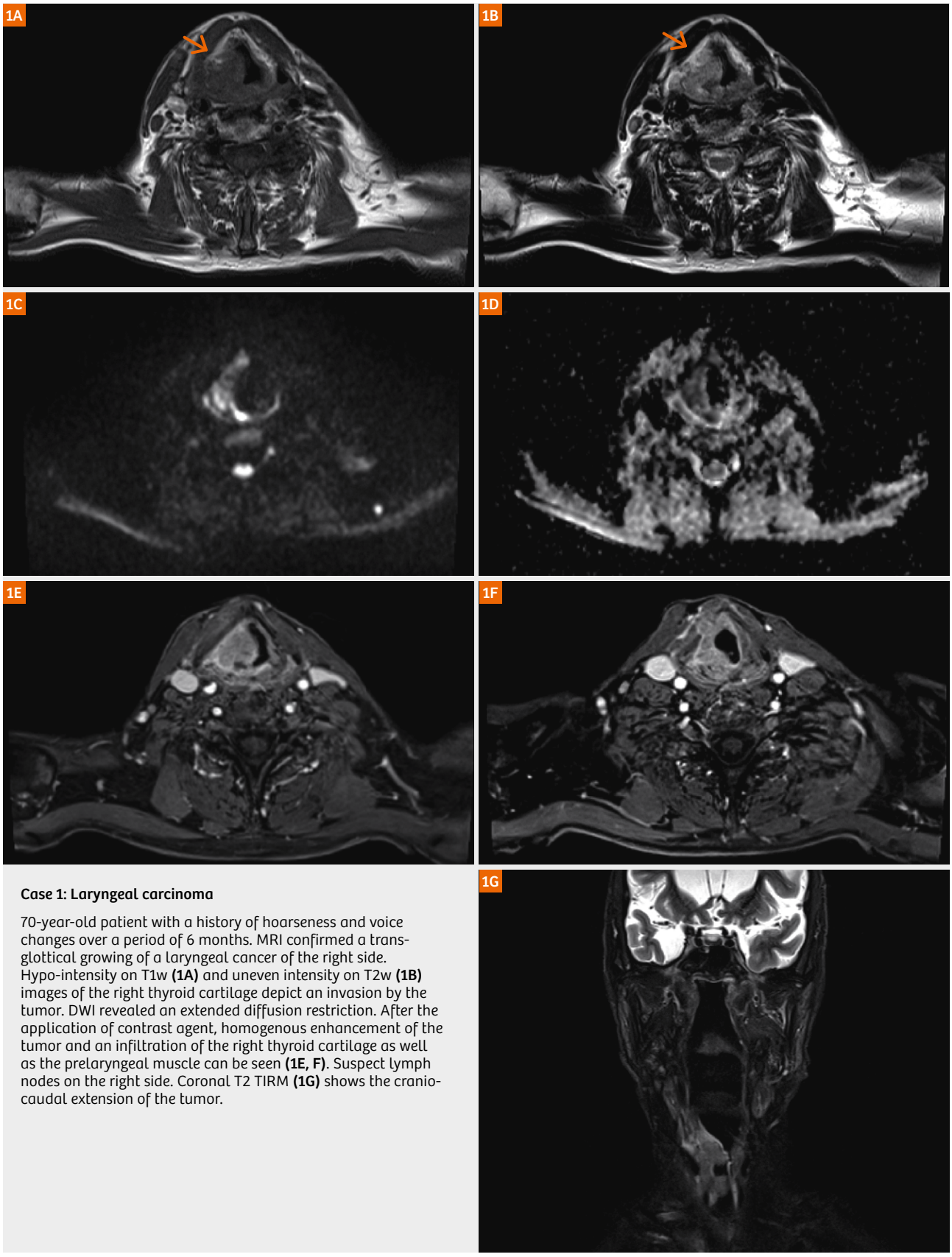

Case 1: Laryngeal carcinoma

70-year-old patient with a history of hoarseness and voice changes over a period of 6 months. MRI confirmed a trans-glottical growing of a laryngeal cancer of the right side. Hypo-intensity on T1w **(1A)** and uneven intensity on T2w **(1B)** images of the right thyroid cartilage depict an invasion by the tumor. DWI revealed an extended diffusion restriction. After the application of contrast agent, homogenous enhancement of the tumor and an infiltration of the right thyroid cartilage as well as the prelaryngeal muscle can be seen **(1E, F)**. Suspect lymph nodes on the right side. Coronal T2 TIRM **(1G)** shows the cranio-caudal extension of the tumor.

Case 2: Von Hippel-Lindau disease

Von Hippel-Lindau disease is a rare disease, characterized by the development of numerous benign and malignant tumors in different organs due to a gene mutation. In this 54-year-old patient we can see the typical presentation of multiple renal cysts and inhomogeneous renal cell carcinomas of the left kidney in T2w axial images **(2A)** and respective post-contrast T1w VIBE **(2B)** with corresponding depiction in DWI and ADC map **(2C, D)**. The examination allows to describe the full abdominopelvic range of disease extent (e.g. phaeochromocytomas, pancreatic cysts, pancreatic adenocarcinomas), with excellent image quality and fat saturation **(2E, F)**.

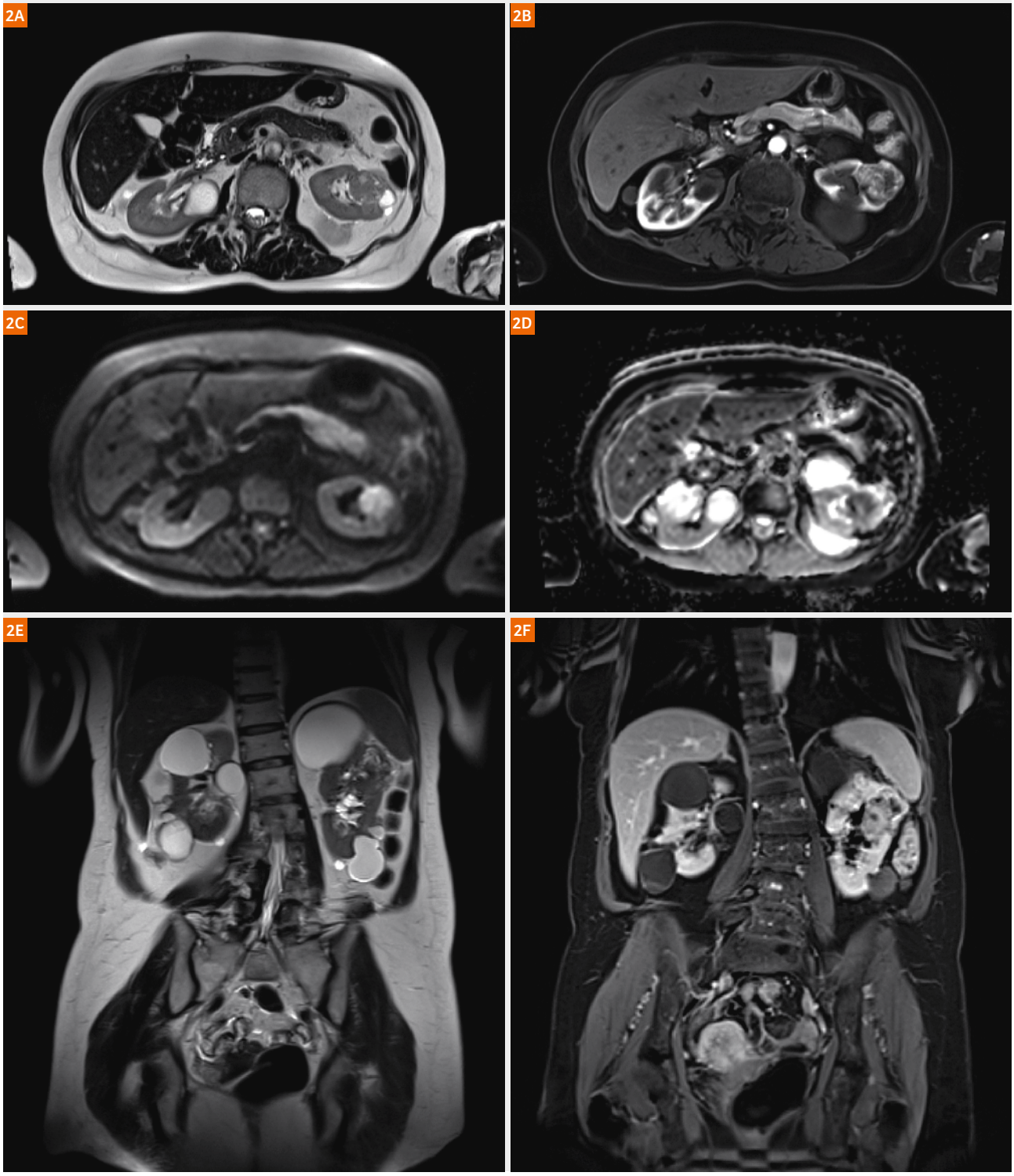

Case 3: Cervix carcinoma recurrence

61-year-old patient with a personal history of cervix carcinoma and Wertheim-surgery. Follow-up MRI presents a recurrent carcinoma, located on the right pelvic wall, engulfing the right iliac vessels (T2w axial, **3A**). Infiltration of the ureter (T2w sagittal, **3B**), the top of the urinary bladder (T2w coronal, **3C**) and the rectum with consecutive fistula (T2w coronal, 3C) is visible. Diffusion-weighed images (b-value 800 s/mm^2, **3D**), ADC map **(3E)** and post-contrast images **(3F)** reveal a probable affection of the nervus ischiadicus.

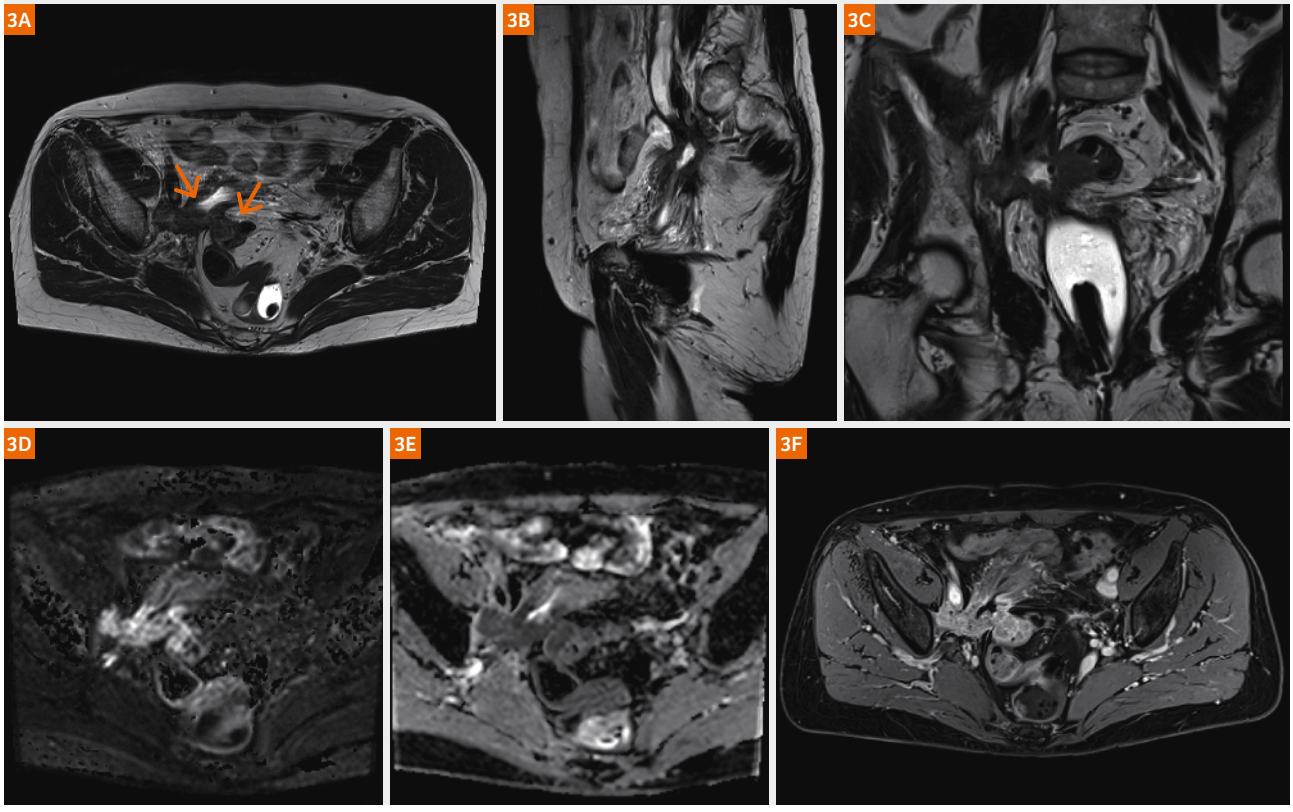

Case 4: Meniscal Tear

32-year-old patient with acute pain after standing up from a squatting posture. MRI of the left knee shows a 'bucket handle' tear of the inner meniscus **(4A, B, C)**. The dislocated fragment is still connected anteriorly and posteriorly, resulting in the characteristic bucket handle sign. Furthermore, the dislocation of meniscus causes a double PCL-sign **(4D)** and fragment-in-notch sign in the intercondylar space.

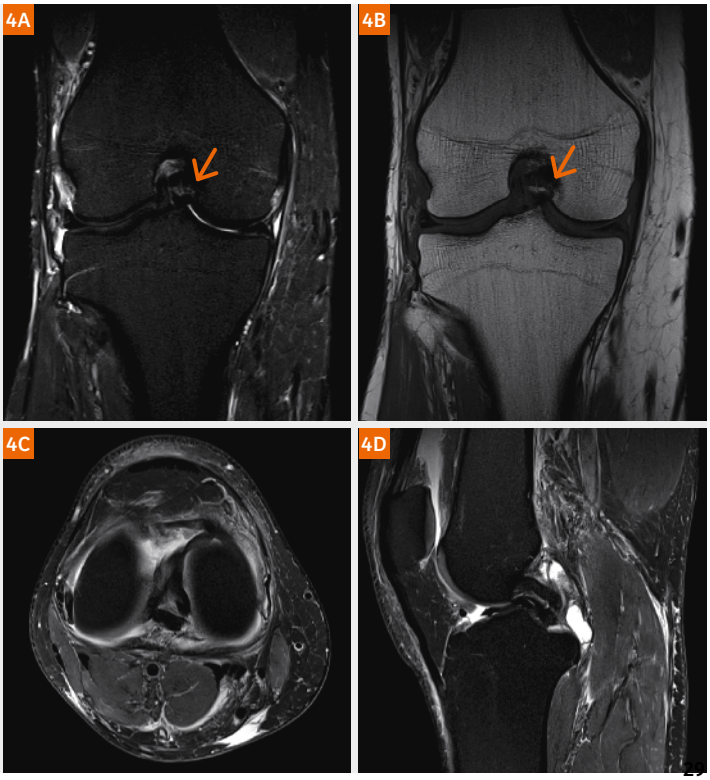

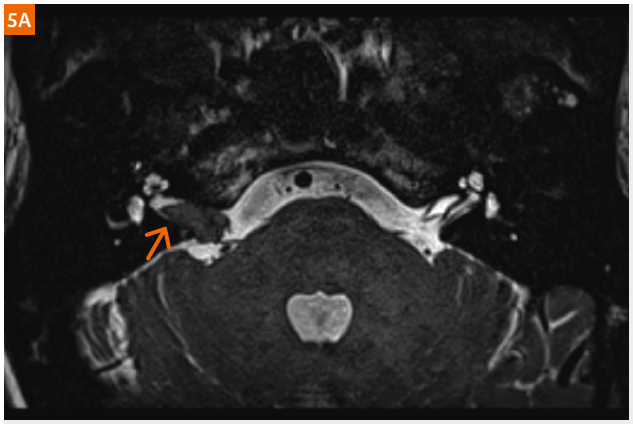

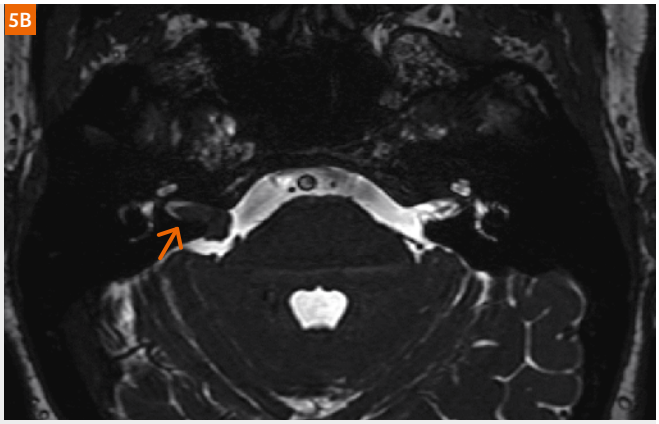

Case 5: Vestibular schwannoma

The patient presented with sensorineural hearing loss and tinnitus. Acoustic schwannomas are benign tumors (WHO grade 1), which usually arise from the intracanalicular segment of the vestibular portion of the vestibulocochlear nerve (CN VIII). They are well-circumscribed encapsulated masses which, unlike neuromas, arise from but are separate from nerve fibres, which they usually splay and displace rather than engulf.

As depicted in the ZOOMit T2 SPACE **(5A)** and CISS (**5B**, cropped image) images, the tumor is located on the right side, it consists of a solid nodular mass with an intracanalicular component that results in a widening of the porus acusticus, described as the trumpeted IAM sign. The extracanalicular extension into the cerebellopontine angle leads to an 'ice cream cone' appearance. Note the improved depiction of contours in the 0.5 mm isotropic zoomed T2 SPACE in comparison to the CISS images. Homogeneous intensive enhancement post contrast can be observed in T1-weighted MPRAGE **(5C, D)**.

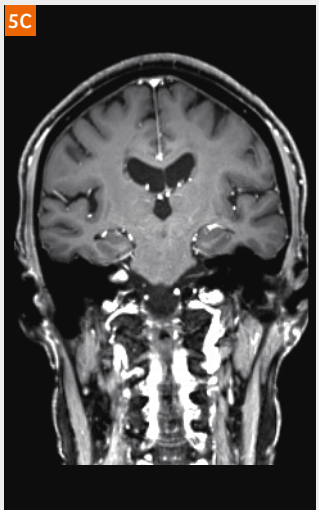

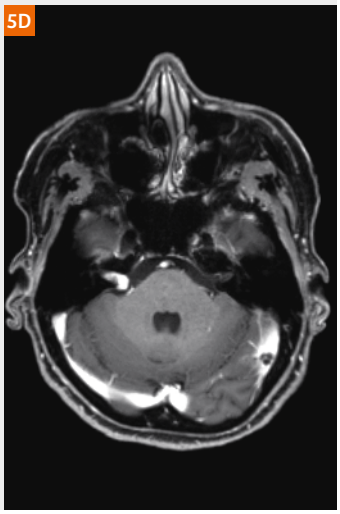

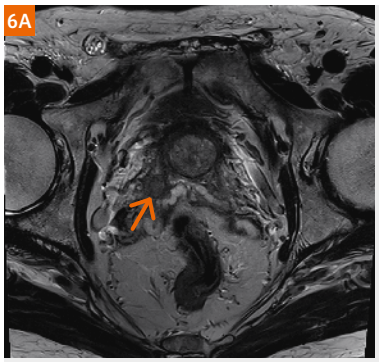

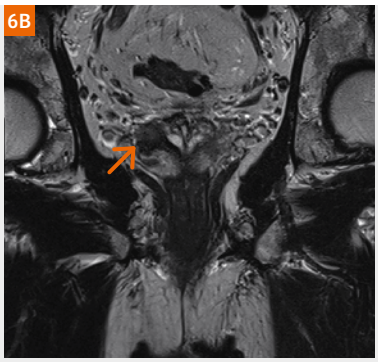

Case 6: Prostate cancer

73-year-old patient with increasing PSA levels. A 1.4 mm large, round hypointense lesion is visible close to the bladder neck and the seminal vesicles on T2w images **(6A, B)**, demonstrating high signal on calculated b1600 images **(6C)**, diffusion-restriction on the ADC map **(6D)** as well as rapid, focal enhancement on the dynamic contrast-enhanced GRASP-VIBE sequence **(6E)**. The lesion was scored PI-RADS 4. Conventional TRUS-biopsy would very probably have missed the location of the lesion.

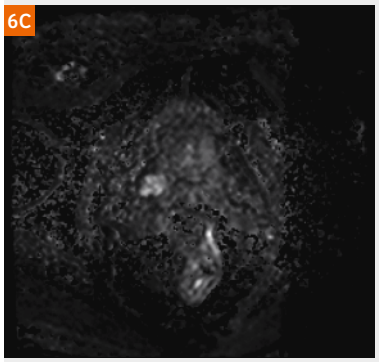

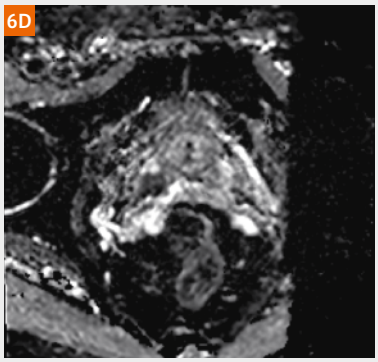

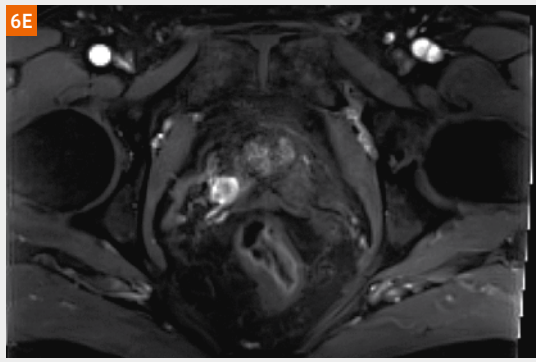

Case 7: Breast cancer

58-year-old woman with a strong family history of breast cancer and a personal history of hormone replacement therapy. MRI was performed because of a new lump in the right breast. It revealed a spiculated mass with intermediate signal on T2w images **(7A)** in the lower lateral right breast with corresponding finding in T2 TIRM **(7B)**. Increased signal in high b-value images **(7C)**, corresponding diffusion-restriction in the ADC map and fast homogeneous contrast enhancement both visible on the subtraction of pre- and first post-contrast phase **(7D)** as well as corresponding MIP **(7E)**. Delayed axial images demonstrated plateau kinetics. Biopsy revealed an invasive carcinoma.

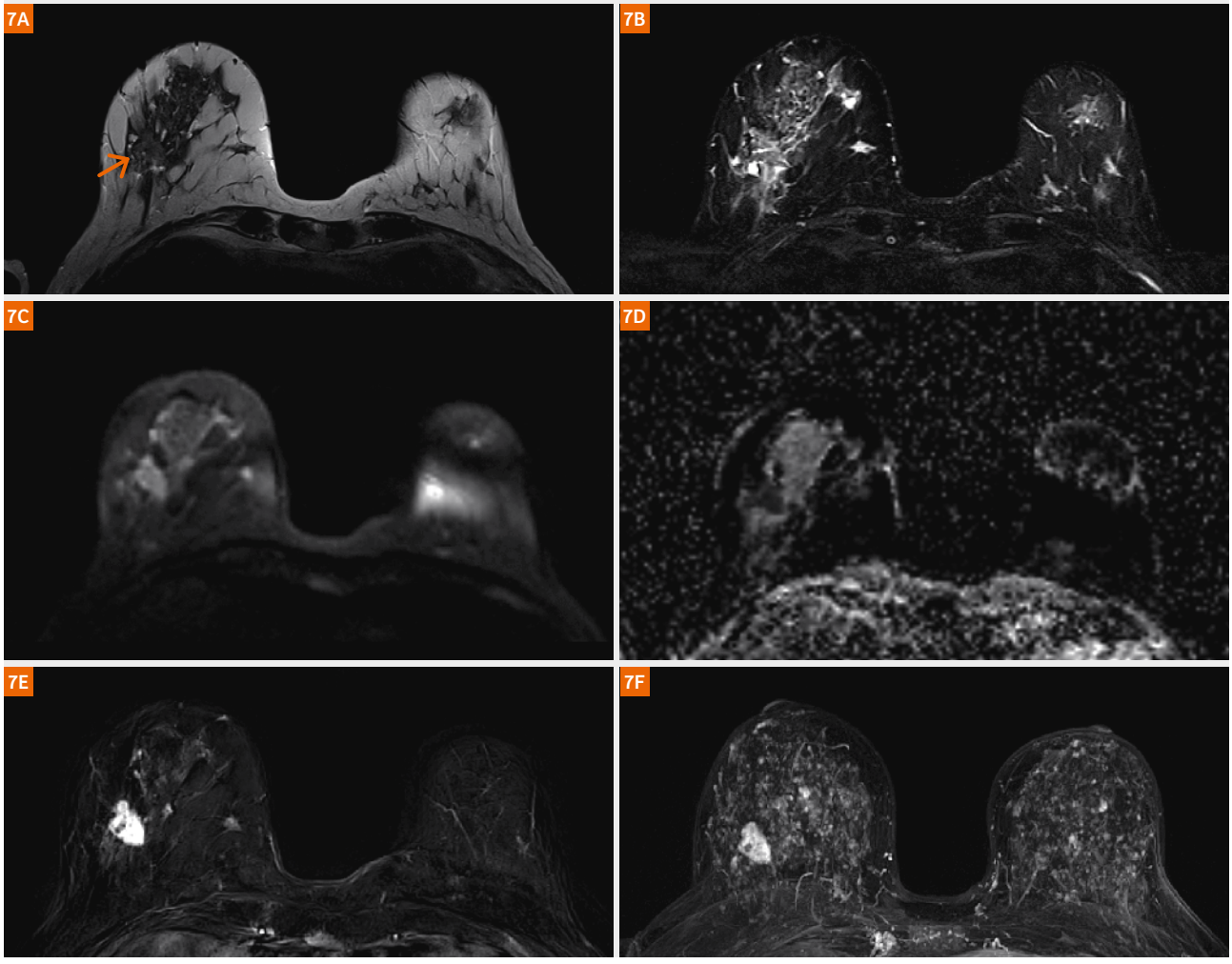

Contact

Professor Mathias Langer, M.D., MBA
Department of Diagnostic Radiology
University Hospital Freiburg

Hugstetter Straße 55
79106 Freiburg
Phone +49 761 27038050
mathias.langer@uniklinik-freiburg.de

Quantitative WB-MRI with ADC Histogram Analysis for Response Assessment in Diffuse Bone Disease

Danoob Dalili[1]; Anwar R. Padhani[2]; Robert Grimm[3]

[1] Imperial College Healthcare NHS Trust, St Mary's Hospital, London, United Kingdom
[2] Paul Strickland Scanner Centre, Mount Vernon Cancer Centre, Northwood, Middlesex, United Kingdom
[3] Siemens Healthineers, Erlangen, Germany

Introduction

Tumor heterogeneity occurs at multiple levels with marked differences in cell mix, size and arrangements. Heterogeneity also exists in microenvironmental factors (including oxygenation, pH, interstitial pressure, blood flow), metabolism and gene expression. This profound heterogeneity is extremely important for prognosis, therapy planning, drug delivery, ultimately affecting patient outcomes. There are numerous ways of investigating tumor heterogeneity, which include using functional and molecular imaging, some of which can be applied to clinical data [1].

Quantitative assessment of tissue water diffusivity using ADC values allows tissue microstructure at a µm–mm scale to be evaluated, thus reflecting tissue cellularity, organisation and blood flow. Most studies investigating

Continued on page 35

Figure 1: Morphological images and 3D DWI MIPs (inverted scale).

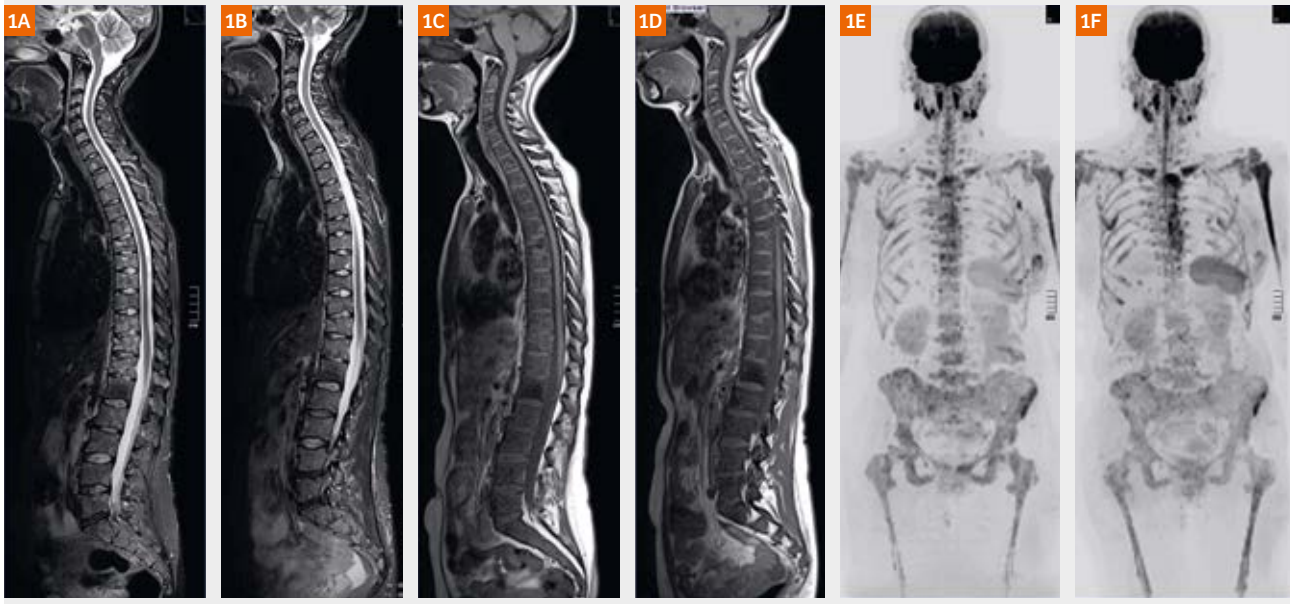

Left 2-columns: Whole-spine sagittal STIR sequences show diffuse bone marrow infiltration at baseline **(1A)** with no interval changes following hormonal therapy **(1B)**. Middle 2-columns: Whole-spine sagittal T1-weighted images show diffuse bone marrow infiltration with no appreciable return of bone marrow fat after therapy **(1D)**.

Right 2-columns: Whole-body b900 3D MIP (inverted scale). The bone marrow is diffusely involved with diffuse regions of high-signal intensity in the axial skeleton and in the proximal limb bones prior to therapy. A minor global reduction in the b900 signal intensity of bone marrow can be seen but this is not very convincing **(1F)**.

Figure 2: Morphologic and diffusion-weighted axial sequences with axial bone window CT images of the L3 vertebral body and sacrum before and on hormonal therapy with bisphosphonates.

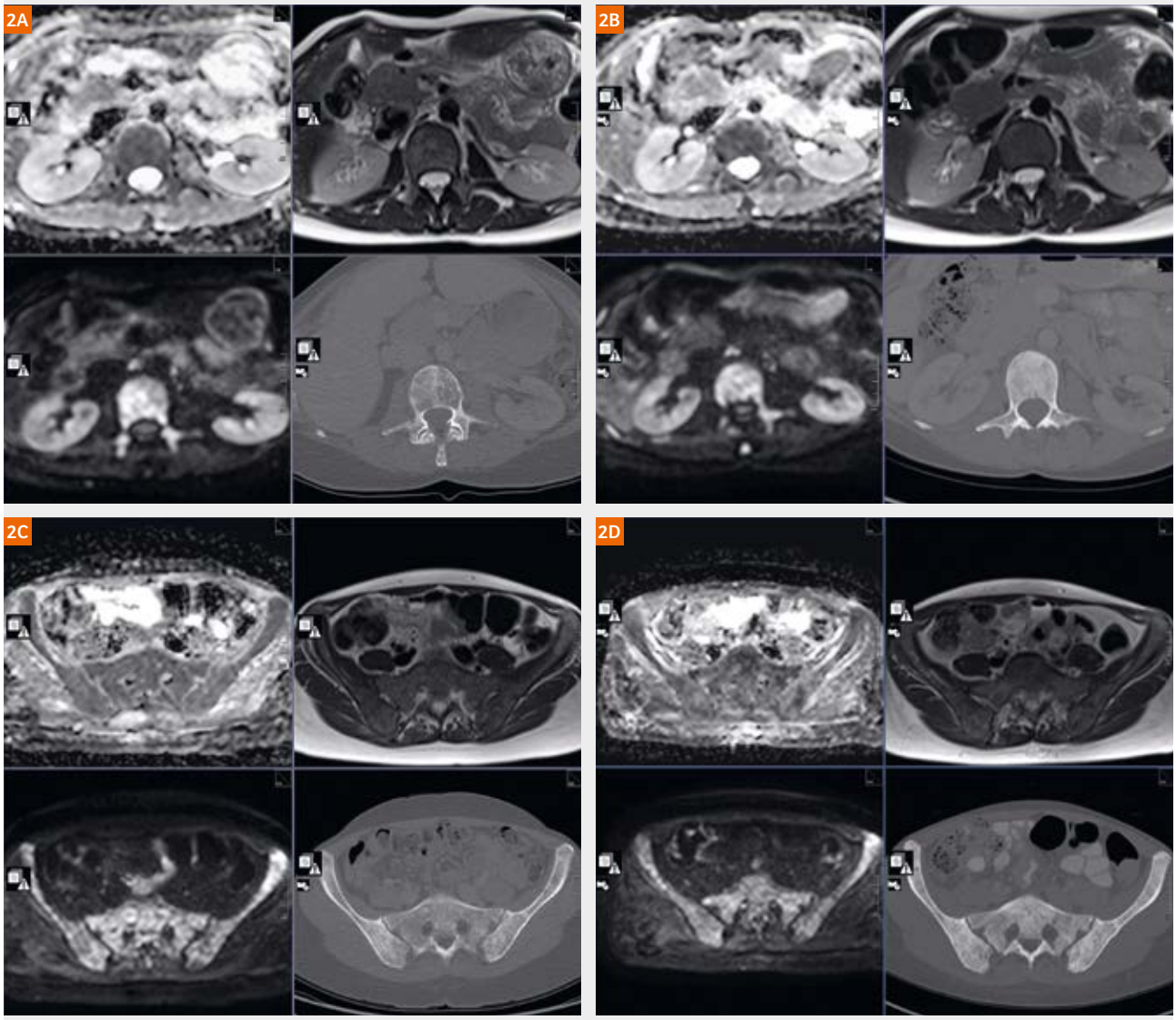

Axial ADC, T2w-HASTE, b900 and axial bone window CT scan images before and during therapy through the L3 vertebral body **(2A, B)** and sacrum **(2C, D)**.

Figures 2A and 2B: the L3 vertebral body marrow shows no change in ADC values but there is some decrease in the b900 signal intensity. A uniform increase in CT density with 'milky appearance' of the bone is consistent with responding disease (CT density 300 HU before therapy and 550 HU after therapy). However, the persistent elevated signal intensity on the b900 images suggests the ongoing presence of active disease.

Figures 2C and 2D: the CT scan shows a uniform increase in bone density (CT density 315 HU before therapy and 530 HU after therapy). Again the CT density change is not high enough to be confident regarding response. However, the ADC maps show intermixing of high and low ADC value voxels resulting in a textural change.

Figure 3: Whole-body tumor load analysis.

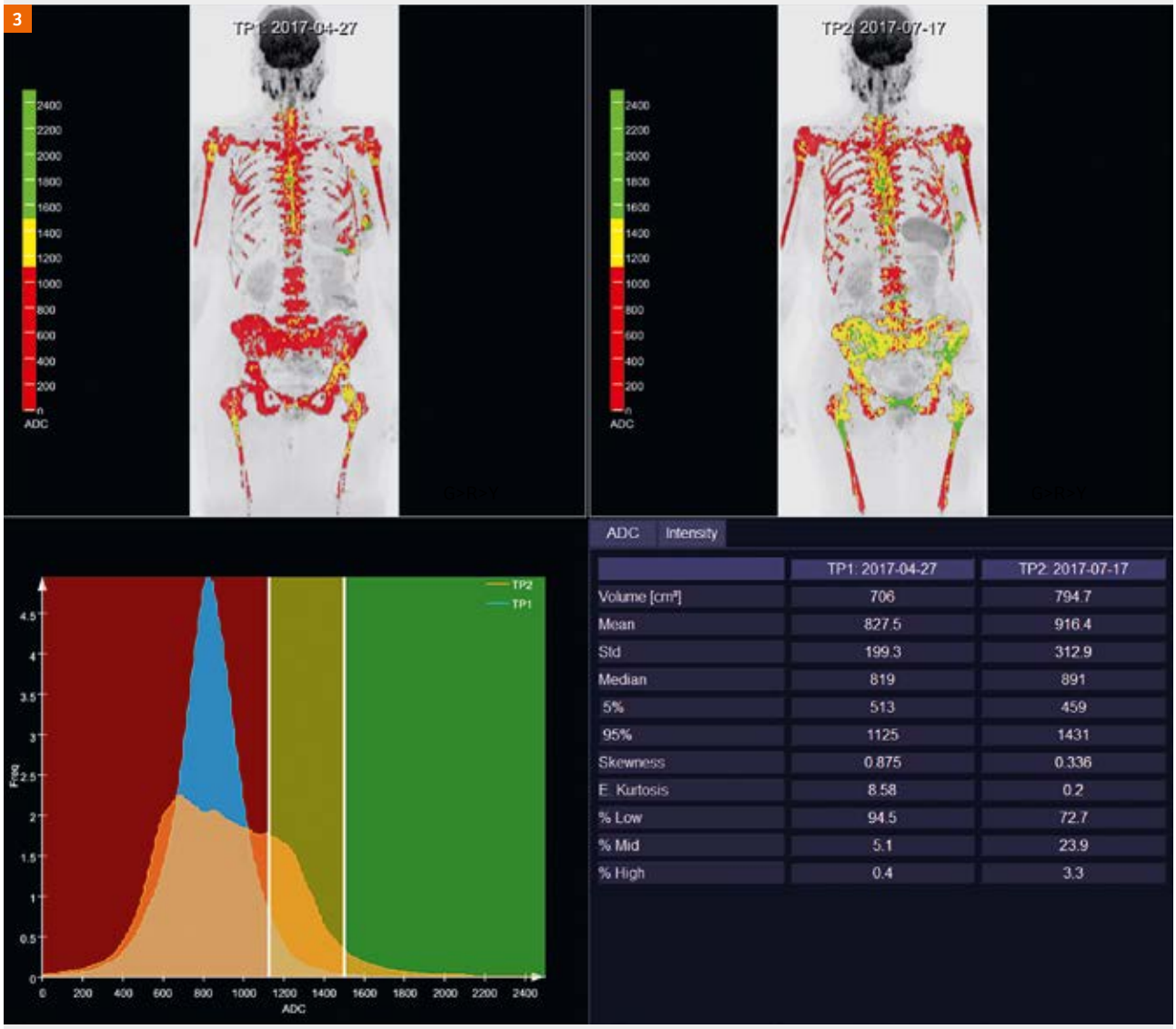

	TP1: 2017-04-27	TP2: 2017-07-17
Volume [cm³]	706	794.7
Mean	827.5	916.4
Std	199.3	312.9
Median	819	891
5%	513	459
95%	1125	1431
Skewness	0.875	0.336
E. Kurtosis	8.58	0.2
% Low	94.5	72.7
% Mid	5.1	23.9
% High	0.4	3.3

WB-tumor load segmentations were undertaken on *syngo*.via Frontier MR Total Tumor Load software[1]. The whole-body b900 images were segmented using computed b-value images of 900–1000 s/mm², setting a signal intensity threshold of 100 AU. Extraneous signals (such as the brain, kidneys, spleen and bowel) were removed, to leave only recognizable bone disease sites. The b900 MIP images are overlaid with ADC value classes using the 95th centile value of the pre-treatment histogram (1125 µm²/s) and 1500 µm²/s.

Red colored voxels represent untreated disease or those with no-detectable response.

Green colored voxels have ADC values ≥1500 µm²/s (representing voxels that are 'highly likely' to be responding).

The yellow voxels lie between the 95th centile value of the pre-treatment histogram (1125 µm²/s) and 1500 µm²/s.
Thus, yellow voxels represent regions 'likely' to be responding.

706 mL of bone marrow was segmented before therapy and 795 mL after therapy. Note that there is no significant increase in median ADC values (819 µm²/s and 891 µm²/s respectively), but a decrease in excess kurtosis (8.6 and 0.2 respectively), and broadening of ADC histogram and an increase in the standard deviation (199 and 313 µm²/s respectively) can be seen on the corresponding relative frequency histograms. There is a unimodal distribution of ADC values at baseline (TP1) and a plateau distribution of the post-treatment (TP2) histogram.

The whole-body ADC color projections focusing on response (ADC maximum intensity projections) for both time points are shown.
A spatial discordant response pattern is visible with responding increasing yellow and green voxels in the pelvis and proximal femora.

[1] *syngo*.via Frontier is for research only, not a medical device. *syngo*.via Frontier MR Total Tumor Load is a released research prototype.

the usefulness of diffusion imaging for disease characterization, prognostication and therapy response use region-of-interest (ROI) approaches deriving mean values of ADC (unit: $\mu m^2/s$). This averaging method can be used to assess heterogeneity between ROIs or between patients, but fundamentally, ignores the heterogeneity within the ROI.

The characterization of tissues can be improved using histogram-based assessments of the distribution of ADC values. Histogram approaches have multiple advantages, including volume-of-interest (VOI) assessments, thus avoiding the subjectivity that is inherent with ROI placements. Importantly, histograms can provide additional metrics that reflect the texture of lesions, thereby allowing heterogeneity of ADC distribution within tissue to be assessed.

Histogram-based ADC analyses have mostly been undertaken in the context of neuroimaging showing added value for brain tumor grading, prognosis and therapy response [2–4]. However, this approach is increasing being applied to extracranial tissues, including evaluations of cervix and breast cancers [5–7], liver fibrosis [8], peritoneal malignancy [9] and bone metastases [10, 11]. These and other studies, have shown the potential of ADC histogram descriptors to improve the characterization of tissues, as well as to serve as prognostic and response biomarkers.

In this report, we describe a patient with breast cancer metastasising to the bone marrow, who underwent hormonal treatment. CT scans, morphologic MR images and ROI derived ADC assessments were confusing when trying to gauge the success of therapy. Volume based assessments of whole-body tumor load and ADC histograms, enabled an accurate assessment of the clinical status allowing therapy to be continued.

Case study

A 37-year-old woman presenting with a 2-year history of lower back pain was found to have diffuse metastatic bone infiltration following an MRI of her lumbar spine. A bone marrow trephine biopsy and core biopsy of an asymptomatic left breast mass showed the presence of metastatic ER-positive, HER2 2+ (FISH-negative), grade 2 invasive ductal carcinoma of the breast. She was commenced on systemic anticancer hormonal therapy with Tamoxifen and Goserelin as well as with Zoledronic acid infusions.

She underwent baseline and 3 month follow-up whole-body MRI scans with diffusion-weighted sequences using a 1.5T MAGNETOM Avanto scanner using a published protocol [12]. The baseline scan demonstrated extensive metastatic bone only disease (Figs. 1, 2) that does not change appreciably on morphological T1w, T2w and STIR images of the spine. CT scans undertaken at the corresponding time points, show uniform increases in bone density with a 'milky texture' which are difficult to interpret regarding the activity of the underlying disease. It's only when CT density increases to >850 HU that it is possible to be confident about the likelihood of inactive disease [13]. There was minimal reduction in b900 signal intensity.

The diffusion-weighted images for both timepoints were analysed using the threshold-based segmentation, *syngio*.via Frontier MR Total Tumor Load software[1] [14]. The pre-treatment ADC histogram has a unimodal distribution of ADC values with high excess kurtosis (Fig. 3). After 3 months of hormonal therapy, a plateau distribution of ADC values can be seen with little change in the mean ADC but a greater spread in ADC values can be appreciated. Responding voxels (yellow/green voxels) are mostly seen in the pelvis and proximal femora on the ADC color projections focusing on response. These ADC histograms are consistent with a favorable therapy response, because of which treatment was continued.

Discussion

There are a variety of approaches for objectively displaying and analyzing ADC images in response assessment settings. Most studies report mean values from single/multiple ROIs placed on high b-value images, which are then copied on ADC maps for quantitate ADC value readouts. Recently, studies have begun to report on central tendency measures (mean, median, mode values) of ADC histograms on volumes of interest (VOIs). Because bone metastases are heterogeneous in their spatial ADC distributions, these simpler, first order measures have limited abilities to detect treatment-related changes, particularly if there are both increases and decreases in ADC in response to treatment (for example, when ADC values increase due to tumor cell kill and decrease due to bone marrow renormalization, fibrosis and dehydration) [15]. As a result, the net mean/median ADC change may be minimal. Furthermore, if large cystic or necrotic areas are present, then the ability to detect therapy response induced changes may be blunted.

More complex changes in ADC values can be evaluated by assessing the spread of the ADC data (variance, standard deviation, range (maximum-minimum difference), centile ranges, histogram entropy). The spread of ADC data allows estimates of the proportions of responding or non-responding tumor volume to be determined by the application of threshold cut-off values. So, in this case,

[1] *syngo.via Frontier is for research only, not a medical device. syngo.via Frontier MR Total Tumor Load is a released research prototype.*

the proportion of voxels in the active range (ADC-low voxels below 1125 μm²/s) is 95% and 73% respectively at the two time-points.

Other higher order descriptors of histograms such as skewness (a measure of the degree of asymmetry of a distribution) and kurtosis (which is the degree of peakedness of a distribution) can also be helpful for evaluating therapy response. Comparison of relative frequency histograms to normal distributions allows quantitative values to be assigned to histogram kurtosis; positive excess kurtosis values >0 (leptokurtic shape) indicates a higher peak than for a normal distribution (normal distribution shape is described as mesokurtic with an excess kurtosis value = 0). After therapy, excess kurtosis decreases often reaching values <0 (platykurtic).

Readers should also be aware that both measurement (e.g. poor SNR) and analysis methods (e.g., two-point fitting for generating ADC values) can alter the skewness of histograms independent of therapy induced effects, because of which the quality of ADC maps images should be critically assessed, before higher order histogram descriptors such as maximum and minimum values, range and skewness are used to infer biologic significance.

ADC histogram analysis for assessing bone metastases
ADC histograms of untreated bone metastases are often positively skewed (tail to the right) with positive excess kurtosis. For our data acquisition protocol that uses b50, b600 and b900 mm²/s diffusion-sensitizing gradients, the majority of tumor ADC pixel values usually lie in the 650–1500 μm²/s range for untreated disease. Positive excess kurtosis is often maintained in the setting of tumor progression or in stable disease, although mean/median values may change depending on the relative extent of tumor infiltration and fat content in the bone marrow. If tumors are necrotic before treatment or if there has been a response to prior treatments, then more complex histogram shapes can be seen.

When tumors respond successfully to therapy, kurtosis values generally decrease and the standard deviation/variance increases. Negative skewness (tail to the left) often develops if the histogram retains a unimodal shape. Thus, the transformation of a positive kurtosis, positively skewed unimodal ADC distribution into a plateau shape in response to a therapy indicates likely response even in the absence of a significant change in mean/median ADC values. Where successful response is accompanied by regeneration of the normal bone marrow as part of the healing process, a distinct second ADC peak below the tumor peak can be observed which is illustrated in two accompanying cases within this issue of MAGNETOM Flash [15, 16].

Radiologists often enquire when there is an absolute need to use ADC histograms in "daily clinical practice"? Generally, we find ADC analyses are most useful in the presence of extensive, diffuse metastatic disease on WB-DWI or when there has been an apparent mixed/heterogeneous response to therapy. In these patients, visual inspections of morphological and diffusion-weighted images can be problematic and applying the MET-RADS response criteria [12] can be challenging due to the high volume of disease present. In these cases, we find histogram analyses indispensable because of the ability to observe changes in the spread, skewness and kurtosis of the ADC data.

References

1 Just N. Improving tumour heterogeneity MRI assessment with histograms. British journal of cancer. 2014 Dec 9;111(12):2205-13.
2. Song YS, Choi SH, Park CK, Yi KS, Lee WJ, Yun TJ, Kim TM, Lee SH, Kim JH, Sohn CH, Park SH. True progression versus pseudoprogression in the treatment of glioblastomas: a comparison study of normalized cerebral blood volume and apparent diffusion coefficient by histogram analysis. Korean journal of radiology. 2013 Aug 1;14(4):662-72.
3. Gutierrez DR, Awwad A, Meijer L, Manita M, Jaspan T, Dineen RA, Grundy RG, Auer DP. Metrics and textural features of MRI diffusion to improve classification of pediatric posterior fossa tumors. American Journal of Neuroradiology. 2014 May 1;35(5):1009-15.
4. Tozer DJ, Jäger HR, Danchaivijitr N, Benton CE, Tofts PS, Rees JH, Waldman AD. Apparent diffusion coefficient histograms may predict low-grade glioma subtype. NMR in biomedicine. 2007 Feb 1;20(1):49-57.
5. Rosenkrantz AB. Histogram-based apparent diffusion coefficient analysis: an emerging tool for cervical cancer characterization?. American Journal of Roentgenology. 2013 Feb;200(2):311-3.
6. Downey K, Riches SF, Morgan VA, Giles SL, Attygalle AD, Ind TE, Barton DP, Shepherd JH, deSouza NM. Relationship between imaging biomarkers of stage I cervical cancer and poor-prognosis histologic features: quantitative histogram analysis of diffusion-weighted MR images. American Journal of Roentgenology. 2013 Feb;200(2):314-20.
7. Johansen R, Jensen LR, Rydland J, Goa PE, Kvistad KA, Bathen TF, Axelson DE, Lundgren S, Gribbestad IS. Predicting survival and early clinical response to primary chemotherapy for patients with locally advanced breast cancer using DCE-MRI. Journal of Magnetic Resonance Imaging. 2009 Jun 1;29(6):1300-7.
8. Fujimoto K, Tonan T, Azuma S, Kage M, Nakashima O, Johkoh T, Hayabuchi N, Okuda K, Kawaguchi T, Sata M, Qayyum A. Evaluation of the mean and entropy of apparent diffusion coefficient values in chronic hepatitis C: correlation with pathologic fibrosis stage and inflammatory activity grade. Radiology. 2011 Mar;258(3):739-48.
9. Kyriazi S, Collins DJ, Messiou C, Pennert K, Davidson RL, Giles SL, Kaye SB, deSouza NM. Metastatic ovarian and primary peritoneal cancer: assessing chemotherapy response with diffusion-weighted MR imaging—value of histogram analysis of apparent diffusion coefficients. Radiology. 2011 Oct;261(1):182-92.
10. Blackledge MD, Collins DJ, Tunariu N, Orton MR, Padhani AR, Leach MO, Koh DM. Assessment of treatment response by total tumor volume and global apparent diffusion coefficient using diffusion-weighted MRI in patients with metastatic bone disease: a feasibility study. PLoS One. 2014 Apr 7;9(4):e91779.

11. Perez-Lopez R, Mateo J, Mossop H, Blackledge MD, Collins DJ, Rata M, Morgan VA, Macdonald A, Sandhu S, Lorente D, Rescigno P. Diffusion-weighted imaging as a treatment response biomarker for evaluating bone metastases in prostate cancer: a pilot study. Radiology. 2016 Nov 22;283(1):168-77.
12. Padhani AR, Lecouvet FE, Tunariu N, Koh DM, De Keyzer F, Collins DJ, Sala E, Schlemmer HP, Petralia G, Vargas HA, Fanti S. METastasis Reporting and Data System for Prostate Cancer: practical guidelines for acquisition, interpretation, and reporting of whole-body magnetic resonance imaging-based evaluations of multiorgan involvement in advanced prostate cancer. European urology. 2017 Jan 31;71(1):81-92.
13. Beheshti M, Vali R, Waldenberger P, Fitz F, Nader M, Hammer J, Loidl W, Pirich C, Fogelman I, Langsteger W. The use of F-18 choline PET in the assessment of bone metastases in prostate cancer: correlation with morphological changes on CT. Molecular imaging and biology. 2010 Feb 1;12(1):98-107.
14. Grimm R, Padhani AR. Whole-body Diffusion-weighted MR Image Analysis with *syngo*.via Frontier MR Total Tumor Load. MAGNETOM Flash (68) 2/2017, 73-75.
15. Dalili D, Joshi P, Grimm R, Padhani AR. Evolution of the malignant bone marrow with successful therapy – quantitative analysis with whole body diffusion MRI. MAGNETOM Flash (69) 3/2017, 47–52.
16. Dalili D, Padhani AR, Grimm R. Quantitative WB-MRI with ADC histogram analysis for demonstrating complex response of bone marrow metastatic disease. MAGNETOM Flash 2017; 69(3): 38–42.

Contact

Dr. Danoob Dalili
Specialist Registrar Clinical Radiology
Imperial College Healthcare NHS Trust
St Mary's Hospital
Praed St
London W2 1NY
United Kingdom
Phone: +44 (0) 20 3312 6666
Dalili@doctors.org.uk

Prof. Anwar R. Padhani
Consultant Radiologist and
Professor of Cancer Imaging
Paul Strickland Scanner Centre
Mount Vernon Cancer Centre
Rickmansworth Road
Northwood, Middlesex HA6 2RN
United Kingdom
Phone (PA): +44-(0) 1923-844751
Fax: ++44-(0) 1923-844600
anwar.padhani@stricklandscanner.org.uk

Whole-body MRI at 1.5T – a How-to Guide, .exar1 protocol file and a video

Whole-body MRI has been used at Paul Strickland Scanner Centre (Northwood, UK) for over 10 years. In that time over 4000 examinations have been performed using a protocol designed to enable the detection and surveillance of metastatic bone and soft tissue disease.

Will McGuire, Deputy Superintendent MRI Radiographer, shares his protocol along with a video demonstrating the use of this protocol.

Visit **www.siemens.com/wb-mri** to download the material.

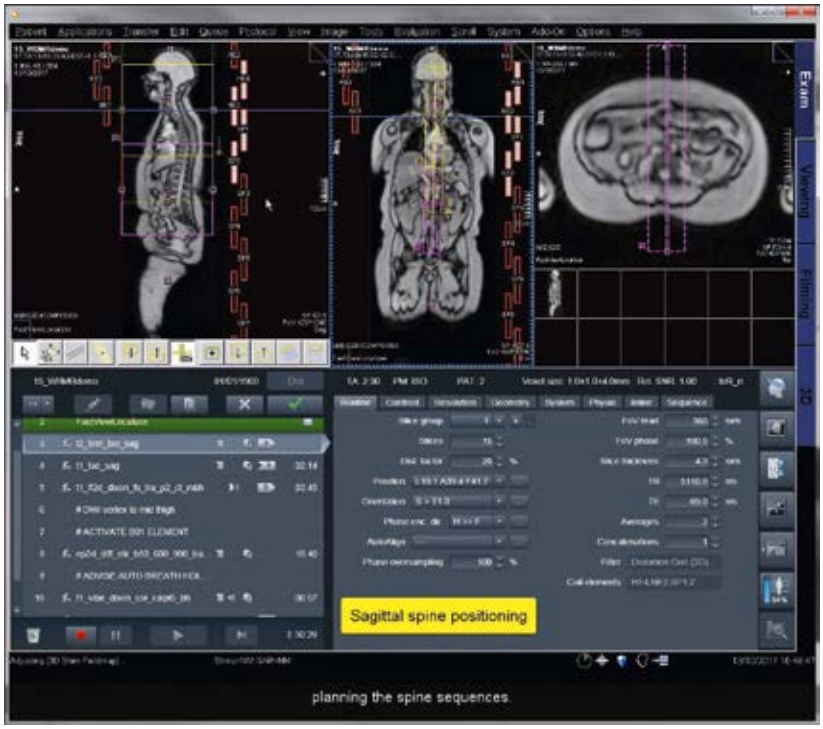

Quantitative WB-MRI with ADC Histogram Analysis for Complex Response of Bone Marrow Metastatic Disease

Danoob Dalili[1]; Anwar R. Padhani[2]; Robert Grimm[3]

[1] Imperial College Healthcare NHS Trust, St Mary's Hospital, London, United Kingdom
[2] Paul Strickland Scanner Centre, Mount Vernon Cancer Centre, Northwood, Middlesex, United Kingdom
[3] Siemens Healthineers, Erlangen, Germany

Introduction

Bone metastases and bone specific malignancies such as multiple myeloma, remain diagnostically challenging not only for disease detection, but also when monitoring disease response to treatments. Recently, whole-body MRI (WB-MRI) incorporating diffusion sequences has been shown to be able to potentially advance the care of breast and prostate cancer patients who have a high metastatic bone disease prevalence, by improving disease detection [1, 2]. In 2015, WB-MRI was accepted into patient care guidelines by the International Myeloma Working Group [3] for disease detection and prognostication.

The incorporation of diffusion imaging sequences into WB-MRI protocols has been shown to improve both bone disease detection and response assessments. WB-MRI with diffusion sequences has the potential to alter clinical diagnostic thinking when assessing bone disease response. This is because it becomes possible to positively assess the success of therapy benefit in diseased bone, which is not possible when using CT and bone scans. Imaging standards for the conduct and systematic reporting of WB-MRI, including therapy response criteria were recently published [4].

Figure 1: Morphological images and high b-value DWI, maximum intensity projections (MIPs).

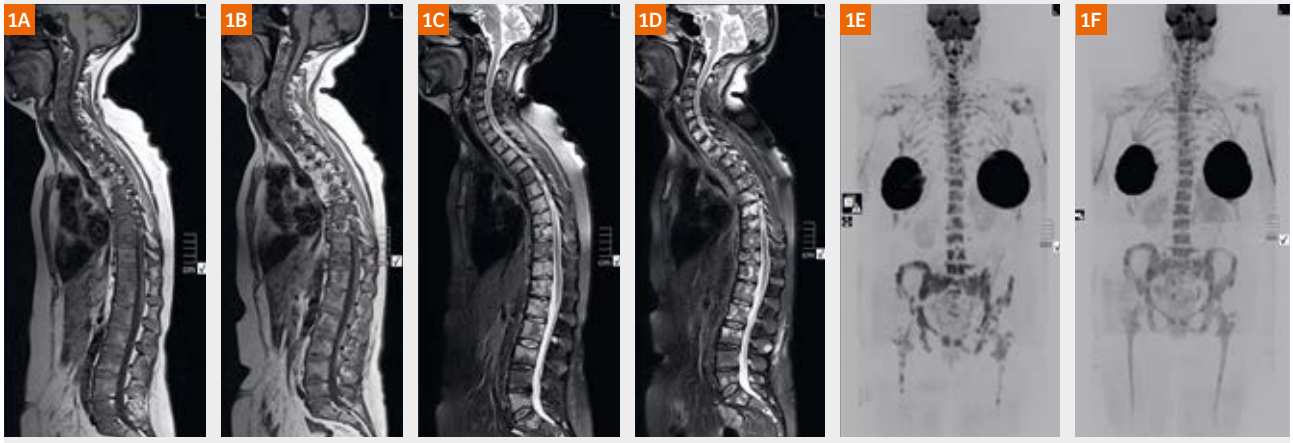

Left 2-columns **(1A, 1B)**: Whole-spine sagittal T1-weighted images show diffuse bone marrow infiltration (1A) with some return of bone marrow fat after chemotherapy (1B).

Middle 2-columns **(1C, 1D)**: Whole-spine sagittal T2w-fs sequences show diffuse bone marrow infiltration (1C) with subtle increases in signal intensity following chemotherapy (1D). The increases in T2w bone marrow signal intensity after therapy are consistent with alternations in tissue water content which is associated with tumor cell kill.

Right 2-columns **(1E, 1F)**: Whole-body b900 3D MIP (inverted scale). The bone marrow is diffusely involved with diffuse regions of high signal intensity in the axial skeleton and in the proximal limb bones before therapy (1E). A global reduction in the b900 signal intensity of bone marrow can be seen, consistent with disease response (1F). There is also uniform increase in extent of signal in the limbs consistent with bone marrow regeneration. Bilateral breast prostheses are also visible.

Uniquely, diffusion imaging brings a degree of objectivity to response assessments, using quantitative apparent diffusion coefficient measurements (ADC; unit $\mu m^2/s$). ADC maps of whole-body disease load, allow objective assessments of bone tumor load and therapy response [5]. There is a high inter and intra-observer agreement of whole-body ADC mapping [6]. Semi-automated threshold-based, quantitative ADC mapping and histogram analysis software, allow deployment of whole-body ADC mapping into the clinic [7].

There is a need for radiologists to understand the biological meaning and likely clinical implications of changes observed in quantitative whole-body ADC maps and histograms. This is particularly the case for malignant bone disease, where diffusion signal changes can arise from the normal bone marrow as well as from malignant tissues, both of which can be intermixed. Several articles have been published in MAGNETOM Flash illustrating the ADC back-mapping technique [7, 8] and tumor therapy response applications [8]. These illustrations have noted that ADC changes reflect on the mechanism of tumor cell death and the re-emergence of tumor cells when therapy resistance arises. In this case report, we demonstrate the ability of the whole-body tumor load software to distinguish ADC changes ascribable to tumor response and bone marrow recovery with successful therapy. Longer-term changes are described in a companion case [9] in this issue of MAGNETOM Flash magazine.

Case study

A 52-year-old woman underwent bilateral mastectomies and reconstructions for multifocal, ER+ bilateral breast cancer in 2010. 4 years later she re-presented with 6 months of bone pain while taking adjuvant Tamoxifen therapy. She was restaged with a whole-body MRI study for disease detection. A response assessment WB-MRI study was undertaken 14 weeks later, following 4 cycles of FEC chemotherapy and bisphosphonates (without growth factor support) (Figs. 1, 2). Unfortunately, 4 months later she developed intracranial metastatic disease and expired.

Continued on page 41.

Figure 2: Morphologic and diffusion-weighted images of the L2 vertebral body.

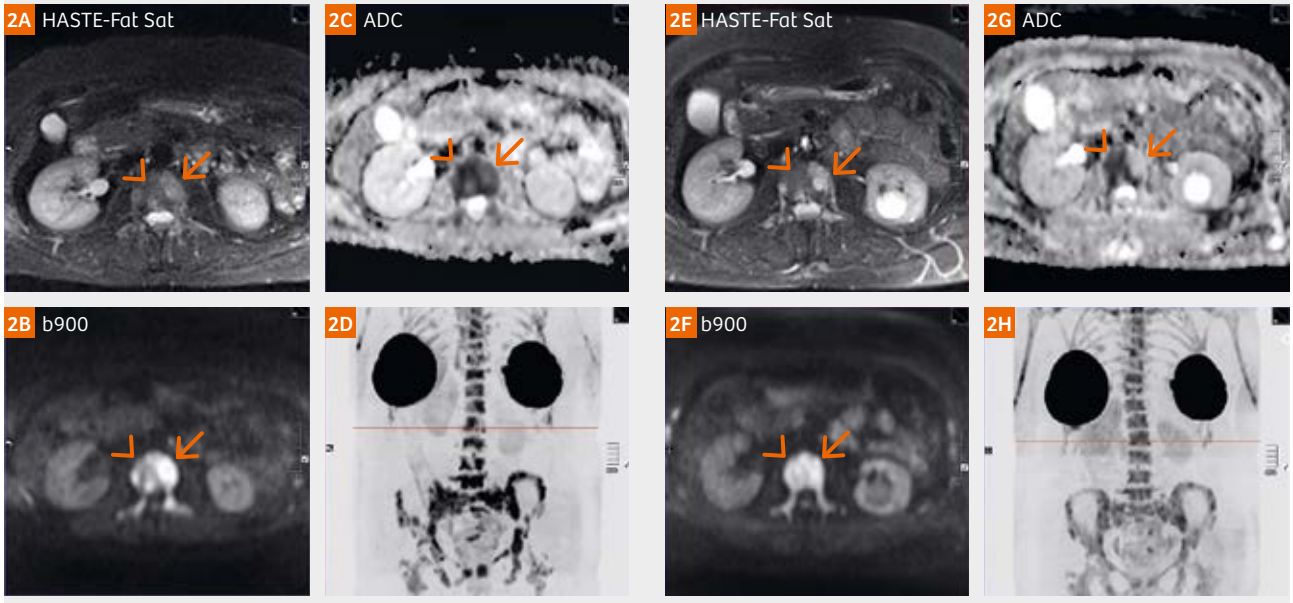

Axial HASTE-Fat Sat, b = 900 s/mm² and ADC images with zoomed whole-body b900 3D MIP (inverted scale) before and after therapy. Axial images are through the L2 vertebral body as indicated by the red reference line. The follow-up images (right 2 columns, **2E-H**) demonstrated excellent response to treatment, with increases in apparent diffusion coefficient (ADC) values for the metastatic deposit in the left side of the vertebral body (arrows). The bone marrow in the right side of the vertebral body (arrow head) demonstrates lowering of ADC values. In this area, the bone marrow T1w-fat percentage (F%) on corresponding Dixon images (not shown) changed from 20% to 26%.

Figure 3: Whole-body tumor load analysis.

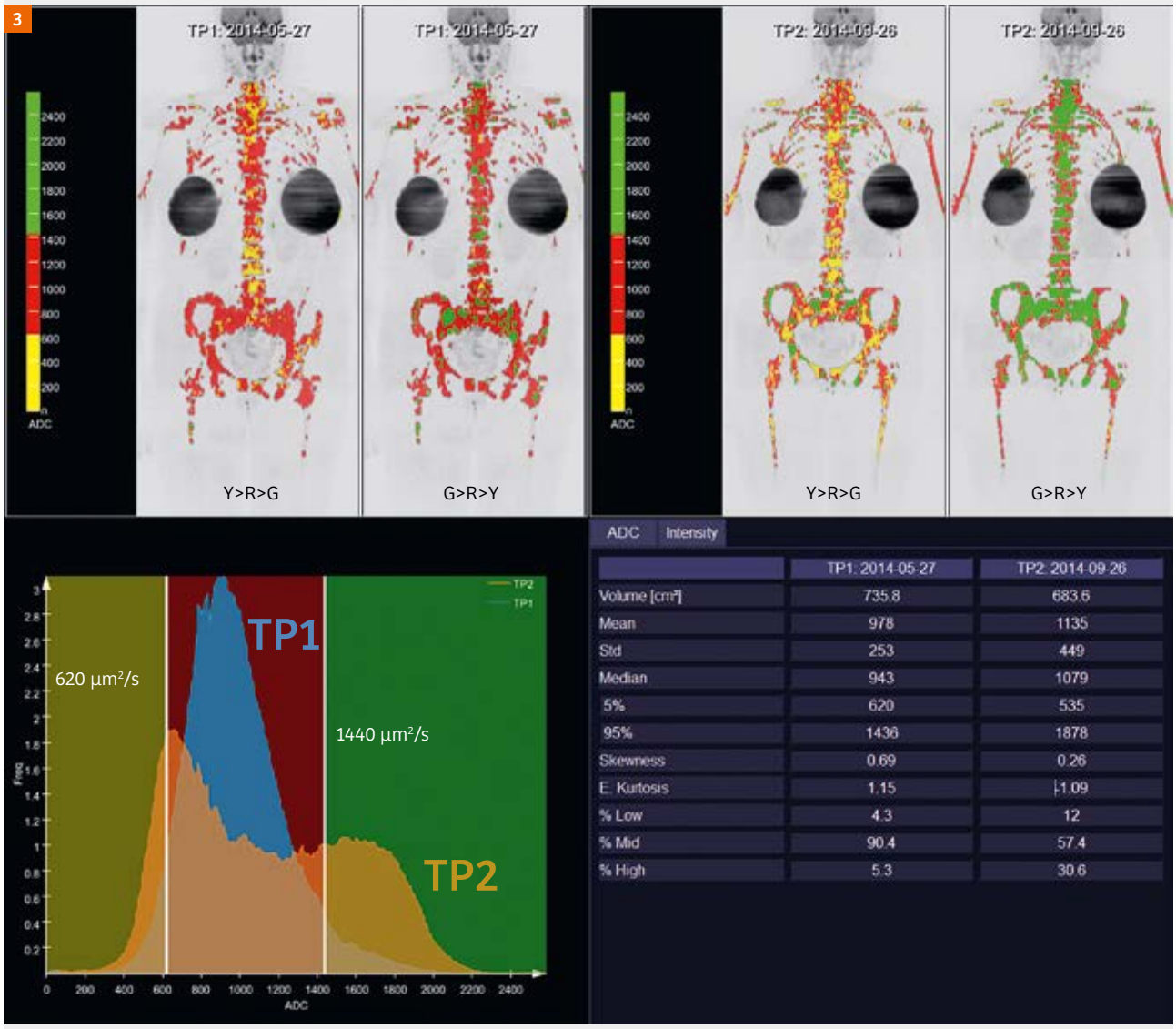

WB-tumor load segmentations were undertaken on *syngo.via* Frontier MR Total Tumor Load software[1] (Siemens Healthcare, released research prototype). The whole-body b900 images were segmented using computed high b-value images of 1000–1200 s/mm², setting a signal intensity threshold of approximately 30 AU. Extraneous signals (such as the brain, thyroid, kidneys, spleen, breast prostheses and bowel) were removed, to leave only recognizable bone sites. The b900 MIP images are overlaid with ADC value classes using the 5th and 95th centile values of the pre-treatment histogram (620 and 1440 µm²/s respectively). Red colored voxels represent untreated disease or those that have no-detected response. Green colored voxels have ADC values ≥ 1440 µm²/s (representing voxels that have increased in ADC values and are 'likely' to be responding). The yellow voxels lie below the 5th centile ADC value of the pre-treatment histogram (620 µm²/s). Thus, yellow voxels represent regions 'likely' to represent normal bone marrow.

736 mL of bone marrow was segmented before therapy and 684 mL after chemotherapy. Note that there is a global increase in median ADC values (943 µm²/s and 1079 µm²/s respectively), a decrease in excess kurtosis (1.15 and -1.1), and broadening of ADC histogram shown by an increase in the ADC standard deviation (253 and 449 µm²/s respectively), of the corresponding relative frequency histograms. There is unimodal distribution of ADC values before (TP1) and a bimodal distribution of the post-treatment (TP2) histogram. Note increasing numbers of yellow and green voxels representing normal bone marrow and cell kill respectively. There are also areas of red indicating residual active disease on TP2.

The color whole-body ADC class back-maps are of two types for each time point. On the left is the ADC color projection focusing on normal bone marrow (yellow voxels; MIP-ADC low image), and on the right of each pair is the ADC color projections focusing on response (green voxels; MIP-ADC high image).

The whole-body MRI scans with diffusion-weighted sequences were undertaken using a 1.5T MAGNETOM Avanto scanner using a published protocol [3]. The baseline scan (TP1) demonstrated extensive metastatic bone only disease (Figs. 1, 2) on morphological T1w and T2w-fs images of the spine.

The follow-up WB-MRI (TP2) demonstrated excellent response to treatment, with decreases in b = 900 s/mm² signal intensity and corresponding increases in apparent diffusion coefficient (ADC) values for individual metastatic deposits (Fig. 2 – arrows). Normal bone marrow return was also noted with increasing fat in the bone marrow (Fig. 2 – arrow heads).

The diffusion-weighted images for both examinations were analysed using threshold-based segmentation with *syngo*.via Frontier MR Total Tumour Load software[1] [7]. The pre-treatment ADC histogram has a unimodal distribution of ADC values (Fig. 3). After 4 cycles of chemotherapy, a bimodal distribution can be seen (Fig. 3). Increased voxels with high ADC values > 1500 µm²/s indicate the presence of tumor cell kill (arrows in Fig. 2). A new peak to the left of the pre-treatment ADC histogram represents the re-emergence of normal bone marrow (Fig. 3).

Discussion

The total tumor load software has been developed to enhance the value of ADC histogram analysis for assessing therapy response. The location of histogram ADC values is undertaken by color-coded projections of ADC classes on the b900 MIP images (MIP-ADC class pairing). In so doing, it is possible to anatomically localize the anatomic site and likely biologic state of the tissues. In this case example, normal bone marrow was assigned to ADC values that are lower than 620 µm²/s [10, 11] and displayed as yellow, voxels between 620 µm²/s and 1440 µm²/s are color coded as red (the 5th–95th centile values of the pre-treatment (TP1) ADC histogram), voxels with an ADC above 1440 µm²/s are shown in green, representing likely response.

The software, allows cycling through these color layers in order to focus the visualization on normal bone marrow (yellow), untreated active disease (red) or likely response (green), respectively (Fig. 4). Since only one color can be projected onto the segmented mask, the following rules are applied for the bone ADC color scheme (from lower to higher ADC values, Yellow-Red-Green).

ADC color projections focusing on marrow are shown on the left of each MIP-ADC class pair, if at least one voxel of the segmented bone has an ADC of less than 620 µm²/s, it will be assigned the yellow color (MIP-ADC low). Otherwise, it will be colored in red if any ADC is between 620 and 1440 µm²/s, or in green, if all ADC values along the projection are above 1440 µm²/s. Thus, the resulting projected color order for normal bone marrow is Yellow > Red > Green.

ADC color projections focusing on response are on the right of each image pair (MIP-ADC high). If at least one voxel of the segmented bone has an ADC of 1440 µm²/s or higher, it will be assigned a green color. Otherwise, it will be colored in red if the ADC falls between 620 and 1440 µm²/s, or in yellow, if all ADC values along the projection are below 620 µm²/s. Thus, the corresponding projected color order for assessing response is Green > Red > Yellow.

The use of ADC color projections, histograms and descriptive histogram statistics enables an easier to understand and objective method of assessing therapy response in bone marrow malignancies. When complex ADC changes occur simultaneously, as in this case (tumor response and bone marrow recovery), the ability to separate and visualize likely active disease, likely response and bone marrow recovery, can enable the success of treatment to be more effectively assessed. This is particularly useful when diffuse disease is present, when morphological images are often uninformative regarding the presence and extent of therapy response.

4

Color coding of ADC ranges:

Yellow (<620 µm²/s):	likely bone marrow
Red (620-1440 µm²/s):	likely untreated disease
Green (>1440 µm²/s):	likely response

(4A) Color projection focusing on normal bone marrow: Yellow voxels cover red and green voxels.

(4B) Color projection focusing on response: Green voxels cover red and yellow voxels.

Figure 4:
ADC color projection modes. In order for color projections to be able to preferentially visualize normal marrow or likely response, the color order for the ray tracing needs to be adjusted. For ADC color projections focusing on normal bone marrow **(4A)**, the ADC-MIP displays low ADC on top (ie, yellow). For ADC-MIP color projections focusing on response **(4B)**, the ADC-MIP displays high ADC on top (green). In this case the threshold for colors are derived from the pretherapy histogram.

[1] *syngo*.via Frontier is for research only, not a medical device. *syngo*.via Frontier MR Total Tumor Load is a released research prototype.

References

1 Woo, S., Suh, C. H., Kim, S. Y., Cho, J. Y., & Kim, S. H. (2017). Diagnostic Performance of Magnetic Resonance Imaging for the Detection of Bone Metastasis in Prostate Cancer: A Systematic Review and Meta-analysis. European Urology. doi:10.1016/j.eururo.2017.03.042.
2 Kosmin, M., Makris, A., Joshi, P. V., Ah-See, M., Woolf, D., & Padhani, A. R. (2017). The addition of whole-body magnetic resonance imaging to body computerised tomography alters treatment decisions in patients with metastatic breast cancer. European Journal of Cancer, 77, 109-116. doi:10.1016/j.ejca.2017.03.001.

Contact

Dr. Danoob Dalili
Specialist Registrar Clinical Radiology
Imperial College Healthcare NHS Trust
St Mary's Hospital
Praed St
London W2 1NY
United Kingdom
Phone: +44 (0) 20 3312 6666
Dalili@doctors.org.uk

Prof. Anwar R. Padhani
Consultant Radiologist and
Professor of Cancer Imaging
Paul Strickland Scanner Centre
Mount Vernon Cancer Centre
Rickmansworth Road
Northwood, Middlesex HA6 2RN
United Kingdom
Phone (PA): +44-(0) 1923-844751
Fax: +44-(0) 1923-844600
anwar.padhani@stricklandscanner.org.uk

3 Dimopoulos, M. A., Hillengass, J., Usmani, S., Zamagni, E., Lentzsch, S., Davies, F. E., & Terpos, E. (2015). Role of Magnetic Resonance Imaging in the Management of Patients With Multiple Myeloma: A Consensus Statement. Journal of Clinical Oncology, 33(6), 657-664. doi:10.1200/jco.2014.57.9961.
4 Padhani AR, Lecouvet FE, Tunariu N, et al. METastasis Reporting and Data System for Prostate Cancer (MET-RADS): Practical Guidelines for Acquisition, Interpretation, and Reporting of Whole-body MRI-based Evaluations of Multiorgan Involvement in Advanced Prostate Cancer. Eur Urol. 2017; 71(1):81-92.
5 Blackledge, M. D., Collins, D. J., Tunariu, N., Orton, M. R., Padhani, A. R., Leach, M. O., & Koh, D. (2014). Assessment of Treatment Response by Total Tumor Volume and Global Apparent Diffusion Coefficient Using Diffusion-Weighted MRI in Patients with Metastatic Bone Disease: A Feasibility Study. PLoS ONE, 9(4), e91779. doi:10.1371/journal.pone.0091779.
6 Blackledge, M. D., Tunariu, N., Orton, M. R., Padhani, A. R., Collins, D. J., Leach, M. O., & Koh, D. (2016). Inter- and Intra-Observer Repeatability of Quantitative Whole-Body, Diffusion-Weighted Imaging (WBDWI) in Metastatic Bone Disease. PLOS ONE, 11(4), e0153840. doi:10.1371/journal.pone.0153840.
7 Grimm R, Padhani AR. Whole-body Diffusion-weighted MR Image Analysis with *syngo.via* Frontier MR Total Tumor Load. MAGNETOM Flash (68) 2/2017, 73-75.
8 Padhani AR. Observing endocrine therapy resistance in metastatic breast cancer with whole body MRI. MAGNETOM Flash (68) 2/2017, 80-83.
9 Dalili D, Joshi P, Grimm R, Padhani AR. Evolution of the malignant bone marrow with successful therapy – quantitative analysis with whole body diffusion MRI. MAGNETOM Flash (69) 3/2017, 43–48.
10 Padhani, A. R., Van Ree, K., Collins, D. J., D'Sa, S., & Makris, A. (2013). Assessing the Relation Between Bone Marrow Signal Intensity and Apparent Diffusion Coefficient in Diffusion-Weighted MRI. American Journal of Roentgenology, 200(1), 163-170. doi:10.2214/ajr.11.8185.
11 Messiou C, Collins DJ, Morgan VA, Desouza NM. Optimising diffusion weighted MRI for imaging metastatic and myeloma bone disease and assessing reproducibility. Eur Radiol. 2011; 21(8):1713-8.

Watch Cancer Develop Multidrug Resistance

In this video Professor Padhani shows how quantitative whole-body MRI is used to monitor therapy response in metastatic breast cancer. Watch the video at

www.siemens.com/WB-MRI

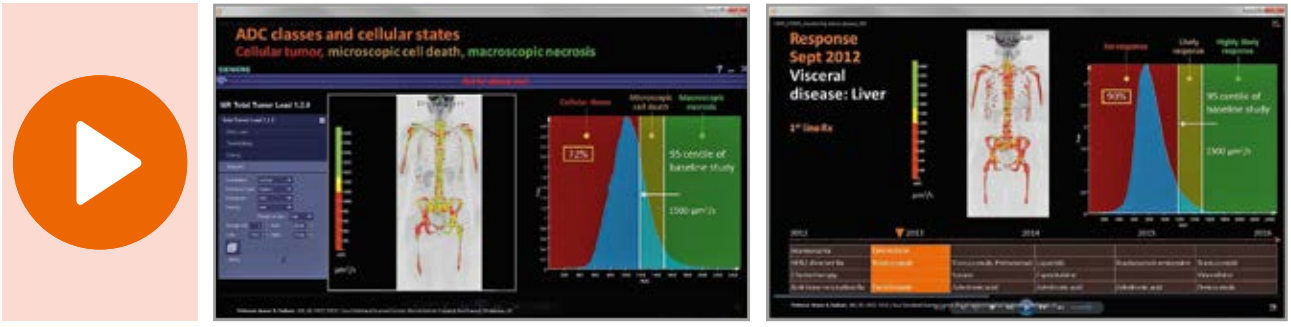

Evolution of the Malignant Bone Marrow with Successful Therapy – Quantitative Analysis with Whole-body Diffusion-weighted MRI

Danoob Dalili[1]; Priya V. Joshi[2]; Robert Grimm[3]; Anwar R. Padhani[4]

[1] Imperial College Healthcare NHS Trust, St Mary's Hospital, London, United Kingdom
[2] Mount Vernon Cancer Centre and the East and North Herts NHS trust hospitals, Northwood, Middlesex, United Kingdom
[3] Siemens Healthineers, Erlangen, Germany
[4] Paul Strickland Scanner Centre, Mount Vernon Cancer Centre, Northwood, Middlesex, United Kingdom

Introduction

Bone disease is a common occurrence in metastatic breast cancer (MBC), but accurate evaluation of treatment benefit is notoriously difficult to do. There is a critical clinical need to develop non-invasive biomarkers to assess therapeutic effects of bone involvement in MBC. This is because the detection of primary non-responders and secondary therapy failure when disease burden is lowest, can help guide therapy decisions [1]. Currently, imaging assessments can only determine bone disease progression, because of which many patients with bone predominant disease receive ineffective medications for prolonged periods, and as a result do not change treatments until disease burdens become large, thus potentially hindering the effectiveness of follow-on treatments. It has been suggested, that aggressive disease detection methods and response monitoring could promote precision oncology in patients with bone involvement in MBC [2].

Guidelines from the American Society of Clinical Oncology and the European School of Oncology have recognized these limitations, advocating the use of serum tumor markers in addition to clinical assessments and imaging for monitoring MBC response [3, 4]. There is however, confusion regarding what constitutes suitable imaging for bone disease monitoring. All guidelines advocate the use of computed tomography (CT) and bone scans (BS), thus side stepping the limitations of CT/BS for assessing response in women with bone predominant metastatic disease.

Figure 1: Serial changes on morphological whole-spine sagittal T1-weighted images.

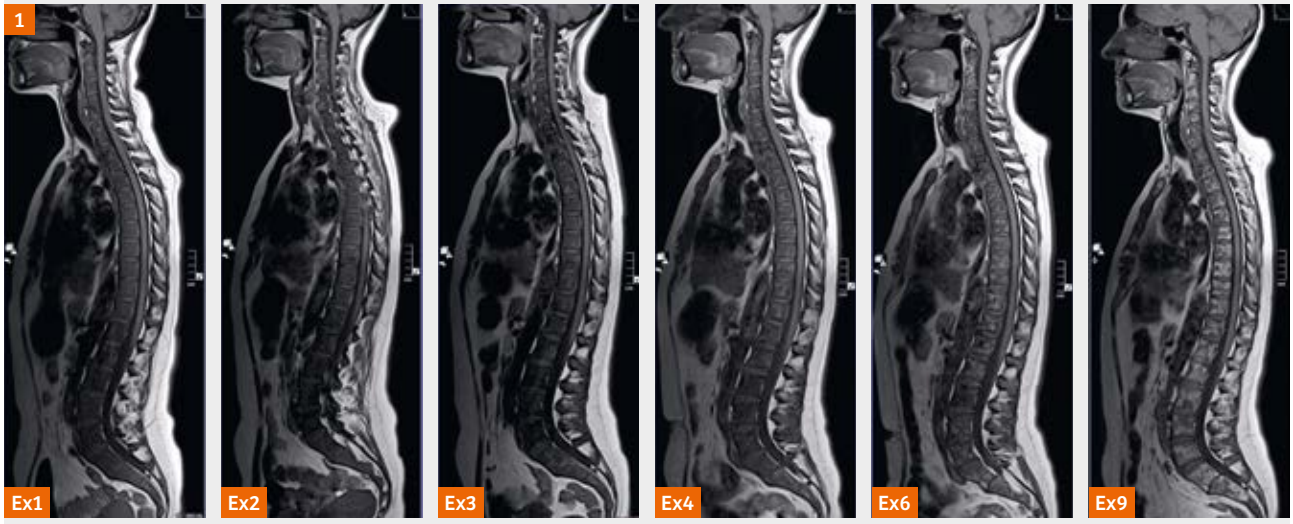

Diffuse metastatic infiltration throughout the spine, however note the small amount of fat on examination 6 (Ex6). The re-emergence of fat signal intensity is best appreciated on the last study (Ex9). The nature of the darker background signals on Ex9 is uncertain, but bone marrow (BM) scarring and/or residual active disease must be considered.

Figure 2: Serial changes on sagittal whole-spine STIR images.

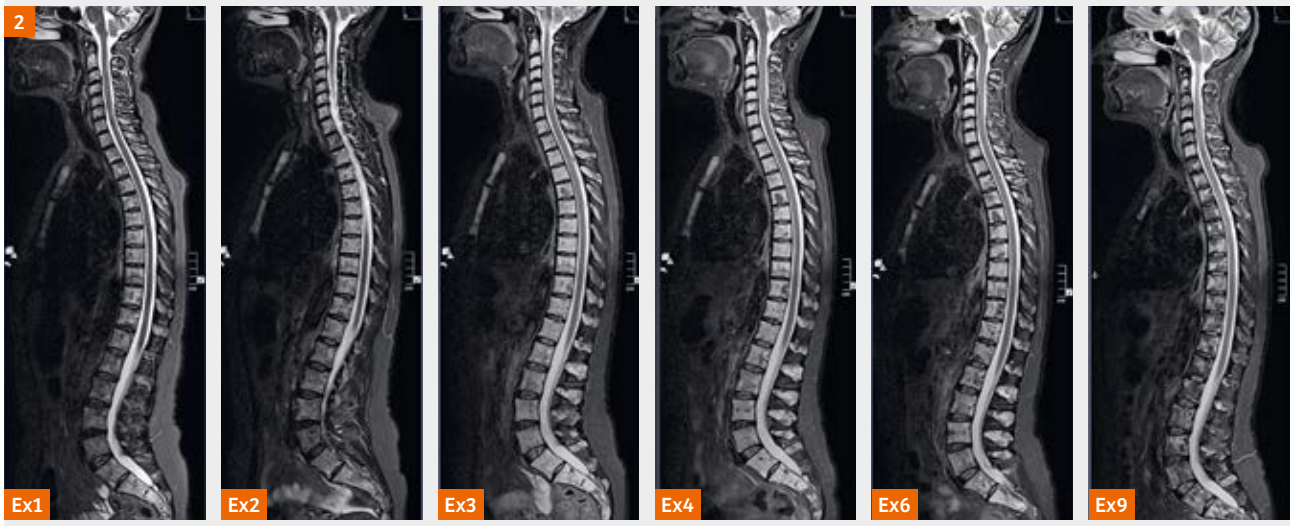

Diffuse metastatic infiltration throughout the spine. Note no appreciable change in signal intensity between Ex1 and Ex2. There is a marked increased in bone marrow signal between Ex3 and Ex6 consistent with increased BM water, which fades on the last examination (Ex9).

Figure 3: Serial changes on whole-body b = 900 s/mm^2 3D MIP images (inverted scale).

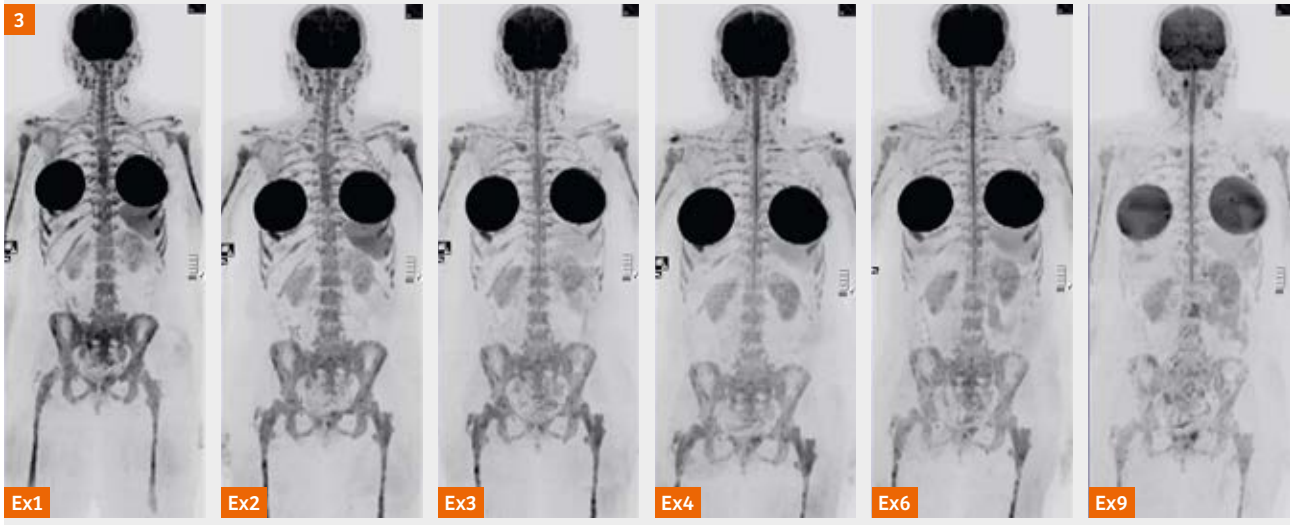

b900 3D MIP images (inverted scale) demonstrate a gradual reduction in signal intensity throughout the course of treatment, which is most evident between Ex1 and Ex2. The signal intensity is lowest on the last examination (Ex9). No extra-osseous disease is detected. Bilateral breast implants are seen in situ.

There is accumulating evidence showing the added value of PET/CT and whole-body MR imaging (WB-MRI) for decision making in metastatic breast cancer [5, 6]. WB-MRI with morphological and diffusion-weighted sequences has emerged as powerful tool for detecting and assessing the response of MBC with good efficacy in the assessment of bone metastases [7]. The key advantage of WB-MRI is that the success of therapies can be positively assessed (CT/BS scans use the 'no evidence of progression' category as meaning therapy success). As a result, WB-MRI has the potential to alter clinical diagnostic thinking when assessing bone disease response [6]. Uniquely, quantitative apparent diffusion coefficient values (ADC; unit μm^2/s) can bring objectivity to therapy response assessments.

Figure 4: Serial changes on MIP-ADC projection images.

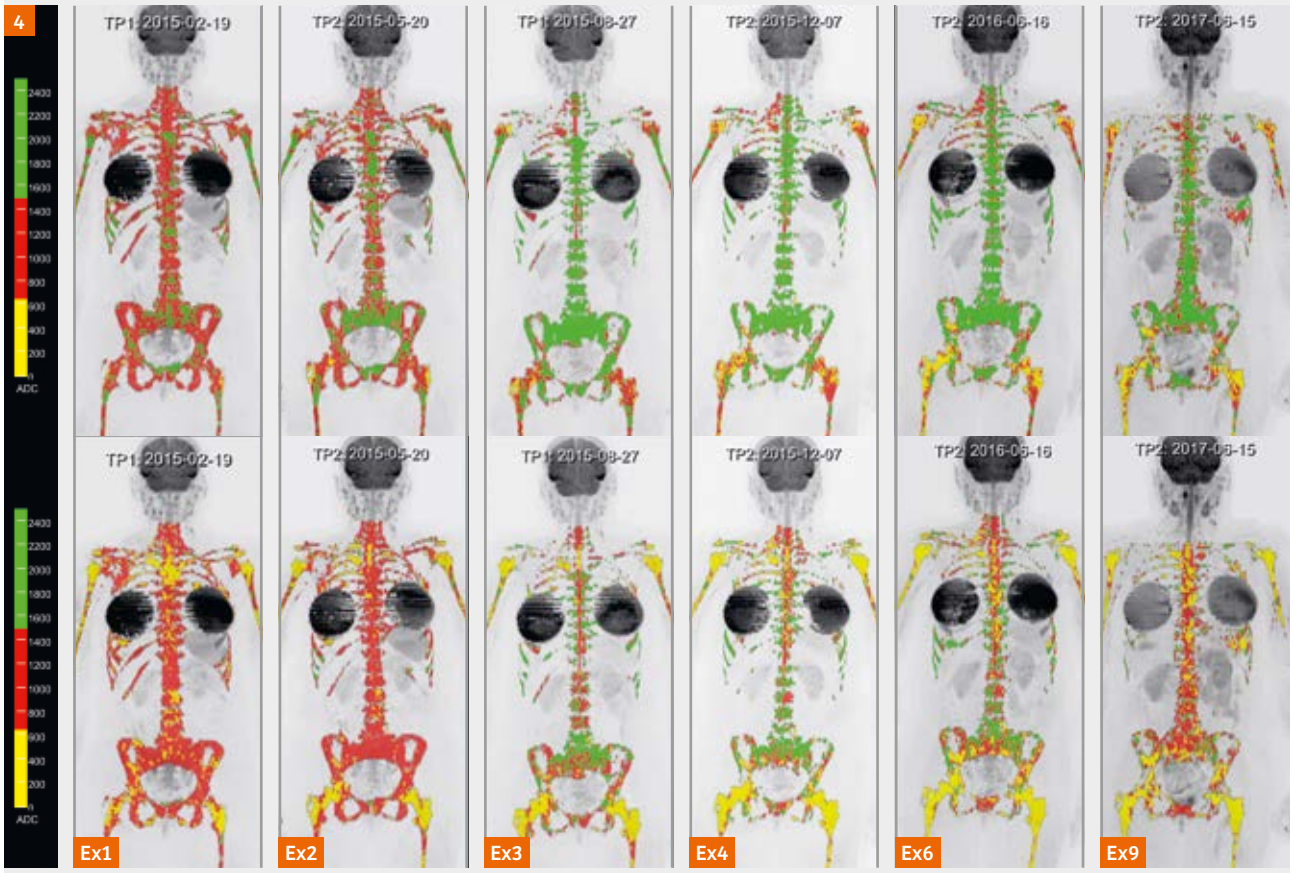

Top row: ADC color projections focusing on response showing serial changes in voxels that are highly likely to be responding (green). Marked response is first observed on Ex3 in voxels co-localized to the axial skeleton. These high ADC voxels only decrease in extent on Ex9.

Bottom row: ADC color projections focusing on marrow showing serial changes in voxels that are likely to represent normal bone marrow (yellow). Their appearance is co-localized to the appendicular skeleton (proximal humeri and femora). The appearance of fat in the spine on Ex9 shown on T1w images in Figure 1 cannot be readily appreciated on these projection images.

Semi-automated threshold-based, quantitative ADC mapping and histogram analysis has been introduced as a viable and efficient tool for whole-body ADC mapping [8].

This case report applies the methodology of the companion article by Dalili et al. on the ability of the *syngo*.via Frontier MR Total Tumor Load software[1] to distinguish ADC changes ascribable to tumor response and bone marrow recovery [9]. We discuss how ADC changes can be explained by the mechanism of tumor cell death and introduce a biologic model that explains imaging observations during the repair phase after effective therapy [10].

[1] *syngo*.via Frontier is for research only, not a medical device. *syngo*.via Frontier MR Total Tumor Load is a released research prototype.

Case study

A 49-year-old peri-menopausal woman presented with bone only metastatic lobular carcinoma (ER-positive, HER2-neu negative) in 2013. Bilateral mastectomy (left breast for risk reduction), axillary node clearance and breast reconstructions were performed with completion radiotherapy to the right supraclavicular fossa and chest wall. She underwent initial systemic anticancer therapy with Tamoxifen and Zoledronic acid infusions. During treatment, she developed bone pain but CT scans were unhelpful regarding the status of her bone disease. Subsequently she was referred for a whole-body MRI scan to assess her disease status (volume and tumor viability). Nine WB-MRI studies were then performed every 3–4 months over the next 3.5 years for therapy response assessments.

Figure 5: ADC histogram changes with time.

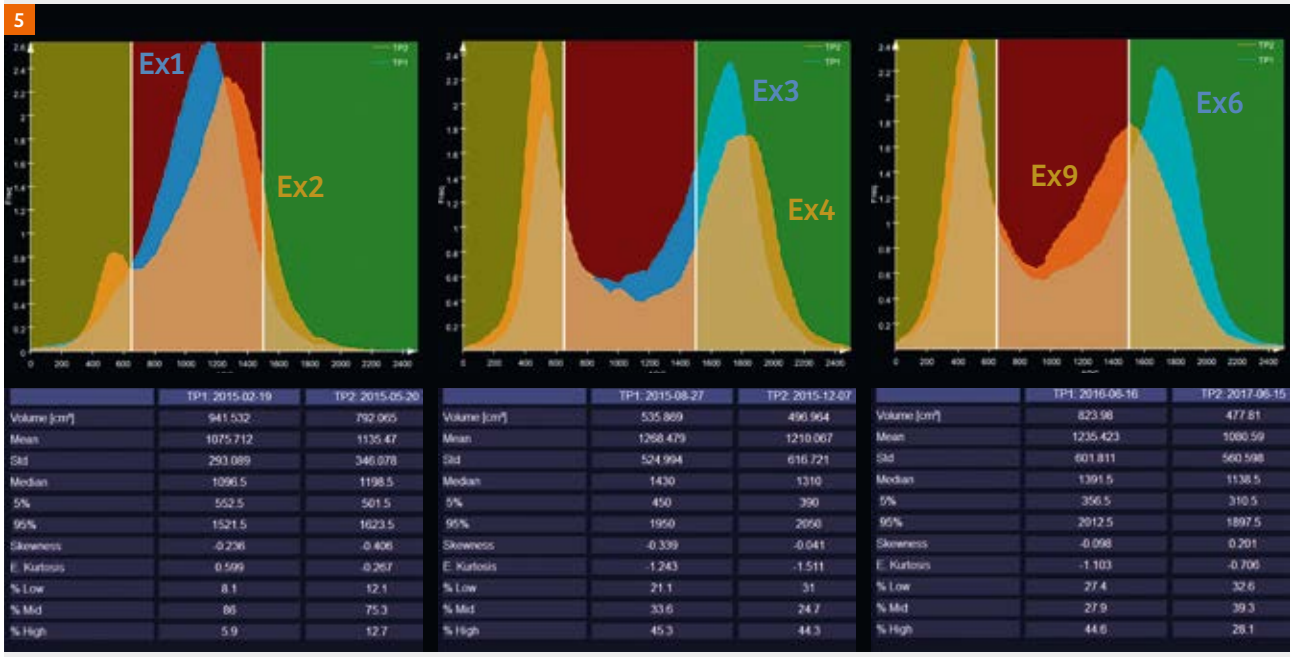

Histograms were created using the methodology of the accompanying article [9] at each time point. Fixed ADC thresholds were chosen (650 and 1500 µm²/s) because examination 1 was an 'on treatment' (Tamoxifen and Zoledronic acid) study (that is, no true pre-therapy baseline study was available). These default thresholds are based on literature values [12, 13]. Therefore, voxels in the red range are likely to represent untreated disease or those that have no-detected response. Green colored voxels have ADC values ≥ 1500 µm²/s (representing voxels that are 'likely' to be responding). Yellow voxels lie below 650 µm² and represent regions 'likely' to represent normal bone marrow.

Ex1 Ex2: At baseline (Ex1), the histogram is negatively skewed (tail to the left) consistent with the therapy effects of Tamoxifen, although 86% of segmented voxels are in the active range (between 650–1500 µm²/s). With the change of treatment to Anastrozole and Goserelin (Ex2), a positive therapy change effect can be detected with a small right sided shift of the histogram. The bulk of the voxels on Ex2 (75%), remain in the red-voxel range (650–1500 µm²/s). The emergence of a new peak below 650 µm²/s is noteworthy and, these yellow voxels seem confined to the limb bones (Fig. 4 – bottom row).

Ex3 Ex4: With the change of treatment to Everolimus and Exemestane (Ex3), a more dramatic histogram change becomes visible with 2 well separated peaks (below 650 µm²/s and above 1500 µm²/s). The peak above 1500 µm²/s indicates large cell kill and highly likely response and these green voxels can be located to the axial skeleton (Fig. 4 – top row). The enlarging peak below 650 µm²/s is consistent with further return of the mixed bone marrow depicted as yellow areas in the limb bones (Fig. 4 – lower row). This twin peak histogram pattern does not change much in the 6 month period between Ex4–Ex6.

Ex6 Ex9: A change of the histogram becomes visible 12 months later, on Ex9. At this point, the higher peak of the ADC histogram has begun to shift towards the red region, visible as increasing red regions on the MIP-ADC low projection images in Fig. 4. However, these emerging red voxels are unlikely to represent tumor regrowth because the b900 signal intensity has remained low (Fig. 3) and fat has remerged in the marrow spaces (Fig. 1). So, it's most likely that the emerging red regions on Ex9 are likely to represent bone marrow scarring/bone sclerosis according to the model in Fig. 6. This remains to be confirmed.

After the first WB-MRI examination (examination 1), therapy was changed to Anastrozole and Goserelin with Zoledronic acid infusions. She remained symptomatic and a follow-up WB-MRI (examination 2) did not demonstrate appreciable cell kill to the therapy change. Subsequently she was switched to Exemestane and Everolimus (mTOR inhibitor) with good symptomatic relief of bone pain. Symptomatic relief of bone pain was accompanied by a good therapy effect on whole-body MRI scans (examinations 3 and 4). However, her blood hemoglobin levels remained below the normal range at 90 g/L between examinations 1 and 4. Eventually she returned to work and currently, she suffers only from minor drug toxicity related side effects. Her hemoglobin recovered to the normal range by examination 6 (120 g/L) at 18 months, and improved further to 130 g/L by examination 9 at 30 months, thus confirming an overall good systemic response.

In this report, we illustrate six WB-MRI examinations, with the initial four studies performed consecutively at 3–4 month intervals (Ex1–Ex4) and the latter two (Ex6 and Ex9) at 18 months and 30 months respectively. All studies were undertaken using the same 1.5T MAGNETOM Avanto scanner, utilizing a published protocol [11]. The diffusion-

Figure 6: Biological model of the relationships between bone marrow state, high b-value signal intensity and ADC values in the setting of therapy response [10].

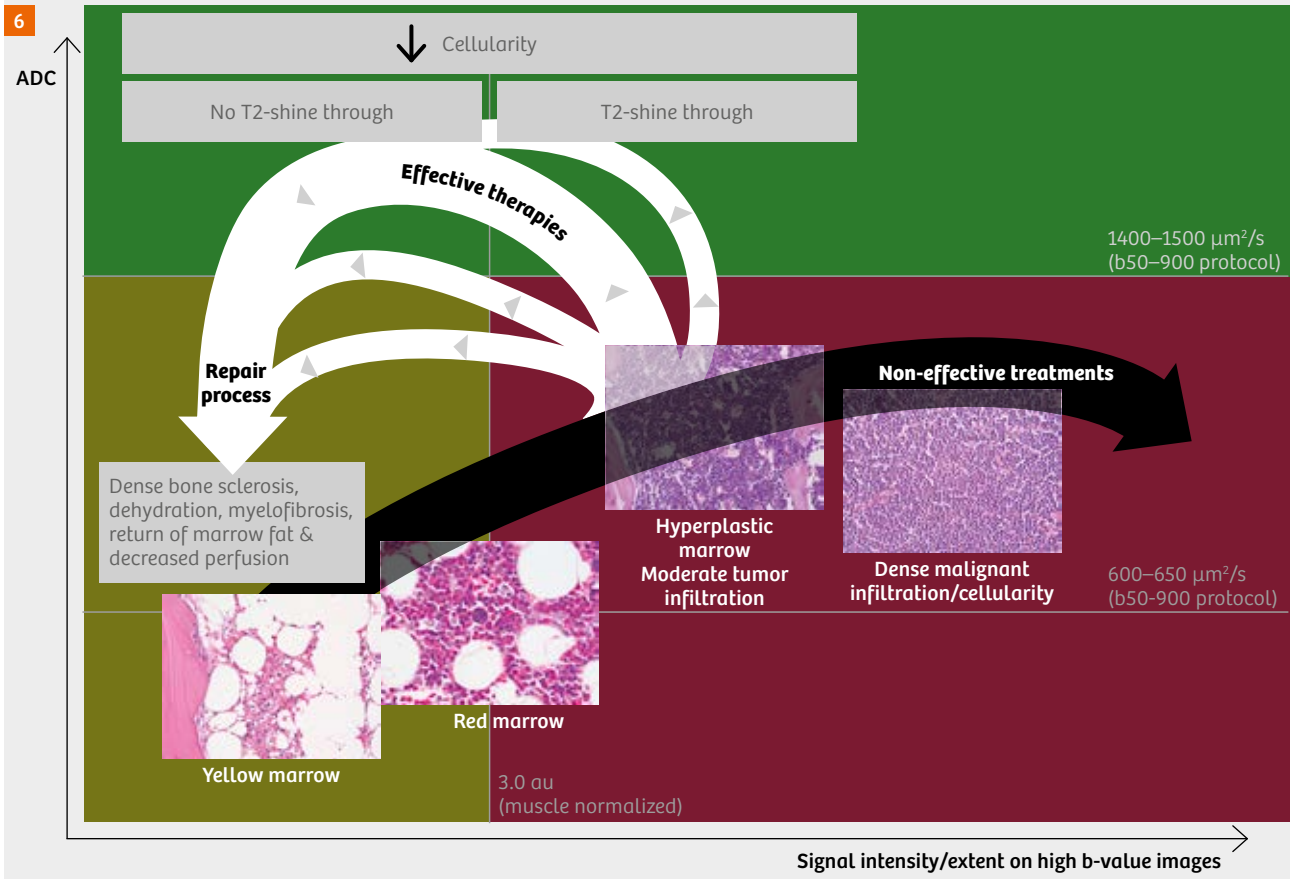

With therapy progression (black arrow), increases in the volume of abnormal signal intensity, new areas of abnormal signal intensity, or increased intensity of abnormalities on high b-value DW images can be seen. Modest increases, unchanged or slight decreases in ADC values compared to pre-therapy values can occur with disease progression. The initial modest increase in ADC values with disease progression occurs because tumor infiltration displaces bone marrow fat cells, increases bone marrow water (including water in the extracellular space) and increases tissue perfusion, thus returning higher ADC values compared to yellow or mixed bone marrow. The important point to note is that these increases in ADC values tend to be of small magnitude, provided that the metastatic lesions remain non-necrotic and in our experience rarely increases > 1400–1500 µm²/s. Stable ADC values occur when unchanged tumor cellularity occurs with increases in the geographic extent of disease. Reductions in ADC values are probably related to increasing cellularity within a fixed bone marrow space.

A variety of high b-value signal and ADC changes can be seen with effective therapy (white arrows). Decreases in signal intensity on high b-value images accompanied by increases in ADC values is the usual pattern (thick white arrow). The extent of ADC increases seems to depend on the type of treatment given with higher ADC values for treatments that cause greater tumor cell death especially when there is a strong inflammatory component. Occasionally, unchanged or minimally decreased high signal intensity on high b-value images associated with marked rises in ADC values is observed, as in this case (Ex2–Ex6). This is termed 'T2-shine through' which also indicates a successful response to therapy. T2-shine through appearances often can take a long time (often more than 1 year) for b-value signal intensity and ADC to decrease to the normal levels. The emergence of bone marrow sclerosis, fibrosis and/or return of bone marrow fat are part of repair processes. Note that these repair processes can decrease b-value signal intensity without affecting ADC values.

weighted images of examinations were analysed using threshold-based segmentation with *syngo*.via Frontier MR Total Tumor Load prototype software[1] [8]. Response to treatment was displayed using the methodology described in the accompanying article [9].

[1] *syngo*.via Frontier is for research only, not a medical device.
syngo.via Frontier MR Total Tumor Load is a released research prototype.

Discussion

The premise for the use of ADC as a parameter of tissue characterization in the setting of treatment response, is that therapy-induced cell death precedes macroscopic lesion size changes. As a result of cellular necrosis, which results in loss of cell membrane integrity and increases in extracellular space water, ADC values typically increase.

During the following weeks to months, tumors may show shrinkage, with a resorption of the free extracellular fluid and fibrotic conversion leading to decreases in ADC values, although tumor recurrence can also result in reduced ADC values.

The degree of increase in ADC with successful therapy is highly dependent on the mode of cellular death with necrotic cell death resulting in higher ADC values due to associated inflammation and increased tissue water. Thus, chemotherapy typically results in greater degrees of tumor cell death and greater increases in ADC values [10]. With hormonal therapy, the mode of cell death is typically apoptotic and ADC value increases are smaller [12] as shown by the small ADC histogram shift between examinations 1 and 2 (Anastrozole and Goserelin therapy). When combination treatments are used, a synergistic, additive therapy effect can be observed clinically. This explains the greater ADC change in this case where Everolimus and Exemestane (mTOR inhibitor and hormonal therapy) were used together (examinations 3–6) resulting in two distinct peaks in the ADC histogram.

The phenomenon of 'T2-shine though' indicates a successful therapeutic effect with bone marrow edema. 'T2-shine through' can take a long time for high b-value signal intensity and ADC to decrease to normal levels [10]. The emergence of bone sclerosis, bone marrow fibrosis and/or return of bone marrow fat are part of repair processes, reducing high b-value signal intensity and lowering ADC values visible on the Ex9 images [10].

This latter phenomenon of decreasing ADC values with tissue repair highlights the need to evacuate all the acquired images (multiparametric assessments) for the correct interpretation of likely tissue disease status. So relying on ADC histograms alone may be misleading in the setting of tissue repair and recovery, making it necessary to take into account morphological appearances and quantitative parameters such as fat fraction and high b-value signal intensity to distinguish between healing processes from recurrent/residual cancer.

Contact

Dr. Danoob Dalili
Specialist Registrar Clinical Radiology
Imperial College Healthcare NHS Trust
St Mary's Hospital
Praed St
London W2 1NY
United Kingdom
Phone: +44 (0) 20 3312 6666
Dalili@doctors.org.uk

Prof. Anwar R. Padhani
Consultant Radiologist and
Professor of Cancer Imaging
Paul Strickland Scanner Centre
Mount Vernon Cancer Centre
Rickmansworth Road
Northwood, Middlesex HA6 2RN
United Kingdom
Phone (PA): +44-(0) 1923-844751
Fax: +44-(0) 1923-844600
anwar.padhani@stricklandscanner.org.uk

References

1 Lin NU, Thomssen C, Cardoso F et al. European School of Oncology-Metastatic Breast Cancer Task Force. International guidelines for management of metastatic breast cancer (MBC) from the European School of Oncology (ESO)-MBC Task Force: Surveillance, staging, and evaluation of patients with early-stage and metastatic breast cancer. Breast. 2013; 22(3):203-10.
2 Graham LJ, Shupe MP, Schneble EJ, et al. Current approaches and challenges in monitoring treatment responses in breast cancer. J Cancer. 2014 Jan 5;5(1):58-68.
3 Harris L, Fritsche H, Mennel R, et al. American Society of Clinical Oncology. American Society of Clinical Oncology 2007 update of recommendations for the use of tumor markers in breast cancer. J Clin Oncol. 2007; 20;25(33):5287-312.
4 Cardoso F, Costa A, Senkus E, et al. 3rd ESO-ESMO International Consensus Guidelines for Advanced Breast Cancer (ABC 3). Ann Oncol. 2017 Jan 1;28(1):16-33.
5 Riedl CC, Pinker K, Ulaner GA, et al. Comparison of FDG-PET/CT and contrast-enhanced CT for monitoring therapy response in patients with metastatic breast cancer. Eur J Nucl Med Mol Imaging. 2017 [epub].
6 Kosmin M, Makris A, Joshi PV, et al. The addition of whole-body magnetic resonance imaging to body computerised tomography alters treatment decisions in patients with metastatic breast cancer. Eur J Cancer. 2017; 77:109-116.
7 Woolf DK, Padhani AR, Makris A. Assessing response to treatment of bone metastases from breast cancer: what should be the standard of care? Ann Oncol. 2015; 26(6):1048-57.
8 Grimm R, Padhani AR. Whole-body Diffusion-weighted MR Image Analysis with syngo.via Frontier MR Total Tumor Load. MAGNETOM Flash 2017; 68(2), 73-75.
9 Danoob Dalili, Anwar R. Padhani, Robert Grimm. Quantitative WB-MRI with ADC histogram analysis for demonstrating complex response of bone marrow metastatic disease. MAGNETOM Flash 2017; 69(3): 38–42.
10 Padhani AR, Makris A, Gall P, et al. Therapy monitoring of skeletal metastases with whole-body diffusion MRI. J Magn Reson Imaging. 2014; 39(5):1049-78.
11 Padhani AR, Lecouvet FE, Tunariu N, et al. METastasis Reporting and Data System for Prostate Cancer (MET-RADS): Practical Guidelines for Acquisition, Interpretation, and Reporting of Whole-body MRI-based Evaluations of Multiorgan Involvement in Advanced Prostate Cancer. Eur Urol. 2017; 71(1):81-92.
12 Padhani, AR, Van Ree, K, Collins DJ, et al Assessing the Relation Between Bone Marrow Signal Intensity and Apparent Diffusion Coefficient in Diffusion-Weighted MRI. American Journal of Roentgenology 2013; 200(1), 163-170.
13 Messiou C, Collins DJ, Morgan VA, Desouza NM. Optimising diffusion weighted MRI for imaging metastatic and myeloma bone disease and assessing reproducibility. Eur Radiol. 2011; 21(8):1713-8.
14 Padhani AR. Observing endocrine therapy resistance in metastatic breast cancer with whole body MRI. Magnetom FLASH 2017; 68(2):80-83.

Whole-body Diffusion-weighted MRI: The Time has Come for a Change

Atul Kapoor; Goldaa Mahajan; Aprajita Kapoor

Department of Radiology and Magnetic Resonance Imaging, Advanced Diagnostics Amritsar, Punjab, India

Abstract

The two functional tools available for detecting and staging cancer are PET/CT and WB-DWMRI [1]. PET/CT has been the established modality for the last two decades. Improvements in MRI technology, however, mean that it is now possible to perform whole-body functional and anatomical imaging without ionizing radiation [2]. In this study, we share our experiences of the first 50 patients with cancer who underwent whole-body imaging. We determined patient compliance, practicality of performing the study, final results, and cost effectiveness. We also performed a review of studies conducted between 2009 and 2016 to compare WB-DWMRI with PET/CT for imaging cancer patients.

NRCL	Score
No discomfort	1
Mild discomfort	2
Moderate discomfort – bearable	3
Severe discomfort – bearable	4
Unbearable – sedative required	5

Table 1: Table to determine nurse-reported comfort levels (NRCL).

PCS	No discomfort	Mild	Severe
Preparation	0	1	2
Sedation	0	1	2
IV use	0	1	2
Radiation dose (mSv)	0	1	2
Examination time			
< 1 hour	0		
1–2 hours		1	
> 2 hours			2
Reading time	Same day	Next day	> 2 days
Time (hours)	0	1	2
Ambient noise, temperature	0	1	2

Table 2: Table to determine patient comfort score (PCS).

Methods

We analyzed data from 50 consecutive cancer patients who underwent whole-body diffusion-weighted MRI (WB-DWMRI) at our institute. We recorded nurse-reported comfort level (NRCL) and patient comfort score (PCS). All patients had previously undergone a PET/CT and were on follow-up treatment for cancer. We provided questions to establish NRCL and PCS (Tables 1 and 2). We also conducted a review of the literature on WB-DWMRI, and determined mean sensitivity and specificity from 19 articles published between 2009 and 2016. Finally, we calculated the incremental cost-effectiveness ratio (ICER) for both WB-DWMRI and PET/CT.

Technique

WB-DWMRI was performed on a 1.5T MAGNETOM Amira system (Siemens Shenzhen Magnetic Resonance Ltd. (SSMR), China) in four stations, using local coils and without contrast medium.Images were taken from the head to the mid-tibia level, and were acquired axially under free breathing. Diffusion gradients were applied in the X, Y, and Z axes before and after a 180-degree inversion pulse in order to have fat-saturated images and diffusion sensitivity b-values of 0, 400, and 800 mm^2/sec. The data obtained underwent multiplanar reformatting to produce whole-body images in the coronal plane, and were inverted to provide grayscale images (Fig. 1A, B) for analysis. Apparent diffusion coefficient (ADC) values for regions of interest (ROI) were determined in order to estimate tumor cellularity, and were expressed in units of 10^{-3} mm^2/s. Another parameter, the lesion-to-spinal-cord ratio, was determined on a high b-value image using the ROI technique. T2w HASTE whole-body coronal images and T1w sagittal images of the spine were also obtained. The complete study lasted a total of 16 minutes.

Results

The analysis of the data obtained from the responses to Tables 1 and 2 revealed that the mean NRCL score for patients in both groups (WB-DWMRI and PET/CT) was quite similar: 1.3 and 1.4 respectively (1.2–1.5: 95% CI) (Fig. 2). The PCS was 1.4 (1.2–1.5: 95% CI) in the WB-DWMRI group, and 6.3 (6.0–6.7: 95% CI) for the PET/CT

group (Fig. 3). The Kruskal-Wallis test was performed for the above results. It showed no statistical difference in the NRCL results between the two groups (p = 0.8), and a statistically significant difference in the PCS of the two groups (p = 0.02) (Fig. 4).

The literature review of the articles listed in Table 3 found that all the studies showed that WB-DWMRI can be used to diagnose and stage malignancy, and to assess treatment response in cancer patients by quantifying changes in ADC. Almost all the studies suggested that the two modalities were comparable in terms of sensitivity and specificity when it came to detecting metastasis. PET/CT had a slight edge in diagnosing small lung metastasis and subcentimeter nodal metastasis, while WB-DWMRI had a slight edge in detecting liver, brain, and bony metastasis. Pooled sensitivity of WB-DWMRI was 97% for bony metastatic detection and 89% for lymph node detection. Overall sensitivity for WB-DWMRI was 93%, while overall pooled sensitivity for PET/CT was 91%. The calculated incremental cost-effectiveness ratio (ICER) was 150.53 for WB-DWMRI, and 263.73 for PET/CT. In India, WB-DWMRI costs 14,000 rupees, and PET/CT costs 24,000 rupees.

Figure 1:
(1A) WB-DWMRI image showing multiple bony metastases.

(1B) WB-DWMRI image showing multiple abdominal metastases in a patient with prostate carcinoma.

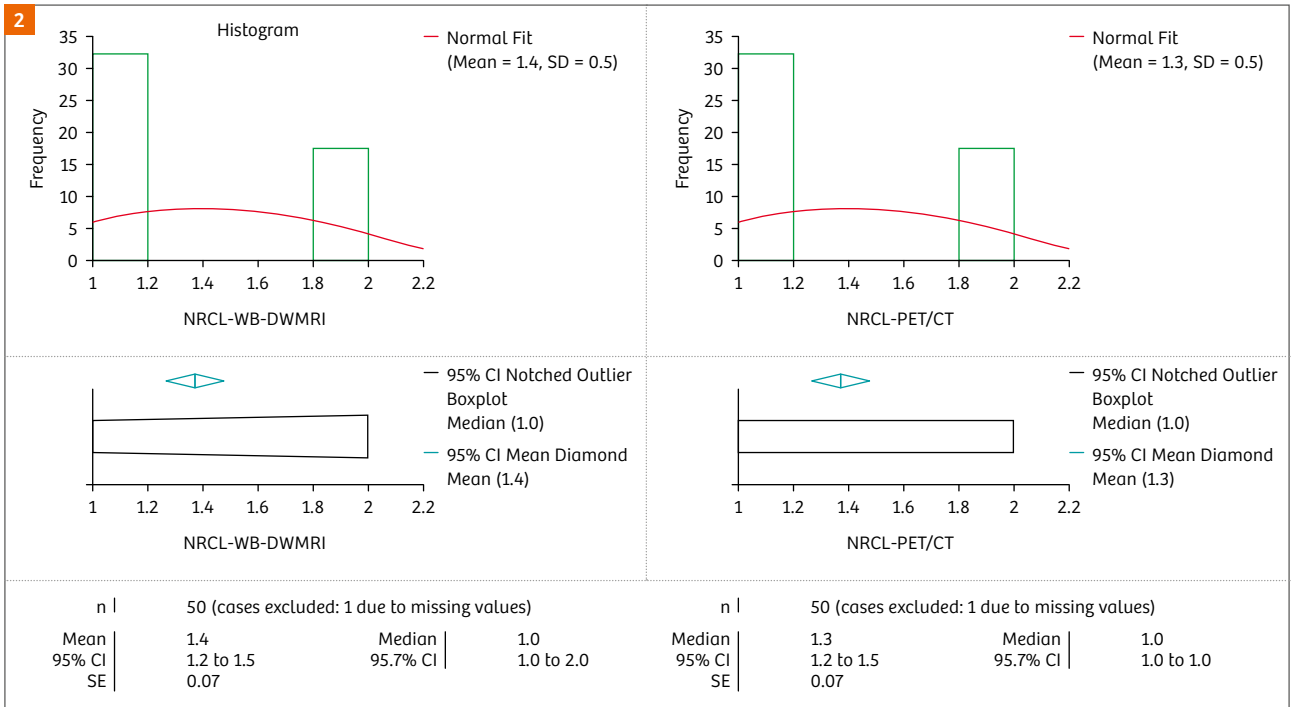

Figure 2: Histogram of NRCL scores in the WB-DWMRI and PET/CT groups.

3

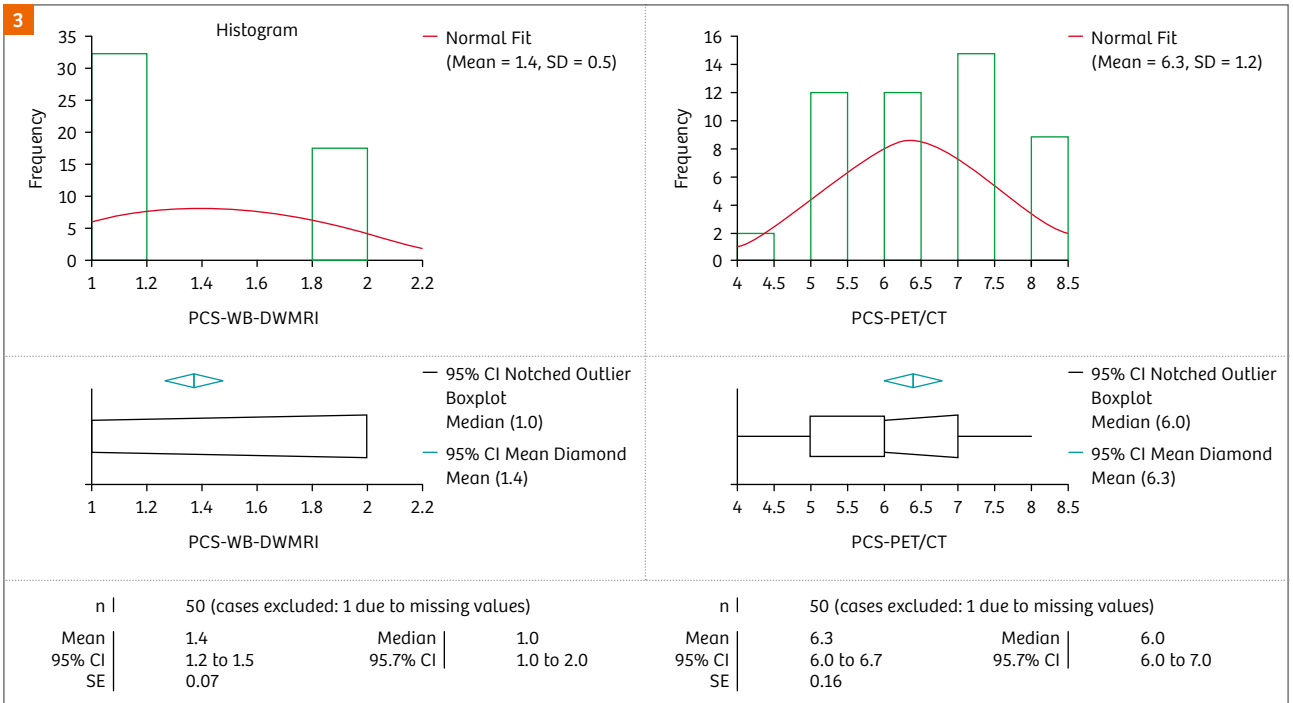

n	50 (cases excluded: 1 due to missing values)		
Mean	1.4	Median	1.0
95% CI	1.2 to 1.5	95.7% CI	1.0 to 2.0
SE	0.07		

n	50 (cases excluded: 1 due to missing values)		
Mean	6.3	Median	6.0
95% CI	6.0 to 6.7	95.7% CI	6.0 to 7.0
SE	0.16		

Figure 3: Histogram of PCS scores in the WB-DWMRI and PET/CT groups.

4

n | 50

WB-DWMRI by PET/CT	n	Rank sum	Mean rank
4	2	33.0	16.50
5	12	248.0	20.67
6	12	248.0	20.67
7	15	497.5	33.17
8	9	248.5	27.61

Kruskal-Wallis' statistic	11.19
X^2 statistic	11.19
DF	4
p	0.0245 (chisqr approximation, corrected for ties)

n | 100

NRCL	n	Rank sum	Mean rank
WB-DWMRI	50	2550.0	51.00
PET/CT	50	2550.0	50.00

Kruskal-Wallis' statistic	0.04
X^2 statistic	0.04
DF	1
p	0.8348 (chisqr approximation, corrected for ties)

Figure 4: Kruskal-Wallis test charts comparing NRCL and PCS in the WB-DWMRI and PET/CT groups.

Discussion

Our study shows that WB-DWMRI is a more viable solution for imaging patients with known cancer. The many reasons for this are related to higher patient comfort scores, lower incremental cost-effectiveness ratios, and matching sensitivity and specificity for cancer detection. Although the NRCL scores are the same in both groups, the PCS data show a statistically significant lower score for the WB-DWMRI group (p = 0.02). This difference was mainly due to faster imaging time, to the lack of radiation, patient preparation, and intravenous contrast and isotope use, and to significantly less radiologist reporting time. These factors had a greater impact on patient comfort and resulted in improved patient compliance. The lower ICER of WB-DWMRI is another argument for using this newer imaging modality, as it means it is more cost effective than PET/CT. With cost-effectiveness currently one of the most robust parameters in deciding between two modalities, a lower ICER certainly tilts the scale toward more frequent use of WB-DWMRI for following up on and managing cancer patients.

No.	Study	Year	No. of Patients	Organ	WB-DWMRI		PET/CT		Conclusions
					Sensitivity (in %)	Specificity (in %)	Sensitivity (in %)	Specificity (in %)	
1	Mori et al. [3]	2008	104	Lung	72	97	70	79	WB-DWMRI better
2	Ohbaet al. [4]	2009	110	Lung	73	96	72	82	Similar
3	Takenakaet al. [5]	2009	115	Lung	75	93.7	73	95.4	Similar
4	Gong et al. [6]	2015	28	Colorectal	81.1	99.1	95.1	99.8	Similar
5	Ono et al. [7]	2009	25	Colorectal	80	76.9	30	100	WB-DWMRI better for nodal detection
6	Schmidt et al. [8]	2004	33	Breast	90	86	91	90	Similar
7	Heusneret al. [9]	2010	20	Breast	91	72	94	99	Similar
8	Pawlynet al. [10]	2016	17	Myeloma	WB-DWI Better than PET/CT				
9	Shen et al. [11]	2014	27	Meta-analysis, Prostate Ca	97	95	91	99	WB-DWMRI better
10	Barchettiet al. [12]	2016	154	Prostate Ca	99	98	99	-	Similar
11	Eschmann et al. [13]	2007	42	Prostate Ca	76	94	96	74	Similar
12	Lin et al. [14]	2010	15	Lymphoma	81	100	90	94	Similar
13	Steccoet al. [15]	2015	17	Lymphoma	100	96	96	100	Similar
14	Gutzeitet al. [16]	2010	36	Any metastasis	97	99	(Scinti-graphy) 91	87	WB-DWMRI better
15	Fischer et al. [17]	2011	68	Any metastasis	72	89	74	91	Similar
16	Li et al. [18]	2013	1067	Any metastasis	89	95	89	97	Similar
17	Steccoet al. [19]	2009	29	Any metastasis	89.1	98.5	100	-	Similar
18	Choi et al. [20]	2009	236	Uterine cervical Ca	86	80	100	-	Similar
19	Hassan et al. [21]	2014	6	Meta-analysis, Head-neck Ca	100	71	68	84	WB-DWMRI better

Table 3: List of studies comparing WB-DWMRI and PET/CT for staging cancer.

References

1 Koh DM, Collins DJ. Diffusion-weighted MRI in the body: applications and challenges in oncology. AJR Am J Roentgenol. 2007; 188:1622-35.
2 Engelhard K, Hollenbach HP, Wohlfart K, von Imhoff E, Fellner FA. Comparison of whole-body MRI with automatic moving table technique and bone scintigraphy for screening for bone metastases in patients with breast cancer. 2004; 14(1):99-105.
3 Mori T, Nomori H, Ikeda K, et al. Diffusion-weighted magnetic resonance imaging for diagnosing malignant pulmonary nodules/masses: comparison with positron emission tomography. J ThoracOncol. 2008;3(4):358-64.
4 Ohba Y, Nomori H, Mori T, et al. Is diffusion-weighted magnetic resonance imaging superior to positron emission tomography with fludeoxyglucose F 18 in imaging non-small cell lung cancer? J ThoracCardiovasc Surg. 2009;138(2):439-45.
5 Takenaka D, Ohno Y, Matsumoto K, et al. Detection of bone metastases in non-small cell lung cancer patients: comparison of whole-body diffusion-weighted imaging (DWI), whole-body MR imaging without and with DWI, whole-body FDG-PET/CT, and bone scintigraphy. J MagnReson Imaging. 2009;30(2): 298-308.
6 Gong J, Cao W, Zhang Z, Deng Y, et al. Diagnostic efficacy of whole-body diffusion-weighted imaging in the detection of tumour recurrence and metastasis by comparison with 18F-2-fluoro-2-deoxy-D-glucose positron emission tomography or computed tomography in patients with gastrointestinal cancer. Gastroenterol Rep (Oxf). 2015; 3(2):128-135.
7 Ono K, Ochiai R, Yoshida T, et al. Comparison of diffusion-weighted MRI and 2-[fluorine-18]-fluoro-2-deoxy-D-glucose positron emission tomography (FDG-PET) for detecting primary colorectal cancer and regional lymph node metastases. J MagnReson Imaging. 2009;29(2):336-40.
8 Schmidt GP, Schmid R, Hahn K, Reiser MF. Whole-body MRI and PET/CT in tumor diagnosis. Radiologe. 2004;44(11):1079-87.

9 Heusner TA, Kuemmel S, Koeninger A, et al. Diagnostic value of diffusion-weighted magnetic resonance imaging (DWI) compared to FDG PET/CT for whole-body breast cancer staging. Eur J Nucl Med Mol Imaging. 2010; 37(6):1077-86.
10 Pawlyn C, Fowkes L, Otero S, Jones J, et al. Whole-body diffusion-weighted MRI: a new gold standard forassessing disease burden in patients with multiple myeloma? Leukemia 2016; 30(6): 1446-8.
11 Shen G, Deng H, Hu S, Jia Z. Comparison of choline-PET/CT, MRI, SPECT, and bone scintigraphy in the diagnosis of bone metastases in patients with prostate cancer: a meta-analysis. Skeletal Radiol. 2014; 43(11):1503-13.
12 Barchetti F, Stagnitti A, Megna V, Ansari NA, et al. Unenhanced whole-body MRI versus PET-CT for the detection of prostate cancer metastases after primary treatment. Eur Rev Med Pharmacol Sci. 2016; 20(18): 3770-3776.
13 Eschmann SM, Pfannenberg AC, Rieger A, et al. Comparison of 11C-choline-PET/CT and whole body-MRI for staging of prostate cancer. Nuklearmedizin. 2007;46(5):161-8.
14 Lin C, Luciani A, Itti E, et al. Whole-body diffusion-weighted magnetic resonance imaging withapparent diffusion coefficient mapping for staging patients with diffuse large B-cell lymphoma. EurRadiol. 2010; 20(8):2027-38.
15 Stecco A, Beumi F, Quagliozzi M, Lombardi M, et al. Staging of Primary Abdominal Lymphomas: Comparison of Whole-Body MRI with Diffusion-Weighted Imaging and (18) F-FDG-PET/CT. Gastroenterol Res Pract. 2015; 2015:104794. doi: 10.1155/2015/104794.
16 Gutzeit A, Doert A, Froehlich JM, et al. Comparison of diffusion-weighted whole body MRI and skeletal scintigraphy for the detection of bone metastases in patients with prostate or breast carcinoma. Skeletal Radiol. 2010; 39(4):333-43.
17 Fischer MA, Nanz D, Hany T, et al. Diagnosticaccuracy of whole-body MRI/DWI image fusionfor detection of malignant tumours: a comparisonwith PET/CT. Eur Radiol. 2011; 21(2):246-55.
18 Liet al. Diagnostic Value of Whole-Body Diffusion-Weighted Magnetic Resonance Imaging for Detection of Primary and Metastatic Malignancies: A Meta-Analysis. EurRadiol. 2014; 83(2): 338-44.
19 Stecco A, Romano G, Negru M, et al. Whole-body diffusion-weighted magneticresonance imaging in the staging of oncological patients: comparison withpositron emission tomography computed tomography (PET-CT) in a pilotstudy. Radiol Med. 2009;114(1):11-17.
20 Choi EK, Kim JK, Choi HJ, et al. Node-by-node correlation between MR and PET-CT in patients with uterine cervical cancer: diffusion-weighted imaging versus size-based criteria on T2WI. EurRadiol. 2009;19:2024–2032.
21 Hassan O, Taha S, Farag W. Diffusion-weighted MRI versus PET-CT in evaluation of clinically N0 neck in patients with HNSCC. Systematic review and meta-analysis study. Egyptian Journal of Ear, Nose, Throat and Allied Sciences. 2014;15:109-116.

Contact

Atul Kapoor
Department of Radiology and
Magnetic Resonance Imaging
Advanced Diagnostics

17/8 Kennedy Avenue Market
The Mall, Opp Session Court
Amritsar, Punjab 143001
India
Phone: +91 183 240 2620
info@advanceddiagnostics.in

Learn more!

Earlier Diagnosis, Improved Classification, Tailored Therapies – the Advent of MRI in Prostate Cancer Care

Professor Heinz-Peter Schlemmer, M.D.
German Cancer Research Center, Heidelberg, Germany

Don't miss the talks delivered by experienced and renowned experts at
www.siemens.com/magnetom-world

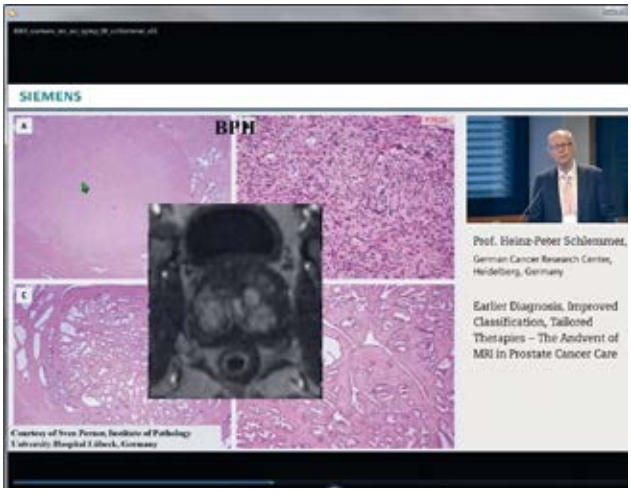

A Rapid, PI-RADS v2 Conform, Multi-parametric MRI Prostate Exam for Improved Patient Care

Mukesh Harisinghani, M.D.[1]; Hamed Kordbacheh, M.D.[1]; Thitinan Chulroek, M.D.[1]; Kamonwon Cattapan, M.D.[1]; Elisabeth Weiland, Ph.D.[2]; Berthold Kiefer, Ph.D.[2]; Ravi Seethamraju, Ph.D.[3]; Gregor Thörmer, Ph.D.[2]

[1] Massachusetts General Hospital, Department of Radiology, Division of Abdominal Imaging, Boston, MA, USA
[2] Siemens Healthineers, Erlangen, Germany
[3] Siemens Healthineers, Burlington, MA, USA

The results of PROMIS, a prospective multicenter-paired validation study, clearly show the value of targeted prostate biopsy with MRI guidance over systematic transrectal ultrasound-guided biopsies (TRUS-Bx) in biopsy-naïve men [1]. Multi-parametric (mp)-MRI prior to first biopsy may not only help to avoid unnecessary biopsies in 30% of patients, it also may reduce the rate of overdiagnosis and overtreatment due to a detection bias of MRI towards significant disease.

Accordingly, mp-MRI to aid in the diagnosis and management of prostate cancer has been one of the fastest growing applications in MRI over the recent years [2]. The downside to this development is that radiological facilities have to manage the increasing number of mp-MRI referrals in their daily business. While a typical head or knee exam requires between 10–15 minutes, an mp-MRI exam of the prostate is commonly scheduled for 30–45 minutes with a net scan time of about 20 minutes.

Furthermore, there is still reluctance to incorporate MR imaging into general guidelines for prostate cancer detection because it is perceived to be an expensive technology. This is also reflected in a recent poll amongst US urologists: when asked if the cost of mp-MRI is prohibitive for its use, 59% of all respondents agreed or strongly agreed [3].

Previous joint and successful efforts by Massachusetts General Hospital and Siemens Healthcare to compare an ultrafast brain MRI protocol to the conventional protocol in motion-prone inpatient clinical settings with the aim to establish a clinically validated 5-minute routine brain

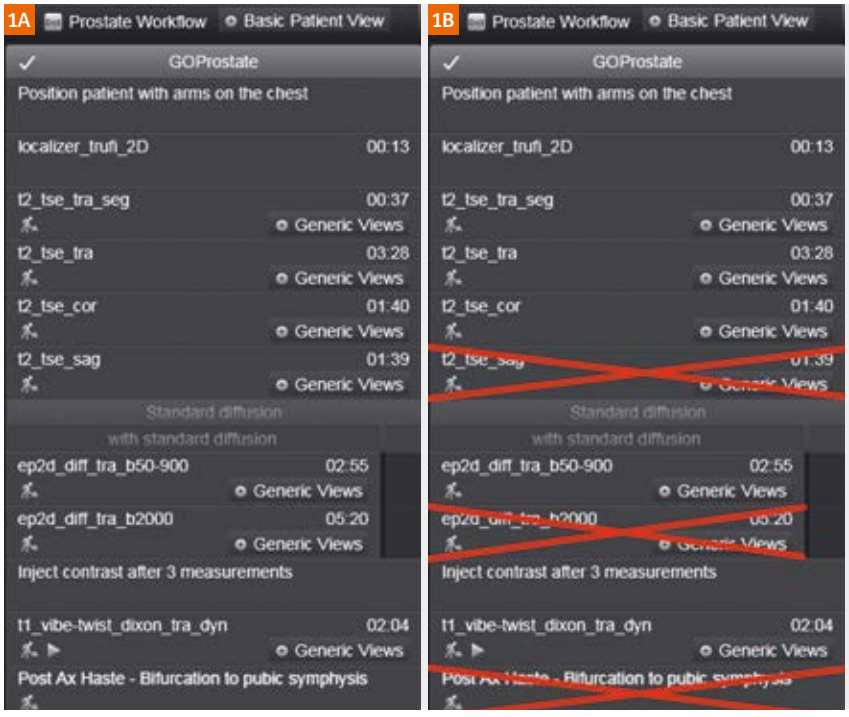

Figure 1:
(1A) Exam workflow of the institutional "full exam" mp-MRI prostate protocol.
(1B) Reduced sub-set of protocols considered in the "rapid exam" reflecting the requirements of PI-RADS v2.

protocol [4] also triggered the investigation of other GO (Generalized Optimized) exam strategies for other high volume MR indications.

For the purpose of developing a rapid prostate protocol, the general structured approach for developing a GO protocol proposed by Otto Rapalino [5] was followed:

1) Establish the time budget for a given core exam
Most high-volume imaging centers generally aim to have standard exam slots of 20–30 minutes per patient. Taking into account the time required for patient preparation and positioning, the net scan time should not exceed 15 minutes. Ideally, this time budget also should include some buffer to react to unanticipated events, e.g. rescans due to patient movement.

2) Define the set of required contrasts based on literature evidence / acceleration methods for acquisition
At our institution, mp-MRI of the prostate typically includes T2-weighted images in 3 orientations, axial diffusion-weighted imaging (DWI) with multiple b-values in a range of b=50 sec/mm^2 to 900 sec/mm^2 plus ADC map, a separately acquired, axial high b-value image with b=2000 sec/mm^2 and axial dynamic contrast-enhanced (DCE) imaging acquired over 2 minutes. All scans are acquired with a slice thickness of 3 millimeters. In addition, a post-contrast HASTE scan covering the pelvis from the aortic bifurcation to the pelvic symphysis is routinely performed at our institution (Fig. 1A). The resulting net acquisition time of our institutional routine protocol is about 22 minutes.

For mp-MRI of the prostate, PI-RADS v2 sets a clear standard as to the contrasts that have to be acquired and the technical requirements, e.g. spatial resolution, to be fulfilled for T2-weighted, DWI and DCE imaging. Applying these rules, a rapid exam protocol was extracted from our full protocol: By removing one T2w TSE orientation, the post-contrast HASTE and the measured high b-value image the net scan time was cut down to 12 minutes (Fig. 1B).

MR technologies which enable the realization of accelerated image acquisition include parallel imaging [6] with high channel density [7]. By using the combination of an 18-channel Body coil and a 32-channel Spine coil, PAT factors of 2 or 3 were applied for acquisition of the individual contrasts.

For increased consistency of scans and higher reproducibility of planning, the decision was taken to use a Works-in-Progress Prostate Dot Engine[1] to assist in the exams. This prototype performs an automatic segmentation of the prostate in a fast 37 seconds, axial T2-weighted TSE scan and derives the volume and outer dimensions of the gland. In addition the landmarks bladder neck and exit point of the urethra from the prostate are automatically detected, to align the slices of the later exams perpendicular to the line between these two landmarks. This enables efficient planning with reproducible automated scan volume positioning and automated coverage adaptation.

3) Test scans to assess image quality in terms of tissue contrast and signal to noise levels
The initial assessment of image quality was satisfactory, except for the contrast of calculated high b-value images: Artificial noise amplification in bony structures reduced the lesion conspicuity in comparison to measured high b-value images, where bony structures appeared less pronounced. This was addressed by using a Works-in-Progress version of the DWI sequence[1] with improved calculated b-value images.

4) Clinical validation of the rapid MR protocol
So far, 75 patients have been examined in a 3T MRI system (MAGNETOM Skyra, Siemens Healthcare, Erlangen, Germany). Images were acquired with a combination of an 18-channel Body coil and a 32-channel Spine coil.

Continued on page 59.

[1] WIP, the product is currently under development and is not for sale in the US and in other countries. Its future availability cannot be ensured.

2

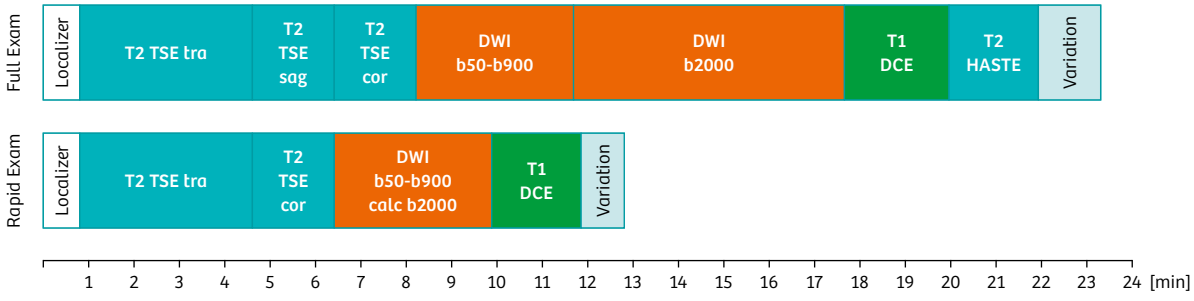

Figure 2: Comparison of exam times with the full and the rapid mp-MRI prostate protocol.

Case 1

Figure 3:
A 73-year-old man with no family history of prostate cancer and with a serum prostate specific antigen (PSA) of 4.5 ng/mL was referred for prostate MRI. mp-MRI revealed a 2.6 x 2.9 cm lesion in the right and left peripheral zone in the apex and mid gland, which was hypointense on axial and coronal T2w TSE **(3A and 3B)**, with a respective diffusion restriction in the calculated **(3C)** and measured **(3D)** high b-value image, corresponding low ADC value **(3E)** and early enhancement on DCE MRI **(3F)**. Accordingly the lesion was assessed as PIRADS 5. Subsequent MR-transrectal ultrasound (TRUS/MRI) fusion guided biopsy showed significant disease with seven out of eleven cores of Gleason 8 (4+4) with 80% to 95% involvement. The patient was offered radiation therapy and 2 years of hormonal therapy.

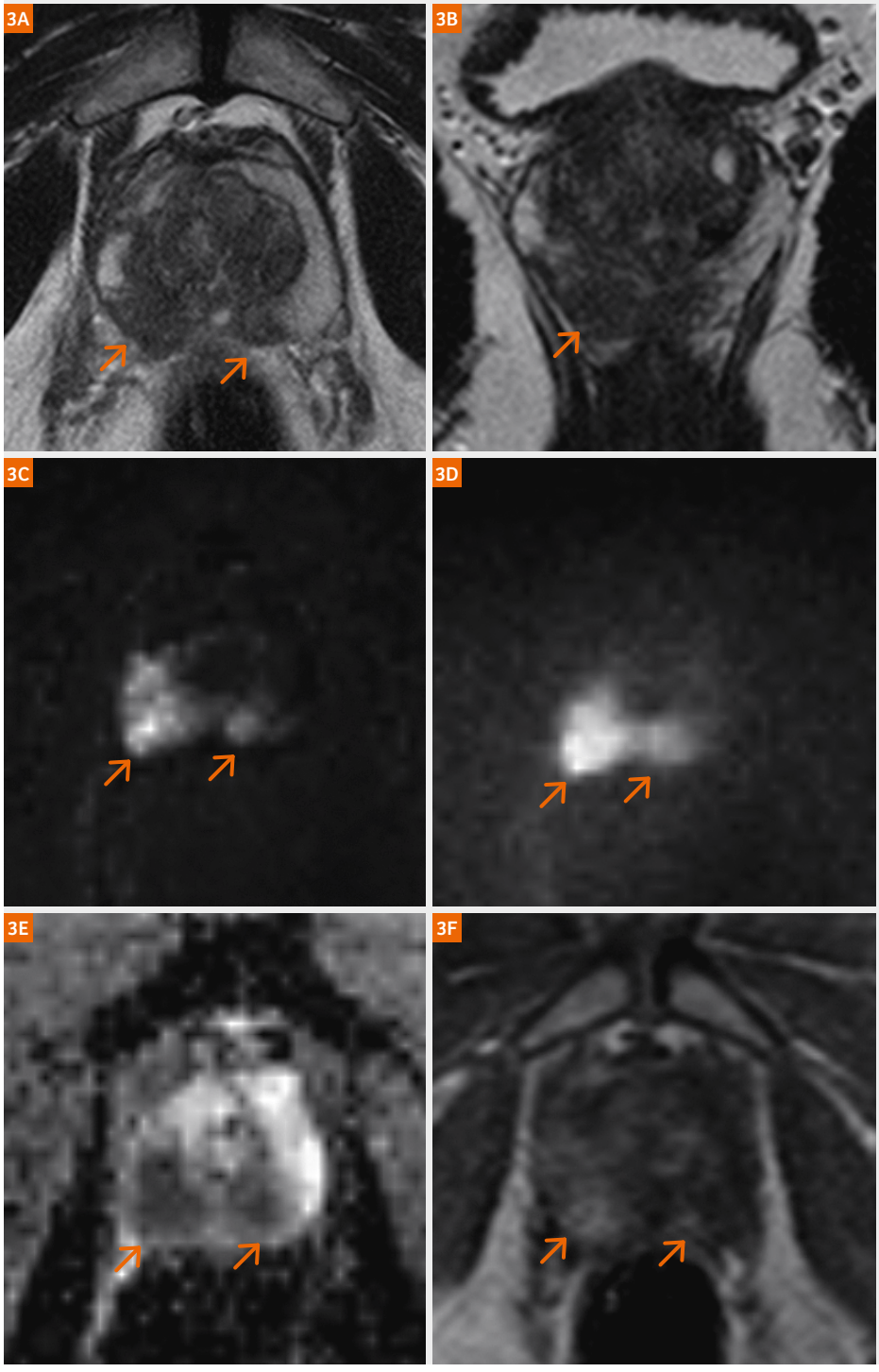

Case 2

Figure 4:
A 62-year-old man with family history of prostate cancer and with rising serum prostate specific antigen (PSA) from 2.8 to 5.6 ng/mL presented for mp-MRI. A dominant, 1.5 cm large lesion in the posterior peripheral zone at the level of right apical to mid gland was found, which showed strongly hyperintense signal in calculated and measured b=2000 sec/mm² images **(4A, B)** and low signal intensity on ADC **(4C)**. While the high-resolution axial T2w images **(4D)** did not allow confirmation of the DWI findings due to massive motion artifacts, the previously acquired, fast T2 TSE scans **(4E)** were sufficient to find a correlate in morphology. The lesion was scored PIRADS 5.

A second, smaller lesion was detected in the right anterior peripheral zone at the level of mid gland with a diameter of 1 cm. The lesion presented with high signal in the b=2000 sec/mm² images **(4F, G)** and restricted diffusion in ADC **(4H)**. Again, low-resolution, fast T2w scans (4J) helped in the correlation to morphology. The lesion was rated PIRADS 4.

Subsequent MR/US fusion biopsy showed Gleason 3+4 at right apex and right mid gland and Gleason 3+3 at right prostatic base, corresponding to the dominant and second lesion seen in MRI. The patient was offered to either undergo radical prostatectomy or external beam radiation with 6 months of androgen deprivation therapy.

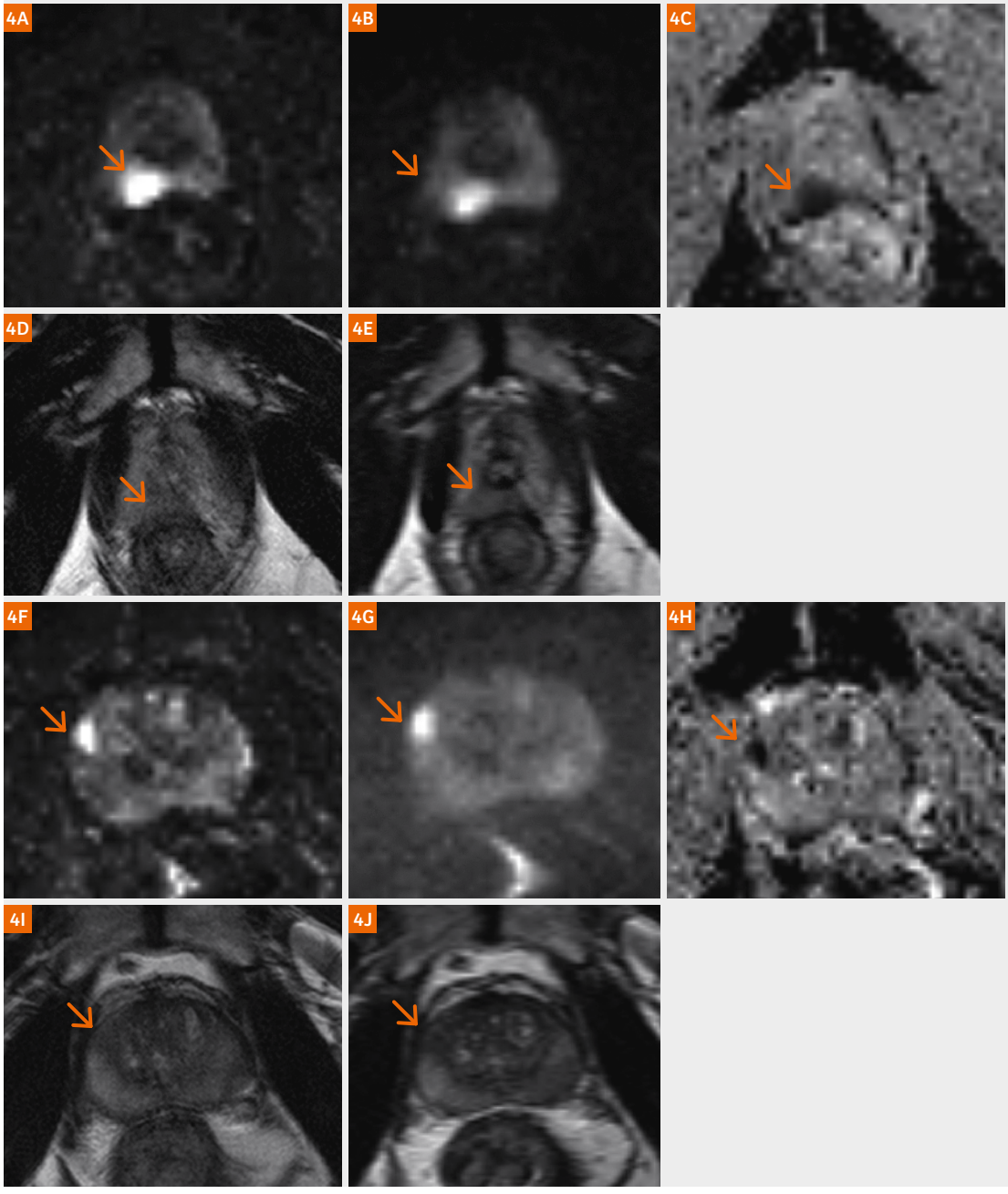

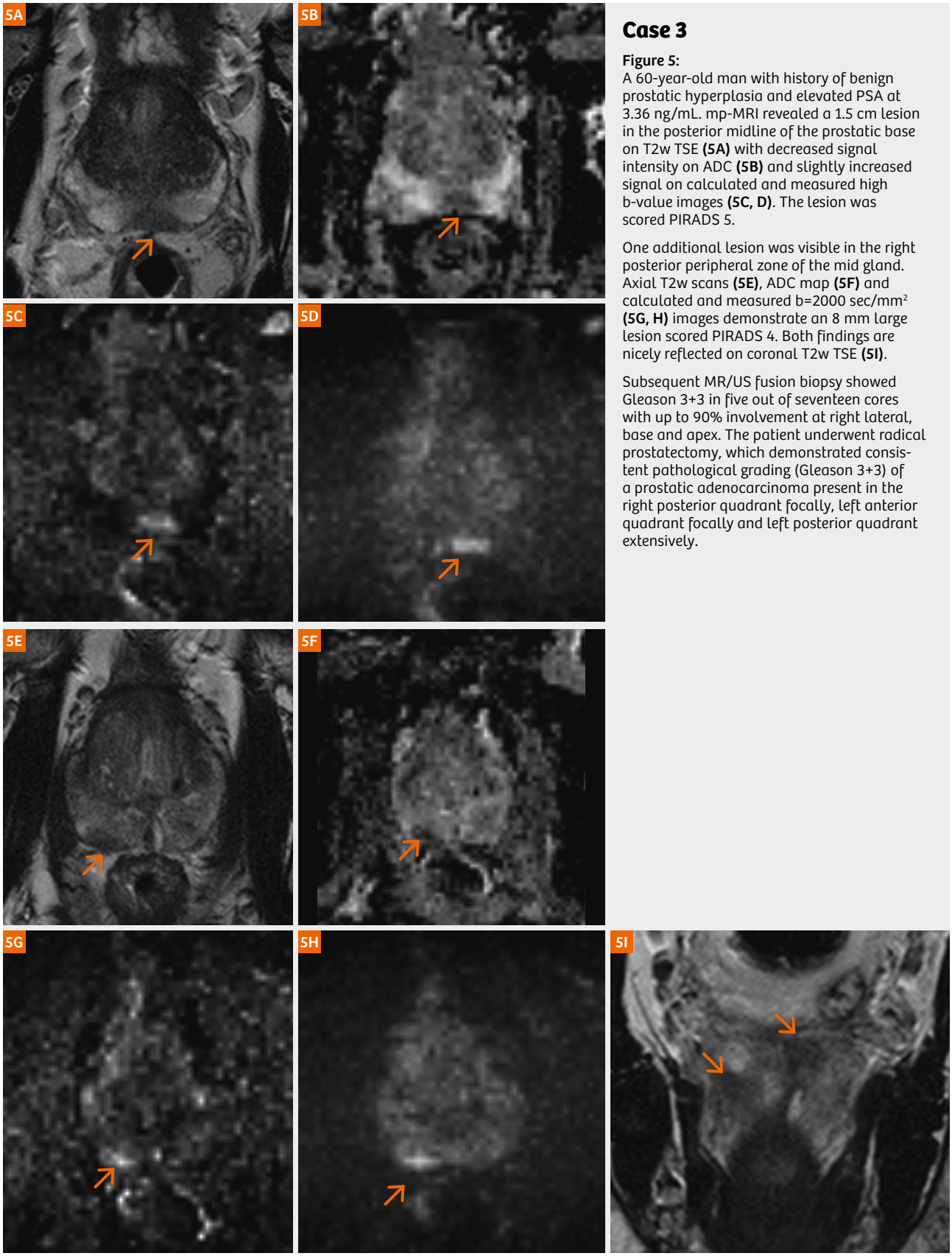

Case 3

Figure 5:
A 60-year-old man with history of benign prostatic hyperplasia and elevated PSA at 3.36 ng/mL. mp-MRI revealed a 1.5 cm lesion in the posterior midline of the prostatic base on T2w TSE **(5A)** with decreased signal intensity on ADC **(5B)** and slightly increased signal on calculated and measured high b-value images **(5C, D)**. The lesion was scored PIRADS 5.

One additional lesion was visible in the right posterior peripheral zone of the mid gland. Axial T2w scans **(5E)**, ADC map **(5F)** and calculated and measured b=2000 sec/mm^2 **(5G, H)** images demonstrate an 8 mm large lesion scored PIRADS 4. Both findings are nicely reflected on coronal T2w TSE **(5I)**.

Subsequent MR/US fusion biopsy showed Gleason 3+3 in five out of seventeen cores with up to 90% involvement at right lateral, base and apex. The patient underwent radical prostatectomy, which demonstrated consistent pathological grading (Gleason 3+3) of a prostatic adenocarcinoma present in the right posterior quadrant focally, left anterior quadrant focally and left posterior quadrant extensively.

Statistical assessment of exam duration in 27 patients revealed the following: For the full exam, the median acquisition time was 22 minutes with a standard deviation of 3:18 minutes due to variations in the required number of slices to cover the entire prostate gland individually. The rapid exam took 12 minutes with a standard deviation of 1:55, resulting in a maximum acquisition time of 13 minutes (Fig. 2). Retrospective analysis also revealed, that as many as 17% of all individual scans were repeated by the technologists, probably due to motion of the patient during image acquisition.

Respective clinical examples can be found in Cases 1–3. Please also note, that motion substantially compromised the diagnostic assessability of the axial high-resolution T2w scans in Case 2. Only the correlation of DWI information with motion-robust, very fast T2w images (TA 37 seconds) allowed confident correlation of the findings with morphologic information.

Discussion and conclusion

With the rapid prostate exam proposed here, all clinically relevant contrasts for a PI-RADS v2 conform mp-MRI protocol can be reliably acquired in 12 to 13 minutes acquisition time. Guided, computer assisted positioning of slices facilitates efficient planning with high reproducibility. Even in the case of rescans the scan time should not exceed 16–17 minutes, giving enough leeway to react to unanticipated events and to stay in a 25–30 minute exam slot per patient. In conclusion, the rapid protocol has potential to address the need for improved patient management and reliable scheduling in light of constantly growing procedure volumes.

References

1 Ahmed HU, El-Shater Bosaily A, Brown LC, et al. Diagnostic accuracy of multi-parametric MRI and TRUS biopsy in prostate cancer (PROMIS): a paired validating confirmatory study. Lancet 2017;389:815-22.
2 2016 imv MRI Market Summary Report, http://www.imvinfo.com
3 Manley BJ, Brockman JA, Raup VT, Fowler KJ, Andriole GL. Prostate MRI: a national survey of Urologist's attitudes and perceptions. Int Braz J Urol. 2016; 42(3): 464–471.
4 Rapalino O, Heberlein K. New Strategies for Protocol Optimization for Clinical MRI: Rapid Examinations and Improved Patient Care. MAGNETOM Flash 2016;65:22-25.
5 Prakkamakul S, Witzel T, Huang S, Boulter D, Borja MJ, Schaefer P, Rosen B, Heberlein K, Ratai E, Gonzalez G, Rapalino O. Ultrafast Brain MRI: Clinical Deployment and Comparison to Conventional Brain MRI at 3T. J Neuroimaging. 2016;26(5):503-10.
6 Griswold MA, Jakob PM, Heidemann RM, Nittka M, Jellus V, Wang J, et al. GeneRalized Autocalibrating Partially Parallel Acqusitions (GRAPPA). Magn Reson Med 2002; 47:1202-1210.
7 Keil B, Wald LL. Massively parallel MRI detector arrays. J Magn Reson 2013; 229: 75-89.liver evaluation. Presented at: Ad Hoc Electronic Poster Session 4446-4464, ISMRM 25th Annual Meeting & Exhibition, Honolulu, HI, USA; 2007, April 22-27.

Contact

Professor Mukesh G. Harisinghani, M.D.
Director Abdominal MRI
Massachusetts General Hospital
Department of Radiology

White Building, Room 270
55 Fruit Street
Boston, MA 02114
USA
Phone: +1 617-726-8396
Fax: +1 617-726-4891
mharisinghani@mgh.harvard.edu

New Contour 24 Coil

Continuing our commitment to delivering high-density lightweight Tim 4G coils, this year we will be introducing a new, ultra-flexible coil design. Contour 24 is a 24-channel coil consisting of highly flexible coil elements encased in soft material to create a blanket-like feeling for the patient.

Contour 24 has a higher density of coil elements per scan field of view than most similar coils available today. It is highly flexible and can be used in various orientations depending on the imaging need.

Contour 24 uses SlideConnect technology and can be combined with the Spine coil. Two coils can even be connected to cover larger imaging fields.

510(k) pending. The product is not commercially available. Future availability cannot be guaranteed.

Contour 24 benefits:

- Lightweight and highly flexible coil with blanket-like feel
- Supports easy positioning and workflow
- Suitable for imaging of general anatomy, such as abdomen and pelvis in both sides and orientations

Automated Fast Liver MR Scan: A Preliminary Evaluation

Chao Ma[1]; Jing Li[1]; Yukun Chen[1]; Aiguo Jin[1]; Qingsong Yang[1]; Berthold Kiefer[2]; Bernd Kuehn[2]; Caixia Fu[3]; Jianping Lu[1]

[1] Department of Radiology, Changhai Hospital of Shanghai, Shanghai, China
[2] Siemens Healthineers, Erlangen, Germany
[3] Siemens Shenzhen Magnetic Resonance Ltd., Shenzhen, China

Introduction

Magnetic resonance imaging (MRI) has become increasingly important in the diagnosis and evaluation of various abdominal diseases in clinical practice, thanks to its advantages of no ionizing radiation and multiple soft-tissue contrasts (T1w, T2w, DWI, etc.). However, compared with computed tomography (CT), MRI still has disadvantages, such as long scanning times and high operational complexity. The abdomen exam workflow, which requires respiratory motion control and strict timing of contrast agent injection, is especially time-consuming and complex. This is a challenge for weak patients who cannot cooperate very well, and for technicians working in a busy setting. A fast and easy abdomen scan workflow is urgently needed to improve both patient comfort and daily throughput. Such a workflow would reduce the cost per exam and allow more patient exams per MRI scanner. With the continuous development of hardware and software technologies, the new generation of MRI systems has been equipped with various accelerated acquisition techniques and one-stop automated scan workflows. With the *syngo* MR D11A software platform, Siemens Healthcare released a technology called Dot (day optimizing throughput) engines, which helps improve the automation of the MRI exam workflow. The technology

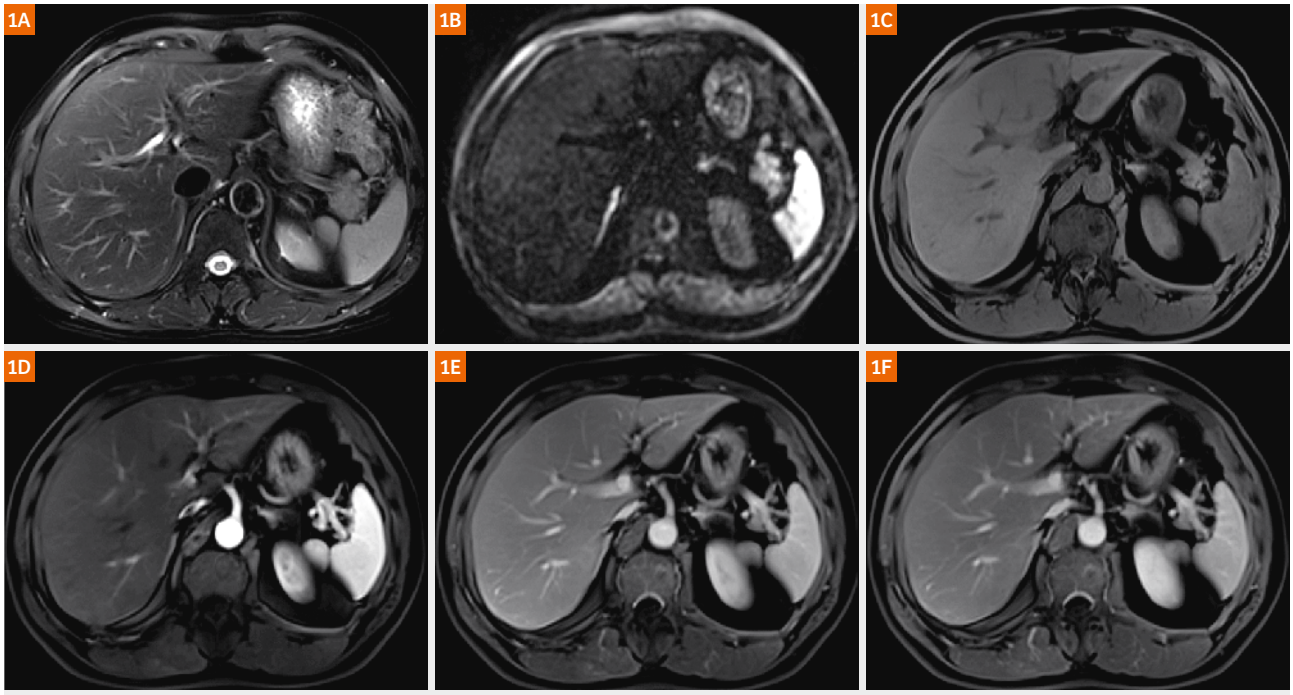

Figure 1: Images of a healthy 53-year-old man: **(1A)** T2-weighted BLADE; **(1B)** DWI, b = 1000 s/mm^2; **(1C)** pre-contrast T1w; **(1D)** arterial phase T1w; **(1E)** venous phase T1w; **(1F)** delayed phase T1w. The images show that the automated fast protocol achieves satisfactory image quality and anatomic structure visualization.

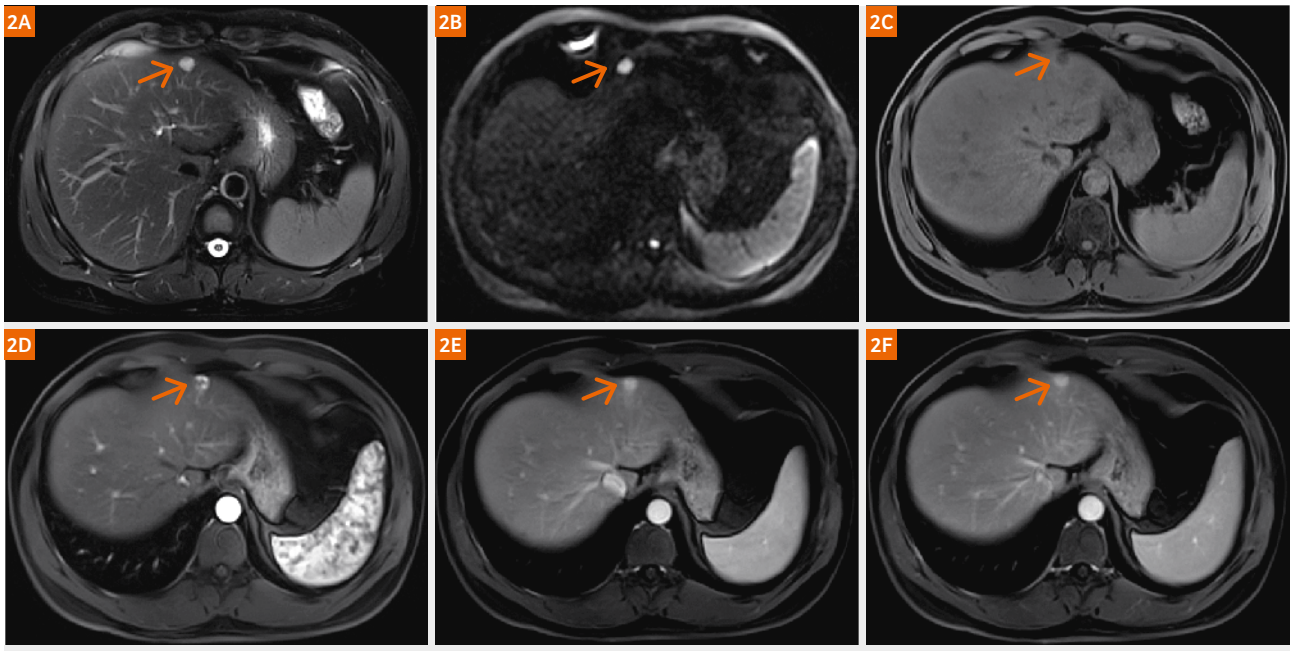

Figure 2: MRI images of a hemangioma: The lesion appears as a hyperintense mass on both the T2-weighted image **(2A)** and DWI b = 1000 s/mm² **(2B)**, and is hypointense on the pre-contrast T1-weighted image **(2C)**. The post-contrast-enhanced T1w images **(2D-F)** show the progressive centripetal contrast enhancement in the hemangioma.

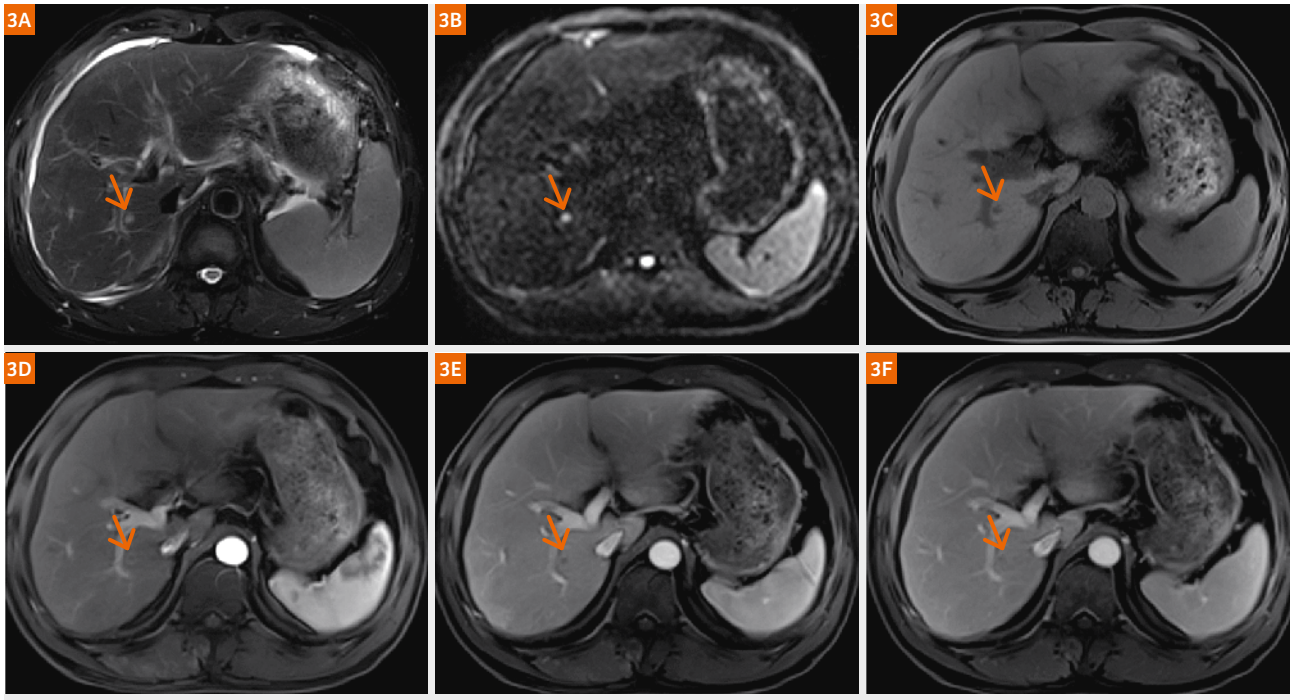

Figure 3: Liver metastasis (primary: colon cancer) in a 46-year-old man: **(3A)** T2-weighted BLADE; **(3B)** DWI, b = 1000 s/mm²; **(3C)** pre-contrast T1-weighted; **(3D-F)** contrast-enhanced T1-weighted. The lesion is isointense to hyperintense in T2-weighted images, is hyperintense in DWI, and has low intensity in T1-weighted images. Annular enhancement is visible in the arterial phase of the enhanced T1-weighted images relative to the surrounding liver parenchyma.

has been successfully applied to workflows for examining areas such as the abdomen, heart, head, knee joint, among others. However, the default workflow provided by the manufacturer contains redundant protocols and has long scanning times. Thus, our goal was to develop a fast and automated liver MR workflow with reproducible exam times for short time slots that can optimize patient throughput.

At ISMRM 2017, we proposed a fast MRI workflow[1] with only ~12 minutes total measurement time for a liver exam [1]. In this workflow, we used an abbreviated protocol set configured with auto-positioning, auto-FOV, auto-voice-command, and auto-care-bolus functions (provided by the Abdomen Dot Engine package) to shorten the exam time, automate the process, and improve throughput while still producing sufficient diagnostic information. This paper outlines our experiences and provides some example cases.

Method

Our workflow includes the following:

1. **Localizer** in one breath-hold of 18 s, with auto-coverage scout for the liver. The scout data is used to process the auto-alignment of the following protocols.

2. **Coronal T2w HASTE** in one breath-hold of 20 s

3. **Axial T2w BLADE** with respiratory triggering

FOV = 400 x 400 mm^2, scan matrix = 320 x 320, TE = 79 ms, TR = respiratory period, slice thickness = 6 mm, number of slices = 28, Grappa iPAT factor = 2, scan duration of 2 to 4 mins

4. **T1w VIBE with 2 echoes and Dixon reconstruction** in one breath-hold of 15 s, acting as:

a) pre-contrast in-phase and opposed-phase T1-weighted scan and

b) pre-contrast T1-weighted scan

FOV = 325 x 400 mm^2, scan matrix = 195 x 320, CAIPIRINHA iPAT factor = 3, TE= 1.26/2.43 ms, TR =3.97 ms, flip angle = 12°

[1] WIP, the product is currently under development and is not for sale in the US and in other countries. Its future availability cannot be ensured.

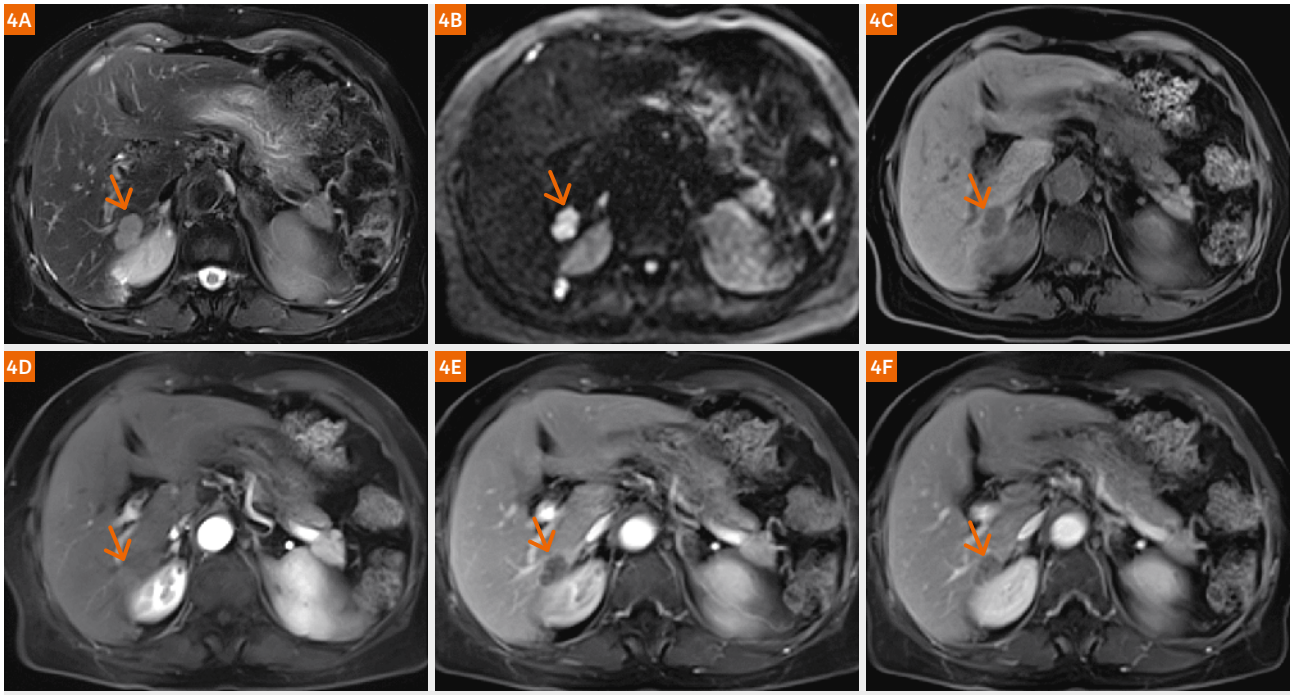

Figure 4: Liver metastasis (primary: colon cancer) in a 69-year-old man: **(4A)** T2-weighted BLADE; **(4B)** DWI, b = 1000 s/mm^2; **(4C)** pre-contrast T1w; **(4D-F)** contrast-enhanced T1w. The lesion is isointense to hyperintense in T2-weighted images, is hyperintense in DWI, and has low intensity in T1-weighted images. Annular enhancement is visible in the venous and delayed phase of enhanced MR imaging relative to the surrounding liver parenchyma.

5. **EPI DWI sequence** with 3-scan trace mode and a single high b-value of 1000 s/mm² in two breath-holds (18 s each). FOV = 400 x 400 mm², scan matrix = 256 x 256 with interpolation, TE = 61 ms, TR = 3100 ms, slice thickness = 6 mm, number of slices = 30, GRAPPA iPAT factor = 2

6. **Auto bolus detection** with 2D FLASH sequence and high temporal resolution of ~0.8 s with automatic ROI placement for the aorta, provided by the Abdomen Dot Engine

7. **Post-contrast T1w VIBE** for arterial, venous, and delayed phase measurements in one breath-hold of 14 s each, using similar parameters as the pre-contrast T1w VIBE scan, except that CAIPIRINHA iPAT factor = 4 was selected and fat saturation was used instead of Dixon.

The total acquisition time of this workflow is between 5.7 and 7 minutes. The total examination time including time for adjustment, shimming, breath-hold commands, etc. for each patient varies from 11 to 13 minutes, depending on the patient's breathing period.

So far, the proposed workflow has been used successfully with 109 liver patients on our 3T MAGNETOM Skyra. The image quality from each sequence is good to excellent.

The average measurement time is about 12 minutes and 36 seconds. The example cases shown in Figures 1-6 demonstrate the high lesion delineation capability of this fast workflow for various liver diseases.

Discussion

We used respiratory-triggered BLADE for T2-weighted acquisition to improve the measurement success rate, since this sequence is more motion-robust than conventional TSE. For DWI, we only acquired a b-value of 1000 s/mm² and ignored ADC maps in the liver examination. This is because our experience shows that ADC maps do not provide any additional information for diagnosing liver diseases in clinical practice. We used the Dixon technique to acquire opposed-phase, in-phase, and pre-contrast T1w images in one sequence, which removes the need for a separate pre-contrast T1w acquisition. Additionally, we applied CAIPIRINHA to increase the PAT acceleration factor for the VIBE sequence to achieve high spatial resolution and significantly shorter scan times. The Abdomen Dot Engine – with its auto-positioning, auto-FOV, auto-voice-command, and auto-care-bolus functions – allowed us to automate the exam workflow and improve scan reproducibility. It also reduced the technician's workload, which is especially important in

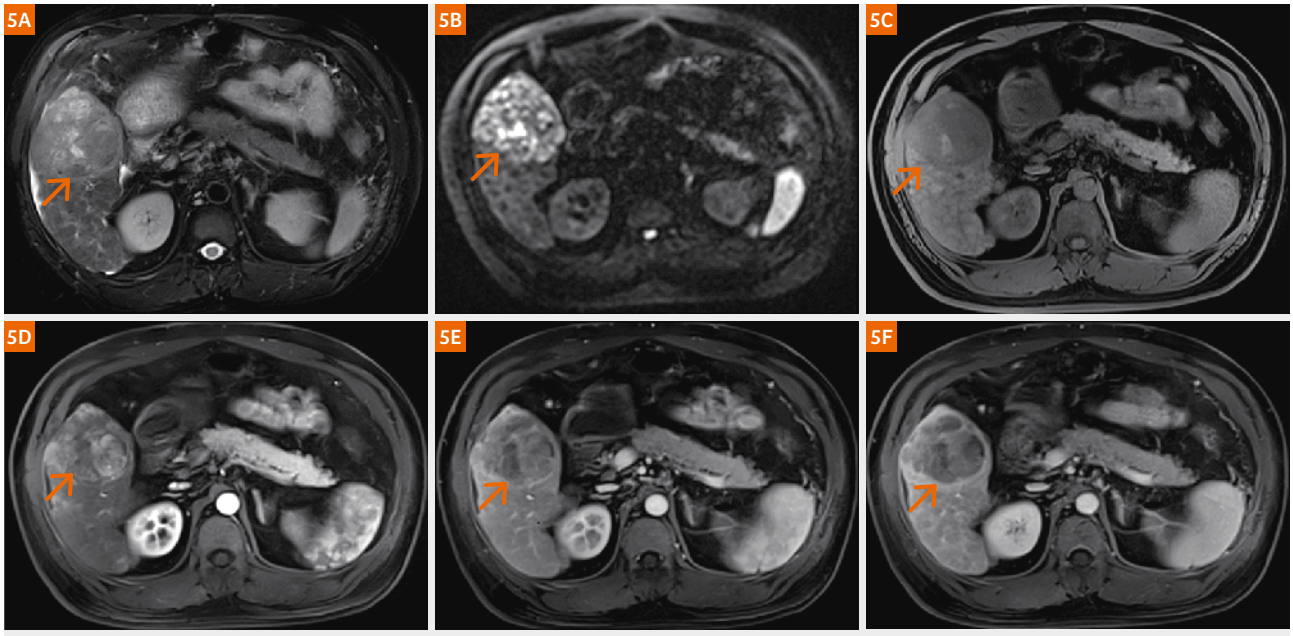

Figure 5: Large HCC in a 43-year-old man with cirrhosis resulting from hepatitis B: The axial T2-weighted MR image **(5A)** and DWI with b = 1000 s/mm² **(5B)** show a heterogeneous mass (arrow) with high signal intensity in the right lobe bordering the liver capsule. The axial T1w image **(5C)** shows the mass as hypointense (arrow). The axial T1w image **(5D)** obtained in the arterial phase shows heterogeneous hypervascular enhancement of the mass (arrow). The axial T1w images obtained in the venous and delayed phases **(5E, F)** show washout (arrow). A thin circumferential hypointense rim is visible around the periphery of the tumor, a finding which is indicative of a capsule, with typical late enhancement after administration of a gadolinium-based contrast medium.

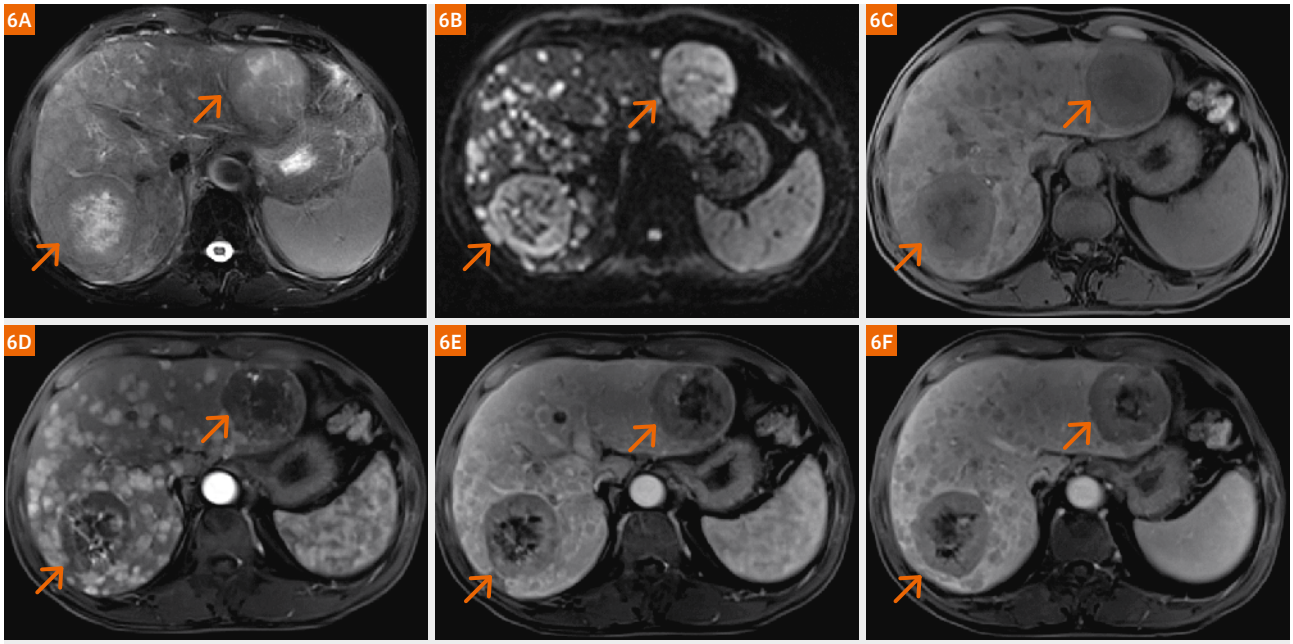

Figure 6: Multiple HCCs in a patient with known hepatitis B and an elevated α-fetoprotein level: Axial T2w image and DW image **(6A, B)** show a cirrhotic liver with multiple slightly high-intensity nodules (arrow). Axial T1w image **(6C)** shows these nodules as hypointense (arrow). Axial arterial phase T1w image **(6D)** shows numerous nodules with variable enhancement throughout the cirrhotic liver (arrow). On venous and delayed phase images **(6E, F)**, most of these nodules show washout (arrow).

our hospital. Normally, our technicians are also responsible for laying out and printing every patient's images via eFilm. With the automated scan workflow, they can complete scanning and printing tasks simultaneously and with minimal effort.

Conclusion

Our automated fast liver MRI workflow is feasible on 3T MRI systems. Combining it with the Dot technology speeds up the scanning process, allows for reproducible patient slot times, and reduces technician workload. The workflow makes it easy to implement and standardize liver examinations, and has good prospects for clinical application.

Reference

1 Yang Q, Chen Y, Fu C, Kuehn B, Kiefer B, Wang Y, et al. A clinically-validated, fast and semi-automated MR workflow for liver evaluation. Presented at: Ad Hoc Electronic Poster Session 4446-4464, ISMRM 25th Annual Meeting & Exhibition, Honolulu, HI, USA; 2007, April 22-27.

Contact

Professor Jianping Lu, M.D.
Director Radiology Department
Changhai Hospital of Shanghai, the Second Military Medical University

10 Building, 168 Changhai Road,
Shanghai, 200433
P. R. China
Phone: +86 21 31162146
Fax: +86 21 81873226
cjr.lujianping@vip.163.com

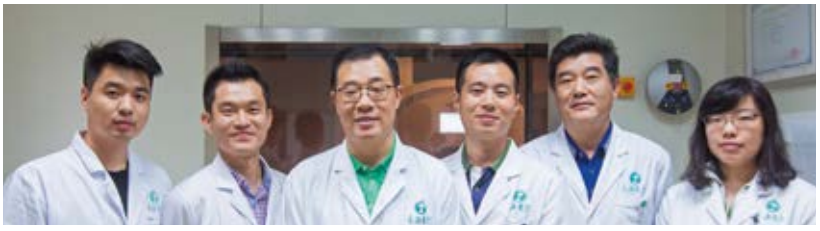

From left to right:
Yukun Chen, Qingsong Yang, Jianping Lu, Chao Ma, Aiguo Jin, Jing Li

Rapid Body Composition Measurements Reveal Detailed Metabolic Changes in Large Scale Population Studies

Mikael F. Forsgren, Ph.D.[1,4]; Janne West, Ph.D.[2,3,4]

[1] Wolfram MathCore, Linköping, Sweden
[2] AMRA (Advanced MR Analytics AB), Linköping, Sweden
[3] Department of Medical and Health Sciences (IMH), Linköping University, Linköping, Sweden
[4] Center for Medical Image Science and Visualization (CMIV), Linköping University, Linköping, Sweden

Introduction

Body composition measurements, such as adipose tissue compartments, muscle volumes, and muscle tissue composition are increasingly important in research and clinical context. Up until recently many MR-protocols in combination with analysis methods for segmenting muscle and fat compartments in the body were laborious and time-consuming. This has hindered implementation in large cohorts and in clinical applications. In this article we present a rapid and robust MR-protocol for body composition profiling and initial clinically relevant findings. This MR-protocol enables accurate measurements of visceral adipose tissue, abdominal subcutaneous adipose tissue, thigh muscle volumes, as well as other specific biomarkers such as liver and intra-muscular fat content. The MR-protocol and analysis method were applied and quality assured in the vast UK Biobank imaging cohort showing excellent results in terms of compliance and scan precision.

The UK Biobank imaging study

The UK Biobank is a very large and detailed prospective study following about 500 000 volunteers in the UK for over 25 years. Participants were aged from 40 to 69 when recruited between 2006 and 2010. The ambitious study collects data ranging from questionnaires and physical measurements to genome-wide genotyping. In 2014 an imaging sub-study was added to the biobank and the plan is to scan 100 000 participants by 2021. Participants are illegible for imaging if they have metal or electronic implants, had surgery within six weeks before imaging, or if they have medical conditions that would make it difficult to conduct the imaging, such as hearing or breathing problems. The UK Biobank imaging sub-study includes detailed MR examinations of the brain, heart, abdomen, and body (neck to knee), as well as ultrasound and dual-energy X-rax absorptiometry (DXA). The North West Multicentre Research Ethics Committee (MREC), UK, approved the study and written informed consent was

	First slab (neck region)	Slabs two to four (torso region)	Slab five (upper leg region)	Slab six (lower leg region)
Repetition time (ms)	6.69	6.69	6.69	6.69
Echo time (ms)	2.39 & 4.77	2.39 & 4.77	2.39 & 4.77	2.39 & 4.77
Bandwidth (Hz)	440	440	440	440
Slices (-)	64	44	72	64
Voxel size (mm³)	2.23 x 2.23 x 3	2.23 x 2.23 x 4.5	2.23 x 2.23 x 3.5	2.23 x 2.23 x 4
Matrix size (-)	224 x 168	224 x 174	224 x 162	224 x 156
Breath-hold time (s)	-	17	-	-

Table 1: Summary of the 6-minute Dixon VIBE-based neck to knee body composition MR-protocol presented per region.

obtained from all participants prior to study entry [1, 2]. The research presented in this communication has been conducted using the UK Biobank Resource under Application Number 6569.

A body composition MR-protocol

All eligible participants were imaged using 1.5T MAGNETOM Aera MR-scanners (Siemens Healthcare, Erlangen, Germany). The participants were imaged in supine position with the arms along the sides, initial isocentering was performed with the laser crosshair on the participant's clavicles and no localizer sequence was used. The MR-protocol was based on T1-weighted VIBE Dixon and had a total cranio-caudal coverage of of 1.1 m divided over six overlapping slabs of axial 3D spoiled gradient dual-echo images. The acquired images covered a region between the neck and the knees. Detailed protocol parameters are presented in Table 1 and the parameters differed between the slabs depending on which anatomical region was being imaged. Over the torso region (slabs two to four) imaging was performed during 17 s expiration breath-hold. The total time for the MR body composition protocol was about 6 minutes. Reconstruction of Dixon water and Dixon fat images was performed using the integrated scanner software. Examples of the reconstructed water and fat images are shown in Figures 1A, B for two participants.

Body composition profiling

The body composition profile of all participants was based on quantifying fat and muscle compartments such as visceral adipose tissue, abdominal subcutaneous adipose tissue, and thigh muscle volumes as well as intra-muscular and liver fat content (hepatic proton-

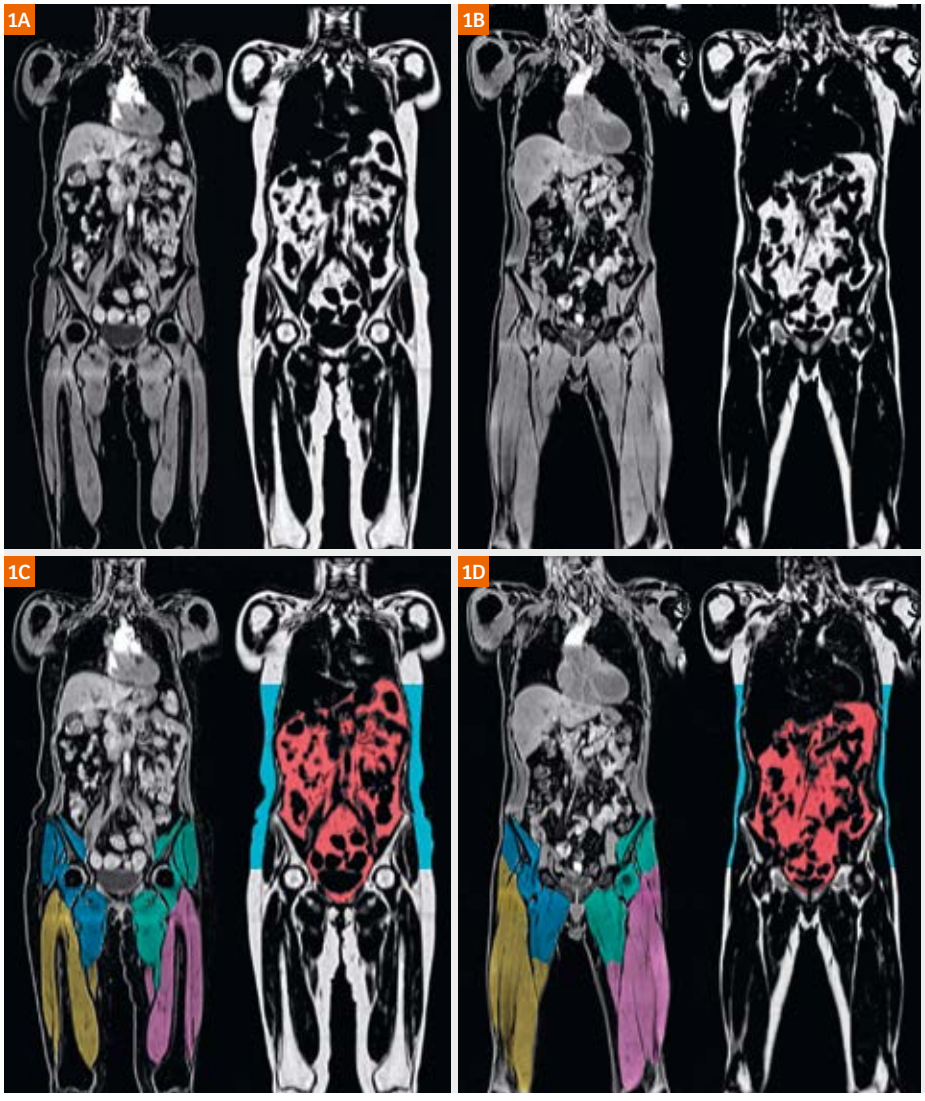

Figure 1:
Top row shows sample reconstructed water- and fat-volumes from the Dixon VIBE-based neck to knee MR-protocol for a female **(1A)** and male **(1B)** participant.

Sample segmentation results are shown in the bottom row for the female **(1C)** and male **(1D)** participants.

In the water images (left) the segmented thigh muscles are presented in false color and in the fat images (right) the segmented visceral (red) and subcutaneous (blue) adipose tissues are shown.

density fat fraction; PDFF). Body composition profiling was performed using the commercially available service AMRA® Profiler (Advanced MR Analytics AB, Linköping, Sweden). The profiling consisted of the following steps:

1. automatic image calibration,
2. automatic labeling and registration of fat and muscle regions to the acquired image volumes,
3. quality control of anatomical regions and MR-data performed by trained analysis engineers at Advanced MR Analytics, and
4. quantification of fat and muscle volumes based on the calibrated images.

Full details of the body composition profiling can be found in [2].

The semi-automated methods for analysing the body composition profile have up to now been shown to provide high repeatability and accuracy for adipose abdominal tissue volume, thigh muscle volumes, and liver fat content Proton Density Fat Fraction [3, 4]. Examples of segmented and labeled fat and water images are presented for two participants in Figures 1C–D, and four participants with normal BMI but different body composition profiles are presented in Figures 2A–D.

Feasibility of using the MR-protocol in a large population study

Quality control of the MR-protocol was analyzed in depth on the first 3 000 participants of the imaging study of UK Biobank. Of those first cases 2 995 (99.83%) were analysable for body fat, 2 775 (92.50%) were fully analysable for body fat and both thigh muscles. The main reasons for the dataset not being analysable were missing slabs in the acquisition, or improper postioning so that large parts of the volume were outside the field-of-view. Most types of artifacts were infrequently observed and water-fat swaps were uncommon. The conclusion was that the short Siemens MR-protocol was well tolerated by most participants and was sufficiently robust to achieve a very high success-rate for body composition profiling in a large population study [2].

Initial clinical findings

Obesity is a worldwide epidemic associated with significant costs. The traditional definition of obesity, based on body mass index (BMI), lacks detailed information on fat distribution. Moreover, the diseases relating to the metabolic syndrome may also affect muscle volumes and fat accumulation in organs such as the liver. Thus we sought to explore how the detailed body composition profile acquired in the UK Biobank imaging study is associated with important disease manifestations. In the analyses discussed below the visceral, total abdominal, and subcutaneous adipose tissue volumes were normalized with the square of the height.

In 2016 an analysis of the first 3 900 participants was presented. From these we analyzed 194 participants with diagnosed type 2 diabetes mellitus with age and gender matched controls and reported a strong association between type 2 diabetes and high visceral and total abdominal adipose tissue volumes, increased liver fat content, and low muscle ratio (defined as the total lean thigh muscle volumes normalized with body weight). When BMI was also included in the matching criteria the association of visceral adipose tissue volume and liver fat content to type 2 diabetes remained [5]. Cardiovascular disease is another disease relating to the metabolic syndrome. When we explored the body composition profiles for 213 participants with a history of cardiovascular events (angina, heart attack, or stroke) with age and gender matched controls with high blood pressure a strong disease association was found for multiple body composition parameters. Specifically, the visceral and total abdominal adipose tissue volume as well as liver fat content was significantly higher in the cardiovascular disease group whereas the muscle ratios were found to be lower, the association between visceral fat and cardiovascular disease remained when BMI was also included in the matching criteria [6].

As the inclusion in the UK Biobank imaging study continued we explored a larger group in 2017 (6 021 participants) and we found that the visceral adipose tissue volume and intra-muscular fat content were significantly associated with prior hospitalization [7]. An obese sub-population in this large group was further explored for the association to previous cardiovascular events and type 2 diabetes. In this case we found that visceral adipose tissue volume was significantly higher for both the diabetic and cardiovascular event groups. The participants that had reported previous diabetes had a lower muscle ratio and higher intra-muscular fat content than the participants without previous diabetes or cardiovascular events. The liver fat content was significantly higher in the diabetic group compared both controls and the cardiovascular event groups, no significant differences were observed comparing controls to the cardiovascular event group [8].

The non-alcoholic fatty liver disease spectrum is of growing concern and multiple pharmaceutical companies and research groups are working diligently to explore potential treatments to this worldwide epidemic. The disease spectrum is initially characterized by increased liver fat content (hepatic steatosis) and in the obese sub-population we explored if a fatty liver was associated

with increased health care burden (defined by the accumulated hospital nights). This analysis was slightly more complex as the association was significantly negative when controlling for visceral and total abdominal adipose tissue volumes (the models were also adjusted for age, sex, smoking, alcohol intake, and physical activity). The observation suggested that hepatic steatosis may have a link to visceral adiposity in participants with an increased health care burden in a phenotype presenting with high visceral adipose tissue volume together with low liver fat content [9].

Sarcopenia is a common problem in the aging population as well as in certain disease states, such as non-alcoholic steatohepatitis. In the UK Biobank imaging study DXA, which is typically used to diagnose sarcopenia, is also acquired and in 2016 we explored the relationship between the body composition profile derived from the MR-examination and the DXA-based biomarker for sarcopenia. We found that the total lean thigh muscle volume divided by the square of the height could be used to identify sarcopenic participants with an AUROC of 0.96. This suggests that sarcopenia can be characterized from this Siemens MR body composition protocol with high sensitivity and specificity [10].

Conclusions

In this article we have presented a robust and rapid neck to knee MR-protocol for Siemens MR-scanners that can deliver high technical success rates in large scale population studies. We have also presented initial clinical findings based on analysing the body composition profile in such a large population. We believe that this is a widely applicable method in a clinical and research setting investigating metabolic disease, muscle degenerative

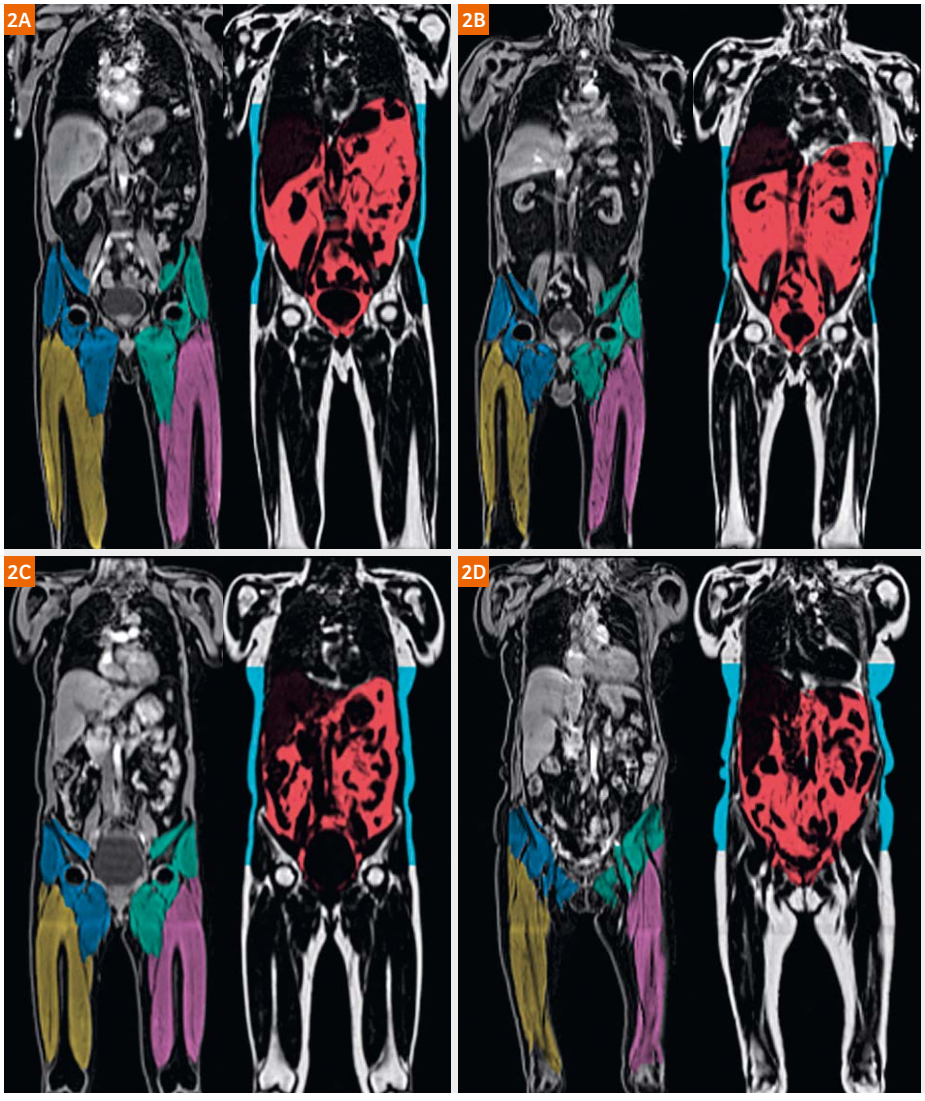

Figure 2:
Four sample reconstructed water- and fat-volumes from the Dixon VIBE-based neck to knee MR-protocol for participants with normal BMI but different body composition profile. In the water images (left) the segmented thigh muscles are presented in false color and in the fat images (right) the segmented visceral (red) and subcutaneous (blue) adipose tissues are shown. The panels show **(2A)** a 63-year-old male with a BMI of 22.7 kg/m^2, **(2B)** a 67-year-old male with a BMI of 24.9 kg/m^2, **(2C)** a 55-year-old female with a BMI of 21.9 kg/m^2, and **(2D)** a 70-year-old female with a BMI of 23.9 kg/m^2.

disease, as well as metabolic components of other diseases. The simultaneous assessment of multiple important fat and muscle compartments increase the understanding of the complex interplay between disease development and metabolic processes.

References

1 Sudlow C, Gallacher J, Allen N, et al.
UK Biobank: An Open Access Resource for Identifying the Causes of a Wide Range of Complex Diseases of Middle and Old Age. PLoS Med. 2015; 12(3):e1001779.
2 West J, Dahlqvist Leinhard O, Romu T, et al.
Feasibility of MR-Based Body Composition Analysis in Large SCale Population Studies. PLoS One. 2016; 11(9):e01633321.
3 Borga M, Thomas EL, Romu T, et al.
Validation of a Fast Method for Quantification of Intra-abdominal and Subcutaneous Adipose Tissue for Large Scale Human Studies. NMR Biomed. 2015; 28(12):1747-1753.
4 Middleton M, Haufe W, Hooker J, et al.
Repeatability and Accuracy of an, MRI-based, Semi-automated Analysis Method for Quantifying Abdominal Adipose Tissue and Thigh Muscle Volumes, and Hepatic Proton Density Fat Fraction. Radiology. 2017; 283(2):438-449.
5 Dahlqvist Leinhard O, Linge J, West J, et al.
Body Composition Profiling using MRI – Normative Data for Subjects with Diabetes Extracted from the UK Biobank Imaging Cohort. In Proc. of the 102nd RSNA Scientific Meeting and Annual Assembly, Chicago, USA. 2016.
6 Dahlqvist Leinhard O, Linge J, West J, et al.
Body Composition Profiling using MRI – Normative Data for Subjects with Cardiovascular Disease Extracted from the UK Biobank Imaging Cohort. In Proc. of the 102nd RSNA Scientific Meeting and Annual Assembly, Chicago, USA. 2016.
7 West J, Linge J, Romu T, et al.
Distribution Matters – Body Composition Profiling Associated with Prior Health Care Burden. In Proc. of the 24th ECO, Porto, Portugal. 2017.
8 Linge J, West J, Romu T, et al.
The Body Composition Profile – Enhancing the Understanding of Obesity using UK Biobank Imaging Data. In Proc. of the 24th ECO, Porto, Portugal. 2017.
9 Romu T, Linge J, Borga M, et al.
Hepatic Steatosis is Associated with Lower Prior Health Care Burden in Visceral Obesity. In Proc. of the 24th ECO, Porto, Portugal. 2017.
10 Karlsson A, Linge J, West J, et al.
Defining Sarcopenia with MRI – Establishing Threshold Values within a Large-Scale Population Study. In Proc. of the 102nd RSNA Scientific Meeting and Annual Assembly, Chicago, USA. 2016.

Contact

Janne West, Ph.D.
Advanced MR Analytics AB

Badhusgatan 5
SE-582 22 Linköping
Sweden
janne.west@amra.se

Visit us at

www.siemens.com/magnetom-world

to download the short body compostion protocols for 1.5T MAGNETOM Aera and 3T MAGNETOM Skyra.

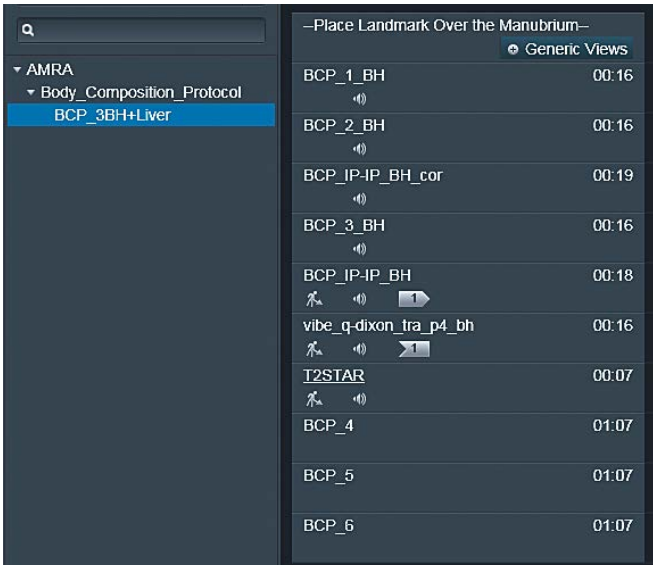

Imaging of the Pancreas: Technique and Clinical Applications

Giovanni Morana[1]; Alex Faccinetto[1]; Alberto Dorigo[1]; Pierluigi Ciet[2]; Silvia Venturini[1]; Michele Fusaro[1]

[1] Department of Radiology, General Hospital Ca' Foncello, Treviso, Italy
[2] Department of Radiology, Erasmus Medical Center, Rotterdam, the Netherlands

Imaging of the pancreas represents a diagnostic challenge for both radiologists and clinicians because of overlapping clinical, radiological, and pathological features.

The wide pathological range of both solid and cystic lesions requires an in-depth knowledge of the pathology, and the application of the best imaging techniques in order to arrive at the correct diagnosis.

MRI has assumed a leading role in imaging of the pancreas thanks to recent technical innovations with either breath-hold T1- and T2-weighted images or respiratory-triggered T2-weighted images. It also owes its success in this field to dynamic imaging with contrast media and secretin, as these techniques offer greater scope for noninvasive exploration of the pancreatic ducts and pancreatic parenchyma, and imaging of the pancreatic vessels.

Visit us at **www.siemens.com/magnetom-world**

to read this comprehensive article.

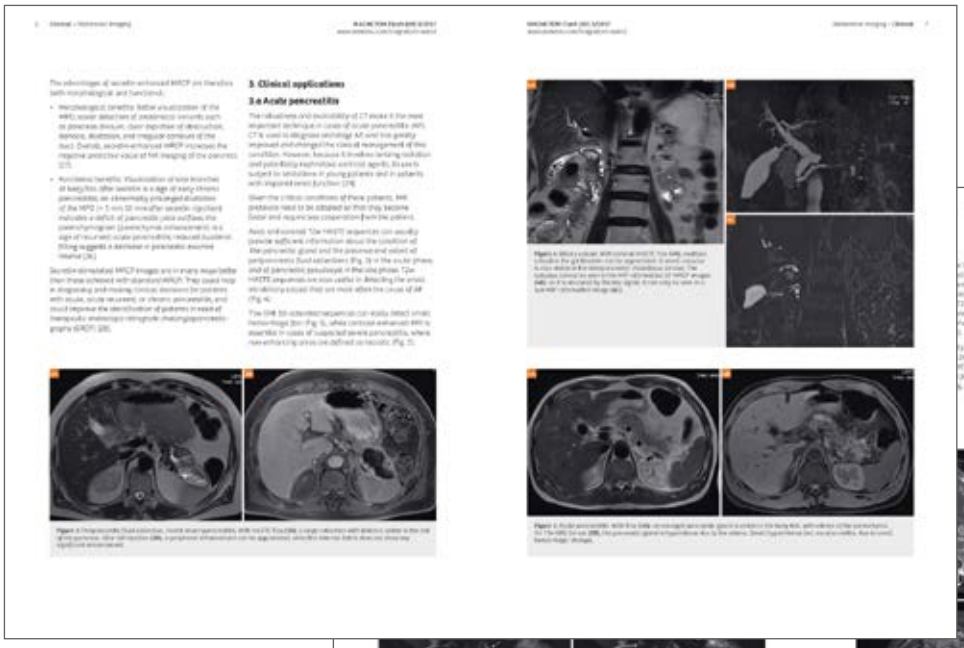

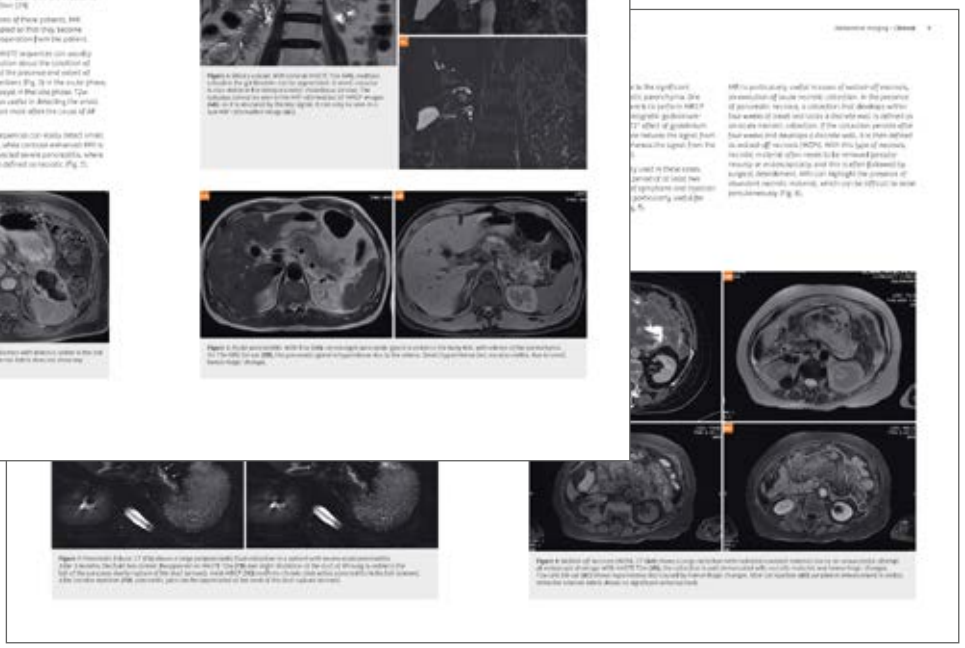

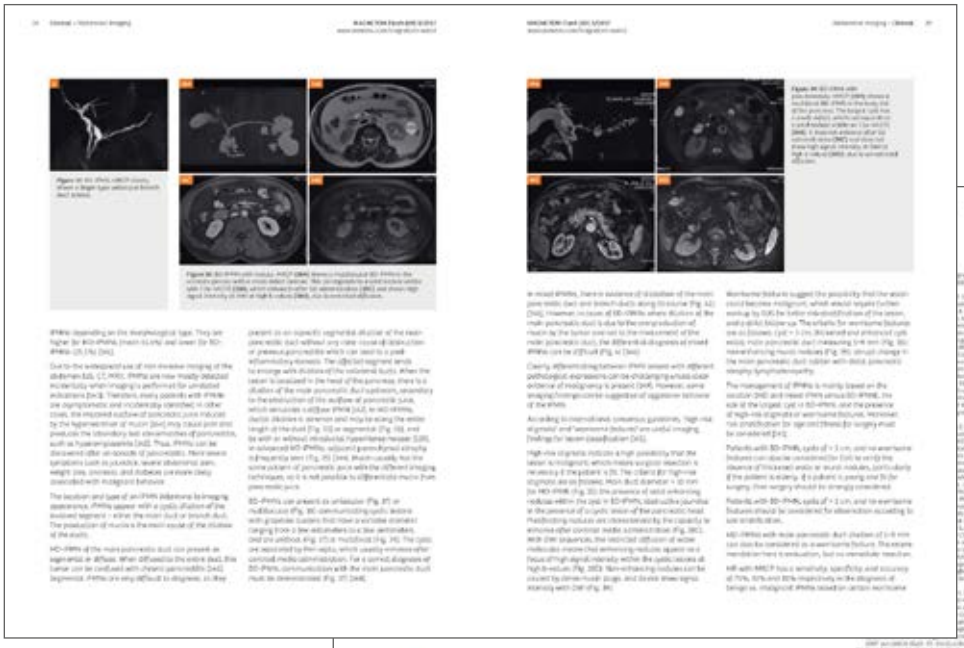

MAGNETOM Vida Clinical Case Studies

Axel Stäbler, M.D.

Radiologie in München Harlaching, Munich, Germany

Case 1

8-year-old boy with Legg-Calvé-Perthes disease left hip. Coronal PDw fatsat and T1w, axial and sagittal PDw fatsat. Legg-Calvé-Perthes disease causes aseptic necrosis of the femoral head in children, mainly between the ages of five and eight. The whole of the left femoral head epiphysis is fragmented and severely flattened, there is a reduction of more than 50% in the height of the lateral pillar, and the epiphysis has been displaced laterally from the hip joint cavity. The acetabulum, too, is already deformed and flattened; signal intensity for the acetabular labrum is regular, low. Only remnants of the epiphyseal nucleus are still visible; the growth plate and adjacent metaphysis are involved, widened, and deformed. Coxa magna.

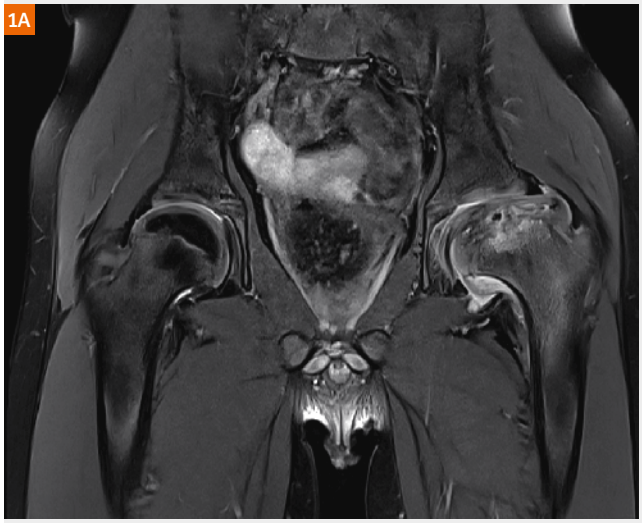

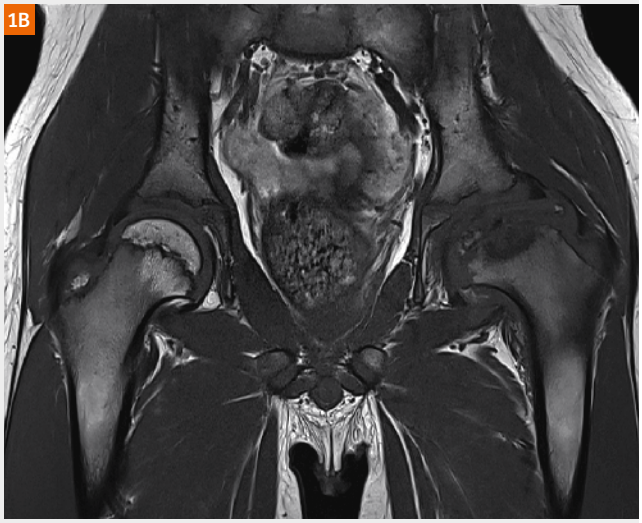

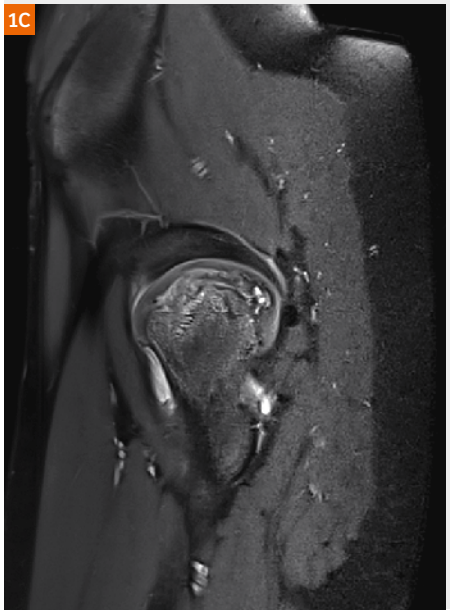

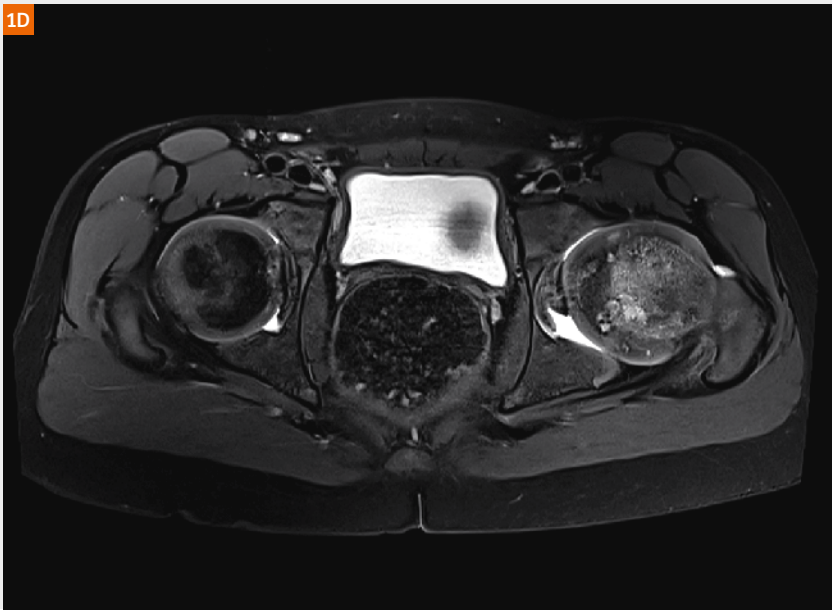

Case 2

73-year-old patient with activated coxarthrosis, right. Coronal PDw fatsat and T1w, sagittal PDw fatsat of the right and left hip. The joint space in the right hip joint is completely narrowed; there is a large resorption cyst in the cranial pressure absorption zone, with active edemata in the femoral neck up to the intertrochanteric region. The left hip, which is still largely normal, is shown for comparison.

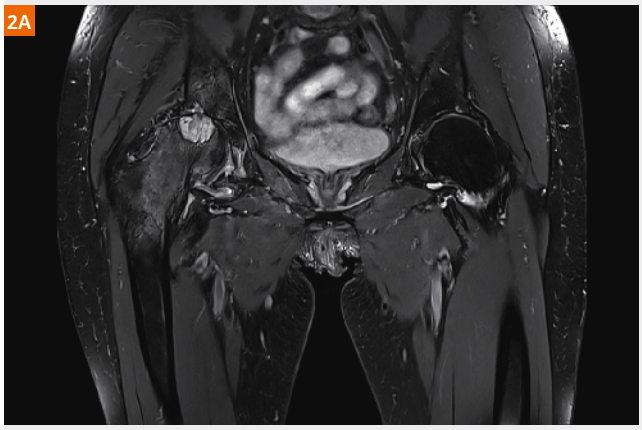

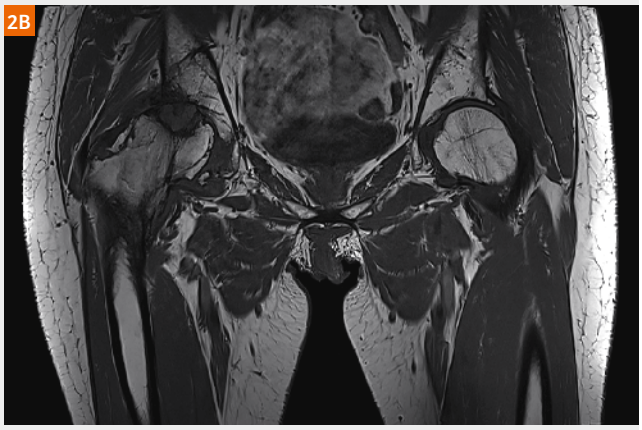

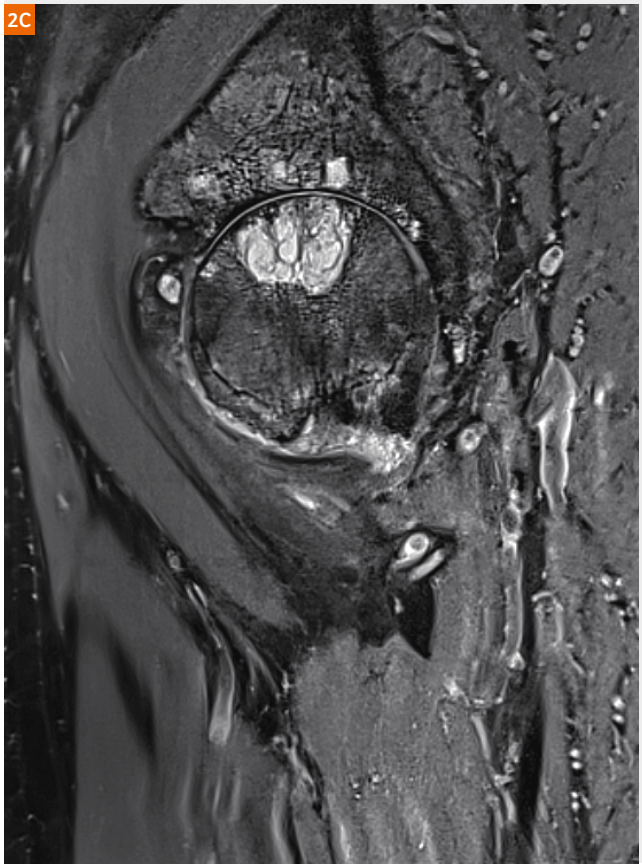

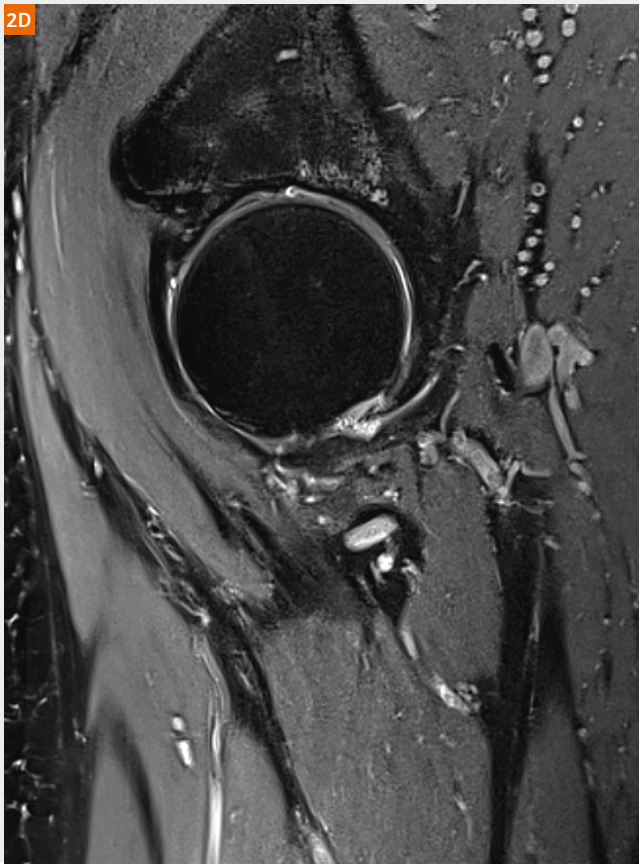

Case 3

61-year-old male with plantar plate rupture at DII. The sagittal PDw fatsat image shows a tear in the plantar plate. There has been fraying/disintegration of the fibrous sheath around the flexor tendon, so the flexor tendon can be differentiated from the plantar plate. The plantar plate is proximally dislocated and extends beyond the condyle in the direction of the metaphysis. The base of the proximal phalanx is slightly decentered towards the dorsum of the foot. MTP joint III is pictured for comparison to show the normal alignment. In the axial T1w image, the flexor tendon is laterally subluxated; with its split/broken down fibrous sheath, it can be differentiated as an exposed structure. The plantar plate has a medial tear and cannot be differentiated. The T1w fatsat, following administration of contrast medium, shows the same result.

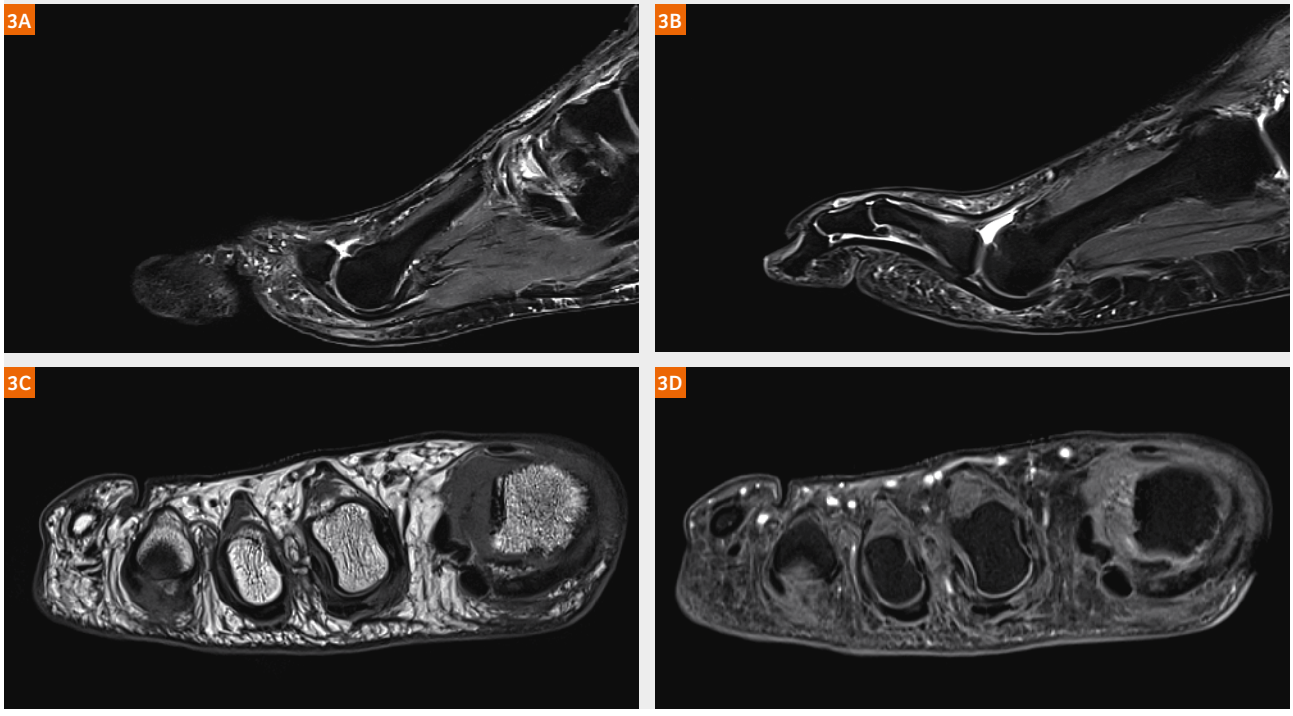

Case 4

38-year-old male, presented with symptoms after fracture of distal fibula eight weeks earlier. The coronal T1w and PDw fatsat images show a persistent Weber type A fracture of distal fibula. The increase in signal intensity in the bone marrow, focused on the subcortical zone, that appear in the PDw fatsat images are indicative of reactive bone marrow change associated with bone dystrophy. There is anterolateral luxation of the peroneal tendons, as well as an anteromedial luxation of the tendon of the tibialis posterior (at the level of the medial malleolus). The axial T2w image shows the medially luxated posterior tibial tendon; at this level, the retinacula of the peroneal tendons are still intact. Anterolateral luxation of the peroneal tendons is shown in the next image. This can also be seen in the oblique axial PDw fatsat image (tendon tilt).

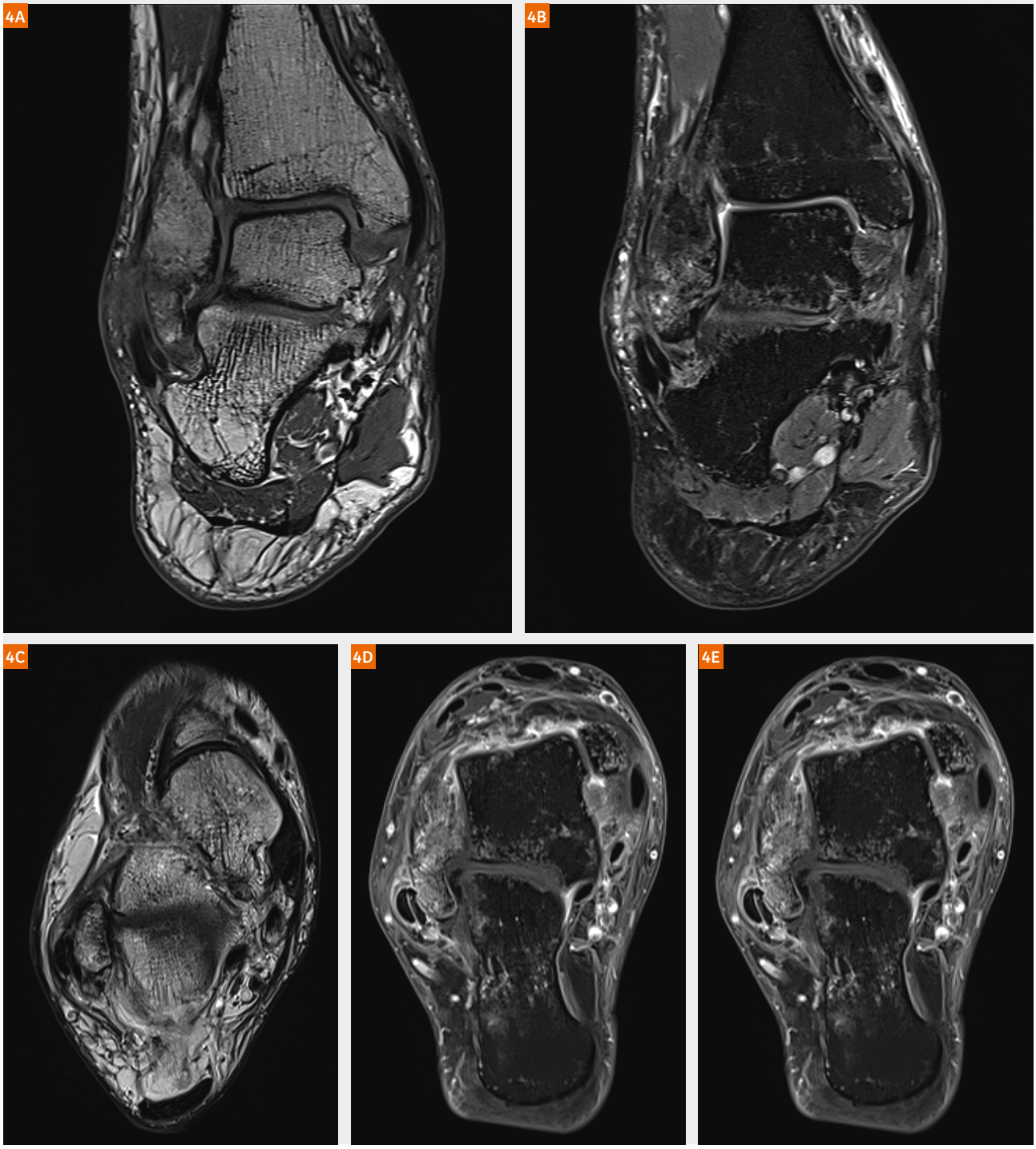

Case 5

70-year-old male with advanced medial gonarthrosis presenting with femoral and tibial chondropathy (grade IV), degenerative disintegration of the medial meniscus, and osteophytic outgrowths (PDw fatsat and coronal T1w). In the PDw fatsat images, extensive cartilage damage and incipient bone loss on the tibial plateau are visible in the medial compartment. In the sagittal image (PDw fatsat) osteophytic spurs at the upper and lower pole of the patella are clearly visible.

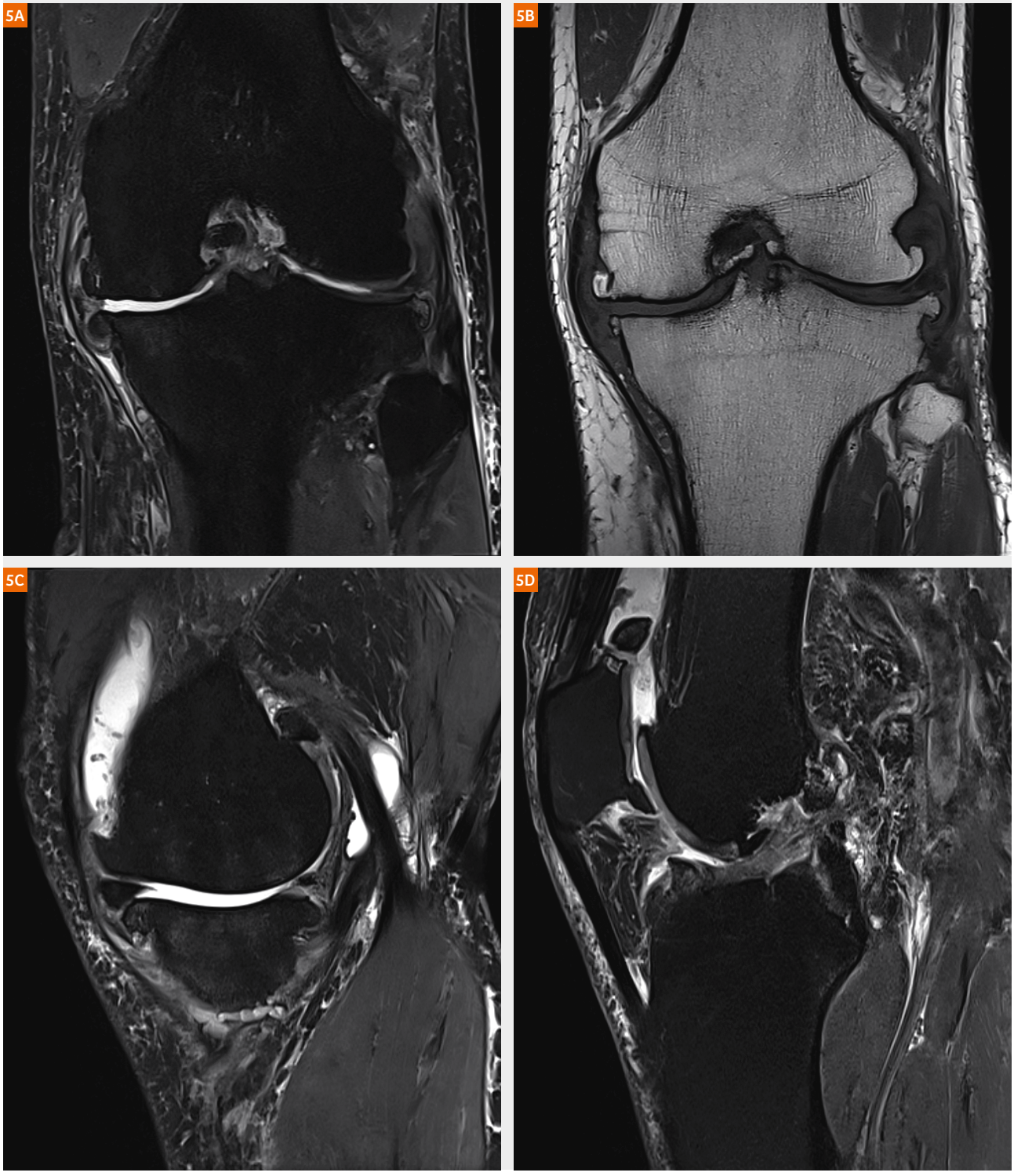

Case 6

54-year-old male with post-traumatic quadriceps tendon rupture (sagittal PDw fatsat and PDw). The rupture occurred at the osseotendinous junction at the superior pole of the patella, marked surrounding edema and effusion and downward angulation of the patella.

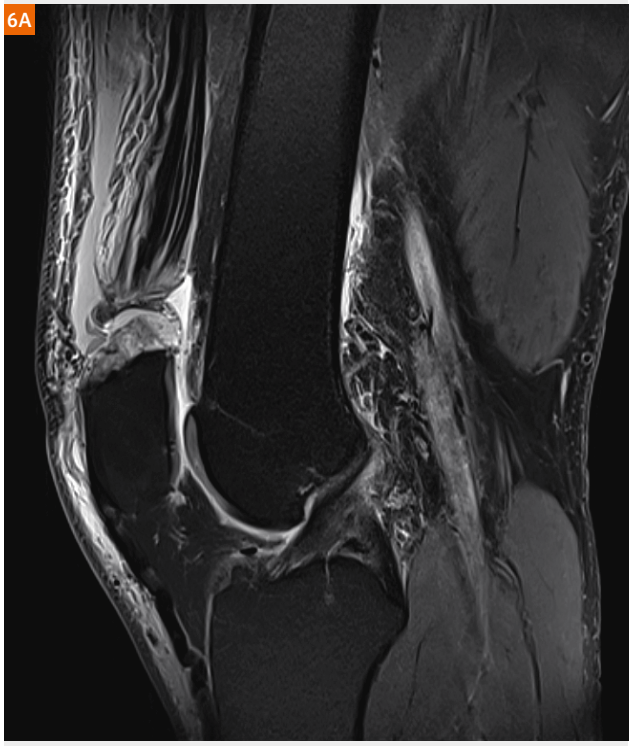

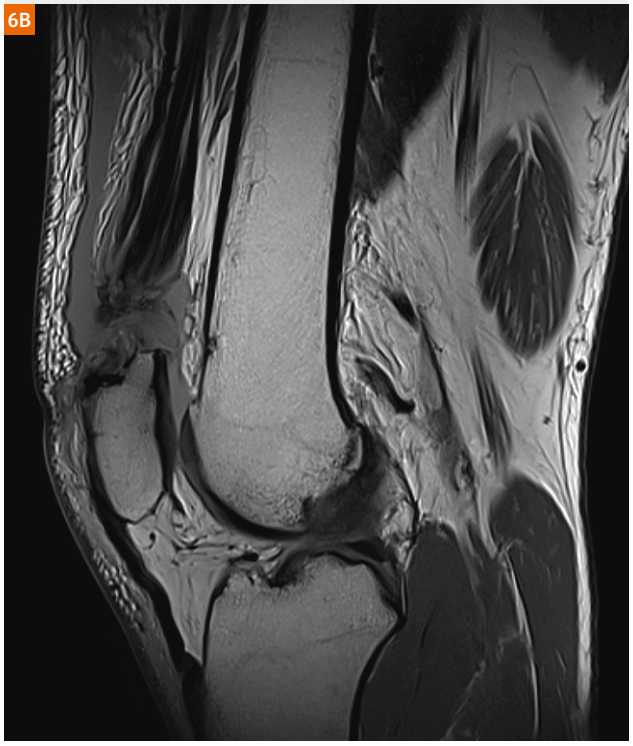

Case 7

57-year-old male with degenerative tearing of the foveal attachments of the discus articularis, leading to instability in the distal radioulnar joint with effusion and fibrovascular scar tissue around the capsule (coronal PDw fatsat, T1w fatsat after intravenous administration of contrast medium, axial T2w).

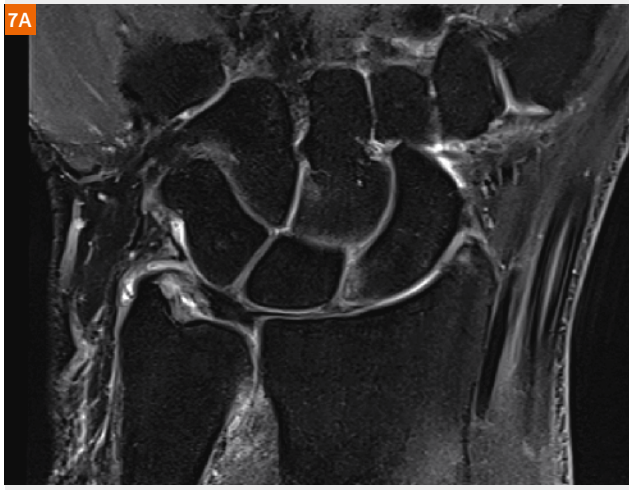

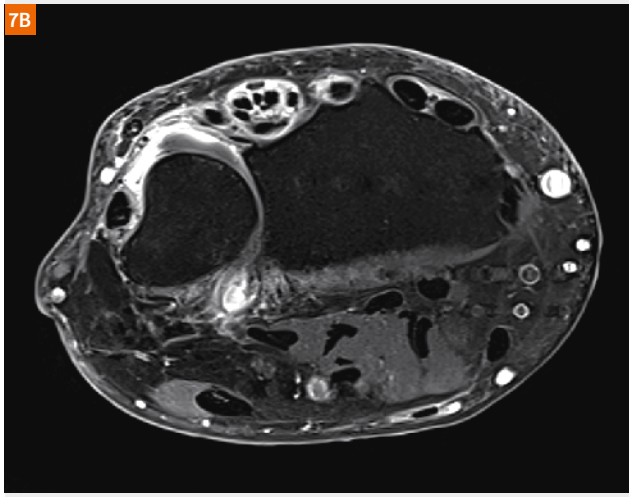

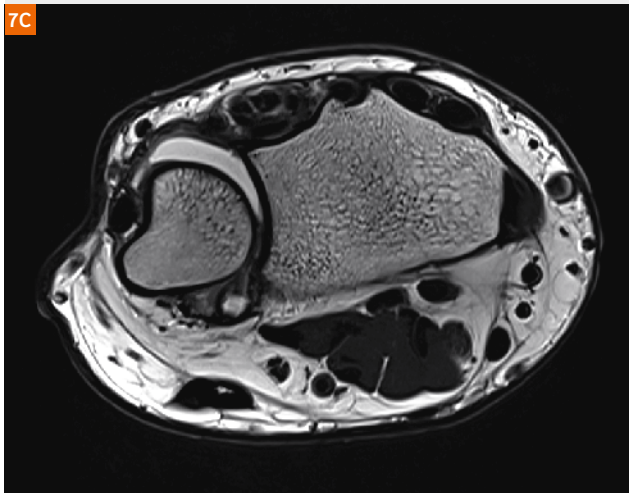

Case 8

86-year-old male with active medial meniscus lesion, an acute meniscal tear of the medial posterior horn. There is vertical-radial tearing with an additional longitudinal rupture, indicative of complex tearing (coronal, axial and sagittal PDw fatsat, coronal T1w).

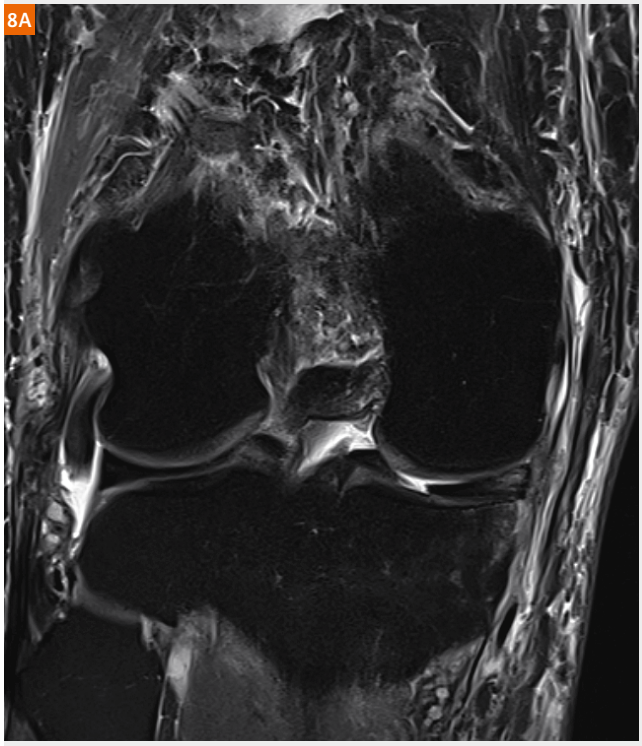

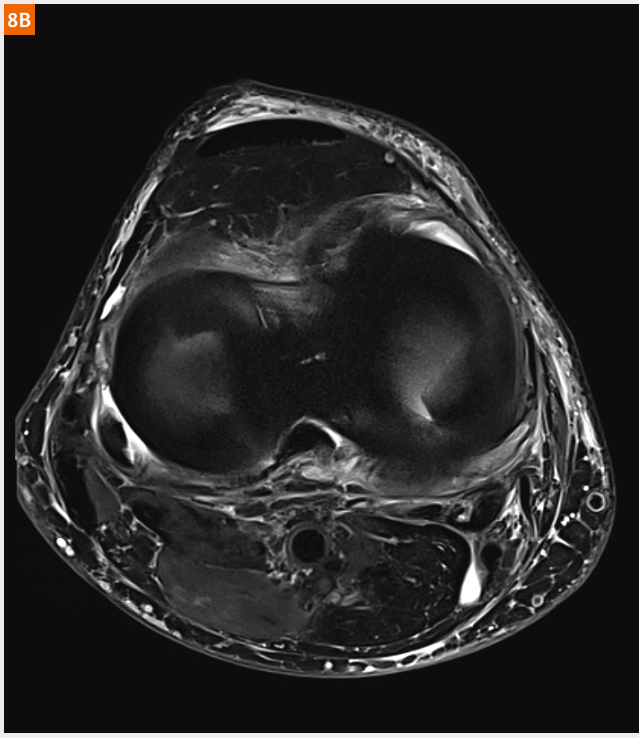

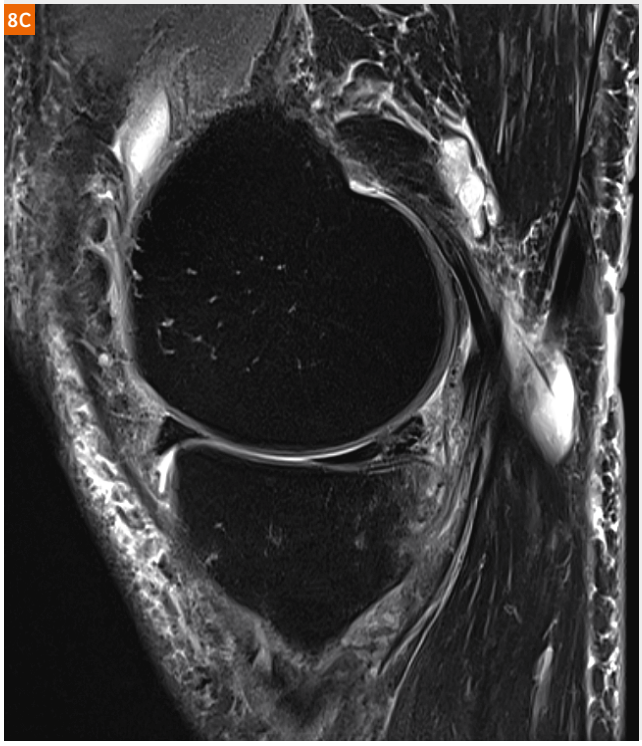

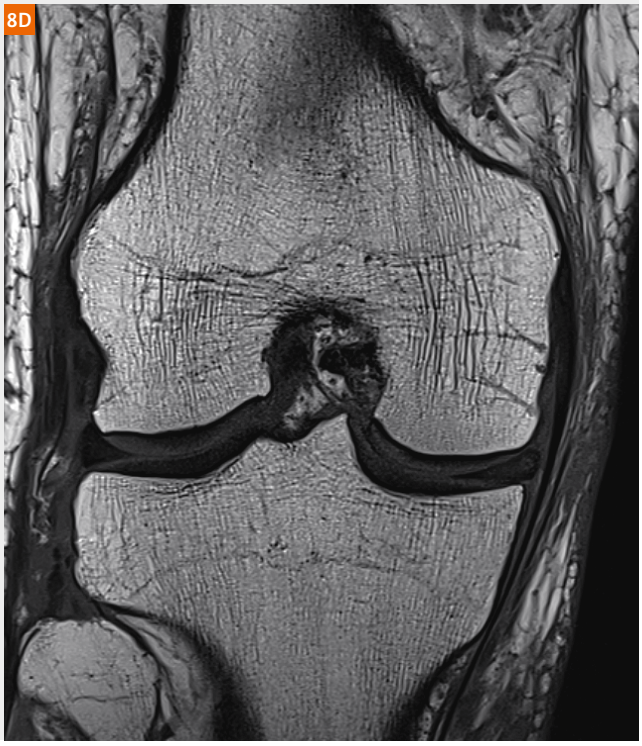

Case 9

53-year-old male with right-sided foraminal disc sequestration at L3/4. The case demonstrates extrusion of disc tissue into the epidural space with cranial migration. The disc tissue is brighter in the T2w image than the original disc during fluid inflow. Signal intensity for the sequestered disc is low in the T1w image and very high in the STIR image. Sequestration was caused by a fibrous ring lesion, visible in the axial T2w image, with displacement of the extraforaminal root L3, right.

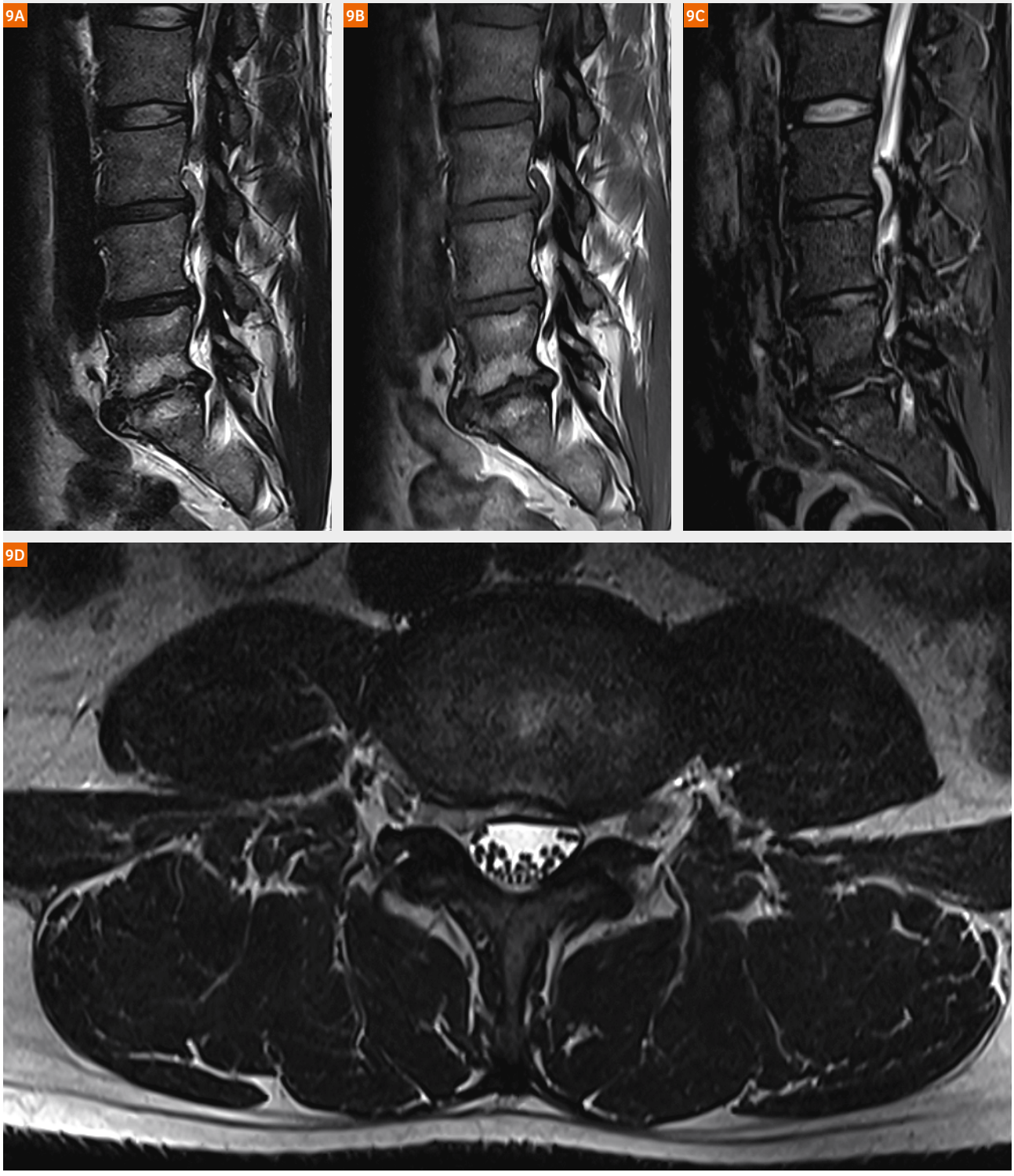

Case 10

32-year-old female with rheumatoid arthritis. The PDw fatsat image shows severe thinning of the supraspinatus tendon, with extensive glenohumeral cartilage damage (grade III–IV). There has been inflammatory bone resorption in the "bare area" and the "footprint" of the supraspinatus tendon. Signal intensity for this is low in the T1w image and is moderately enhanced in the T1w fatsat image after administration of contrast medium. Proliferative synovitis, an effusion, and synovial proliferations (enhanced by contrast medium) are visible on the axial PDw fatsat and T1w fatsat image.

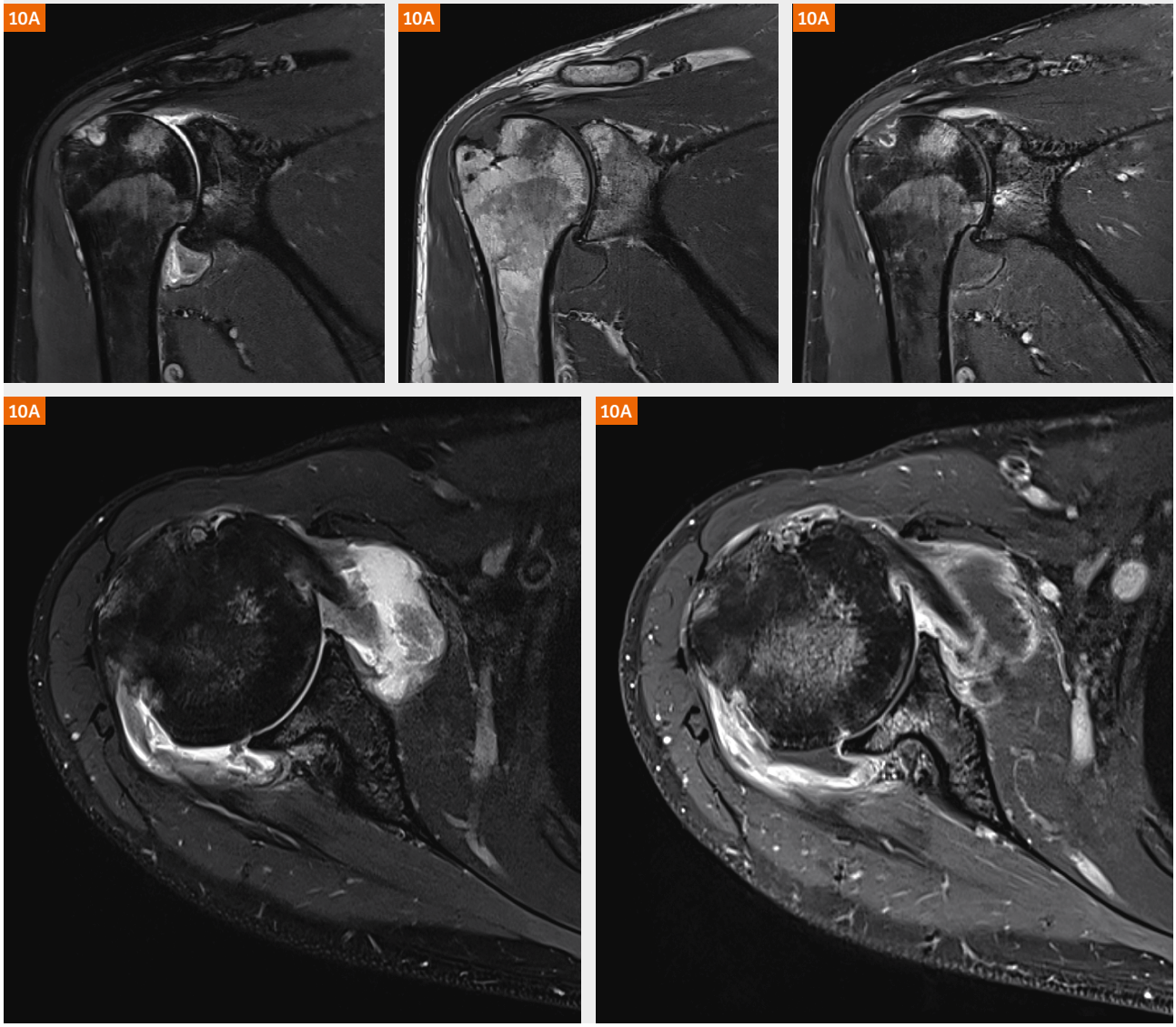

Contact

Professor Axel Stäbler, M.D.
Radiologie in München Harlaching

Grünwalder Straße 72
81547 Munich
Germany
+49 (0)89 6202 1630
staebler@radiologie-muenchen-harlaching.de

GOKnee3D – Fully-automated One-button-push High-resolution MRI of the Knee

Jan Fritz, M.D., P.D., D.A.B.R.; Filippo Del Grande, M.D., MBA, MHEM; Neil Kumar, M.D.; Derek F Papp, M.D.; Rushyuan J Lee, M.D.

Johns Hopkins University School of Medicine, Baltimore, MD, USA

Magnetic resonance imaging (MRI) plays a key role in the workup of acute and chronic injuries, pain syndromes, and dysfunction of the knee. While radiographic and computed tomography evaluations provide excellent osseous detail, MRI is most accurate for the detection of bone marrow edema in the setting of radiographically occult bone contusion injuries and osseous stress reactions, non-displaced fractures, acute chondral shear injuries, and degenerative cartilage defects, tears of the collateral and cruciate ligaments, muscle-tendon injuries, and meniscal tears. Also, MRI can diagnose synovitis not only by the presence of a joint effusion, but also by visualizing synovial thickening, edema pattern, and frond-like hypertrophy.

Most MRI protocols of the knee for the assessment of internal derangement include pulse sequences that are tailored for the morphological assessment of anatomic structures, as well as pulse sequences that are tailored to maximize the conspicuity of findings with long T2 constants, such as fluid and edema.

For morphological assessment of the integrity of anatomical structures, intermediate-weighted MR images with echo times around 30 ms and no fat suppression are ideally suited due to their high signal yield, intermediate-to-high fluid signal, and high contrast-to-noise ratios of low signal intensity structures such as menisci, ligaments, and cartilage. The addition of a T1-weighted pulse sequence to the protocol can be beneficial for bone marrow assessment due to their exquisite specificity for fat signal, including osteomyelitis, marrow replacing diseases, and possibly fractures. However, T1-weighted pulse sequences have a lower sensitivity for detecting cartilage defects, ligamentous injuries, and meniscal tears due to absent fluid signal. Structural pulse sequences are often designed with a higher spatial resolution to maximize structural detail and the detection of small abnormalities, such cartilage fissures, and coapted tears.

For the assessment of signal abnormalities, pulse sequences with longer echo times and fat suppression

1

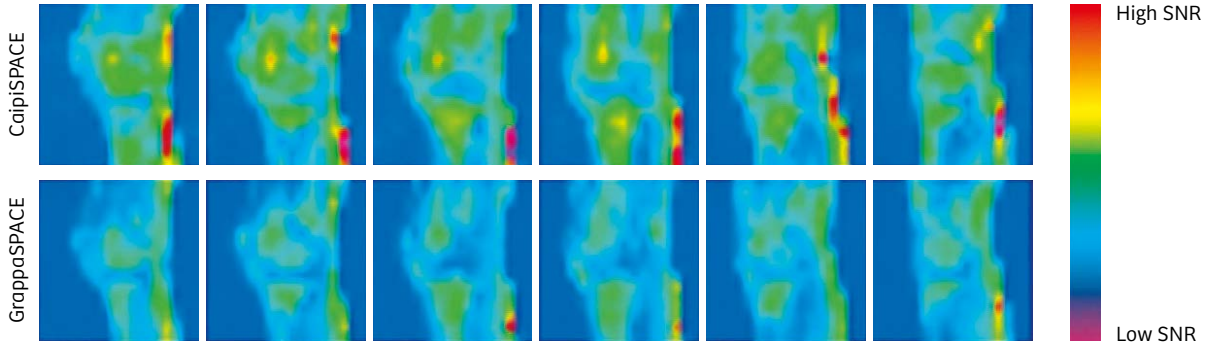

Figure 1:
3-Dimensional Signal-to-Noise Ratio maps illustrate the higher signal yield of CAIPIRINHA-accelerated 3D SPACE over GRAPPA-accelerated 3D SPACE.

510(k) pending. The product is not commercially available. Future availability cannot be guaranteed.

are typically used to increase the conspicuity of findings with long T2 constants, such as joint fluid, collections, and edema. The presence of an edema pattern in bone, ligaments, muscles, and fatty tissues often allows the differentiation of an acute injury or inflammation from chronic remodeling. Abnormally T2 hyperintense areas also have a higher suspicion to be a pain generator. Fast and turbo spin echo (TSE) pulse sequences with effective echo times of 60–70 ms and spectral fat suppression result in exquisite fluid sensitivity. The use of Spectral Attenuated Inversion Recovery (SPAIR) technique, instead of conventional spectral fat suppression can improve the homogeneity of fat suppression across the field-of-view [1]. Alternatively, STIR (Short Tau Inversion Recovery) technique may be used. Fluid sensitive sequences can be designed with less spatial resolution, as it does not interfere with their fluid-sensitivity but can improve efficiency and compensate for the lack of signal from suppressed fat-bound protons.

Two-dimensional (2D) TSE pulse sequences can be acquired with a high in-plane spatial resolution, *e.g.*, with a pixel size of 0.5 x 0.5 mm^2 and less. However, to gain enough MR signal, a slice thickness of 2–4 mm is required, which lowers the effective spatial resolution and results in partial volume effects. The anisotropic voxel size prevents multiplanar reformations and requires the separate acquisition of images in axial, sagittal, and coronal orientation, which can be a time-consuming process and often requires total protocol acquisition times of 20 minutes.

Three dimensional (3D) TSE techniques such as Sampling Perfection with Application optimized Contrast using different flip angle Evolutions (SPACE) yield markedly more MR signal, due to volume-based excitation and use of multiple additional phase-encoding steps in a second direction. Together with the much higher signal yield, 3D data sets allow for the generation of much thinner slices partitions and facilitate 3D MRI with isotropic voxels size.

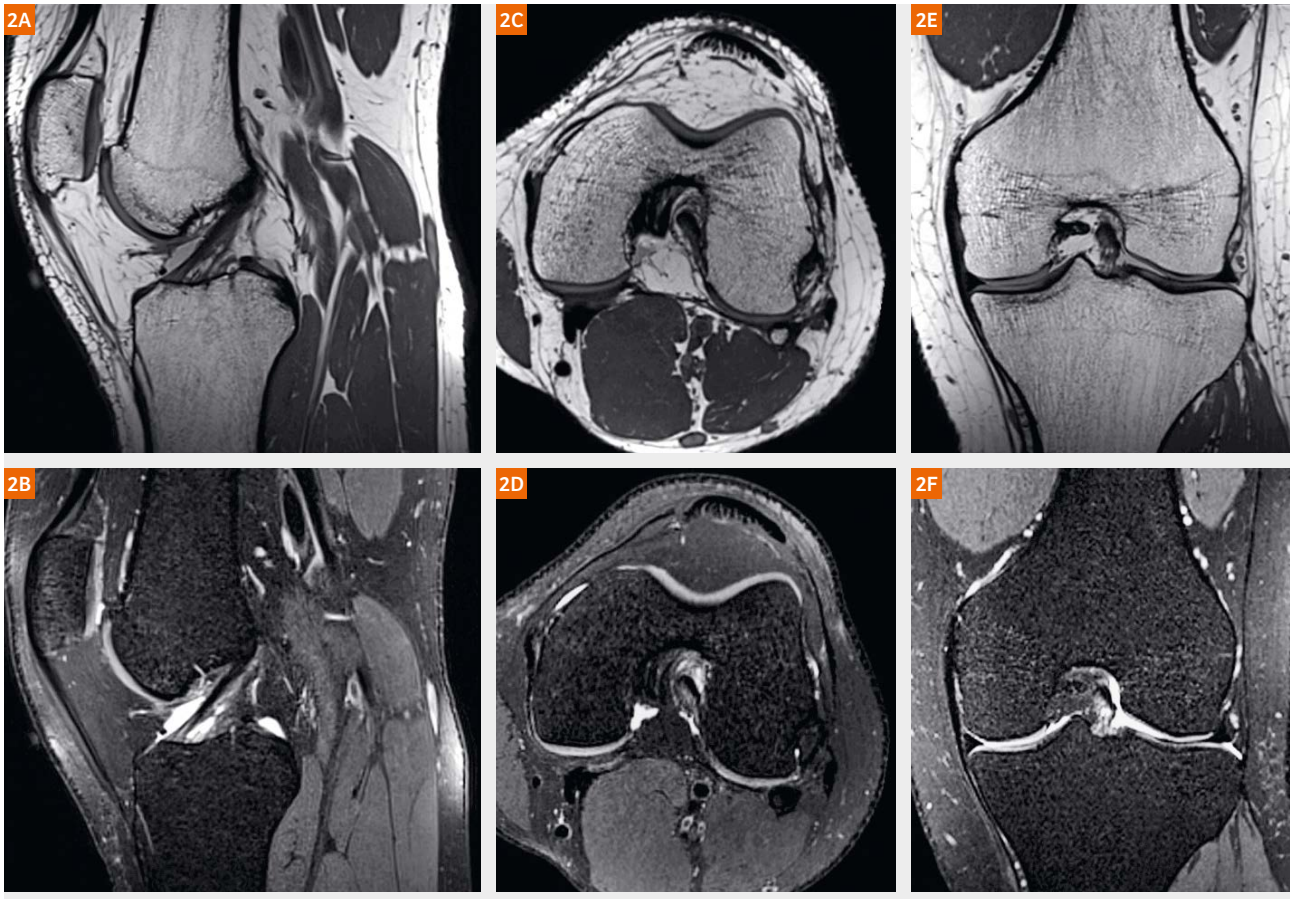

Figure 2:
Normal left knee of a 37-year-old healthy man. Sagittal isotropic 0.5 mm intermediate-weighted and 0.6 mm T2-SPAIR-weighted 3D CAIPIRINHA SPACE source MR images **(2A, B)** with standard axial **(2C, D)** and coronal **(2E, F)** reformats.

3

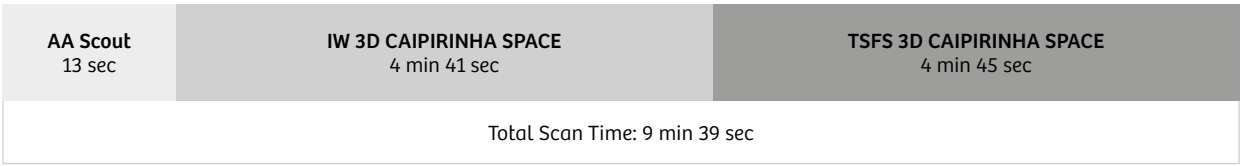

Figure 3:
GOKnee3D protocol for 3T MRI of the knee in under 10 minutes.

Such isotropic data sets with sufficiently small voxel size virtually eliminate partial volume effects and provide an opportunity for the improved display of small anatomic detail. Also, virtually any imaging plane can be reformatted from a single parent dataset (Fig. 1), including standard axial, sagittal, and coronal MR images, as well as oblique and curved planar reformations and 3D volume-rendered MR images.

The two phase-encoding directions of 3D SPACE provide an opportunity for bi-directional acceleration. A 2 x 2 parallel imaging using a Generalized Autocalibrating Partial Parallel Acquisition (GRAPPA) sampling pattern facilitates a 4-fold acceleration without the occurrence of acceleration and aliasing artifacts. As a further development, the use of a shifted Controlled Aliasing In Parallel Imaging Results IN Higher Acceleration (CAIPIRINHA) sampling pattern results in the optimized use of differential coil spatial sensitivities and improved geometry (g) factor performance [2, 3]. When compared to GRAPPA SPACE, CAIRPINIHA SPACE is characterized by increased image quality and 10–20% higher signal-to-noise ratios (Fig. 1). CAIPIRINHA-based 4-fold acceleration substantially reduces the time required for data acquisition and eliminates the need for compromises, including long echo trains, partial Fourier undersampling, and anisotropic data acquisition (Fig. 2) [4–6]. CAIPIRINHA SPACE with integrated anatomical landmark-based AutoAlign Knee technology, which provides automatic field-of-view and slice positioning, builds the foundation for GOKnee3D – a fully automated, one-button-push, high-resolution, 3D isotropic diagnostic knee exam with intermediate- and T2-SPAIR-weighted image contrasts and a total acquisition time of fewer than 10 minutes (Fig. 3).

The development of GOKnee3D adopted a similar strategic approach as earlier GO (Generalized Optimized) strategies [7–9]. The clinical validation study of GOKnee3D included head-to-head comparisons with conventional exams of 100 patients that were scanned at the MAGNETOM Skyra (3T) and 50 patients that were scanned at the MAGNETOM Aera (1.5T) [10]. All patients underwent the 10-minute GOKnee3D exam as well as a high-quality conventional 20-minute 2D exam that included six separately acquired pulse sequences of standard non-fat-suppressed and fat-suppressed clinical contrasts in three orientations. All images were independently evaluated by two board-certified, fellowship-trained musculoskeletal radiologists. The images were assessed for the presence or absence of joint effusion, joint bodies, popliteal cysts, lateral and medial meniscal tears, medial and lateral collateral ligament tears, anterior and posterior cruciate ligament tears, quadriceps and patella tendon tears, cartilage defects, bone marrow edema, and fractures. Additionally, the overall image quality and severity of motion artifact were also evaluated.

The study results indicate that the images generated by the 10-minute GOKnee3D protocol are at least diagnostically equivalent to the images of a 20-minute 2D TSE standard of reference protocol. There were no significant differences in the diagnosis of abnormal findings between GOKnee3D and the 2D TSE exams at both 1.5T and 3T. For both, 1.5T and 3T GOKnee3D protocols, the inter-reader agreement was consistently higher for the 3D images when compared to the 2D images.

An ongoing study evaluating the diagnostic accuracy of GOKnee3D for the detection of internal derangement in children[1] and adolescents, with arthroscopy as the standard of reference, indicates sensitivities of 83–100% and specificities of 93–100% for the diagnoses of discoid menisci, meniscus tears, ligament injuries, and osteochondritis dissecans lesions [11]. This study is currently being extended to adult patients.

The following clinical cases with surgical correlation illustrate the application of GOKnee3D for the evaluation of internal derangement in adults and children. All images were acquired on a 3T MAGNETOM Skyra MR imaging system (Siemens Healthcare, Erlangen, Germany) and Tx/Rx Knee 15 (QED, Mayfield Village, OH, USA) surface coil.

[1] MR scanning has not been established as safe for imaging fetuses and infants less than two years of age. The responsible physician must evaluate the benefits of the MR examination compared to those of other imaging procedures.

Case 1

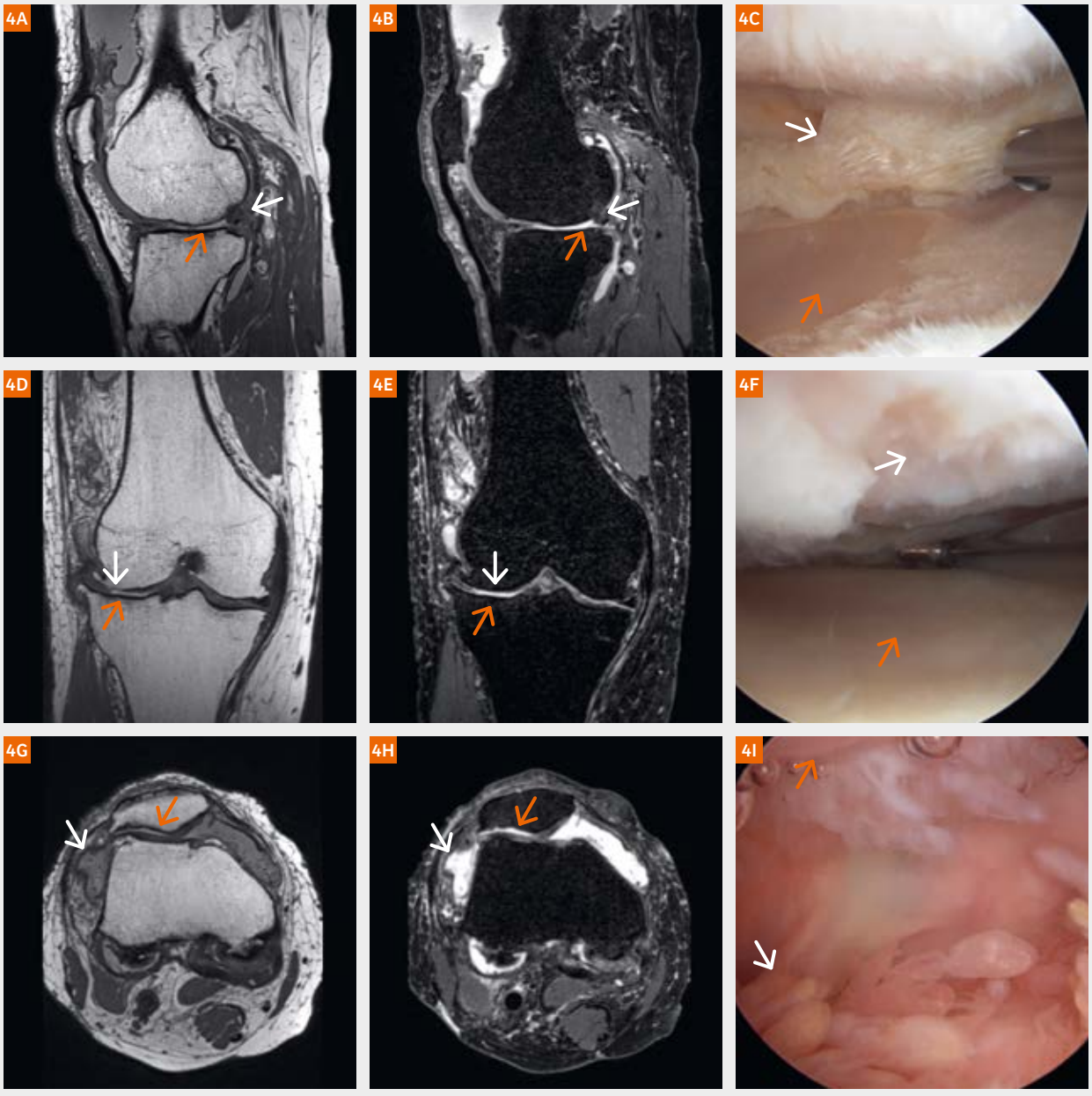

Indication: 60-year-old woman with intermittent pain and swelling of the right knee.

MRI findings: Sagittal, coronal, and axial intermediate-weighted and T2-SPAIR GOKnee3D images demonstrate a degenerative, complex tear of the posterior lateral meniscus (white arrows, **4A and 4B**). There is full-thickness cartilage loss over the lateral femoral condyle and lateral tibia plateau with focal bone-on-bone apposition (orange arrows, **4A and 4B**; white and orange arrows, **4D and 4E**). There is full-thickness cartilage loss of the lateral facet of the patella (orange arrow, **4G and 4H**) and synovitis with frond-like proliferations (white arrow, **4G and 4H**).

Arthroscopy findings: Degenerative, complex, tear of the posterior lateral meniscus (white arrow, **4C**). Full-thickness cartilage defects of the central femur (orange arrow, **4C and 4F**), tibia plateau (white arrow, **4F**), and lateral patella (orange arrow, **8I**) with synovitis (white arrow, **4I**).

Case 2

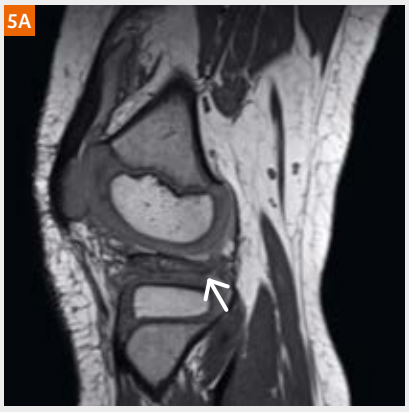

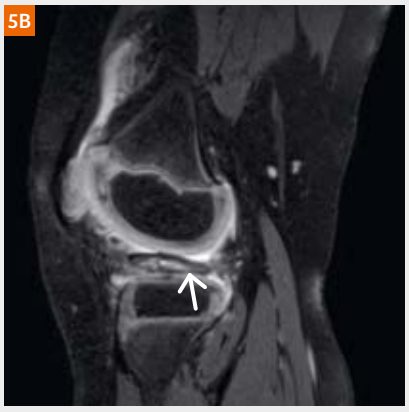

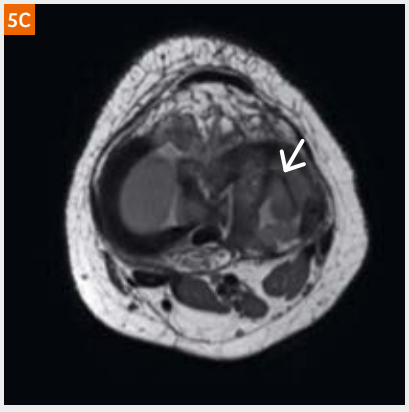

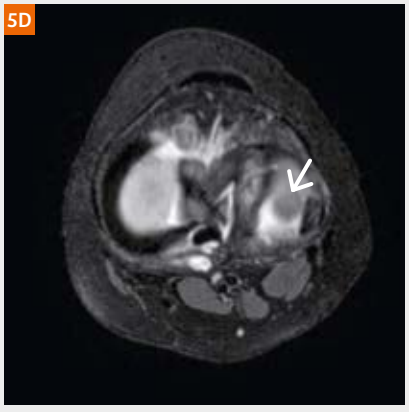

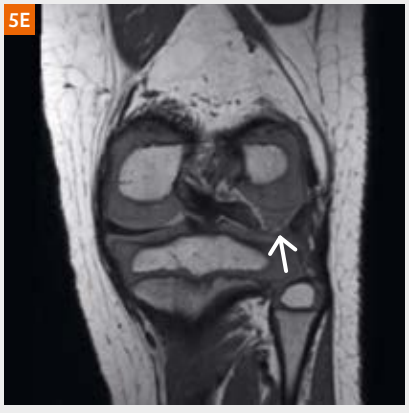

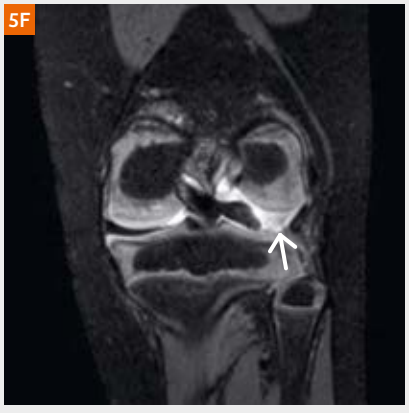

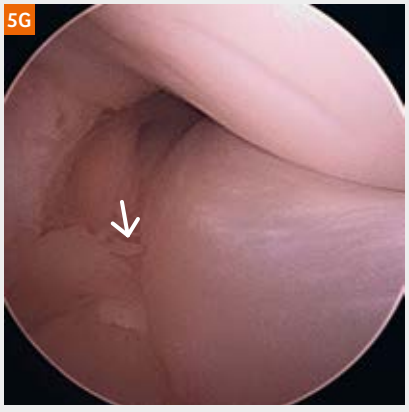

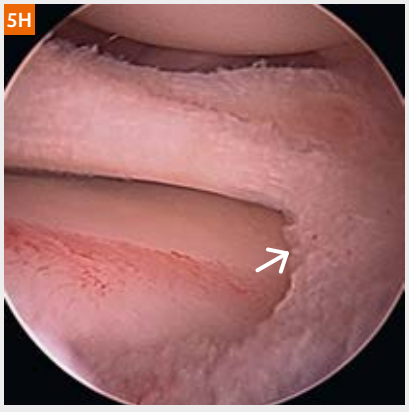

Indication: 4-year-old girl with mild knee pain and locking with motion.

MRI findings: Sagittal, coronal, and axial GOKnee3D images demonstrate a near complete discoid lateral meniscus with a complex tear (arrows). The medial meniscus, anterior and posterior cruciate ligaments, medial and lateral collateral ligaments, and articular cartilage are intact. There is a mild synovitis with small joint effusion.

Arthroscopy findings: Discoid lateral meniscus with a complex tear (arrow, **5G**), which was treated with resection of the tear and saucerization to create the crescent shape of a normal lateral meniscus **(5H).**

Case 3

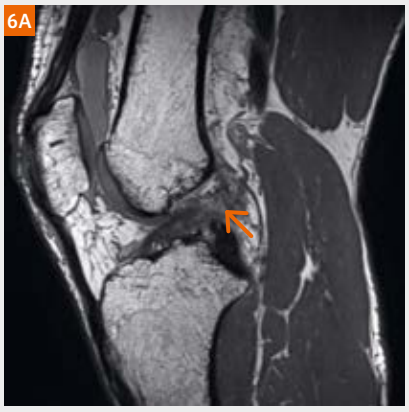

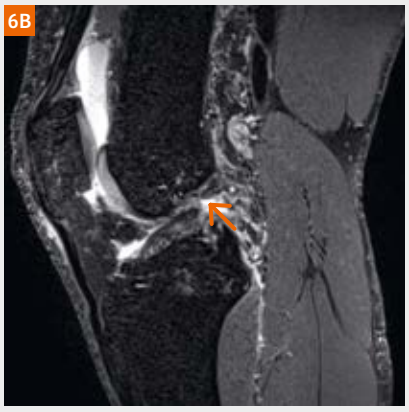

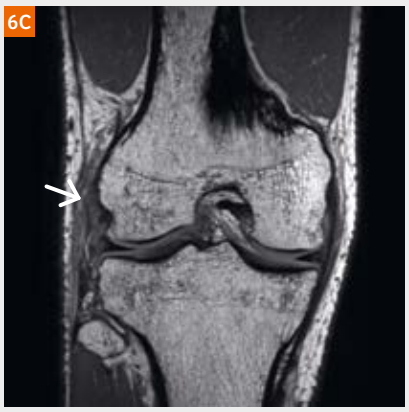

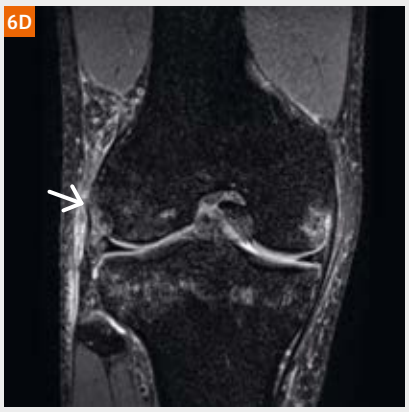

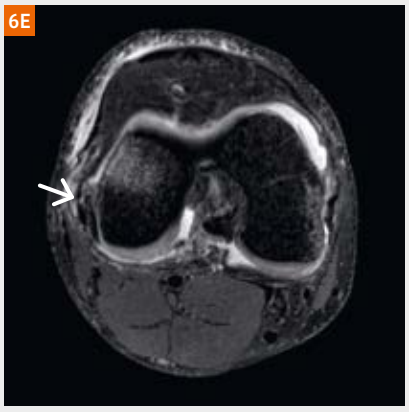

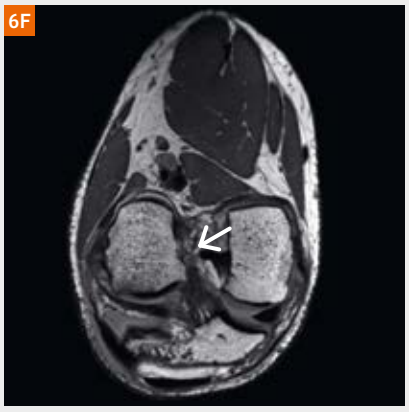

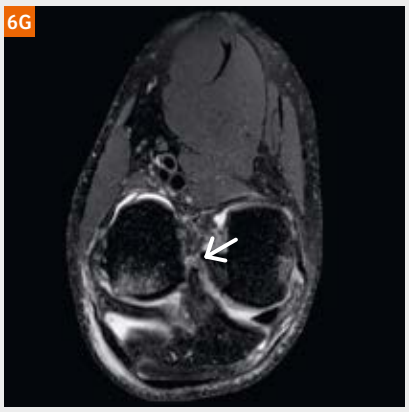

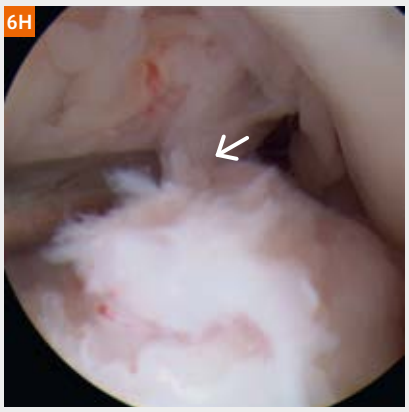

Indication: 30-year-old man with pain, swelling, and instability of the right knee following an American football injury.

MRI findings: Sagittal, coronal, axial and axial oblique GOKnee3D images demonstrate a full-thickness tear of the anterior cruciate ligament near the femoral attachment (arrow, **6A, B, F, G**). Additionally, there is a hemorrhagic joint effusion, a partial thickness tear of the lateral collateral origin (arrow, **6C–E**), and bone contusions of the femur and tibia.

Arthroscopy findings: Full-thickness tear of the anterior cruciate ligament near the femoral attachment (arrow, **6H**).

Case 4

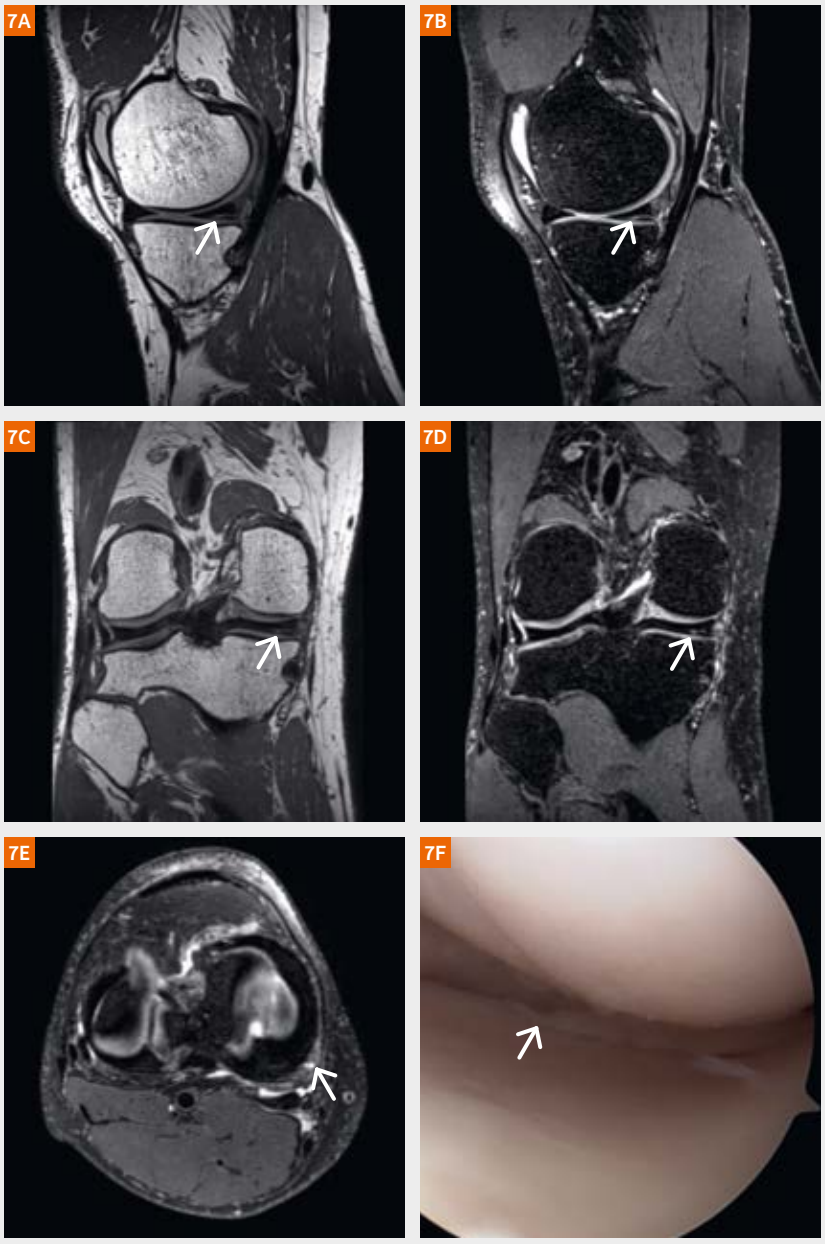

Indication: 52-year-old man with intermittent pain along the medial joint line of the knee.

MRI findings: Sagittal, coronal, and axial intermediate-weighted and T2-SPAIR GOKnee3D images demonstrate a complex, partial depth tear of the peripheral zone 1 of the posterior medial meniscus (arrows, **7A–D**). The meniscal tissue quality appears preserved. Additionally, there are small paramensical cysts at the location of the tear (arrow, **7E**).

Arthroscopy findings: Complex, partial depth tear of the peripheral zone 1 of the posterior medial meniscus (arrow, **7F**).

References

1 Horger W, Kiefer B. Fat suppression techniques – a short overview. MAGNETOM Flash 2011; 46: 56-59.
2 Breuer FA, Blaimer M, Mueller MF, Seiberlich N, Heidemann RM, Griswold M, Jakob PM. Controlled aliasing in volumetric parallel imaging (2D CAIPIRINHA). Mag Reson Med 2006; 55: 549-556.
3 Breuer F, Blaimer M, Griswold M, Jakob P. Controlled aliasing in Parallel Imaging Results IN Higher Acceleration (CAIPIRINHA). MAGNETOM Flash 2012; 49: 135-142.
4 Thawait GK, Lee RJ, Papp DF, Fritz J. High resolution isotropic 3D CAIPIRINHA SPACE MRI of the musculoskeletal system. MAGNETOM Flash 2016; 66: 30-38.
5 Fritz J, Fritz B, Thawait GG, Meyer H, Gilson WD, Raithel E. Three-Dimensional CAIPIRINHA SPACE TSE for 5-Minute High-Resolution MRI of the Knee. Invest Radiol. 2016 Oct;51(10):609-17.
6 Kalia V, Fritz B, Johnson R, Gilson WD, Raithel E, Fritz J. CAIPIRINHA accelerated SPACE enables 10-min isotropic 3D TSE MRI of the ankle for optimized visualization of curved and oblique ligaments and tendons. Eur Radiol. 2017 Sep;27(9):3652-3661.

Case 5

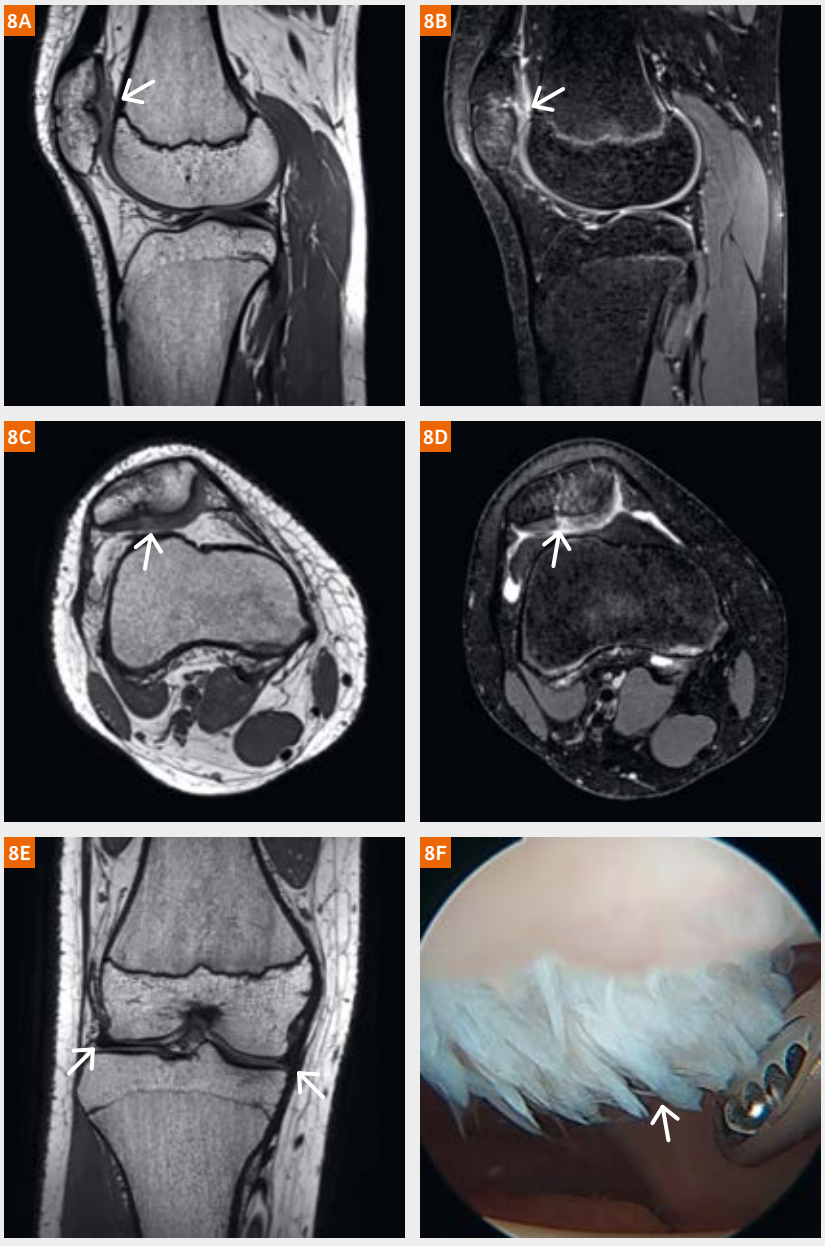

Indication: 14-year-old boy with anterior knee pain.

MRI findings: Sagittal, coronal, and axial oblique GOKnee3D images demonstrate patella alta alignment, hypoplasia of the trochlea, lateral patellar shift, and a full-thickness cartilage defect (arrows, **8A–D**) of the central patella with subcortical cyst formation and a small area of bone marrow edema pattern. There is a small joint effusion. The lateral and medial meniscus (arrows, **8E**) are intact.

Arthroscopy findings: Patellar chondromalacia with full-thickness cartilage defect (arrow, **8F**).

7 Rapalino O, Heberlein K. New strategies for protocol optimization for clinical MRI: Rapid examinations and improved patient care. MAGNETOM Flash 2016; 65: 22-25.
8 Prakkamakul S, Witzel T, Huang S, Boulter D, Borja MJ, Schaefer P, Rosen B, Heberlein K, Ratai E, Gonzalez G, Rapalino O. Ultrafast brain MRI: Clinical deployment and comparison to conventional brain MRI at 3T. J Neuroimaging 2016; 26(5): 503-510.
9 Fagundes J, Longo MG, Huang SY, Rosen BR, Witzel T, Heberlein K, Gonzalez RG, Schaefer P, Rapalino O. Diagnostic performance of a 10-minute gadolinium-enhanced brain MRI protocol compared with the standard clinical protocol for detection of intracranial enhancing lesions. Am J Neuradiol 2017; 38(9): 1689-1694.
10 Del Grande F and Fritz J. GOKnee3D Study. Unpublished data.
11 Fritz J, Ahlawat S, Thawait GK, Raithel E, Gilson W, Lee RJ. 3D MRI of Knee in Pediatric Patients with CAIPIRINHA SPACE: Diagnostic Performance Assessment with Arthroscopic Correlation. 25th ISMRM Annual Scientific Meeting & Exhibition; 2017; Hawaii, USA.

Case 6

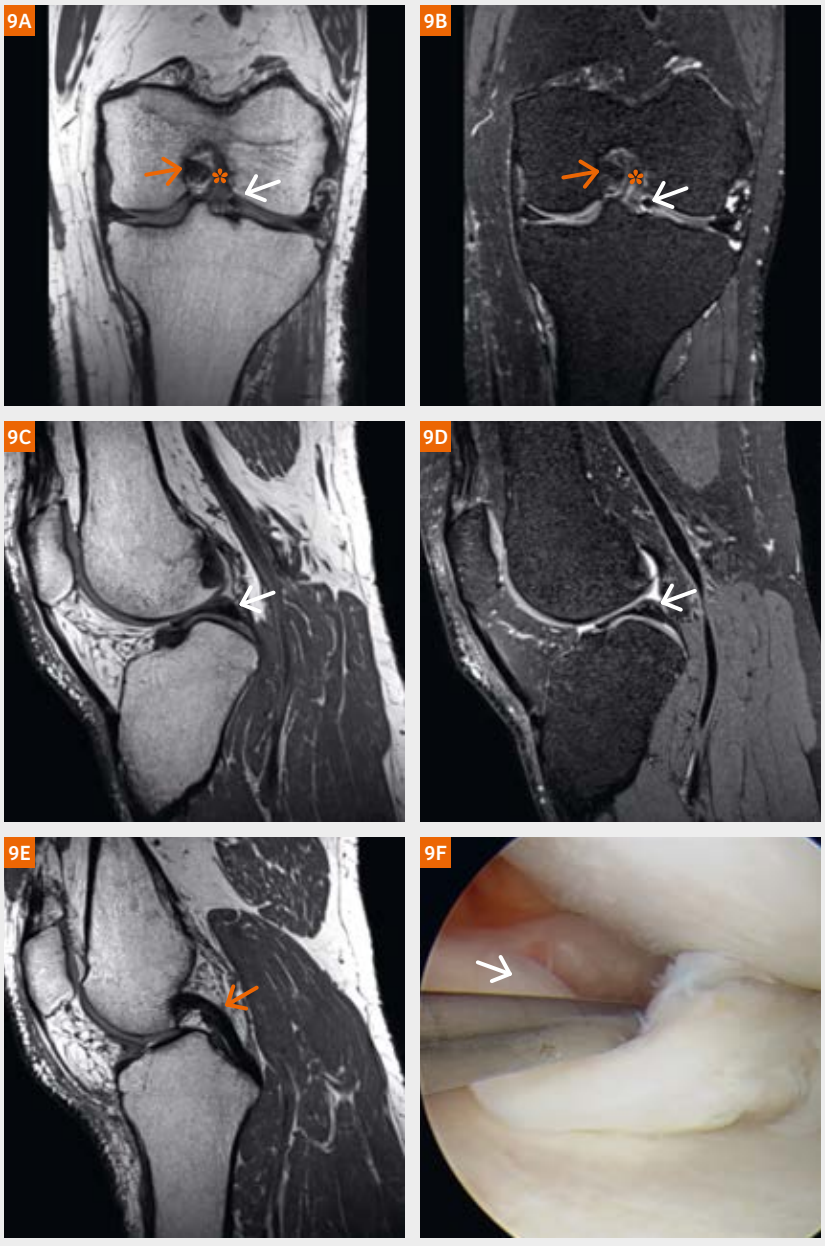

Indication: 51-year-old man with intermittent pain and locking of the left knee.

MRI findings: Sagittal and coronal intermediate-weighted and T2-SPAIR GOKnee3D images demonstrate a bucket handle tear of the lateral meniscus (white arrow, **9A–D**). The anterior cruciate ligament (asterisk, **9A–D**) and the posterior cruciate ligament (orange arrow, **9A** and **9B**) are intact.

Arthroscopy findings: Bucket handle tear of the lateral meniscus (arrow, **9F**).

Contact

Jan Fritz, M.D., P.D., D.A.B.R.
Director of Interventional MR Imaging
Associate Director MSK Fellowship
Assistant Professor of Radiology and Radiological Sciences
Johns Hopkins University School of Medicine
Russell H. Morgan Department of Radiology
and Radiological Science
Musculoskeletal Radiology

601 N. Caroline Street, JHOC 3140A
Baltimore, MD 21287
USA
jfritz9@jhmi.edu

Metal Artifact Reduction Sequence (MARS) Magnetic Resonance Neurography (MRN) Evaluation of the Lumbosacral Plexus in Patients with Metallic Implants

Shivani Ahlawat, M.D.; Jan Fritz, M.D., P.D., D.A.B.R.

Johns Hopkins University School of Medicine, Baltimore, MD, USA

Abstract

Magnetic resonance neurography (MRN) is a reliable and accurate modality in the assessment of patients with peripheral neuropathy, which can be useful for distinguishing intrinsic and extrinsic etiologies of neuropathy following surgery. However, MRN surrounding metal implants[1] can be challenging to both perform and interpret. The diagnosis of abnormal peripheral nerves often heavily relies on fluid sensitive MR pulse sequences, but the presence of metal in the field of view introduces image artifacts, distortion and interferes with fat suppression. Conventional turbo spin echo pulse sequences with optimization for metal artifact reduction[1] are best suited for nerve imaging as advanced multi-spectral, and multi-spatial pulse sequences introduce a degree of blur that obscure nerve details. As such, metal artifact reduction sequence (MARS) techniques[1] can be applied to improve the image quality of MRN in patients with pelvic metallic implants, when compared with standard fast spin echo sequences. We describe a high-resolution MARS MRN protocol that yields high image quality and validated diagnostic accuracy for the assessment of lumbosacral neuropathies in patients with metallic implants of the pelvis and hips.

	Intermediate-weighted Turbo Spin Echo	STIR Turbo Spin Echo
Orientation	transversal	transversal
Repetition time [ms]	5700	3660
Time to echo [ms]	38	6.9
Inversion time [ms]	-	150
Echo train length	16	16
Slice thickness/gap [mm]	4.5/0.45	5/0.5
Pixel size [mm^2]	0.5 x 0.5	0.7 x 0.7
Bandwidth [Hz/px]	560	545
Flip angle [degree]	150	130
Number of slices	2 x 35	2 x 27
Number of excitations	1.5	2
In-plane frequency encoding direction	Right to left	Right to left
Total acquisition time [min:sec]	8:42	13:36

Table 1:
Detailed MARS MR imaging protocol optimized for the evaluation of lumbosacral plexus and pelvic nerves in patients with metallic implants[1].

Introduction

Traumatic nerve palsy in the setting of previous pelvic instrumentation and hip arthroplasty is a rare but serious complication [1–9]. Diverse mechanisms of peripheral nerve injury have been described including lesions intrinsic and extrinsic to the affected peripheral nerve. Intrinsic causes of peripheral neuropathy in the postoperative setting include stretch injury, nerve lacerations, and vascular compromise. Extrinsic causes of peripheral neuropathy in the postoperative setting include mass effect by implant components, heterotopic ossification, fluid collections such as hematoma, distended peri-articular bursae, and abscesses, and adverse local tissue reactions. The current standard of care for the detection and characterization of peripheral neuropathy is clinical examination and electrodiagnostic testing. However, evaluation of sensory and deep intra-pelvic nerves can be challenging, representing a gap in the clinical management of patients with a pelvic peripheral nerve injury in the post-operative setting.

[1] The MRI restrictions (if any) of the metal implant must be considered prior to patient undergoing MRI exam. MR imaging of patients with metallic implants brings specific risks. However, certain implants are approved by the governing regulatory bodies to be MR conditionally safe. For such implants, the previously mentioned warning may not be applicable. Please contact the implant manufacturer for the specific conditional information. The conditions for MR safety are the responsibility of the implant manufacturer, not of Siemens.

Magnetic resonance neurography (MRN) is a reliable and accurate modality for the assessment of patients with peripheral neuropathy that can be useful for identifying intrinsic or extrinsic etiologies of neuropathy. However, the presence of metal in the field-of-view generates local magnetic field heterogeneity and results in image artifacts including signal voids, failure of fat suppression, and spatial misregistration [10]. As such, MR imaging surrounding metal implants, including arthroplasty and osteosynthesis implants, can be challenging to interpret [10]. Metal artifact reduction strategies include the use of lower magnetic field strength, such as 1.5 instead of 3 Tesla, turbo spin echo (TSE) rather than gradient echo based sequences, high receiver bandwidth, and inversion recovery rather than frequency-selective fat suppression [10–19]. The application of such metal artifact reduction sequence (MARS) techniques results in substantially improved image quality when compared with standard TSE pulse sequences [12].

TSE pulse sequences with optimization for metal artifact reduction are ideal for peripheral nerve imaging as advanced multi-spectral and multi-spatial pulse sequences, such as Multi-acquisition Variable-resonance Image Combination (MAVRIC, GE Healthcare, Wauwatosa, WI, USA) and Slice Encoding for Metal Artifact Correction (SEMAC) introduce a degree of blurring that can obscure the fine architecture of peripheral nerves [12, 1]. We describe a validated, high-resolution MARS MRN protocol that yields high image quality and accuracy for the diagnosis of lumbosacral neuropathies in patients with metallic implants of the pelvis and hips [20].

MARS MRN acquisition

At our institution, we perform MARS MRN of the lumbosacral plexus for the evaluation of patients with metallic implants on a 1.5 Tesla MR imaging system (MAGNETOM Aera, Siemens Healthcare, Erlangen, Germany) with 48 radio-frequency receive channels, 45 mT/m maximum gradient field amplitude and 200 T/m/s slew rate [20]. Patients are positioned supine, and imaging is acquired using two 18-channel receive-only body matrix surface coils (Siemens Healthcare) and 12 elements of a spine matrix coil in 'sandwich configuration' to cover the lower lumbar spine, pelvis and proximal thighs. Table 1 describes the imaging protocol in detail (Fig. 1). The short tau inversion recovery (STIR)

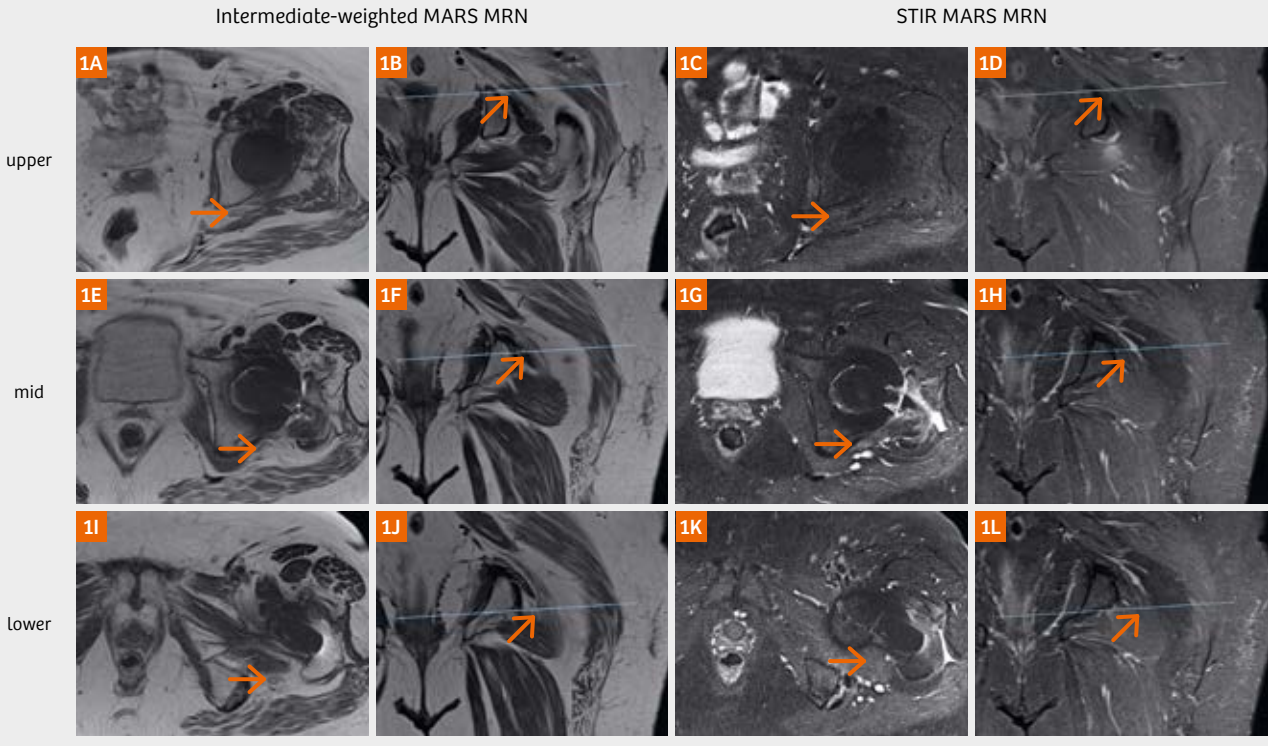

Figure 1:
Metal Artifact Reduction Magnetic Resonance Neurography in a patient with left hip arthroplasty implants demonstrates a normal appearing sciatic nerve (arrows) at the upper, mid and lower levels (reference lines) of the hip replacement without obscuration by implant-induced artifacts and with solid fat suppression.

TSE pulse sequence employs a radio-frequency pulse that matches the high receiver bandwidth [16]. Because the field-of-view extends from the L5 vertebral body to the ischial tuberosity, contiguous stacks of axial intermediate-weighted and STIR TSE pulse sequences are obtained. Intravenous contrast material administration is typically not required. The total acquisition time of the axial pulse sequences of this particular MARS MRN protocol is approximately 25 minutes, predominantly due to the long acquisition time necessary for high-quality STIR images. Optional coronal or sagittal pulse sequences can be helpful to identify landmarks for surgical interventions. The length of this protocol may be difficult to tolerate for acutely ill patients, but is similar to other investigations [14, 15, 20].

MARS MRN Interpretation

There is a paucity of literature of MRN in the setting of metal implants [19–21]. Our validated MARS MRN protocol offers high diagnostic quality, inter-rater agreement and overall high diagnostic accuracy for the presence of MR features of neuropathy [20]. With this MARS MRN protocol, both primary and secondary features of peripheral neuropathy can be visualized at the level of many metallic implants.

Primary features of peripheral neuropathy include abnormal course, caliber, signal intensity, and architecture (Fig. 2). Secondary features of peripheral neuropathy include skeletal muscle denervation. Of note, elevated

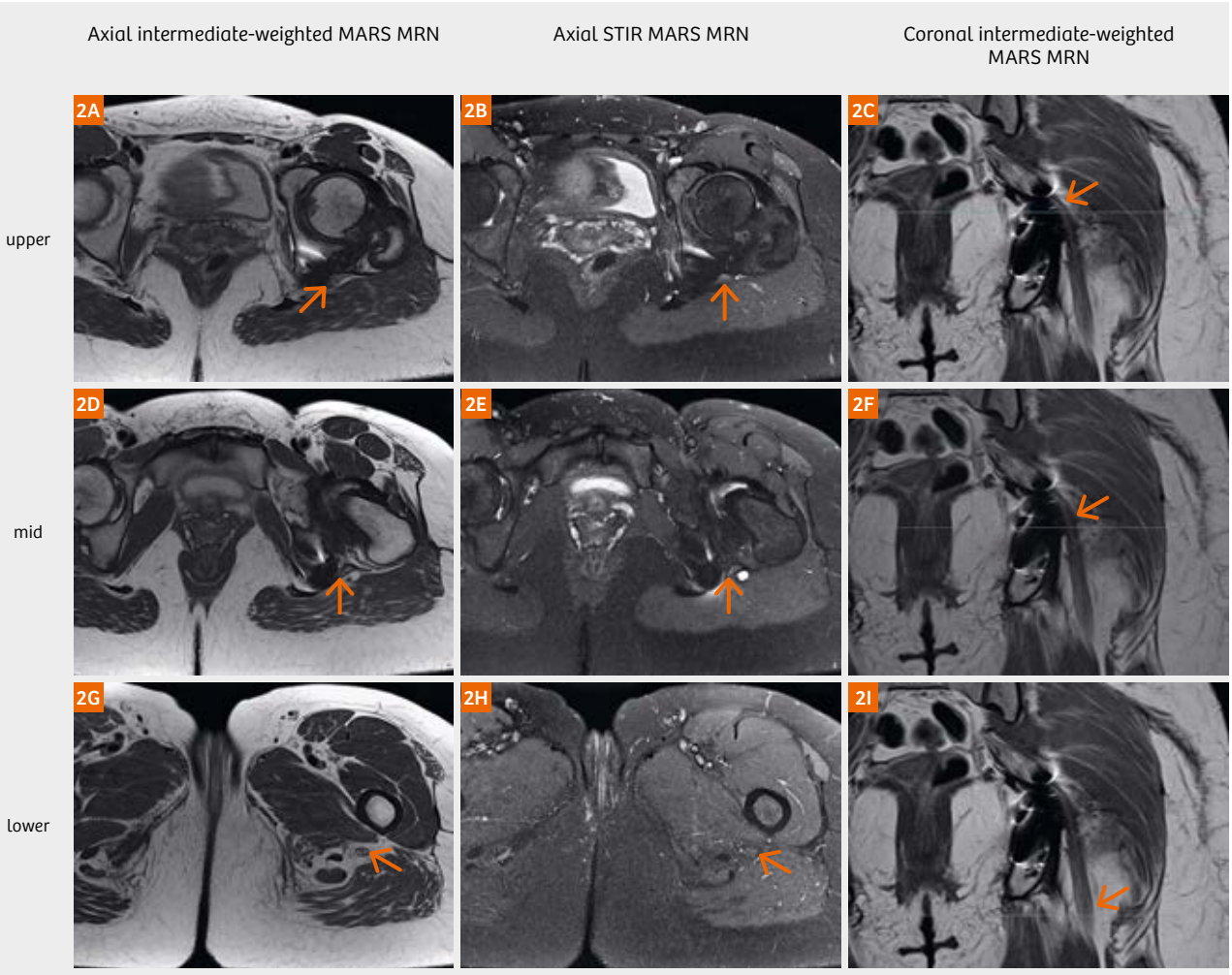

Figure 2:
Metal Artifact Reduction Magnetic Resonance Neurography in a patient with prior pelvic osteosynthesis and metallic implants of the left posterior acetabulum and ischium demonstrates unilateral, abnormal signal hyperintensity of the left sciatic nerve (arrow, **2A–C**), indicating neuropathy. At the mid level, there is unilateral left perineural scarring and tethering of the sciatic nerve (arrows, **2D–F**) to the metallic implants, as well as abnormal signal hyperintensity of the nerve. At the lower level, below of the site of surgical instrumentation, the sciatic nerve (arrow, **2G–I**) is normal in morphology and signal intensity.

peripheral nerve signal on fluid sensitive sequences alone is common, but not necessarily a reliable finding, that can result in high sensitivity but low specificity, when used in isolation, [22, 23]. The presence of additional imaging features such as abnormal nerve caliber including flattening and enlargement can add specificity [23]. Bulbous enlargement and architectural distortion in otherwise longitudinally intact nerves may suggest the presence of a traumatic neuroma-in-continuity [9]. Lastly, nerve discontinuity can serve as a marker for a high-grade peripheral nerve injury or nerve laceration, which are rare causes of neuropathy in the postoperative setting [9].

Concerning secondary features of peripheral neuropathy, MARS MRN can detect and characterize the extent of skeletal muscle denervation, if the muscles of interest are included, which may require adding additional stacks of images. MRN features of skeletal muscle denervation include intramuscular edema-like signal, fatty replacement, and loss of muscle bulk. Skeletal muscle atrophy and fatty replacement have been described in patients following hip arthroplasty and can be present in asymptomatic patients [21]. Hence, it is important to interpret MARS MRN in the individual clinical context rather than in isolation.

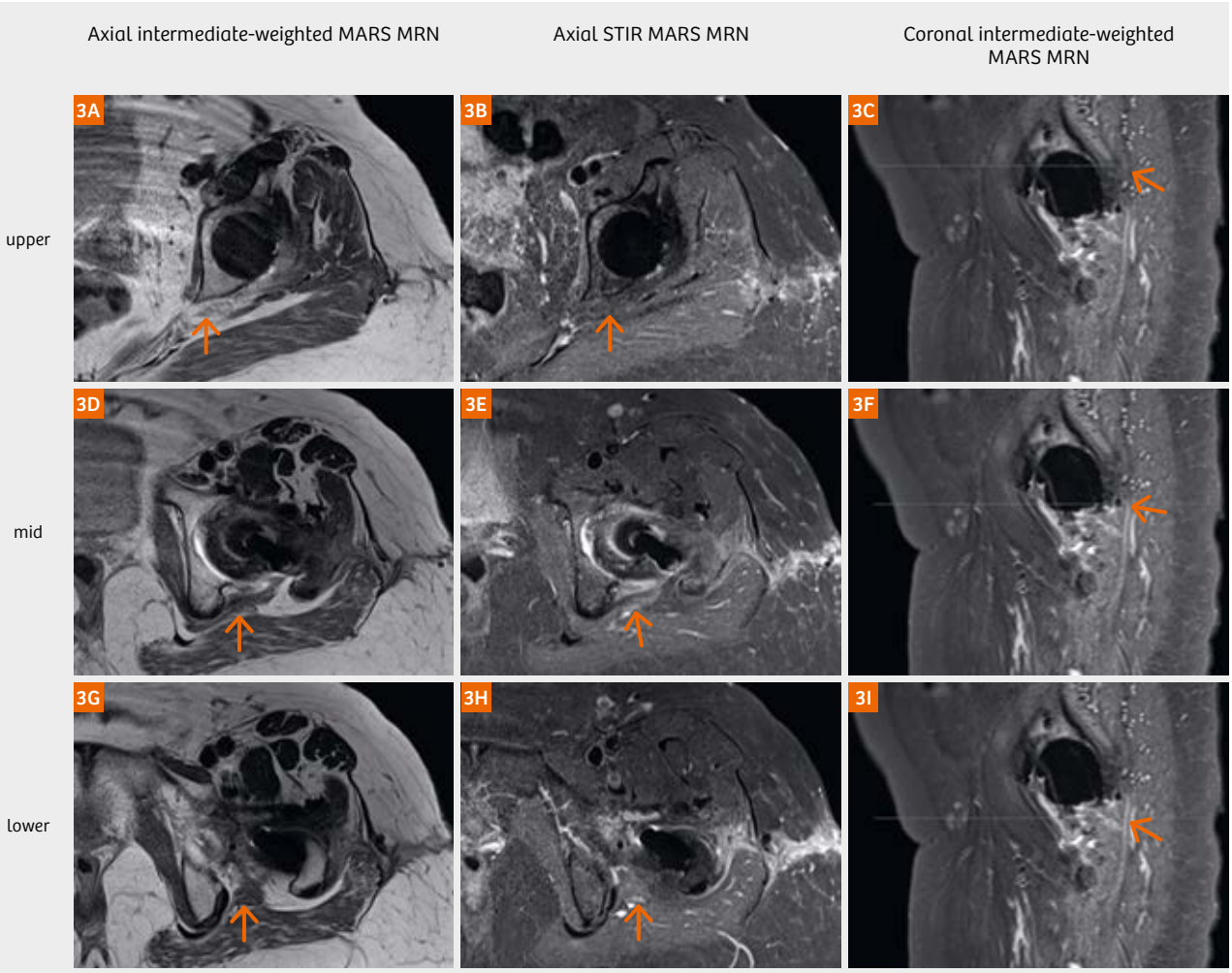

Figure 3:
Metal Artifact Reduction Magnetic Resonance Neurography in a patient with new-onset foot extension and flexion weakness following recent left hip arthroplasty demonstrates normal morphology and signal hyperintensity of the left sciatic nerve (arrow, **3A–C**) at the upper level. At the mid level, there is abnormal signal hyperintensity of the sciatic nerve (arrows, **3D–F**) in the subgluteal space. At the lower level, there is perineural scarring of the sciatic nerve and abnormal signal intensity of the sciatic nerve (arrow, **3G–I**), indicative of neuropathy.

Lastly, MARS MRN also demonstrates the soft tissues surrounding the pelvic nerves, including perineural fibrosis (Fig. 3), collections causing course deviations and mass effect, which can provide added value to electrodiagnostic testing and the clinical management of these patients.

Conclusion

MARS MRN provides high image quality of the pelvic peripheral nerves and lumbosacral plexus with validated accuracy for the diagnosis of lumbosacral plexopathy in patients with metallic pelvic implants.

References

1 Burge AJ, Gold SL, Kuong S, Potter HG. High-resolution magnetic resonance imaging of the lower extremity nerves. Neuroimaging Clin N Am. 2014;24(1):151-70.
2 Brown GD, Swanson EA, Nercessian OA. Neurologic injuries after total hip arthroplasty. Am J Orthop 2008;374:191-197.
3 Farrell CM, Springer BD, Haidukewych Gj, Morrey BF Motor nerve palsy following primary total hip arthroplasty. J Bone Joint Surg Am 2005; 87(12):2619-2625.
4 Navarro RA, Schmalzried TO, Amstutz HC, Dorey FJ Surgical approach and nerve palsy in total hip arthroplasty. J Arthroplasty 1995; 10:1-5.
5 Zappe B, Glauser PM, Majewski M, Stöckli HR, Ochsner PE. Long-term prognosis of nerve palsy after total hip arthroplasty: results of two-year-follow-ups and long-term results after a mean time of 8 years. Arch Orthop Trauma Surg. 2014;134:1477-82.
6 Schmalzried TP, Amstutz HC, Dorey FJ. Nerve palsy associated with total hip replacement. Risk factors and prognosis. J Bone Joint Surg Am. 1991;73:1074-80.
7 Melamed NB, Satya-Murti. S. Obturator neuropathy after total hip replacement. Ann Neurol. 1983;13:578-9.
8 Weber ER, Daube JR, Coventry MF. Peripheral neuropathies associated with total hip arthroplasty. J Bone Joint Surg [Am] 1976;58:66-69.
9 BN Edwards, Tullos HS, Noble PC. Contributory factors and etiology of sciatic nerve palsy in total hip arthroplasty. Clin Orthop 1987; 218:136.
10 Fritz J, Lurie B, Miller TT, Potter HG. MR Imaging of Hip Arthroplasty Implants. Radiographics. 2014; 34(4): E106-132.
11 Potter HG, Nestor BJ, Sofka CM, Ho ST, Peters LE, Salvati EA. Magnetic resonance imaging after total hip arthroplasty: evaluation of periprosthetic soft tissue. J Bone Joint Surg Am; 2004(86):1947–1954.
12 Hayter CL, Koff MF, Shah P, Koch KM, Miller TT, Potter HG. MRI after arthroplasty: comparison of MAVRIC and conventional fast spin-echo techniques. AJR Am J Roentgenol 2011;197: W405–W411.
13 Hayter CL, Koff MF, Potter HG. Magnetic resonance imaging of the postoperative hip. J Magn Reson Imaging 2012;35:1013–1025
14 Fritz J, Ahlawat S, Demehri S, Thawait GK, Raithel E, Gilson WD, Nittka M.Compressed Sensing SEMAC: 8-fold Accelerated High Resolution Metal Artifact Reduction MRI of Cobalt-Chromium Knee Arthroplasty Implants. Invest Radiol. 2016;51(10):666-76.
15 Fritz J, Fritz B, Thawait GK, Raithel E, Gilson WD, Nittka M, Mont MA. Advanced metal artifact reduction MRI of metal-on-metal hip resurfacing arthroplasty implants: compressed sensing acceleration enables the time-neutral use of SEMAC. Skeletal Radiol. 2016 Oct;45(10):1345-56.
16 Ulbrich EJ, Sutter R, Aguiar RF, Nittka M, Pfirrmann CW. STIR sequence with increased receiver bandwidth of the inversion pulse for reduction of metallic artifacts. AJR Am J Roentgenol. 2012 Dec;199(6):W735-42.
17 Sutter R, Ulbrich EJ, Jellus V, Nittka M, Pfirrmann CW. Reduction of metal artifacts in patients with total hip arthroplasty with slice-encoding metal artifact correction and view-angle tilting MR imaging. Radiology 2012;265:204–214.
18 Muller GM, Lundin B, von Schewelov T, Muller MF, Ekberg O, Mansson S. Evaluation of metal artifacts in clinical MR images of patients with total hip arthroplasty using different metal artifact reducing sequences. Skeletal Radiol. 2015:44:353-09.
19 Wolf M, Bäumer P, Pedro M, Dombert T, Staub F, et al. Sciatic Nerve Injury Related to Hip Replacement Surgery: Imaging Detection by MR Neurography Despite Susceptibility Artifacts. PLoS ONE 2014;92: e89154.
20 Ahlawat S, Stern SE, Belzberg AJ, Fritz J. High-resolution metal artifact reduction MR imaging of the lumbosacral plexus in patients with metallic implants. Skeletal Radiol. 2017 Jul;46(7):897-908.
21 Pfirrmann CW, Notzli HP, Dora C, Hodler J, Zanetti M. Abductor tendons and muscles assessed at MR imaging after total hip arthroplasty in asymptomatic and symptomatic patients. Radiology 2005;235:969–976.
22 Chhabra A, Chalian M, Soldatos T, Andreisek G, Faridian-Aragh N, Williams E, Belzberg AJ, Carrino JA. 3-T high-resolution MR neurography of sciatic neuropathy. AJR Am J Roentgenol. 2012;1984:W357-64.
23 Kwee RM, Chhabra A, Wang KC, Marker DR, Carrino JA. Accuracy of MRI in diagnosing peripheral nerve disease: a systematic review of the literature. AJR Am J Roentgenol. 2014;203:1303-9.
24 Ahlawat S, Belzberg AJ, Montgomery EA, Fayad LM. MRI features of peripheral traumatic neuromas. Eur Radiol. 2016;26:1204-12.

Contact

Shivani Ahlawat, M.D.
Director MSK Fellowship
Assistant Professor of Radiology and Radiological Sciences
Johns Hopkins University School of Medicine
Russell H. Morgan Department of Radiology and Radiological Science
Musculoskeletal Radiology
601 N. Caroline Street
Baltimore, MD 21287, USA
sahlawa1@jhmi.edu

Jan Fritz, M.D., P.D., D.A.B.R.
Director of Interventional MR Imaging
Associate Director MSK Fellowship
Assistant Professor of Radiology and Radiological Sciences
Johns Hopkins University School of Medicine
Russell H. Morgan Department of Radiology and Radiological Science
Musculoskeletal Radiology
601 N. Caroline Street, JHOC 3140A
Baltimore, MD 21287, USA
jfritz9@jhmi.edu

Thoracic Outlet Syndrome on Tim 4G Systems

Bac Nguyen, BSc, RT (R) (MR)

Oslo University Hospital, Rikshospitalet, Oslo, Norway

Introduction

Thoracic outlet syndrome (TOS) is a condition in which nerves, arteries or veins are compressed. This can lead to pain, weakness, and occasionally loss of muscle at the base of the thumb. Further symptoms may include coldness and paleness of the arm. TOS can result from trauma, repetitive arm movements, tumors or just abnormal anatomy [1].

At our institution, we rarely use MRI in cases of TOS; these patients are typically imaged with CT. However, occationally, these cases are referred to MRI and I would like to share my experience of how such scans can be performed easily, efficiently, and accurately on Tim 4G systems (3T MAGNETOM Skyra, 1.5T MAGNETOM Aera etc.).

Equipment and positioning

Perform this exam in the feet-first supine position. Remember to position the patient's feet as far as possible toward the head end of the table. This is due to the spine coil elements on the table that we want to use in combination with one Body Matrix coil.

This exam is divided in two parts: Part 1 with the patient's arms by their side. In part 2, the patient's arms are raised above the head.

Part 1: Arms by the patient's side
Position the patient's arms by their side using pads underneath the elbows and hands with a pillow under the legs for comfort and a small pillow under the head (Fig. 1). Avoid using a large pillow as we want the neck region to be as close to the table as possible for optimal signal contribution from the spine coil elements in this area. If a patient is lying comfortably, they are more likely to remain still, thus increasing the likelihood of a successful exam.

Part 2: Arms above the patient's head
Position the patient's arms raised above their head with a pillow for support, a small pillow under the head, and a pillow under the legs (Fig. 2).

Sequence and contrast timing

Sequence
We use a 3D FLASH sequence for contrast-enhanced MRA (Table 1). Extracellular contrast agent (0.5 mmol/ml) is administered in two doses (0.2 mL/kg x 2): one dose for each part of the exam.

Contrast timing
Test bolus timing was used in this case. CARE Bolus technique could, however, also be used but will not be explained in detail here. We begin part 1 of the exam

Figure 1:
Patient positioning for part 1 of the exam with the patient's arms by their side.

Figure 2:
Patient positioning for part 2 of the exam with the patient's arms above the head.

3D FLASH CE MRA	
Orientation	Coronal
Phase enc. dir.	R-L
Phase oversampling	21%
Slice oversampling	7.1%
Slice per slab	112
TR	3.07 ms
TE	1.05 ms
Averages	1
Flip angle	30 deg
FOV read	380 mm
FOV phase	100%
Slice thickness	1.19 mm
Base resolution (matrix)	320
Phase resolution	75%
Slice resolution	62%
Phase partial Fourier	6/8.
Slice partial Fourier	6/8.
PAT mode	GRAPPA
Accel. Factor PE	3
Ref. lines PE	24
Accel. Factor 3D	1
Bandwidth	450 Hz/Px

Table 1: 3D FLASH CE MRA parameters for 1.5T MAGNETOM Aera.

3

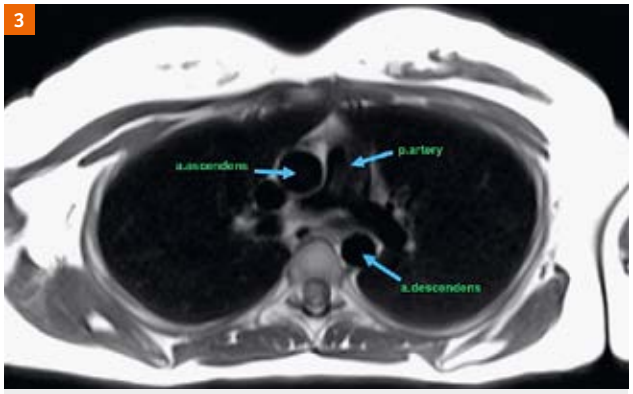

Figure 3: Area of test bolus

with the patient's arms by their side. Prior to the test bolus, a 3D pre-contrast measurement is performed. We then position the test bolus slice transversal to the area in which the aorta ascendens/descendens and the pulmonary arteries are visible (Fig. 3).

In the first test bolus, 1 mL of contrast agent is administered. We use an Excel™ sheet to record information to calculate the delay and optimal flow rate (Fig. 4). This method is simple as long as the right values are entered into the white fields. Optimal bolus length is half the scan time, whereas flow rate is controlled by the contrast dosage / optimal bolus length. The value for time to center of the CE MRA can be found in the Angio-Common tab card. Circulation time is the value derived from the test bolus when the contrast reaches a peak signal intensity in the area of interest, i.e. aorta ascendens (Fig. 5). When all the values are entered, you can calculate the delay. The delay is calculated using the following equation:

Delay = circulation time
+ 50% injection time
- time to center

This may seem very advanced; however, in our daily practice we set only the white field values to find the optimal flow rate and perform a test bolus to determine the delay. Other color areas in the sheet are locked so that no one can change the equation. This method is both fast and robust as there is no need to remember the equation. Any radiographer can use this sheet with ease without needing to know the background to the equation.

The scan and test bolus injection are started simultaneously while the patient is breathing normally. When the contrast arrives at the area of interest, the scan can be halted. Go to the Patient Browser, select the test bolus measurement, and load it into Mean Curve. Position the ROI in the area of interest and calculate. The test bolus slices are acquired at 1 image per second, which means

4

Scan time (s)	Contrast dosage (mL)	Optimal bolus length (s)	Flow (ml/s)
17	13.5	8.5	1.6

Time to center	Circulation time (s)	Injection time (s)
7.6	23	8.5

Delay (s)	19.7	Delay = circulation time + 50% injection time - time to center

Figure 4:
Extract from Excel™ sheet recording values used to calculate the delay and optimal flow rate for the given exam.
This sheet was created by Rolf Svendsmark.

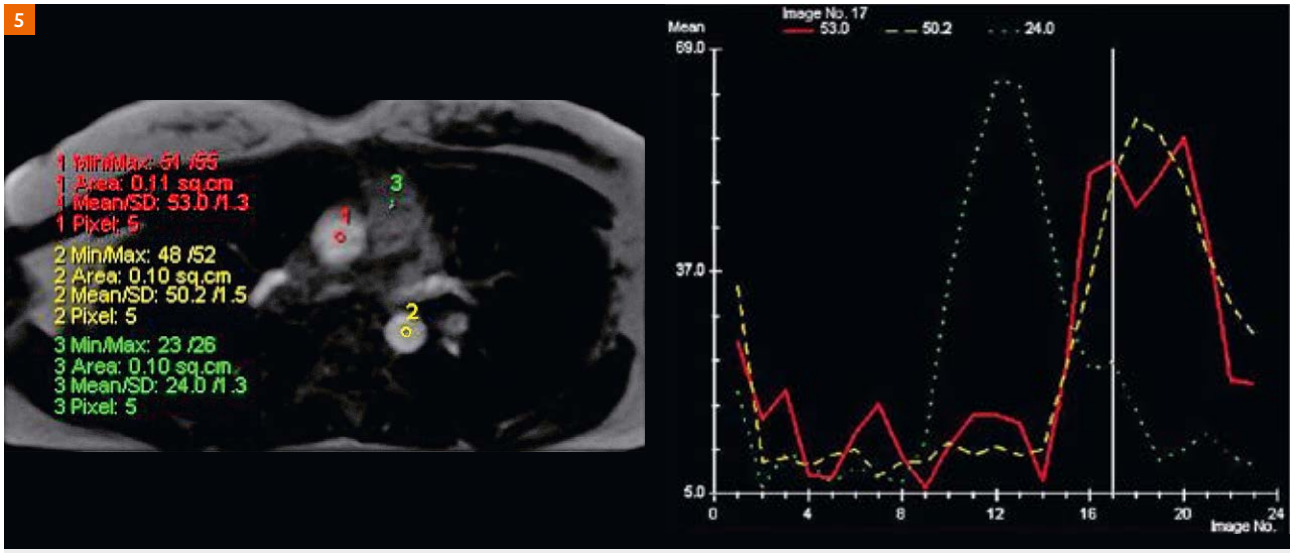

Figure 5: Signal intensity at the ROI (aorta ascendens)

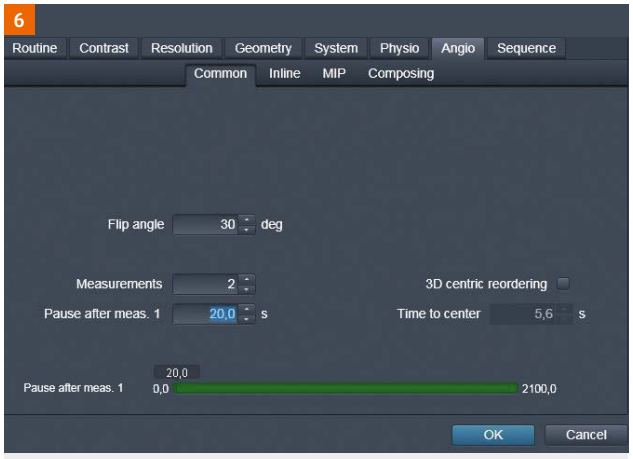

Figure 6:
Two measurements are configured with a 20-second break after the first scan.

Figure 7:
Delay configured directly on the injector for the first measurement using the value from the Excel™ sheet (Delay: Scan).

that peak signal intensity in the aorta ascendens occurs at image 17 in this case. In other words, circulation time is 17 seconds. This is why it is important to start the scan and the test bolus measurement at the same time.

Once we have calculated the delay, we can continue with the post-contrast measurement. We simply acquire two measurements with a 20-second break in between (Fig. 6). We enter the first delay value from the Excel™ sheet into the injector (Bayer, Medrad® Spectris Solaris®) (Fig. 7). This is then followed by the second delay lasting 20 seconds, which we configure in the measurement sequence. When there are approximately 6–7 seconds left before the second measurement starts, we instruct the patient to hold their breath.

When the CE MRA is finished, we reposition the patient's arms for part 2. The patient is asked to lie still while we remove the body coil, position the arms above the head, and reposition the body coil. Apart from this, there is no need to move the patient. A new fast localizer is performed for part 2 of the exam.

Part 2 starts with a pre-contrast measurement as in part 1 followed again by a 1 mL test bolus to determine the delay when the patient's arms are raised. In theory, there is no need for a further test bolus if we assume the delay will be the same. However, this may not always be the case – in this patient, when arms were by the side, circulation time was 17 seconds, whereas circulation time with the arms above the head was 15 seconds (Fig. 9). It is not easy

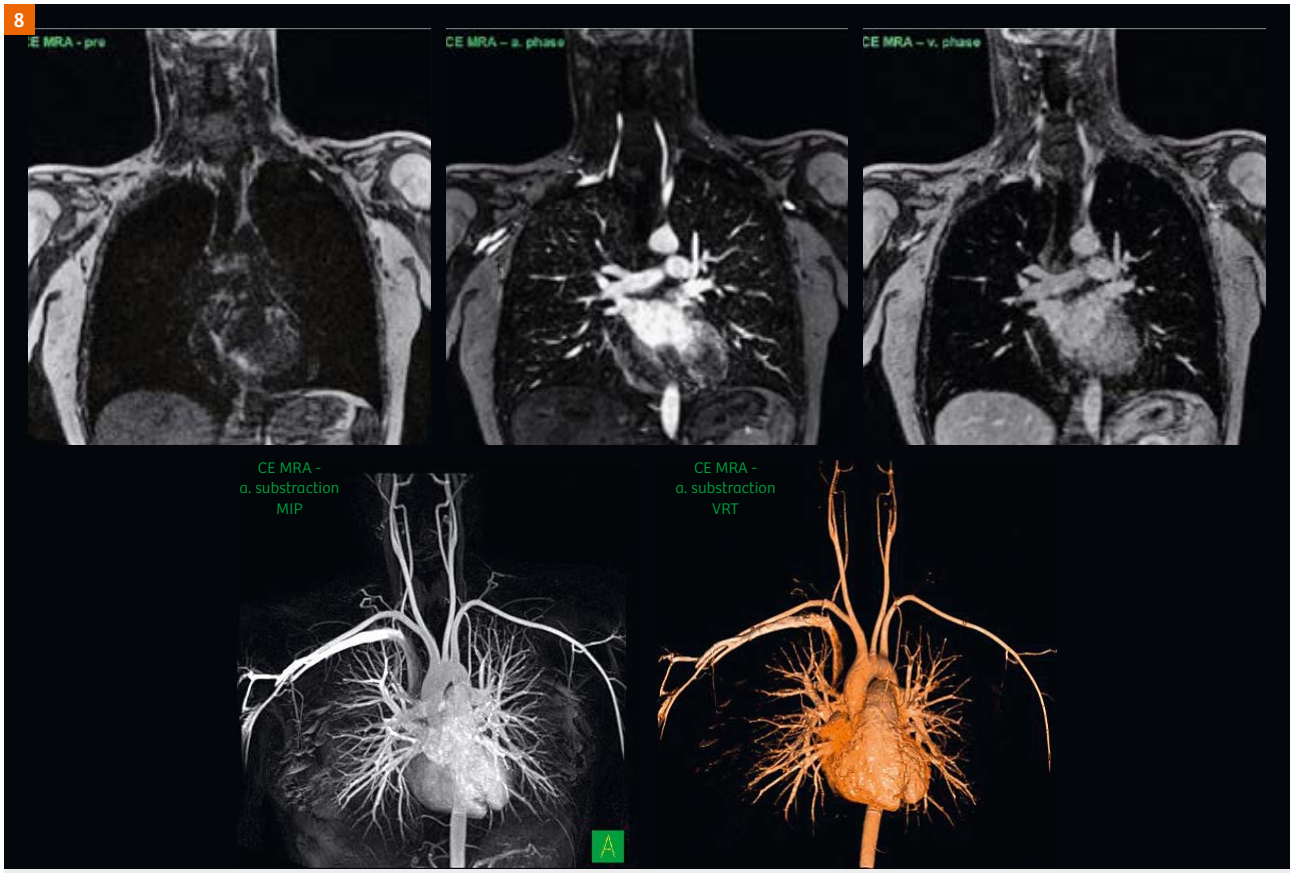

Figure 8:
Part 1 scan images along with postprocessing of MIP and VRT.
Notice the high signal intensity of the carotids, using only spine coil elements.

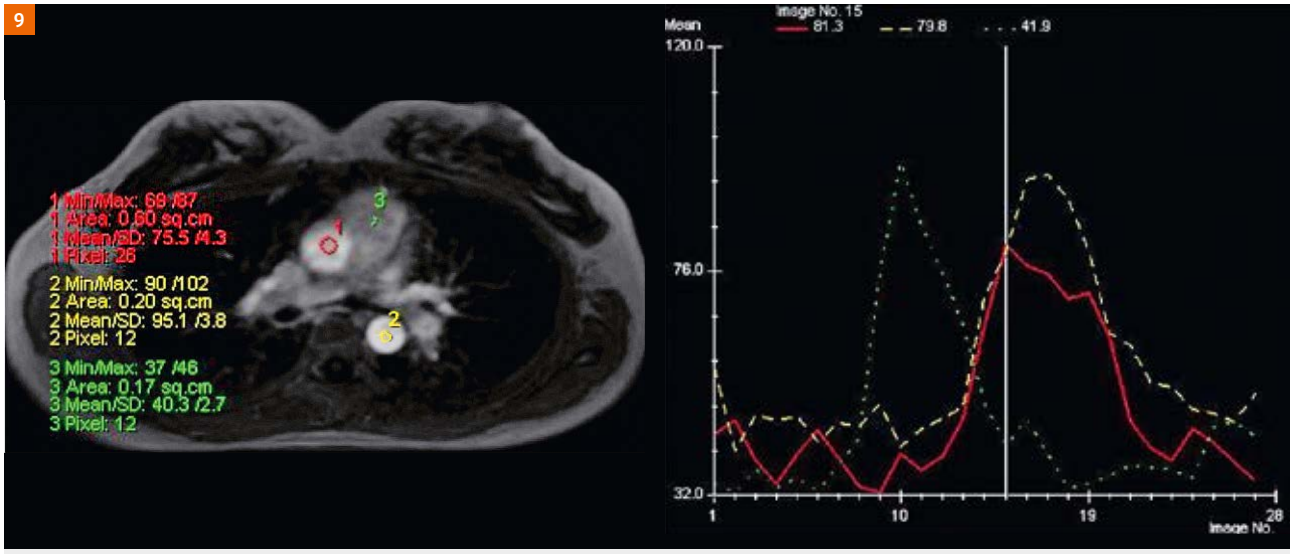

Figure 9: Part 2 shows a 15-second delay with the patient's arms above the head compared with a 17-second delay with the patient's arms by the side.

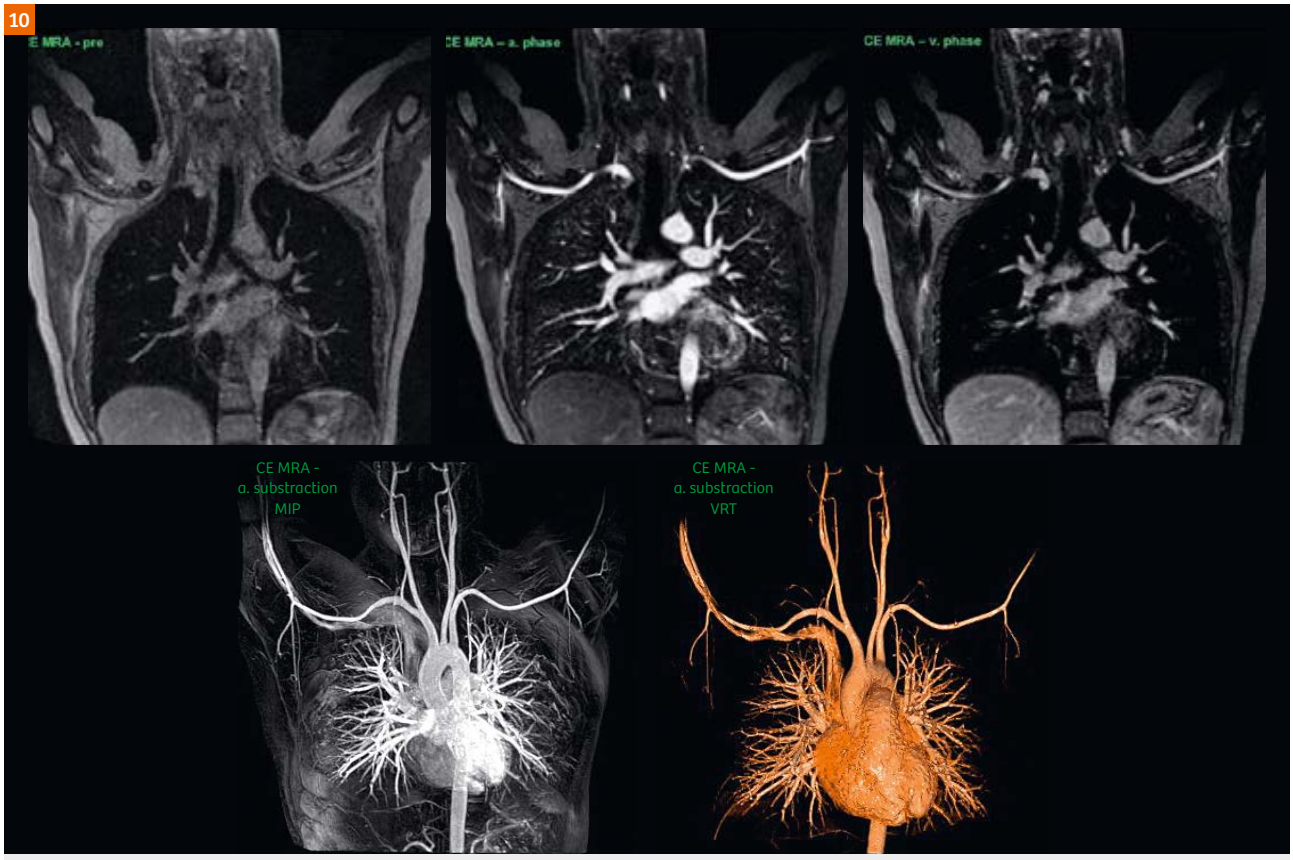

Figure 10:
Part 2 scan images along with postprocessing of MIP and VRT.
Note the remarkable signal intensity of the carotids, using only spine coil elements.

to explain why the delays were different as a number of factors may be involved. While two seconds may not seem significant, this can affect the results of the arterial phase. As such, you might consider to run a second test bolus.

Conclusion

The intent of this article was to show how easy it is to perform examinations with arms by the patient's side and above the head. If you have good CE MRA protocols and good routines for successful CE MRA exams, then I advise you not to change anything. Just keep in mind these tips on hardware and notes on how to position the patient optimally. One last take-home message on our technique of choice, TWIST. This time-resolved technique requires no timing and enables high temporal resolution. Make sure that the first measurement is without contrast for subtraction purposes.

Acknowledgments

I would like to thank my good friend and MR mentor Rolf Svendsmark, my colleague Line Espe who always helps me out, along with the rest of my team at Rikshospitalet.

References/ further reading

1 Wikipedia: https://en.wikipedia.org/wiki/Thoracic_outlet_syndrome.
2 Chandra, T., et.al. Contrast-Enhanced Magnetic Resonance Angiography. Magn Reson Imaging Clin N Am 20 (2012) 687–698.
3 Ersoy, H., et.al. Vascular Thoracic Outlet Syndrome: Protocol Design and Diagnostic Value of Contrast- Enhanced 3D MR Angiography and Equilibrium Phase Imaging on 1.5- and 3-T MRI Scanners. AJR Am J Roentgenol (2012); 198:1180–1187.
4 Hartung, M., P., et.al. Magnetic resonance angiography: current status and future directions. Journal of Cardiovascular Magnetic Resonance (2011), 13:19.
5 Ivancevic, M., K., et.al. Technical Principles of MR Angiography Methods. Magn Reson Imaging Clin N Am 17 (2009) 1–11.
6 Ciura, V.,A., et.al. MRA: Current Applications in Body Vascular Imaging. Canadian Association of Radiologists Journal 60 (2009) 133e142.

Contact

Bac Nguyen, BSc, RT (R) (MR)
Senior MR Radiographer
Oslo University Hospital,
Rikshospitalet

Sognsvannsveien 20
0372, Oslo
Norway
Phone: +47 97702111
og_23@hotmail.com

FLAIR Fusion in Multiple Sclerosis Follow-up: An Indispensable Tool in Clinical Routine

Stéphane Cantin[1]; Thomas Troalen[2]; Emeline Lamain[1]; Melisa Bakir[2]

[1] Groupe Clinique du Mail, Grenoble, France
[2] Siemens Healthineers, Saint-Denis, France

Abstract

Multiple sclerosis (MS) follow-up leads to millions of brain MRI scans around the world. Depending on the number and size of inflammatory lesions, comparing successive exams to assess dissemination in time can be a challenging and lengthy process.

This article aims to describe FLAIR image fusion with *syngo*.via, and to highlight the benefits in terms of new lesion detection capacity and interpretation time saving, compared to conventional frame-by-frame 3D FLAIR comparison.

Equipment

All images were acquired using a 1.5T MAGNETOM Aera system with *syngo* MR E11 software and the 20-channel head coil. Postprocessing was performed using *syngo*.via VB10 software.

Introduction

Multiple sclerosis (MS) involves an immune-mediated process in which an abnormal response of the body's immune system is directed against the central nervous system (brain, spinal cord, and optic nerves). Magnetic resonance imaging (MRI) has revolutionized non-invasive diagnosis and follow-up for MS patients, leading to millions of MRI examinations around the world [1, 2]. MR imaging is performed before clinical modifications, during treatment to assess treatment response, and to assess dissemination of new MS lesions over time. The MAGNIMS 2016 criteria are commonly used to assess time dissemination and, in particular, the appearance of new hyperintensities on FLAIR images [3]. In some cases, detecting new lesions can be relatively cumbersome and uncertain.

The common way of identifying new FLAIR hyperintensities is via the frame-by-frame comparison of successive FLAIR sequences. This can be time-consuming, especially with patients who have a high lesion load. Moreover, the comparison is very challenging with coalescing lesions, as subtle increases in size are more difficult to detect than independent new lesions.

According to the literature, the best technique appears to be the subtraction of successive FLAIR sequences [4–5]. However, tools for the co-registration and subtraction of MRI exams acquired at different time points, or even for automatic segmentation are not always available in a clinical environment [6–7].

The third technique is FLAIR fusion, which is easily achievable using *syngo*.via postprocessing software. Three-dimensional isotropic datasets are recommended in MS patient follow-up due to the achievable high spatial resolution, thin slice thickness, and multiplanar reconstruction (MPR). A long TR of more than 7,000 ms is also recommended to better enhance lesion hyperintensity. Table 1 lists the optimized protocol parameters.

Workflow

The first step is to load two exams acquired at different time-points. This step can be automated using the auto-fetch feature of *syngo*.via connected to the PACS system. The latest FLAIR sequence (called Current) is selected first and then the oldest (called Prior) using the CTRL button

Parameters	Plane	TR (ms)	TE (ms)	TI (ms)	FOV (mm)	Matrix	Slice thickness (mm)	Slice resolution	Interpolation	Fat saturation
3D SPACE FLAIR	Sag	7000	401	2300	270 x 236	256 x 180	0.6	50%	On	On

Table 1: 3D SPACE FLAIR sequence parameters (MAGNETOM Aera 1.5T).

(both series are outlined with blue squares). The selected series are then fused by selecting MPR/MPR from the bottom-left corner of the context menu in the Current series.

To match the data as closely as possible, *syngo*.via can coregister the two volumes using the Automatic Registration option, which is located in the menu in the top-left corner of the fused image. If the system does not perform motion correction correctly, users can choose manual alignment to correct both the rotation and translation in x, y, and z.

MPR/MPR fusion and registration tools are common *syngo*.via features. Easy Reading Mode was introduced with *syngo* MR B10, making image fusion and coregistration easy in all *syngo*.via workflows. For instance, if users select the thumbnails mode in the series navigator, they can drag and drop the Prior series directly over the Current series by right-clicking and selecting 'Fuse (MPR/MPR)' from the context menu. The dropped series will become the 'overlay', and will use a 'body-heat' color look-up table (LUT) by default.

Experience shows that lesion detection is easier using a single-color LUT, such as the parathyroid-blue LUT. In our setting, the Prior series is mapped as blue while the Current series remains as grayscale. Moving the mouse over the right-hand side of the generated image allows users to adjust the contrast of the oldest series with the color LUT. The contrast is then adapted to differentiate between blue and white lesions. Keep in mind that the Current series contrast should remain unchanged, so the user should avoid moving the mouse over the left-hand side of the image. On the fused MPR, new lesions remain in white, whereas old lesions are shown in deep blue (Fig. 1A).

It is important to stress the importance of the order in which the series are selected. An incorrect order can lead to misleading fused images with the wrong color LUT. This could lead to false-negative lesion assessment, as there would be no difference in color between new and old lesions (Fig. 1B).

A description of the workflow is presented in the video available at **www.siemens.com/magnetom-world.**

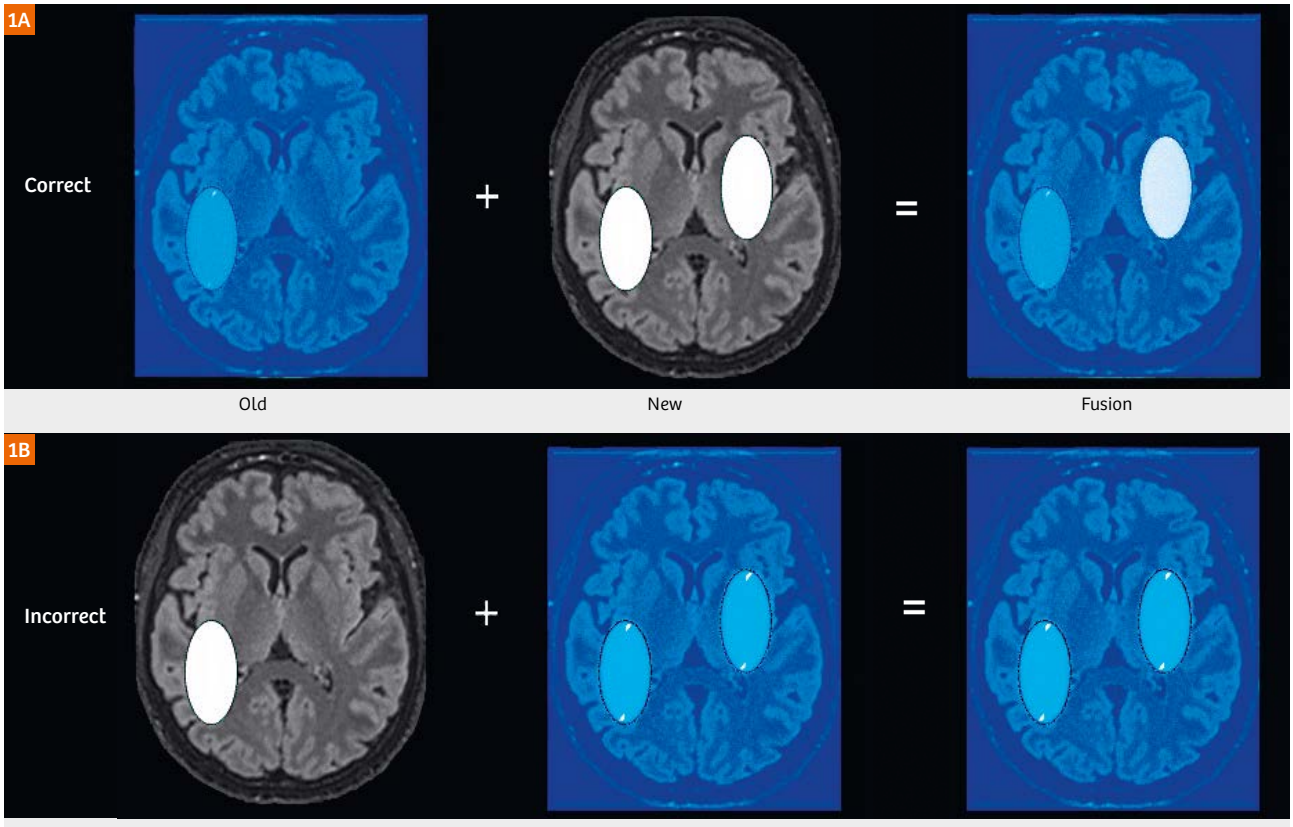

Figure 1:
Basic principle of image fusion using *syngo*.via postprocessing software.
(1A) Correct processing with the color LUT applied to the oldest series. New lesions are in white, while old lesions remain in blue.
(1B) Incorrect processing with color LUT applied to the newest series. Both lesions are colored, so analysis is not possible.

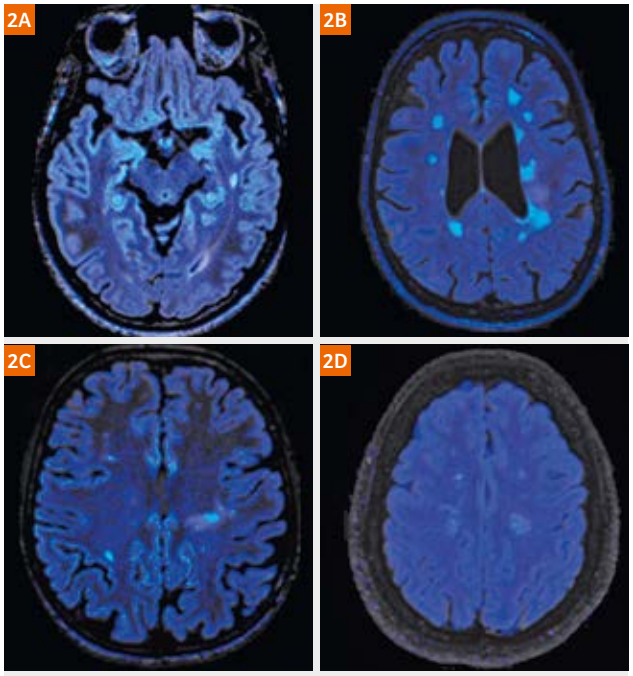

Figure 2:
Clinical example of periventricular / deep white matter lesions:
(2A) New lesion at the margin of the occipital horn of the left lateral ventricle
(2B) New lesion at the margin of the left lateral ventricle
(2C) Evolution of independent lesions into more coalescing lesions (left hemisphere)
(2D) New lesion in deep white matter, left hemisphere

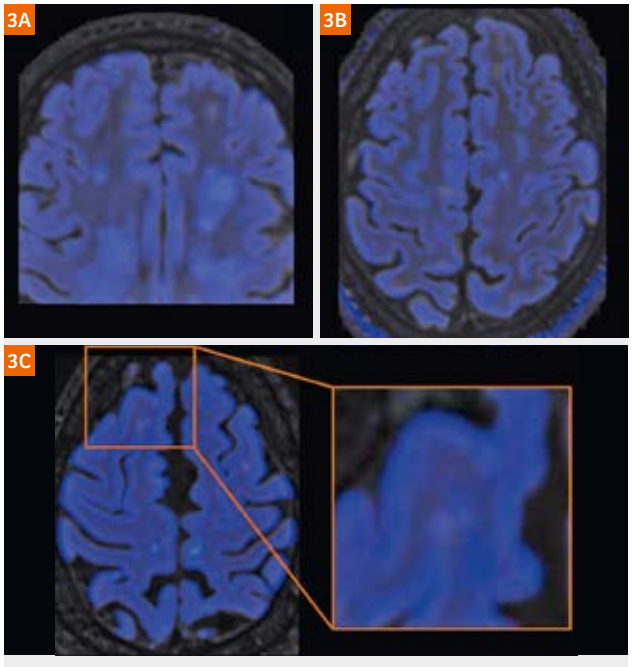

Figure 3:
Clinical example of subtle subcortical lesions:
(3A, B) Subcortical frontal lesion (right hemisphere)
(3C) New subtle subcortical lesion, magnified

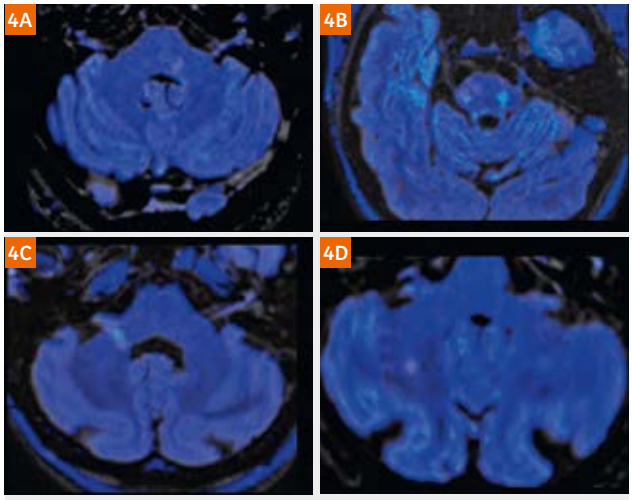

Figure 4:
Clinical example of posterior fossa lesions:
(4A, B) New pontine lesions
(4C) Growing lesion in the right cerebellar peduncle
(4D) New lesion in the right cerebellar hemisphere

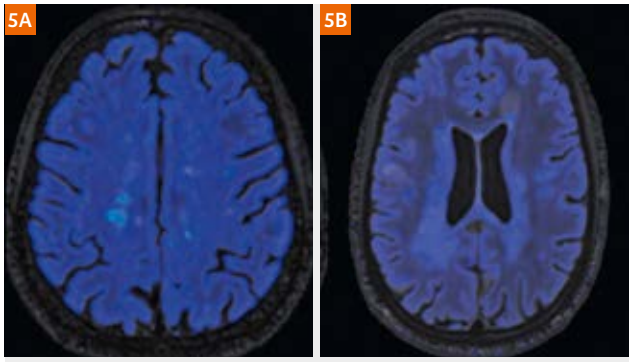

Figure 5:
Clinical example of high lesion load:
(5A) Punctate lesions
(5B) More coalescing and large lesions

This workflow, which we currently use in our imaging center, allows the detection of new lesions in all topographies: Periventricular lesions, deep white matter lesions, subcortical lesions, and posterior fossa lesions. Clinical examples are shown in Figures 2 to 4. Furthermore, this technique is particularly beneficial for patients with a high lesion load (Fig. 5).

A retrospective blinded study of 21 patients that was presented at the ASNR 55th Annual Meeting in 2017 [8] found that the fusion approach significantly reduced interpretation time, and that the number of new lesions detected was never lower than using frame-by-frame comparison (Fig. 6). The non-parametric Man Whitney test was used to compare the interpretation time of the two

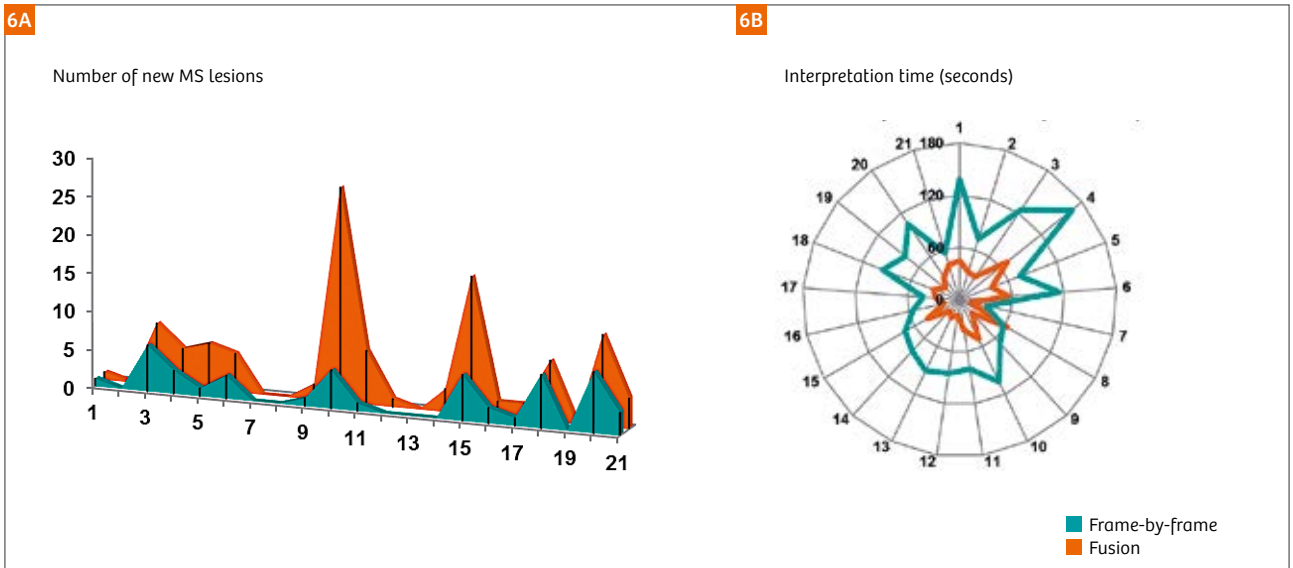

Figure 6: FLAIR Fusion vs. frame-by-frame comparison: Results from 21 patients [8].

methods and the number of new MS lesions detected by the neuroradiologist. The interpretation time with FLAIR fusion was significantly shorter, with a time-gain of about 60%, while lesion detection increased by 25%.

Conclusion

In our radiology center, FLAIR image fusion for follow-up in multiple sclerosis patients is now an indispensable tool in clinical routine. The technique is very easy to implement and is cost-effective. It allows for faster and more precise patient care, and increases the number of new lesions detected.

Other clinical applications are also possible, in particular for following FLAIR hyperintensity in microvascular micro-angiopathy, systemic diseases, or the extent of the edema surrounding expansive brain lesions.

References

1 Traboulsee AL, Li DK. The role of MRI in the diagnosis of multiple sclerosis. Adv Neurol. 2006; 98:125-46.
2 Wattjes MP, Steenwijk MD, Stangel M. MRI in the Diagnosis and Monitoring of Multiple Sclerosis: An Update. Clin Neuroradiol. 2015 Oct; 25 Suppl 2:157-65.
3 Filippi M, Rocca MA, Ciccarelli O, De Stefano N, Evangelou N, Kappos L, Rovira A, Sastre-Garriga J, Tintorè M, Frederiksen JL, Gasperini C, Palace J, Reich DS, Banwell B, Montalban X, Barkhof F; MAGNIMS Study Group. MRI criteria for the diagnosis of multiple sclerosis: MAGNIMS consensus guidelines. Lancet Neurol. 2016 Mar; 15(3):292-303.
4 Horsfield MA, Rocca MA, Pagani E, Storelli L, Preziosa P, Messina R, Camesasca F, Copetti M, Filippi M. Estimating Brain Lesion Volume Change in Multiple Sclerosis by Subtraction of Magnetic Resonance Images. J Neuroimaging. 2016; 26(4):395-402.
5 Moraal B, Meier DS, Poppe PA, Geurts JJ, Vrenken H, Jonker WM, Knol DL, van Schijndel RA, Pouwels PJ, Pohl C, Bauer L, Sandbrink R, Guttmann CR, Barkhof F. Subtraction MR images in a multiple sclerosis multicenter clinical trial setting. Radiology. 2009 Feb; 250(2):506-14.
6 Duan Y, Hildenbrand PG, Sampat MP, Tate DF, Csapo I, Moraal B, Bakshi R, Barkhof F, Meier DS, Guttmann CR. Segmentation of subtraction images for the measurement of lesion change in multiple sclerosis. AJNR Am J Neuroradiol. 2008 Feb; 29(2):340-6.
7 Ganiler O, Oliver A, Diez Y, Freixenet J, Vilanova JC, Beltran B, Ramió-Torrentà L, Rovira A, Lladó X. A subtraction pipeline for automatic detection of new appearing multiple sclerosis lesions in longitudinal studies. Neuroradiology. 2014 May; 56(5):363-74.
8 Lamain E, Casez O, Vaillant M, Lefournier V, Tourret P, Bakir M, Roux P, Savatovsky J, Cantin S. FLAIR Fusion in Multiple Sclerosis follow up: an unavoidable tool in Private Practice. ASNR 2017 – Oral 505.

Contact

Stéphane Cantin
Clinique du Mail

19, avenue Marie Reynoard
38100 Grenoble
France
stephane.cantin@groupe-du-mail.com

Visualization of Endolymphatic Hydrops with 1.5T MRI in Ménière's Disease: A Preliminary Study

Frédérique Chapon[1]; Mélanie Sanjuan[2]; Olivier Monnet[1]; Arnaud Devèze[3]; Maya Elziere[3]; Christine Fatou-Balansard[4]; Gilles Plasse-Fauque[2]; Michèle Rakedjian[2]; Catherine Cannoni[2]; Philippe Derome[2]; Rym Djouri[5]

[1] Department of Radiology, Saint Joseph Hospital, Marseille, France
[2] Department of Otolaryngology, Saint Joseph Hospital, Marseille, France
[3] Department of Otolaryngology, Clairval Hospital, Marseille, France
[4] Department of Otolaryngology, Aix en Provence Hospital, France
[5] Siemens Healthineers, MRI Application, France

Introduction

Ménière's disease is associated with endolymphatic hydrops (EH). This has been described in postmortem histological samples of patients with Meniere's disease [1]. There is no current data to determine whether this EH is the cause or consequence of another etiology (traumatic, autoimmune, electrolyte imbalance, viral) at the origin of the symptoms.

In its complete form, the pathology is characterized by episodes of vertigo, tinnitus, and hearing loss. Its evolution is erratic and many patients present incomplete forms. Since 2007 and the work of Nakashima et al. [2], MRI has been among the examinations that can help diagnose Ménière's disease by allowing an *in vivo* visualization of EH.

Numerous recent studies have shown that 3T MRI can visualize EH by using different routes for contrast agent administration (intratympanic versus intravenous), by varying the contrast dose (single, double, triple dose), and by modifying the technical parameters of the acquisition (coils and number of channels) and sequences (3D FLAIR and 3D-real IR). Our study aims to validate EH detection with 1.5T MRI after intravenous contrast injection.

Material and methods

From September 2016 to September 2017, 53 patients with clinical signs of Ménière's disease (35 women and 18 men ranging from 14 to 80 years of age) underwent 1.5T MRI of the temporal bone to demonstrate EH (3D Fluid Attenuation Inversion Recovery with variable Flip Angle Turbo Spin Echo – 3D SPACE FLAIR – sequence).

The examination was performed on a MAGNETOM Avanto^{fit} system with a 20-channel Head coil. The main parameters of the sequence were: FOV 200 x 190 mm; Slice thickness 0.85 mm; TR 7000 ms; TE 536 ms; number of excitations 4; TI 2200 ms; matrix 256 x 256; bandwidth 448 Hz/px; scan time 10 minutes. The intravenous double-dose contrast agent injection (Gadovist 1.0 mmol/mL, Bayer Healthcare, Germany) was administered 4 hours prior to image acquisition.

Before the study, all patients underwent 1.5T MRI to rule out other causes of their symptoms. Examinations of eight patients were excluded from the study because of motion artifacts. A retrospective collection of clinical data was carried out. For statistical analysis, we selected 21 patients with clinically definite disease (definite Ménière's disease according to the revised AAO-HNS criteria [3, 4]) in order to be certain of the presence of EH.

The MRI data of these 21 patients were retrospectively and qualitatively analyzed by two experienced neuroradiologists who were blinded to the side of the symptoms (unilateral or bilateral) and to the clinical score of Ménière's disease.

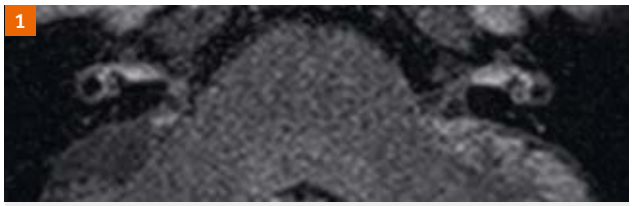

Figure 1: Normal bilateral vestibule.

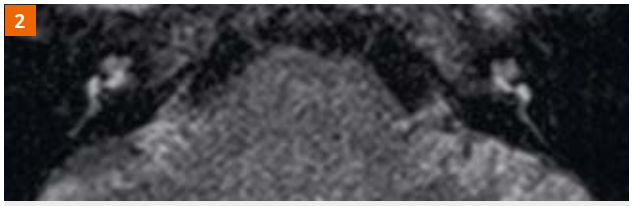

Figure 2: Normal bilateral cochlea.

Hydrops of the cochlea and vestibule were separately assessed by visual comparison of the relative areas of the unenhanced endolymphatic space versus the contrast-enhanced perilymphatic space.

MR imaging findings

In the normal vestibule on the delayed 3D FLAIR sequence, the added surface areas of the saccule and utricle are less than half of the area of the vestibule at horizontal semicircular canal level. Vestibular EH is defined as distension of the endolymphatic space (saccule, utricle, or both) to > 50% of the vestibule.

In the cochlea, absence of hydrops is defined as the absence of displacement of Reissner's membrane. Cochlear EH is defined as distension of the cochlear duct in the scala vestibuli.

Statistical analysis for interobserver agreement in detecting cochlear and vestibular EH was performed with the adjusted kappa test and Bowker's test. The agreement between the radiologists' response and the laterality of the clinical impairment was performed by Cohen's kappa test.

Results

MRI EH detection

Vestibular EH was detected in 19 out of 21 cases. Both radiologists agreed on the absence of hydrops in the two remaining cases. The kappa test for interobserver agreement was 0.74 with a match rate of 90%. Cochlear EH was seen in 14 out of 21 cases. Both radiologists agreed on the absence of hydrops in the remaining 7 cases. The kappa test for interobserver agreement was 0.95 with a match rate of 95%.

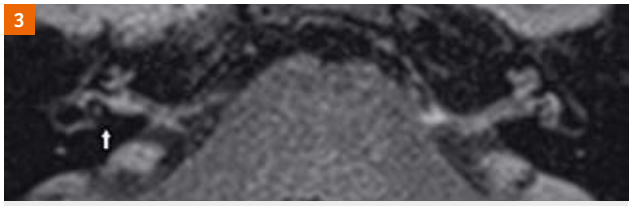

Figure 3: Hydrops in right vestibule (white arrow).

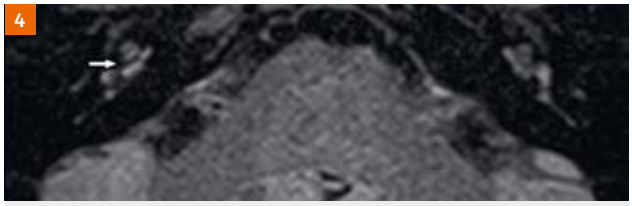

Figure 4: Hydrops in right cochlea (white arrow).

Table 1: Inter-radiologist agreement: Vestibule.

		Radiologist 2			
		0	R > L	L > R	Total
Radiologist 1	0	2	0	0	2
	R > L	0	10	0	10
	L > R	2	0	7	9
	Total	4	10	7	21

Match rate: 19/21 (90%)
Weighted kappa[1]**:** 0.74 [IC95 0.42–1.00]; Strong agreement between radiologists
Bowker's test of symmetry: p = 0.5724; Non symmetry hypotheses between radiologists rejected
R = right, L = left

Table 2: Inter-radiologist agreement: Cochlea.

		Radiologist 2				
		0	R	L	Bilateral	Total
Radiologist 1	0	7	0	0	0	7
	R	0	7	0	1	8
	L	0	0	6	0	6
	Total	7	7	6	1	21

Match rate: 20/21 (95%)
Weighted kappa[1]**:** 0.95 [IC95 0.84–1.00]; Almost total agreement
Bowker's test of symmetry: p = 0.8013; Non symmetry hypothesis between radiologist rejected

[1] Kappa Index: < 0 (disagreement); 0–0.20 (very week agreement); 0.21–0.40 (weak agreement); 0.41–0.60 (moderate agreement); 0.61–0.80 (strong agreement); 0.81–0.99 (almost perfect agreement); 1.00 (perfect agreement)

Correlation between imaging and clinical diagnosis

There was a high level of agreement between the radiologists and the clinical diagnosis for both cochlear and vestibular EH: 82% for cochlear (Cohen's Kappa test 0.64) and 92% for vestibular (Cohen's Kappa test 0.85).

Table 3: Agreement between radiologists and clinical data: Vestibular.

		Clinical Data		
		R	L	Total
Radiologists	R	8	2	10
	L	1	6	7
	Total	9	8	17
	Undetermined	1	1	2
	Disagreement	0	2	2

Match rate L/R: 14/17 (82%); Only in the upper part of the table (L/R)
Total agreement: 14/21 (67%); Taking into account the whole table
Kappa simple: 0.64 (0.28–1.00); Strong agreement
Symmetry test: p = 0.5637; Non symmetry hypothesis between radiologists and clinical data rejected

Table 4: Agreement between radiologists and clinical data: Cochlear.

		Clinical Data		
		R	L	Total
Radiologists	R	6	1	7
	L	0	6	6
	Total	6	7	13
	Undetermined	3	4	7
	Disagreement	1	0	1

Match rate D/G: 12/13 (92%); Only in the upper part of the table (L/R)
Total agreement: 12/21 (57%); Taking into account the whole table
Kappa simple: 0.85 (0.56–1.00); Almost full agreement
Symmetry test: p = 0.3173; Non symmetry hypothesis between radiologists and clinical data rejected

Discussion

Apart from major episodes of vertigo, hearing loss, and tinnitus, many patients suffer from incomplete forms of Ménière's disease and experience fluctuating hearing loss, recurring vertigo without hearing loss, or hearing loss preceding a few months or years of dizzy spells. The diagnosis is based on the recently revised AAO-HNS criteria [3, 4].

We chose to analyze the results of patients with definite Ménière's disease in order to be sure that EH was present.

The main aim of using MRI to visualize EH is to confirm the diagnosis at an early stage and thus begin treatment before possible hearing sequelae occur.

As mentioned above, since Nakashima et al. described the visualization of EH in 2007 [2], numerous studies have been carried out that confirm the possibility of visualizing EH with 3T MRI scanners (with 3D SPACE FLAIR or 3D-real IR [1]). To our knowledge, few studies have been published on MRI at 1.5T [12].

In our study, we used a 3D FLAIR sequence after administering contrast media intravenously (which is less restrictive, less painful, and avoids local complications).

Visualization of EH at 1.5T is possible and reproducible with a strong agreement between radiologists (adjusted kappa: 0.74; agreement: 90%). For the cochlear, the agreement between radiologists is very strong (adjusted kappa: 0.95; agreement: 95%).

The impossibility of distinguishing the saccule and utricle in our images (with the anatomical structures appearing 'fused') and the asymmetry of the dilation are strong indications of vestibular impairment.

In our study, cochlear involvement appears to be a very strong and reproducible criterion.

On correlation of radiological and clinical findings, there was a high agreement in both vestibular and cochlear involvement, with EH found in 19 out of 21 cases with clinically significant disease.

The radiologists agreed on the absence of vestibular and cochlear hydrops in two cases. These results match those published by Fraysse et al. [8] and Barath et al. [9]. The assumptions used for these patients were the short duration of the disease (< 6 months) and an examination carried out between episodes. Indeed, the reversibility of EH displayed in MRI is commonly accepted [6].

Based on asymmetry between the vestibules, two patients showed a more pronounced hydrops on the contralateral side to the clinical attack. Nonsymptomatic ear involvement is frequently reported in the literature [10, 11], with some papers suggesting a systemic origin for Ménière's disease.

In our study, the grading of the vestibular lesion as proposed by Nakashima [2] is not reproducible, which led to disagreement between radiologists. These results demonstrate the limitations of the sequence at this field level.

The duration of the sequence at 1.5T (10 minutes, vs. 7 minutes at 3T) is an important factor to take into account. It causes motion artifacts and required us to exclude 8 patients from the study. Simple immobilization of the head during patient preparation can significantly decrease artifacts.

Conclusion

Using MRI to visualize EH means that patients suffering from Ménière's disease can receive treatment at an early stage and before the appearance of auditory sequelae. Hydrops can be visualized with a 1.5T MRI system, and 3D FLAIR is a robust sequence for visualizing cochlear and vestibular hydrops.

The possibility of performing these routine examinations at 1.5T is a significant step forward in terms of treating these patients. It facilitates their access to imaging and can optimize the management of their condition.

References

1 Merchant SN, Adams JC, Nadol JB Jr. Pathophysiology of Meniere's syndrome: are symptoms caused by endolymphatic hydrops? Otol Neurotol. 2005;26(1):74-8.
2 Nakashima T, Naganawa S, Sugiura M, Teranishi M, Sone M, Hayashi H, Nakata S, Katayama N, Ishida IM. Visualization of endolymphatic hydrops in patients with Meniere's disease. Laryngoscope. 2007 Mar; 117(3):415-20.
3 Committee on Hearing and Equilibrium guidelines for the diagnosis and evaluation of therapy in Menière's disease: American Academy of Otolaryngology-Head and Neck Foundation, Inc. Otolaryngol Head Neck Surg. 1995; 113(3):181-85.
4 Lopez-Escamez JA, Carey J, Chung WH, Goebel JA, Magnusson M, Mandala M, Newman-Toker DE, Strupp M, Suzuki M, Trabalzini F, Bisdorff A. Diagnostic criteria for Menière's disease. J Vestib Res. 2015; 25(1):1-7.
5 Nakashima T, Naganawa S, Pyykko I, et al. Grading of endolymphatic hydrops using magnetic resonance imaging. Acta Otolaryngol. 2009; 129 Suppl 560:5-8.
6 Sepahdari AR, Vorasubin N, Ishiyama G, Ishiyama A. Endolymphatic Hydrops Reversal following Acetazolamide Therapy: Demonstration with Delayed Intravenous Contrast-Enhanced 3D-FLAIR MRI. AJNR Am J Neuroradiol. 2016 Jan; 37(1):151-4.
7 Hallpike CS, Cairns H. Observations on the Pathology of Ménière's Syndrome. Proc R Soc Med. 1938; 31(11):1317-36.
8 Fraysse BG, Alonso A, House WF. Menière's disease and endolymphatic hydrops: clinical-histopathological correlations. Ann Otol Rhinol Laryngol Suppl. 1980; 89(6 Pt 3):2-22.
9 Baráth K, Schuknecht B, Naldi AM, Schrepfer T, Bockisch CJ, Hegemann SC. Detection and grading of endolymphatic hydrops in Ménière disease using MR imaging. AJNR Am J Neuroradiol. 2014 Jul; 35(7):1387-92.
10 Pyykkö I, Nakashima T, Yoshida T, Zou J, Naganawa S. Meniere's disease: a reappraisal supported by a variable latency of symptoms and the MRI visualisation of endolymphatic hydrops. BMJ Open. 2013;3(2).
11 Naganawa S, Nakashima T. Visualization of endolymphatic hydrops with MR imaging in patients with Ménière's disease and related pathologies: current status of its methods and clinical significance. Jpn J Radiol. 2014; 32(4):191-204.
12 Naganawa S, Yamakasi M, Kawai H, Bokura K, Sone M, Nakashima T. Visualization of endolymphatic hydrops in Ménières's disease after intravenous administration of single-dose gadodiamide at 1.5T. Magn Reson Med Sci. 2013; 12(2):137-9.

Contact

Frédérique Chapon
Hôpital Saint Joseph

26 boulevard de Louvain
13008 Marseille
France
frederiquechapon@icloud.com

To Add Myelin Detection to Your Neuro Protocol Without Additional Scan Time

Akifumi Hagiwara, M.D.[1]; Christina Andica, M.D.[2]; Marcel Warntjes, Ph.D.[3, 4]

[1] Department of Radiology, University of Tokyo Hospital and Juntendo University Hospital, Tokyo, Japan
[2] Juntendo University Graduate School of Medicine, Tokyo, Japan
[3] SyntheticMR, Linköping, Sweden
[4] Center for Medical Imaging Science and Visualization, CMIV, Linköping, Sweden

SyntheticMR provides REMyDI (Rapid Estimation of Myelin for Diagnostic Imaging)[1], which was introduced on the Siemens Healthineers booth at RSNA 2016. REMyDI pro-vides a method of myelin detection in the brain, using a scan time of only 5 to 6 minutes. Based on the same sequence data, however, conventional images such as T1w, T2w and FLAIR can also be generated. If these images are taken for diagnosis, instead of acquiring them conventionally, valuable examination time is saved.

The secret behind this efficient way of data collection is MR quantification; a sequence is acquired that provides maps of physical properties of the patient, such as the T1 relaxation time, T2 relaxation time and Proton Density (PD). It is well known that these physical properties govern the signal intensity of MR images, but normally we can only speak in terms of weighting: an image is T1-weighted if the MR scanners parameters are set such that differences in tissue T1 relaxation result in contrast differences in image signal intensity. Similarly, an image is T2-weighted if the MR scanners parameters are set such that differences in tissue T2 relaxation result in contrast differences in image signal intensity. These conventionally weighted images, however, are arbitrarily scaled and do not provide a measurement of the actual T1 or T2 value. Without this absolute scale, radiologists are forced to interpret the images based on contrast differences only.

[1] REMyDI is currently under development at SyntheticMR and is not for sale in the US and in other countries. Its future availability cannot be ensured.

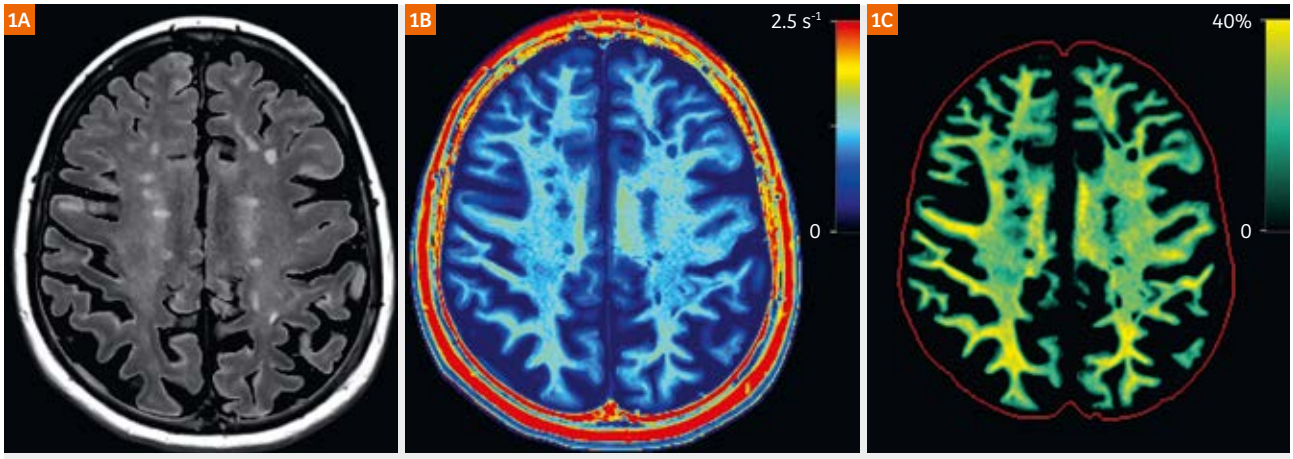

Figure 1:
Example images showing the application of REMyDI on a patient with multiple sclerosis (60-year-old female). A synthetic T2w-FLAIR of an axial slice of the brain is shown **(1A)**. This image is synthesized based on quantitative maps of R1 relaxation rate (shown on a scale 0–2.5 s^{-1} in **1B**, the R1 relaxation rate is the inverse of T1 relaxation time), R2 relaxation rate (1/T2) and proton density PD (not shown), together with virtual scanner settings TE/TR/TI = 100/15000/3000 ms. Using the same quantitative maps also myelin partial volume is calculated (shown on a scale 0–40% in **1C**). At the location of the MS plaques the myelin values are clearly lower than the surrounding normal appearing white matter. All images were generated on a 3T MAGNETOM Prisma system from a single acquisition of 5 minutes and 8 seconds.

In 2008, an efficient method of MR quantification was introduced [1], where T1, T2 and PD could be obtained in 6 minutes, covering the entire head. The post-processing software SyMRI was created that did not only display these maps, but also had the ability to synthesize conventional T1w, T2w, FLAIR, PSIR and DIR images. The approach of synthesizing conventional images based on a single quantification sequence has been known since the eighties, but became clinically available only in the recent years. A large, prospective study on 109 subjects, rated by 7 neuroradiologists, showed the clinical viability of synthetic MRI [2]. The advantage of this approach is that radiologists can continue to interpret the images they are comfortable with, or even optimize the image contrast after the patient has left, while the imaging data actually consists of quantitative T1, T2 and PD maps. The maps reflect patient tissue properties only and hence are entirely independent of MR scanner settings and identical for all scanners at a specific field-strength. It is an important step towards more standardization in MR. Moreover, the maps provide a robust input for computer algorithms to automatically detect tissue. For example, in neuroimaging white matter, grey matter and cerebrospinal fluid can automatically be found, providing an accurate means to monitor brain atrophy in neuro-degenerative diseases [3].

Recently, a model was proposed, with which it is possible to detect myelin partial volume based on the T1, T2 and PD maps [4]. Owing to the magnetization exchange between the rapidly relaxing myelin water and surrounding intra- and extracellular water, the presence of myelin is inferred using the observed changes in relaxation

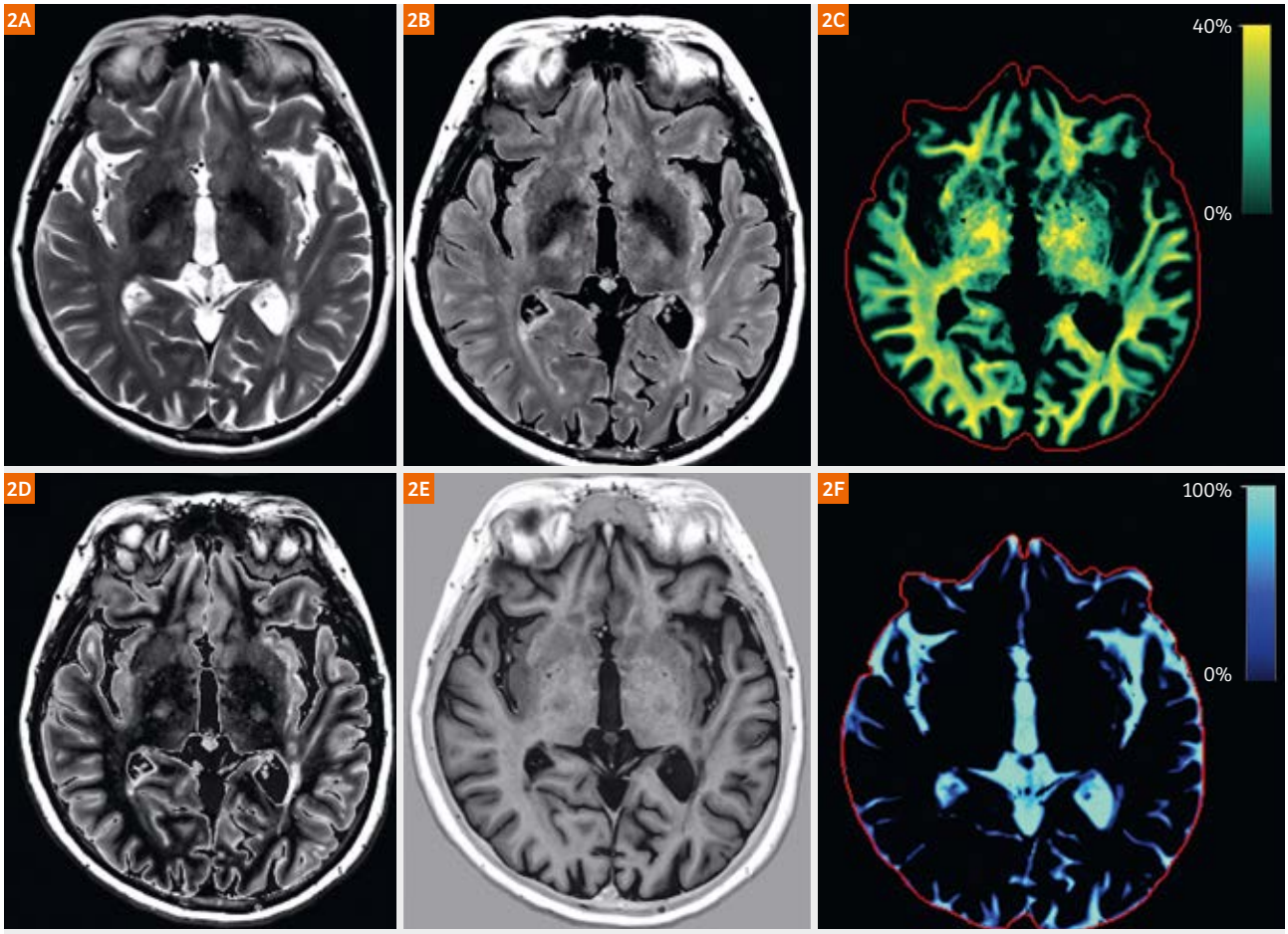

Figure 2:
An example of a subcortical MS plaque in the right temporal lobe. The synthetic T2-weighted image **(2A)** and T2w-FLAIR **(2B)** show the lesion well, but the contrast is actually higher in the synthetic Double IR **(2D)** and Phase-Sensitive IR **(2E)** images, facilitating detection. The myelin map **(2C)** clearly shows lower values at the location of the MS plaque. The intracranial volume is indicated by the red line. CSF segmentation **(2F)** in combination with the ICV provides the brain volume. The total myelin volume of the patient was 154 mL, the brain volume was 1214 mL and the intracranial volume was 1595 mL, meaning that myelin was 12.7% of the brain, and the brain was 76.1% of the ICV. All images were generated on a 3T MAGNETOM Prisma system from a single acquisition of 5 minutes and 8 seconds.

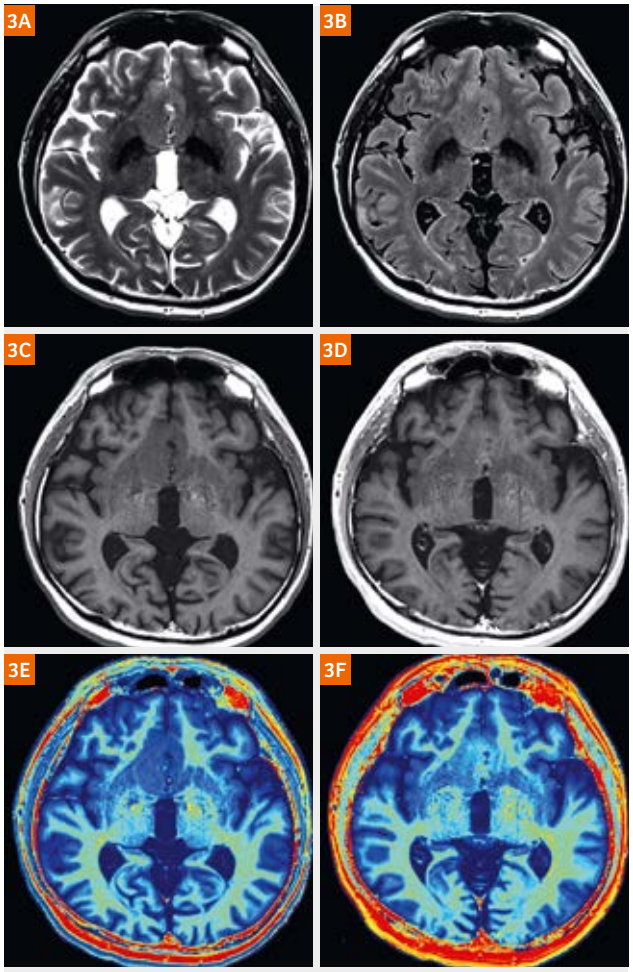

Figure 3:
An example of glioma, prior to and after Gadolinium administration. The synthetic T2-weighted image **(3A)** and T2w-FLAIR **(3B)** shows a hyper-intense lesion spreading to bilateral frontal lobes. Subtle contrast enhancement is shown in the synthetic T1w image before **(3C)** and after contrast administration **(3D)**. The shown T1w images are synthesized with a TR of 100 ms, which increases the T1w contrast with about a factor 2 in comparison to the more normal TR of 500 ms. The R1 relaxation maps (pre-Gd in **3E**, post-Gd in **3F**) show that the mean R1 value in the lesion increases from 0.83 s^{-1} before to 0.99 s^{-1} after Gd, corresponding to a decrease in T1 relaxation of 1210 ms to 1001 ms.

times and PD. The model was later verified on 12 human cadavers, where the results of the myelin model were compared with slices of the brain that were histologically stained with Luxol Fast Blue during autopsy [5]. The myelin detection algorithm was introduced into the SyMRI product as REMyDI. Myelin volume measured by REMyDI has been shown to increase according to age in children, especially ages under 3[1], indicating that this method correlates with normal myelination [6].

At Juntendo University Hospital all aspects of SyMRI – quantification, synthetic imaging and automatic brain segmentation –, were evaluated on various scanner models [7]. Our initial investigation showed that REMyDI had a very low error (coefficient of variation, 0.59% for 0.8 mm in-plane resolution) for estimation of whole brain myelin volume [8]. In addition, we have shown that REMyDI correlated well with magnetization transfer imaging, which is considered to be a criterion standard of myelin imaging [9]. These studies show the reliability of REMyDI. Indeed, REMyDI does not increase the scan time because contrast-weighted images can be created based on the same acquired quantitative values, which is an advantage over other myelin imaging methods.
We have examined the use of REMyDI in patients with multiple sclerosis (MS) and Sturge-Weber syndrome. ROI analysis provides a value for myelin partial volume per voxel. We have shown that myelin values are reduced in MS plaques in comparison to normal-appearing white matter. In addition, we have also revealed that even peri-lesional white matter has lower myelin values than normal-appearing white matter. This suggests that the myelin detection method is sensitive to pathological changes that are difficult to discern on conventional images [10, 11]. An example of a patient with MS is given in Figure 1.

Sturge-Weber syndrome is a neurocutaneous disorder and known to show white matter abnormality on the affected side in pediatric populations, and this phenomenon is presumably due to accelerated myelination. We recently reported that the affected side of the brain in a 4-month-old patient[1] with Sturge-Weber syndrome showed decreased T1, T2 and PD values, and increased myelin [12, 13]. Although this case does not have definite pathology, we think this report showed the potential utility of REMyDI for revealing pathophysiology of Sturge-Weber syndrome.

Synthetic MRI can create any combination of TE, TR and inversion delay TI, even more exotic combinations such as DIR and PSIR images, which generally are not acquired routinely due to scan time constrains. DIR and PSIR images are known to be sensitive to cortical and subcortical MS plaques. Previously, we reported that synthetic MRI with DIR and PSIR is more sensitive than conventional MRI with comparative scan times [14]. Figure 2 shows a representative case of DIR and PSIR images, clearly showing a subcortical MS plaque. In our study, we adjusted the DIR images to each patient by

[1] MR scanning has not been established as safe for imaging fetuses and infants less than two years of age. The responsible physician must evaluate the benefits of the MR examination compared to those of other imaging procedures.

changing the virtual inversion time after image acquisition. The synthetic DIR images had better lesion-to-white matter contrast than conventional DIR images.

When all myelin partial volumes of the entire brain are added up, REMyDI can also show whole myelin volume of the brain, which provides an objective means of patient monitoring. In Figure 2 the volumes of myelin, brain and intracranial volume are indicated. These values can be compared with an age-matched healthy group and over time.

Quantification of absolute R1, R2, and PD values is a strong advantage of this method. We view this as an important step towards more standardization in MR imaging. Currently we are investigating the quantitative enhancement of lesions after Gd administration, which is usually evaluated using conventional T1-weighted images. Quantitative R1 maps may provide us with a more direct and objective evaluation of contrast enhancement (Fig. 3). We are looking forward to more investigations and clinical application of SyMRI in the future.

Contact

Akifumi Hagiwara, M.D.
Department of Radiology
Juntendo University Hospital
3-1-3, Hongo, Bunkyo-ku
Tokyo 113-8431
Japan
a-hagiwara@juntendo.ac.jp

Christina Andica, M.D.
Department of Radiology
Juntendo University Hospital
3-1-3, Hongo, Bunkyo-ku
Tokyo 113-8431
Japan
andicach@gmail.com

Marcel Warntjes, Ph.D.
SyntheticMR AB
Storgatan 11, 58224, Linköping, Sweden
Center for Medical Imaging Science and Visualization, CMIV
University Hospital, 58185, Linköping, Sweden
marcel.warntjes@syntheticmr.com

References

1 Rapid Magnetic Resonance Quantification on the Brain: Optimization for Clinical Usage. JBM Warntjes et al. Magn Reson Med 2008;60:320–329.
2 Synthetic MRI for Clinical Neuroimaging: Results of the Magnetic Resonance Image Compilation (MAGiC) Prospective, Multicenter, Multireader Trial. LN Tanenbaum et al. AJNR Am J Neuroradiol. 2017;38:1103-1110.
3 Brain parenchymal fraction in an age-stratified healthy population — determined by MRI using manual segmentation and three automated segmentation methods. M Vågberg et al. J Neuroradiol 2016;43:384-391.
4 Modeling the Presence of Myelin and Edema in the Brain Based on Multi-Parametric Quantitative MRI. JBM Warntjes et al. Front Neurol 2016;7:16. doi: 10.3389
5 Myelin Detection Using Rapid Quantitative MR Imaging Correlated to Macroscopically Registered Luxol Fast Blue–Stained Brain Specimens. JBM Warntjes et al. AJNR Am J Neuroradiol 2017;38:1096-1102.
6 Quantification of myelin in children using multiparametric quantitative MRI: a pilot study. H Kim HG, et al. Neuroradiology 2017 [Epub ahead of print] doi:10.1007/s00234-017-1889-9
7 SyMRI of the Brain: Rapid Quantification of Relaxation Rates and Proton Density, With Synthetic MRI, Automatic Brain Segmentation, and Myelin Measurement. A Hagiwara et al. Invest Radiol 2017 Mar 3. doi:10.1097/RLI.0000000000000365
8 Automated Brain Tissue and Myelin Volumetry Based on Quantitative MR Imaging with Various In-plane Resolutions. C Andica et al. [submitted]
9 A Comparison Study of Three Rapid Myelin Measurement Techniques: SyMRI (Simultaneous Tissue Relaxometry), Magnetatization Transfer Saturation Index, and T1w/T2w ratio. A Hagiwara et al. [submitted]
10 Analysis of White Matter Damage in Patients with Multiple Sclerosis via a Novel In Vivo MR Method for Measuring Myelin, Axons, and G-Ratio. A Hagiwara et al. AJNR Am J Neuroradiol 2017 Aug 3. doi: 10.3174/ajnr.A5312
11 Utility of a Multiparametric Quantitative MRI Model That Assesses Myelin and Edema for Evaluating Plaques, Periplaque White Matter, and Normal-Appearing White Matter in Patients with Multiple Sclerosis: A Feasibility Study. A Hagiwara et al. AJNR Am J Neuroradiol 2017;38(2) 237-242
12 Synthetic MRI showed increased myelin partial volume in the white matter of a patient with Sturge-Weber syndrome. A Hagiwara et al. Neuroradiology 2017 Aug 26. doi: 10.1007/s00234-017-1908-x
13 The Advantage of Synthetic MRI for the Visualization of Early White Matter Change in an Infant with Sturge-Weber Syndrome. C Andica et al. Magn Reson Med Sci 2016;15(4) 347-348
14 Synthetic MRI in the Detection of Multiple Sclerosis Plaques. A Hagiwara et al. AJNR Am J Neuroradiol 2017;38(2) 257-263

A Within-subject Comparison of Common Neuroimaging Protocols on MAGNETOM Prisma^{fit} and MAGNETOM Trio Scanners

Ross W. Mair[1, 2]; Stephanie McMains[1]

[1] Center for Brain Science, Harvard University, Cambridge, MA, USA
[2] Athinoula A. Martinos Center for Biomedical Imaging, Massachusetts General Hospital, Charlestown, MA, USA

Introduction

The Center for Brain Science – Neuroimaging Facility (CBS) at Harvard University is a key imaging resource for a wide array of university psychology department and medical school faculty in the Boston area. Started with the installation of a MAGNETOM Trio (Siemens Healthcare, Erlangen, Germany) in 2008, the center achieves a funded average usage by researchers of ~2000 hours per year with an approximately 1000 additional hours per year of use for maintenance, development, and educational purposes. As such, the scanner is used consistently and at near-capacity by an active and diverse group of scientists from Harvard and from other institutions, including Harvard teaching hospitals, in the Boston community.

The vast majority of this MRI data is task-based or resting-state functional MRI employing T2*-weighted echo-planar imaging, or blood-oxygen level dependent (BOLD) techniques. Sessions also include a T1-weighted high-resolution structural or anatomical scan for co-registration to the BOLD images, and sometimes for brain morphometry. Many researchers also supplement their sessions with a short diffusion-weighted MRI scan. While most user-groups are eager to embrace new imaging technology and techniques when there is an appropriate benefit to the quality of their neuroimaging data, a key factor to ensuring quality data over studies that may run over periods stretching from 2 months to 2 years

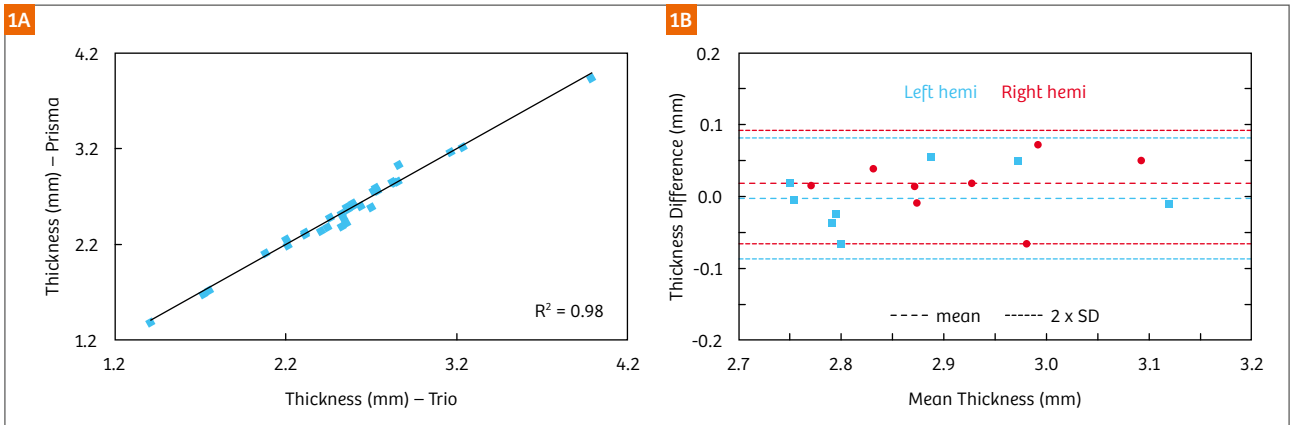

Figure 1:
(1A) Example correlation of cortical thickness of all 33 cortical regions of the Desikan-Killiany atlas from a single subject from T1-weighted images acquired on the MAGNETOM Trio and the MAGNETOM Prisma^{fit}. **(1B)** Example Bland-Altman difference plot of cortical thickness in the temporal lobes for 8 subjects from T1-weighted images acquired on the MAGNETOM Trio and the MAGNETOM Prisma^{fit}.

is stability and consistency of scanner performance, and continuity in image acquisition protocols and the resultant MRI data itself. At CBS, we have placed a very high priority on maintaining a stable and consistent scanning environment. As a result, when major imaging advances and hardware or software upgrades arrive, there are equal parts anticipation and trepidation for many of our user groups.

We upgraded the MAGNETOM Trio to the MAGNETOM Prisma^{fit} in the summer of 2015. The Prisma^{fit} represented a significant upgrade in performance capability over the Trio. The MAGNETOM Prisma platform included a major advance in gradient strength (80 mT/m, up from 45 mT/m), new highly-parallel array receive coils for the head, a digital RF transmit/receive architecture, and a much faster reconstruction computer. While the new gradient coil was expected to offer significant improvements in diffusion experiments, any change to the gradient system has the potential to bias brain morphometry data if there were changes in gradient linearity and performance. We believed the digital RF chain had the potential to significantly improve BOLD imaging with improved RF fidelity and a reduction in spurious noise pick-up, however it was unclear whether such benefits would hold up in the human head with its attendant physiological noise effects. In addition, as Simultaneous Multi-Slice imaging techniques were beginning to be adopted, the improved reconstruction system was seen as a key component that would allow routine use of this technique for high-temporal resolution BOLD imaging with real-time image reconstruction, rather than suffering often intolerable reconstruction lags, as was the case on the Trio.

To quantify the impacts and improvements offered by such a significant system upgrade, we scanned 8 subjects using a variety of anatomical, functional and diffusion protocols commonly employed at the time on the Trio platform, and then repeated the same scans with the same protocols on the Prisma^{fit} after the upgrade process. In addition, we devoted effort to assessing where the new hardware would permit improvements to temporal and spatial resolution in conventional BOLD imaging, both immediately after the hardware upgrade, and again following the software upgrade from *syngo* MR D13D to E11C in late 2016.

Methods

8 subjects were scanned on the 3T MAGNETOM Trio in July 2015. The same 8 subjects were scanned a second time on the MAGNETOM Prisma^{fit} in October 2015, after the scanner conversion. The relevant 32-channel head coil was used on each system. The scans included a 1.0 mm resolution multi-echo MPRAGE [1] anatomical scan acquired with FreeSurfer-recommended parameters (6:03 min, TR/TI = 2530/1100 ms, matrix 256 x 256 x 176, resolution = 1 x 1 x 1 mm (no partial fourier), parallel imaging acceleration (GRAPPA) = 2, pre-scan normalize enabled). Two resting state BOLD scans of 8-min duration were acquired, one with 3 mm resolution and TR = 3 s, the other with 2 mm nominal resolution, slice-acceleration [2, 3] (SMS) of 8 and TR = 750 ms. Additionally, a third BOLD scan employing a protocol commonly used for task studies at the time was acquired: 2 mm nominal resolution, SMS 3 and TR = 2 s. Two diffusion MRI protocols were employed, both with nominal 2 mm resolution: no SMS, 30 *b* directions, $b = 1000$ mm^2/s; and SMS 2, 64 *b* directions, $b = 1000$ mm^2/s. On the Prisma^{fit}, the diffusion protocols were reproduced exactly as implemented on the Trio, and then repeated utilizing the monopolar diffusion encoding scheme available in *syngo* MR D13 and E11, the performance gradient mode allowed by the Prisma^{fit} gradient set, and then optimizing the echo spacing and minimizing TE and TR. No changes were made to spatial resolution, number of *b* directions or *b* values, although it is widely expected such advances will become commonly employed on Prisma^{fit} system and similar scanners.

Anatomical images were analyzed using a FreeSurfer [4] processing stream. They were first corrected for gradient non-linearities according to the different scanner gradient coil parameters, after which the pairs of scans from each subject were aligned using the FreeSurfer robust registration tool [5]. FreeSurfer v.5.3 was used to perform an automated parcellation of the cortex, subcortical and white matter structures. The 33 cortical regions of the Desikan-Killiany atlas [6] were combined into five principal cortical lobes for simpler analysis [7]. Correlation and Bland-Altman difference plots were made for the thickness and volume of each principal cortical lobe determined from each scan, and for the volume of key sub-cortical structures. Surface-based plots were made to show regions of thickness difference and significance of difference. Diffusion scans were analyzed from raw DWI images and ADC and FA maps generated by the scanner software at the scanner console. In addition, diffusion scans were post-processed with a detailed stream that included gradient non-linearity correction, motion correction/realignment, eddy-current distortion correction, and registration to the anatomical space of the T1-weighted image. This alignment enabled the ADC and FA to be probed in the parcellated corpus callosum only, while the whole brain and white-matter-only masked images were analyzed for stability. BOLD scans were analyzed by assessing tSNR for each voxel, and averaged over the whole brain, after motion correction and detrending. Functional-connectivity

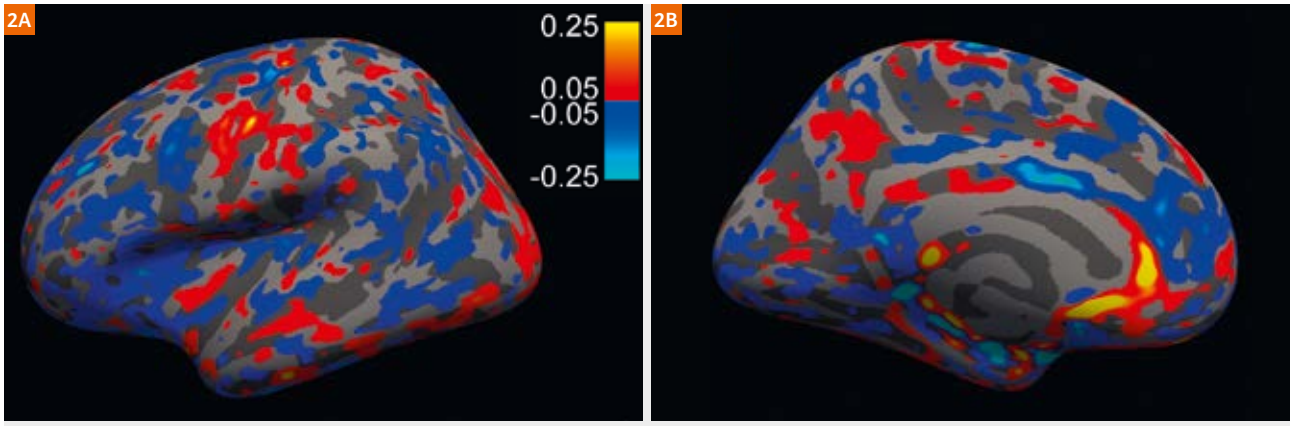

Figure 2:
Surface plots of average cortical thickness difference for pairs of T1-weighted images acquired on the MAGNETOM Trio and the MAGNETOM Prisma^{fit}. Thickness differences are threshold at ± 50–250 µm, color bars are in mm. The left hemisphere is shown – results are similar for the right hemisphere.

analysis was performed on the two resting-state BOLD scans with a seed-based correlation procedure using correlations between major network seeds [8].

Results/discussion – anatomical scans

The anatomical scans from each subject, acquired on the MAGNETOM Trio and on the MAGNETOM Prisma^{fit} appeared visually very similar. The offline gradient non-linearity correction modified the appearance of the neck/spine region on scans acquired on the Trio, but the brain and skull appeared unaffected. On the Prisma^{fit}, in addition to modification of neck/spine region, a slight extension to the crown of the skull and the parietal cortex just below it could be observed for some subjects following gradient non-linearity correction. Therefore, for comparison of brain morphometric data, gradient non-linearity correction was performed on the anatomical scans from each scanner, prior to robust registration of the pairs of scans to an unbiased base-space, after which the standard FreeSurfer processing stream was performed.

Figure 1A shows an example correlation plot for the thickness of all 33 cortical regions of the Desikan-Killiany atlas, from a single subject, as determined from images acquired on the Trio and on the Prisma^{fit}. Similar correlation plots were obtained for gray matter volume for the 33 cortical regions, and for the volumes of sub-cortical/white matter structures. Correlation Coefficients (R^2) were routinely ~0.95–1.00 for all subjects, and were especially high for the sub-cortical/white matter structure volumes. However, while intuitively simple, correlation plots can hide systematic biases, and so a Bland-Altman difference analysis was also performed. Figure 1B shows an example Bland-Altman difference plot, plotting the difference of the measured average cortical thickness of the temporal lobes for all eight subjects, when scanned on the Trio and on the Prisma^{fit}. The average thickness value was obtained from aggregating the relevant cortical regions from the Desikan-Killiany atlas for each subject [7]. The mean difference for both the left and right hemispheres was close to zero, with a standard-deviation inside ± 0.1 mm. Similar plots were obtained for the other principal cortical lobes, with differences always considerably less than ± 50 µm. Such differences are on the order of those seen for test-re-test scans on the same scanner on the same day [9]. For the sub-cortical/white matter structures, a wider range of differences were observed – up to ± 5%, but again were respectable compared to prior studies of variation between head coils or repeated measures on different days [10].

Figure 2 shows inflated-surface plots of cortical thickness difference for groups of scans on the Trio and on the Prisma^{fit}. Cortical thickness difference was determined using all 33 cortical regions of the Desikan-Killiany atlas for each scan, with each subject registered to FreeSurfer average-space, so differences can be analyzed on a single surface. Thickness differences are thresholded at ± 50 µm – the vast majority of difference observed is either below 50 µm (masked out), or between 50 and 100 µm. Only the inner surface of the temporal lobe and a spot in the central gyrus shows values higher. However, a t-test determined that none of the thickness differences are statistically relevant ($p > 0.01$).

In combination, the results from Figures 1 and 2 indicate that, with careful control for gradient non-linearity and

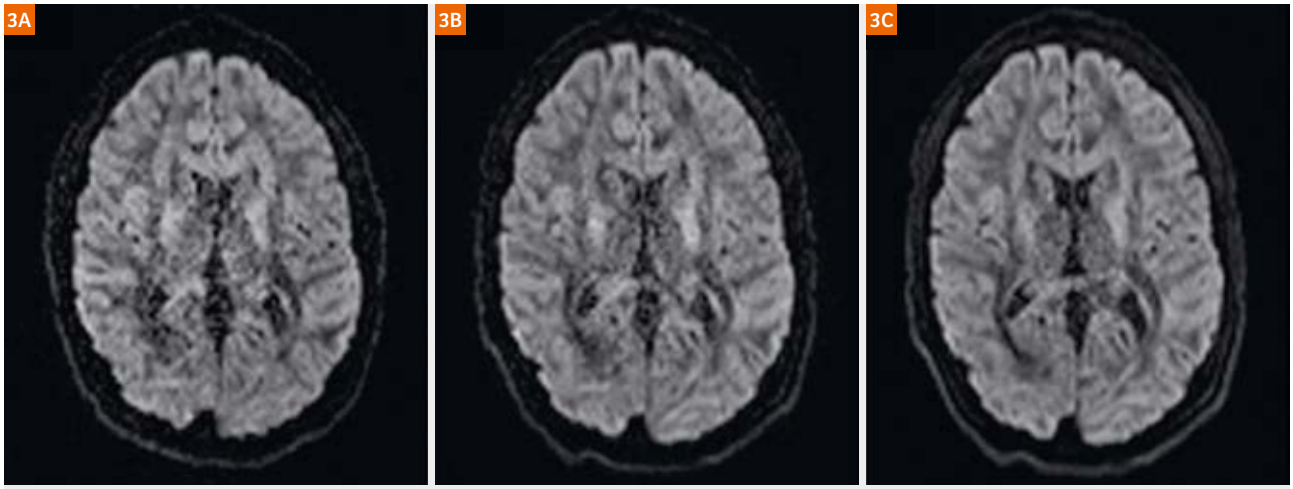

MAGNETOM Trio

MAGNETOM Trio protocol on MAGNETOM Prisma^{fit}

MAGNETOM Prisma^{fit} optimized

Figure 3:
Representative DWI images, as displayed at the scanner console, from the same subject acquired on the MAGNETOM Trio and the MAGNETOM Prisma^{fit}. A 2 mm isotropic, SMS = 2, 64-direction, *b* = 1000 s/mm^2 DTI protocol was used. **(3A)** Image from the Trio. **(3B)** Image from the Prisma^{fit} when the Trio protocol was implemented. **(3C)** Image from the Prisma^{fit} after optimizing echo-spacing, bandwidth, and TE as permitted by the Prisma^{fit} hardware.

robust registration, brain morphometric data should not be biased by scanner whether a Trio or Prisma^{fit} is used, or when the former is upgraded to the latter.

Results/discussion – diffusion scans

For the diffusion scans, the protocols used on the Trio were implemented exactly on the Prisma^{fit} without modification, to check for between-scanner variation, being cognizant of reducing bias for ongoing studies that straddled the upgrade period. Using "fast" gradient mode on the Sequence/Part 2 tab restricts the Prisma^{fit} gradient to the maximum strength and slew-rates employed on the Trio. These scans are referred to as "Trio protocol on Prisma", which we hoped would show insignificant variation from the scan on the Trio. The scans were then repeated employing the hardware and software advances of the Prisma^{fit}, principally the use of the monopolar diffusion encoding scheme which significantly reduces TE; the performance gradient mode allowed by the Prisma^{fit} gradient set allowing stronger gradient strengths with shorter gradient durations; and then optimizing the echo spacing and minimizing TE and TR as a result of the above changes. These scans are referred to as "Prisma optimized", although no changes were made to the spatial resolution, number of *b* directions or *b* values, as is likely for diffusion protocols truly optimized for the Prisma^{fit}.

Figure 3 shows a single slice from a diffusion-weighted image on the Trio, and the two corresponding scans on the Prisma^{fit}, all acquired with the 64-direction / SMS = 2 protocol. The reduction in TE, from 90 to 57 ms in the "Prisma optimized" protocol, results in a noticeable improvement in SNR in the DWI. The same impact is seen in the color-coded FA maps as generated by the scanner software without offline processing, which are shown in Figure 4. Again, the "Prisma optimized" protocol results in a noticeable improvement in SNR in the FA map. For the three marked ROI's shown in the images, which were chosen to comprise regions of highly uniform fiber orientation and density, an average reduction in the standard-deviation of FA in the three ROIs in the "Prisma optimized" image was found to be ~25%. For the same three ROI's, the average ADC standard-deviation fell by ~40% with the "Prisma optimized" protocol, but were otherwise similar for the Trio and the "Trio protocol on Prisma" scan.

To more carefully quantify the effect of the SNR increase and improved signal stability with the "Prisma optimized" protocol, the diffusion scans were also processed offline using a conventional processing stream including alignment to the T1-weighted image native space before recalculation of the ADC and FA images. The resultant ADC and FA images were then masked by the corpus callosum as derived from the FreeSurfer-processed T1-weighted image for each subject. Figure 5 shows the average of the standard-deviation of ADC and FA within the corpus callosum for the 8 subjects, using the two

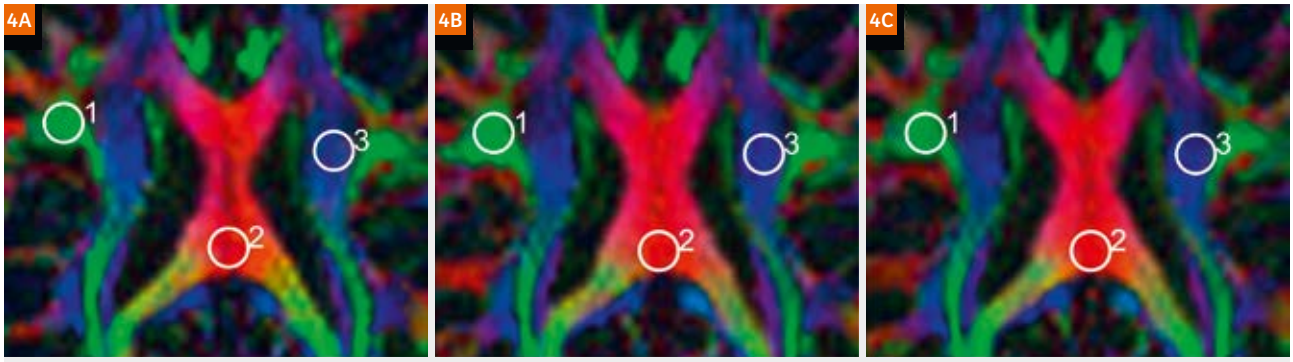

MAGNETOM Trio

MAGNETOM Trio protocol on MAGNETOM Prisma^{fit}

MAGNETOM Prisma^{fit} optimized

Figure 4:
A portion of the scanner-generated Color-FA maps from the same subject acquired on the MAGNETOM Trio and the MAGNETOM Prisma^{fit}. The same protocol from Figure 3 was used. **(4A)** FA image from the Trio. **(4B)** FA image from the Prisma^{fit} using the Trio protocol without modification. **(4C)** FA image from the Prisma^{fit} after optimizing as permitted by the Prisma^{fit} hardware. In the three ROIs shown, the ADC std-dev is ~40% lower and the FA std-dev is ~25% lower when the Prisma^{fit}-optimized protocol was used with this subject.

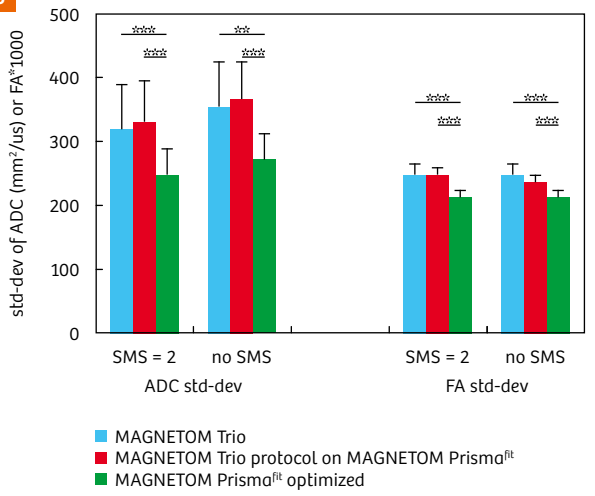

Figure 5:
Standard-deviation of the values of ADC and FA in the segmented corpus callosum, after detailed offline processing, for the three different scan procedures described in Figures 3 and 4 on the MAGNETOM Trio and MAGNETOM Prisma^{fit}, averaged over 8 subjects. Here, data from the SMS = 2 / 64-direction and the no SMS / 30-direction DTI protocols are shown.

acquisition protocols (SMS 2 / 64 directions, and no SMS / 30 directions) on the Trio, and for the "Trio protocol on Prisma" and "Prisma optimized" scans on the Prisma^{fit}. Noticeable reductions are seen in both the ADC and FA standard-deviations for the "Prisma optimized" scans for both protocols (all $p < 0.001$, except, "Trio protocol on Prisma" versus "Prisma optimized", $p < 0.01$); while the "Trio protocol on Prisma" and the original scan on the Trio essentially give indistinguishable results ($p > 0.05$).

Signal stability was also assessed from the repeated $b = 0$ images in each diffusion scan, in the same way it would be done for BOLD scans – dividing the mean image (after realignment) by the standard-deviation, to give a "time-series SNR" or tSNR image. This was done with 5 $b = 0$ images from each scan for the no SMS / 30 direction protocol, and 10 $b = 0$ images for the SMS 2 / 64 direction protocol. In each case, the metric was calculated on the whole brain after brain extraction, and on an image masked to show only the segmented white matter from the FreeSurfer-processed T1-weighted image for each subject. As shown in Figure 6, the "Prisma optimized" scans for both protocols exhibited improvements in tSNR of ~30–40% compared to the "Trio protocol on Prisma" and the original scan on the Trio (all $p < 0.001$), while the "Trio protocol on Prisma" and the original scan on the Trio were similar ($p > 0.05$).

These results show that the new, high-performance gradient coil that is the heart of the Prisma indeed delivers the expected boost of SNR to MRI diffusion scans, when the acquisition protocols are optimized to take full use of the new gradient strength and slew rate. The reduction in TE of ~30–40% for a commonly employed acquisition protocol can yield similar increases in diffusion-scan signal stability, and reduce the uncertainties in derived diffusion metrics by similar amounts. Of course, these new gradient capabilities are also being used to bring more advanced diffusion acquisition protocols into the mainstream, employing higher, and multiple, b values, and more diffusion directions; to improve fiber-tracking definition in areas where fibers cross. The multi-site Human Connectome Projects on Aging and Development, and the Adolescent Brain Cognitive Development (ABCD)

6

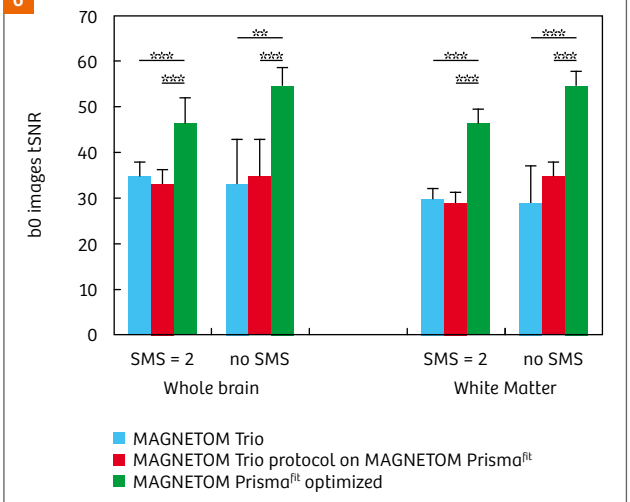

Figure 6:
DTI signal stability from repeated *b* = 0 images (labeled "tSNR"), averaged over 8 subjects, in the whole brain and in masked white matter, for the three different scan procedures described in Figures 3 and 4 on the MAGNETOM Trio and MAGNETOM Prisma^{fit}. The SMS = 2 / 64-direction protocol acquired 10 *b* = 0 images, and the no SMS / 30-direction protocol acquired 5 *b* = 0 images.

7

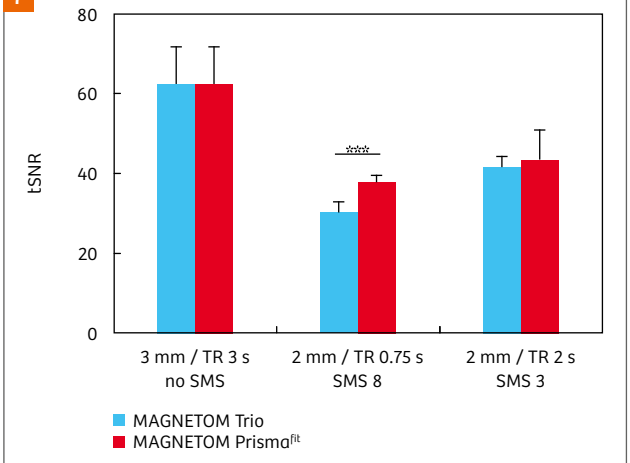

Figure 7:
Average whole-brain tSNR values measured in BOLD scans acquired on the MAGNETOM Trio and the MAGNETOM Prisma^{fit}.

study, both in the US, are both employing *b* values up to 3000 s/mm^2 with 100–200 *b*-vectors for routine use in studies that will scan thousands of subjects. Alternatively, for those wishing to replicate the diffusion protocol and data quality for studies ongoing from Trio scanners, the identical implementation of a protocol, with the gradient mode restricted to "Fast" mode, should give equivalent data on the Prisma.

Results/discussion – functional scans

Although Siemens Healthcare had not promised improvement to the quality and stability of EPI-BOLD scanning, we had initial hopes that some of the other hardware improvements, such as the all-optical transmit/receive chain between the magnet and the equipment room, the new sold-state RF amplifier system on the side of the magnet, and the fact that BOLD imaging would use a lower % of the maximum gradient strength (same gradient strength as used on the Trio, to avoid severe peripheral nerve and possibly cardiac stimulation) might serve to reduce instrumental noise and so increase the time-series SNR (tSNR) that determines the ability to detect BOLD activations.

Initial tests with the standard water phantom bore this expectation out. Using the 32-channel head coil, and the 3 mm / 500-timepoint EPI-stability protocol we run daily for scanner quality assurance, we observed a ~25% increase in tSNR when the protocol was first implemented on the Prisma^{fit}. However, the BOLD scans conducted on the 8 human subjects suggest that physiological noise in humans, at this frequency and field strength, is a great equalizer [11]. Figure 7 summarizes the tSNR results. The 3 mm / TR = 3 sec / no SMS resting state BOLD scans showed no change in average tSNR across the whole brain for the 8 subjects ($p > 0.05$). At higher spatial resolution, there were small gains in tSNR observed with the Prisma^{fit}. The TR = 2 s / SMS 3 protocol showed a ~5% gain in tSNR – although not statistically significant given the number of subjects ($p > 0.05$). The high temporal resolution resting-state BOLD scans (TR = 750 ms / SMS = 8) showed a modest gain of ~20% when averaged across all subjects ($p < 0.001$). However, benefits for resting-state network analysis were minimal, with improved definition of the networks seen in some subjects, but no quantifiable improvement observed in other subjects, or when averaged over all eight subjects. It is possible that certain tasks that yield weak activations may provide better results on the Prisma^{fit} under conditions of high spatial and/or temporal resolution. But for routine BOLD scans as commonly carried out in neuroimaging studies, with a spatial resolution of ~2.5–3 mm and TR of 2–3 sec, the Prisma will provide similar quality BOLD data to the Trio.

However, the new hardware of the Prisma^{fit} led us to re-evaluate what should be baseline acquisition protocols for BOLD scanning for routine use, with respect to either spatial or temporal resolution. The full details of this BOLD optimization is beyond the scope of this article. However, one example warrants brief mention, for it relies on a combination of improvements in the gradient coil and the improved speed of the new reconstruction

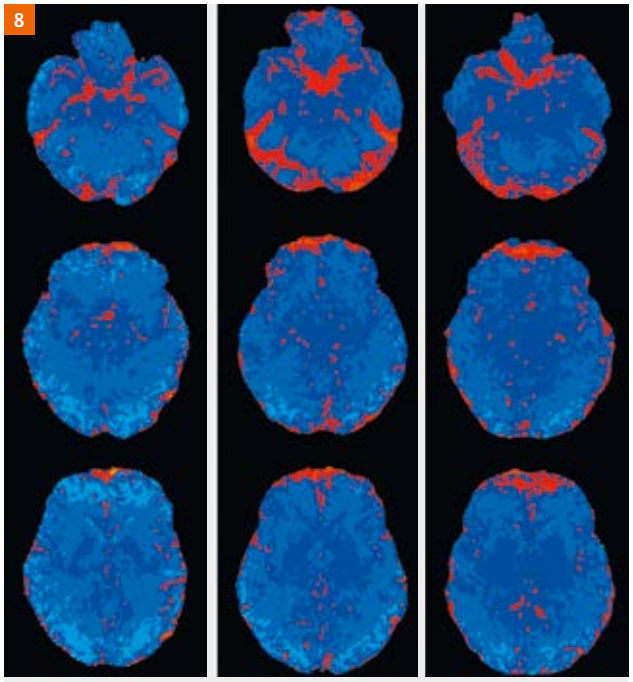

Figure 8:
Maps of tSNR difference in resting-state BOLD scans from three axial slices in three subjects, acquired on the MAGNETOM Prisma^{fit}. Red / orange indicates regions where tSNR is higher using a 1.7 mm resolution / GRAPPA = 2 / SMS = 3 protocol. Blue indicates regions where tSNR is higher with a 2.2 mm / no GRAPPA / SMS = 3 protocol.

computer, combined with simultaneous multi-slice techniques, which allowed us to push the envelope of spatial resolution for whole-brain BOLD scanning beyond what was routinely possible on the Trio, and achieve 1.5 mm and 1.7 mm isotropic resolution that our psychology faculty are now using successfully in standard neuroimaging studies. While not technically impossible on the Trio, the improved slew rate of the Prisma gradient coil and the higher "forbidden echo spacing" range due to acoustic resonances (0.78–0.93 ms vs ~0.58–0.69 ms on the Trio), enable the very large matrix size required for this spatial resolution with only two-fold GRAPPA acceleration to keep the TE to around 30 ms. Along with the improved echo-spacing that makes each echo train slightly shorter, the use of SMS allows the ~80–90 slices required for full brain coverage to be acquired in a 2-second TR, while the improved reconstruction system enables the data to be reconstructed without lagging behind the acquisition, despite the large matrix size and number of slices. Acquiring such data would certainly tax the older reconstruction hardware of the Trio.

The main benefits of using such a high spatial-resolution is to reduce partial volume effects over the cortical surface and to further ameliorate susceptibility-induced dropout and distortion in high-susceptibility areas of the human brain such as the orbital frontal cortex and the temporal poles. In these areas, EPI signal, and BOLD activations, may be seen from brain regions that are often not detected at 3T. (The benefits of higher spatial resolution, while maintaining high MR signal despite using smaller voxels, is one of the benefits of using an ultra-high field MRI system such as the 7T MAGNETOM Terra.) While the tSNR is lower in much of the brain than for acquisition protocols with ~2.0–2.5 mm spatial resolution, on the MAGNETOM Prisma^{fit}, we found the tSNR remained high enough to detect robust BOLD activations such as those of the principal resting-state networks with similar BOLD sensitivity to what was achieved at coarser spatial resolutions. In addition, not only was tSNR improved in the frontal and temporal regions, but we have detected – in numerous subjects – increased tSNR around much of the cortical surface, specifically in visual and parietal regions, where we did not initially expect significant benefit. This improved tSNR at high resolution presumably results from decreased partial-volume effects around the cortical surface, where larger voxels are contaminated by significant amounts of CSF with inherent physiological fluctuations. Figure 8 shows, for 3 axial slices in 3 different subjects, areas in red where tSNR is higher when using a 1.7 mm / TR 2 sec protocol than when using a 2.2 mm / TR 2 sec protocol (2.2 mm being the highest spatial resolution we could achieve without using in-plane acceleration, while keeping TE below 35 ms). The blue regions indicate where the 2.2 mm protocol had higher tSNR, as a result of higher mean signal in the larger voxels. Figure 9 shows group-average functional connectivity maps for 2 different protocols trialed on the Prisma^{fit}, namely the 2.2 mm spatial resolution protocol used in Figure 8 and the 1.5 mm protocol described above. The network maps, from two different seed regions, were remarkably similar despite the reduction in voxel size. Work from some of CBS's psychology faculty users employing the 1.5 mm spatial resolution protocol at 3T is already appearing in the literature [12], while others have employed increased temporal resolution in new studies [13].

Conclusions

The MAGNETOM Prisma^{fit} has been an incredible resource and superb tool for high-quality neuroimaging studies at Harvard's Center for Brain Science Neuroimaging facility. The hardware advances in the MAGNETOM Prisma^{fit}, as compared to the MAGNETOM Trio, provide the potential for significant improvements in diffusion imaging acquisition protocols, while functional (BOLD) imaging can benefit in a narrower range of optimized high-resolution protocols making higher spatial or temporal

9

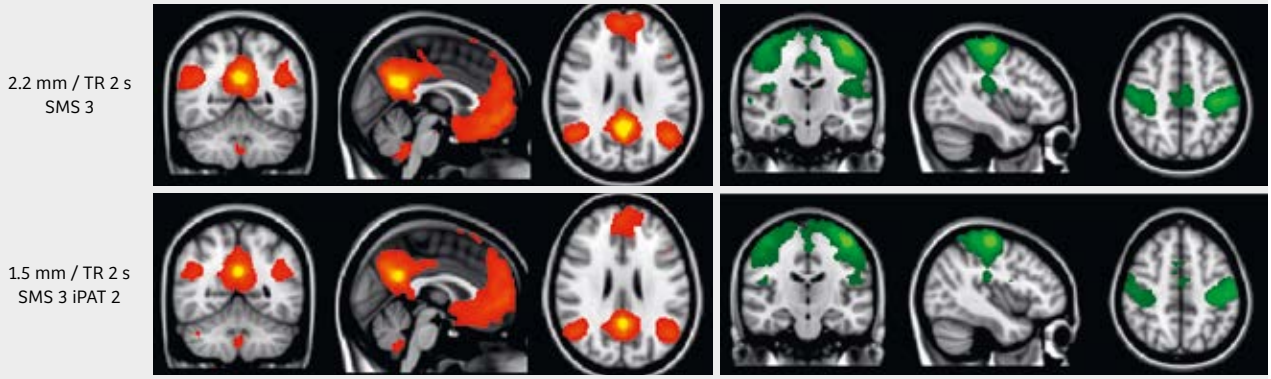

Figure 9:
Group average maps over 8 subjects of two different functional connectivity networks (Default Network from the posterior Cingulate cortex seed, and the Motor network from the left hemisphere Hand region seed) acquired with 2 different acquisition protocols on the MAGNETOM Prisma^{fit}: 2.2 mm / TR 2 sec / SMS = 3, and 1.5 mm / TR 2 sec / iPAT (GRAPPA) = 2 / SMS = 3.

resolution routinely attainable. However, of importance to those running long-term studies that require system stability, we have shown that coarser-resolution BOLD protocols and older, simpler diffusion protocols can be translated from the Trio to the Prisma^{fit} and provide data of a similar quality in terms of signal stability (tSNR), resting state BOLD activation, and standard-deviation of ADC and FA for fixed ROIs of ordered white matter. Additionally, minimal variation is observed in brain morphometric data derived from T1-weighted images from the same subjects, acquired over a 4-month interval, on the Trio and the Prisma^{fit}, indicating that scanner upgrade, in this case, should not bias long-running morphometric studies, provided gradient non-linearity is accounted for.

Acknowledgements

Harvard Center for Brain Science; NIH Shared Instrumentation Grant S10OD020039; NIH Grants P41-RR14075, U24-RR021382.

References

1 van der Kouwe AJ, Benner T, Salat DH, Fischl B. Brain morphometry with multiecho MPRAGE. NeuroImage, 40(2):559–569 (2008).
2 Moeller S, Yacoub E, Olman CA, Auerbach E, Strupp J, Harel N, Uğurbil K. Multiband multislice GE-EPI at 7 Tesla with 16-fold acceleration using Partial Parallel Imaging with application to high spatial and temporal whole-brain fMRI. Magnetic Resonance in Medicine, 63(5);1144–1153 (2010).
3 Setsompop K, Gagoski BA, Polimeni JR, Witzel T, Wedeen VJ, Wald LL. Blipped-controlled aliasing in parallel imaging for simultaneous multislice echo planar imaging with reduced g-factor penalty. Magnetic Resonance in Medicine, 67(5);1210-1224 (2012).
4 Fischl B, Dale AM. Measuring the thickness of the human cerebral cortex from magnetic resonance images. Proceedings of the National Academy of Sciences USA, 97(20):11050-11055 (2000).
5 Reuter M, Rosas HD, Fischl B. Highly Accurate Inverse Consistent Registration: A Robust Approach. NeuroImage, 53(4):1181–1196 (2010).
6 Desikan RS, Segonne F, Fischl B, Quinn BT, Dickerson BC, Blacker D, Buckner RL, Dale AM, Maguire RP, Hyman BT, Albert MS, Killiany RJ. An automated labeling system for subdividing the human cerebral cortex on MRI scans into gyral based regions of interest. NeuroImage, 31(3):968-980 (2006).
7 surfer.nmr.mgh.harvard.edu/fswiki/CorticalParcellation
8 Yeo BT, Krienen FM, Sepulcre J, Sabuncu MR, Lashkari D, Hollinshead M, Roffman JL, Smoller JW, Zöllei L, Polimeni JR, Fischl B, Liu H, Buckner RL. The organization of the human cerebral cortex estimated by intrinsic functional connectivity. Journal of Neuropyhsiology, 106(3);1125-1165 (2011).
9 Mair RW, Reuter M, van der Kouwe AJ. Validation of Cortical Thickness/Volume Data from Multi-Echo MPRAGE Scans with Variable Acceleration in Young and Elderly Populations. Proceedings of ISMRM, 22:1795 (2014).
10 Mair RW, Reuter M, van der Kouwe AJ, Fischl B, Buckner RL. Quantitative Comparison of Morphometric Data from Multi-Echo MPRAGE Variable Acceleration and Different Head Coils. Proceedings of ISMRM, 21:947 (2013).
11 Triantafyllou C, Polimeni JR, Wald LL. Physiological noise and signal-to-noise ratio in fMRI with multi-channel array coils. NeuroImage, 55(2):597-606 (2011).
12 Thakral PP, Benoit RG, Schacter DL. Imagining the future: The core episodic simulation network dissociates as a function of timecourse and the amount of simulated information. Cortex, 90(1):12-30 (2017).
13 Braga RM, Buckner RL. Parallel Interdigitated Distributed Networks within the Individual Estimated by Intrinsic Functional Connectivity. Neuron, 95(1):457–471 (2017).

Contact

Ross W Mair, Ph.D.
Harvard University
Center for Brain Science

NW 231.10
52 Oxford St
Cambridge, MA, 02138
USA
rmair@fas.harvard.edu

GOBrain 5-Minute MRI in Children: Shown to Reduce the Need for Sedation

Nadja Kadom, M.D.[1,2]; Anna Trofimova[1], M.D.

[1] Emory University School of Medicine, Department of Radiology and Imaging Sciences, Atlanta, GA, USA
[2] Children's of Atlanta (CHOA-Egleston), Department of Radiology, Atlanta, GA, USA

Abstract

Shorter MR imaging protocols can be very valuable in pediatrics[1], specifically when they reduce the need for sedation. In a pilot assessment of children under the age 8 years undergoing a 5-minute brain MR for primary headache, we found that the need for sedation was reduced by 70%. A current barrier to wide adoption of this imaging protocol is the lack of data directly comparing diagnostic quality between a 5-minute brain MRI protocol and a conventional MRI brain protocol.

1

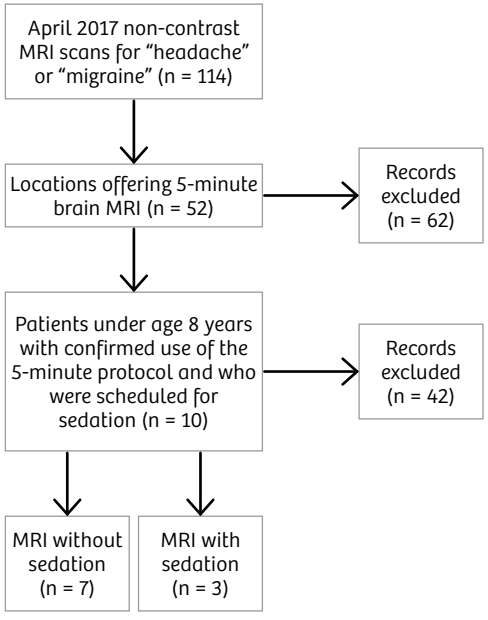

Figure 1: Study setup.

Background

The number of MRI studies requiring sedation in children increases at a rate of 8.5% annually, slightly exceeding the growth rate of CT and MRI imaging studies (8.1%) [1]. While sedation of children for imaging studies has been shown to be extremely safe, there has been some concern regarding potential neurotoxicity of certain anesthetics [2]. Sedation also adds cost to an MRI study, driving up health care expenses for individuals and for society [2]. From the patient and family perspective, use of sedation significantly increases the amount of time spent at the imaging facility and children may experience side effects post-sedation, such as motor imbalance, gastrointestinal symptoms, agitation, and restlessness [3].

Several strategies have been proposed to decrease the use of sedation in children. Child-life specialists can coach patients through MRI exams without sedation, but this may require training on 'mock' scanners, which are expensive and not widely available. Child-life coaching may lead to frequent interruptions during the scan, which could disrupt the MRI schedule. Video and audio technologies have been successful in serving this purpose and resulted in up to 45% decrease in sedation utilization [4]. In infants, feeding and bundling can be used to reduce motion artifacts, although this could result in overheating and respiratory compromise [5].

Here, we collected pilot data on using a 5-minute brain MRI protocol and its effect on the need for sedation in children with presumed primary headaches under the age of 8 years.

[1] MR scanning has not been established as safe for imaging fetuses and infants less than two years of age. The responsible physician must evaluate the benefits of the MR examination compared to those of other imaging procedures.

Material and methods

The pilot assessment was performed at a freestanding pediatric hospital that serves as a level I trauma center. We used a software application (Montage Health Solutions Inc, Philadelphia, PA, USA) to search radiology reports for any patients with an imaging indication containing the words "headache" or "migraine" and who underwent a non-contrast brain MRI. The study period was April 1–30, 2017. We excluded any patients 9 years or older assuming that they would be able to undergo MRI brain imaging without sedation. We also excluded two locations within our health care system that do not offer the 5-minute brain MRI protocol. We included only patients in whom we could confirm that the 5-minute brain MRI protocol had been used. For patients meeting inclusion criteria, we checked the medical records to determine whether they were scheduled as a sedated MRI and whether they were completed as a sedated or a non-sedated MRI.

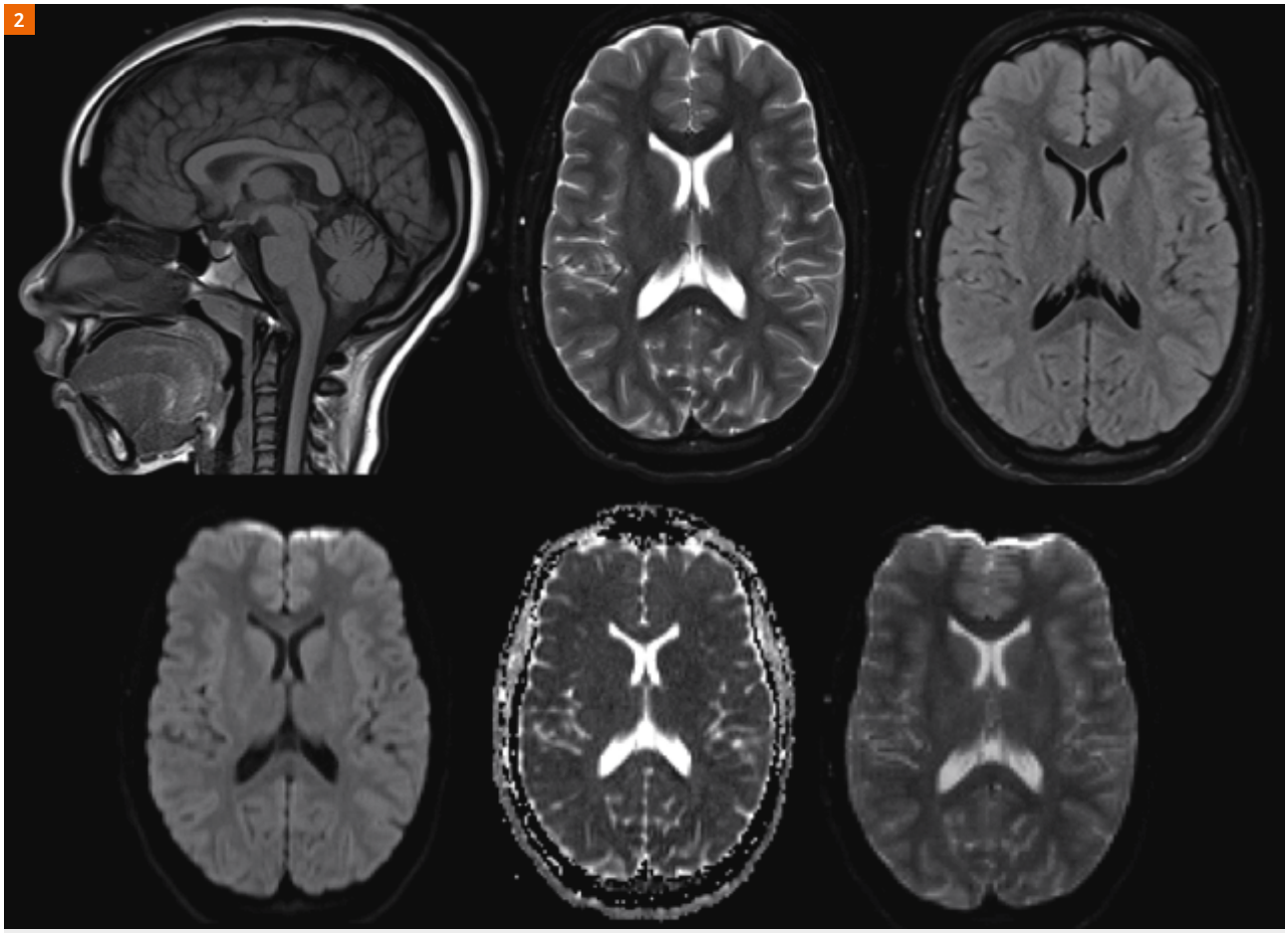

Figure 2: GOBrain 5-minute protocol.

Results

In the study period April 1–30, 2017 we found 114 non-contrast brain MRI studies done for indications containing the words "headache" or "migraine", 52 were done at locations that offer the 5-minute brain MRI protocol, and, of these, there were 10 patients under the age of 8 years in whom we confirmed that the 5-min brain protocol was used and who were scheduled to undergo the MRI with sedation. Of these, 7 were able to complete the MRI without sedation and 3 patients were imaged with sedation (Fig. 1). The percentage of patients converted to a non-sedated exam was 70% (7/10), which equals 6% of the entire cohort (7/114).

Discussion

By using the GOBrain 5-minute protocol we were able to reduce the number of sedated MRI's in the target cohort by 70%. This effect is stronger than the 45% reduction that can be achieved through use of audio-visual distraction. There is potential for increasing the cohort that can benefit from the GOBrain 5-minute protocol by >50% if this protocol was offered at other locations within our network. While the focus of this pilot data assessment was to observe the impact of a 5-minute brain MRI protocol on sedation requirements, we observed other benefits: given that the MRI slots are still 30 minutes long, the conversion of a full brain MRI to a 5-minute protocol opened up time on the MRI schedule that could be used for inpatient imaging or catching up on schedule delays.

The image quality of the 5-minute protocol was good (Fig. 2), but may not meet diagnostic quality standards for certain imaging findings. For example, small parenchymal lesions or small blood products may not be as readily visible given the constraints of the image acquisition in order to achieve short scan times. For this reason, we are limiting the use of this MRI protocol to a patient cohort with "headache" or "migraine" as the sole indication, where most patients are presumed to be screened in the setting of a primary headache with low probability of underlying structural pathology of the brain. Future studies will be needed to compare the diagnostic performance of short MRI protocols in direct comparison to MRI protocols with conventional exam length.

Contact

Nadja Kadom, M.D.
Director of Pediatric Neuroradiology, Children's Healthcare of Atlanta (Egleston)
Associate Professor, Emory University School of Medicine
Department of Radiology and Imaging Sciences

1405 Clifton Rd NE
Atlanta, GA 30322
USA
Cell/text: +1 703 585 6554
nkadom@emory.edu

Nadja Kadom

Dr Anna Trofimova

Acknowledgement

We would like to thank the MRI technologists at CHOA-Egleston and CHOA-Towncenter for their help with data collection and for their enthusiasm and engagement towards the goal of minimizing sedation for children, without compromising the quality of care: Nicole Chin, Melissa Weisel, Jennifer Bagley, and Shane Stewart.

References

1 Wachtel RE, Dexter F, Dow AJ (2009) Growth rates in pediatric diagnostic imaging and sedation. Anesth Analg 108:1616–1621.
2 Barton K, Nickerson JP, Higgins T, Williams RK. Pediatric anesthesia and neurotoxicity: what the radiologist needs to know. Pediatr Radiol. 2017 May 3.doi: 10.1007/s00247-017-3871-4. [Epub ahead of print] Review. PubMed PMID: 28470388.
3 Malviya S, Voepel-Lewis T, Prochaska G, Tait AR. Prolonged recovery and delayed side effects of sedation for diagnostic imaging studies in children. Pediatrics. 2000 Mar;105(3):E42. PubMed PMID: 10699144.
4 Khan JJ, Donnelly LF, Koch BL et al (2007). A program to decrease the need for pediatric sedation for CT and MRI. Appl Radiol 36:30–33.
5 Antonov NK, Ruzal-Shapiro CB, Morel KD, Millar WS, Kashyap S, Lauren CT, Garzon MC. Feed and Wrap MRI Technique in Infants. Clin Pediatr (Phila). 2016 Nov 20. pii: 0009922816677806. [Epub ahead of print] PubMed PMID: 27872353.

Diffusion and Perfusion Fraction Parameters Extracted by a Biexponential Model can be Markers of Healthy Human Placenta Development

Lucia Manganaro[1]; Silvia Capuani[2]; Amanda Antonelli[1]; Michele Guerreri[3]; Silvia Bernardo[1]; Roberta Petrillo[1]; Carlo Catalano[1]

[1] Department of Radiological, Oncological, and Pathological Sciences, Sapienza University of Rome, Italy
[2] CNR-ISC Roma Sapienza, Physics Department, Rome, Italy
[3] CNR-ISC Roma Sapienza, Physics Department and SAIMLAL Department, Morphogenesis & Tissue Engineering, Sapienza University of Rome, Italy

Introduction

The placenta is a temporary organ that forms in the uterus during pregnancy. The primary function of the placenta is to allow metabolic and gaseous exchange between fetal and maternal blood [1] to nourish, protect, and support fetal growth.

1

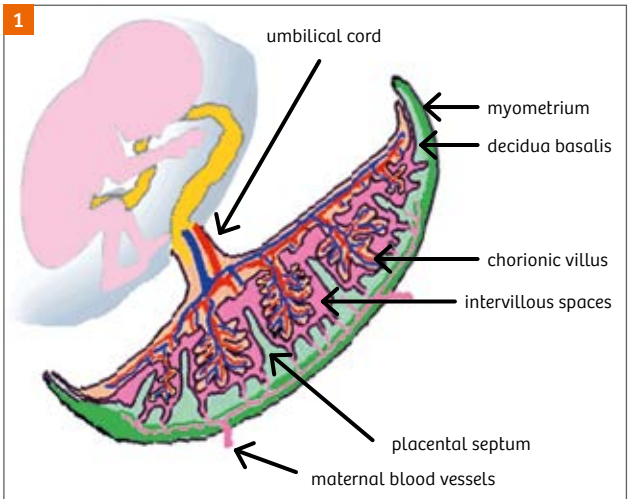

Figure 1:
A schematic representation of the complex placental tissue. The main structure that is repeated in the placenta is placentone (a placentone is a villous tree plus the related part of the intervillous space). Placental tissue contains different diffusion and perfusion compartments. Perfusion processes mainly concern the umbilical cord and villi, whereas diffusion processes mainly concern the decidua basalis and placental septum. In intervillous spaces, diffusion and perfusion are equally present.

To carry out this function, the placenta consists of complex tissue microstructures with a broad variety of differently structured villi, and perfusion functions (Fig. 1). The maternal blood basin, which is supplied by spiral arteries and drained by maternal veins [2], contains villous trees, inside which fetal blood travels from the umbilical arteries to the umbilical vein through fetal capillaries. Maternal blood percolates through the same arborous structures on the outside [3].

Abnormalities in placentation are responsible for pregnancy complications such as preeclampsia, severe growth restriction, and late intrauterine death [4, 5]. Moreover, morphological and physiological characteristics of the placenta are related to the health of the newborn and the future adult [6].

Since ultrasound examinations are limited in their ability to detect early evidence of placental dysfunction at a macroscopic level [7, 8], finding alternative tools for making sensitive and early diagnoses is highly desirable.

Diffusion-weighted imaging (DWI) is a powerful magnetic resonance (MR) technique[1] that provides microstructural and physiological information about human tissues without requiring exogenous contrast agents [9]. DWI can measure water proton displacement within tissues by examining molecular motion at the micrometer scale. Therefore, the diffusion and perfusion compartments (Fig. 1) found in placental tissue can be investigated

[1] MR scanning has not been established as safe for imaging fetuses and infants less than two years of age. The responsible physician must evaluate the benefits of the MR examination compared to those of other imaging procedures.

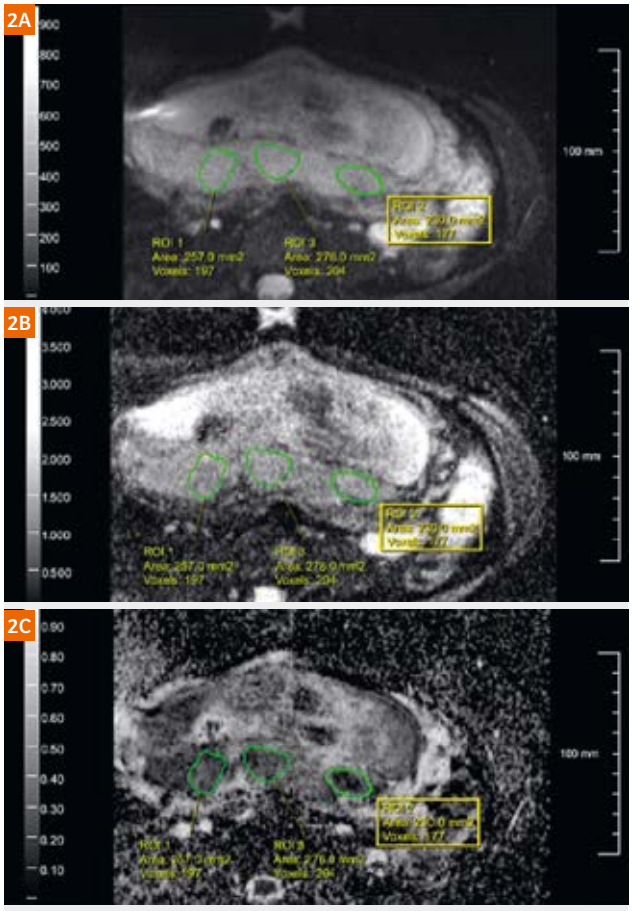

Figure 2:
Axial S0 **(2A)**, ADC **(2B)**, and f-maps **(2C)** of a subject's placenta. The green zones indicate the regions of interest (ROIs) evaluated in this study. ROI 1 is the umbilical region of interest; ROI 2 is the peripheral placenta region of interest; ROI 3 is the central placenta region of interest.

using diffusion and perfusion parameters that are especially sensitive to microscopic tissue changes.

The apparent diffusion coefficient (ADC) of water molecules in tissues can be measured by DWI signal decay as a function of the different degrees of diffusion weights (b-values) [9] through a simple fit of acquired data to a monoexponential function. By using a biexponential decay function and a wider range of b-values, perfusion parameters such as perfusion fraction (f) and pseudo-diffusion coefficient (D*) are also obtainable.

Currently, studies that address DWI as an adjunct to placental MRI are limited [10–15]. Moreover, the potential of ADC, f, and D* measurements in the placenta to detect microstructural and vascular changes remains poorly defined. In particular, the promising role of ADC in detecting microstructural changes in the placenta is controversial [10, 13, 14].

Since knowledge of the ADC, f, and D* values indicative of normal placenta development is essential for detecting abnormalities and understanding their pathogenesis, in this study we quantify both water ADC and blood perfusion in placentas of normal pregnancies as a function of the fetus gestational age (GA) using DWI acquisitions. We examined the placenta of pregnant women at 1.5T and used a biexponential model of diffusion to quantify water ADC and blood perfusion parameters f and D* in different placental sites, and assessed their associations with the respective GA.

Methods

Thirty-eight normal singleton pregnancies (GA range 19–37 weeks) that fulfilled the initial study inclusion criteria underwent MRI examination without maternal-fetal sedation. The study was approved by the local Ethics Committee, and written informed consent was obtained from all women before commencing the study.

Study participants were recruited at the General Hospital of Sapienza University of Rome, Italy, between July 2016 and March 2017. All women in our cohort had at least two ultrasound evaluations (including umbilical and uterine artery Doppler) obtained at different GA to assess them for normal pregnancy.

Patients with suspected uteroplacental insufficiency or placental anomalies were excluded. Women with chronic hypertension, diabetes mellitus, or pre-existing renal disease, and women with contraindications for MRI were not included in the study. A normal pregnancy was defined as a single pregnancy in a woman who gave birth at term (> 37 weeks of gestation) to a newborn appropriate for the GA (birth weight within ±2 standard deviation of the standard reference for newborns) [16] (postdelivery criteria). GA was assessed by an early second trimester ultrasound and by last menstrual period (LMP) dating.

The maternal position was supine. The MRI protocol performed with a 1.5T scanner (MAGNETOM Avanto, Siemens Healthcare, Erlangen, Germany) included diffusion-weighted spin-echo echo-planar imaging with repetition time / echo time of TR 4000 ms and TE 79 ms, bandwidth of 1628 Hz/px, and matrix of 192 x 192. The number of slices ranged from 18 to 30. The in-plane resolution was 2.0 x 2.0 mm^2 and the slice thickness was STK 4 mm. The diffusion encoding gradients were applied along 3 non-coplanar directions using seven different b-values (0, 50, 100, 150, 400, 700, 1000 s/mm^2). The number of signal averages (NSA) for each b-value was 4, and the total acquisition time for the DW protocol was 6 minutes.

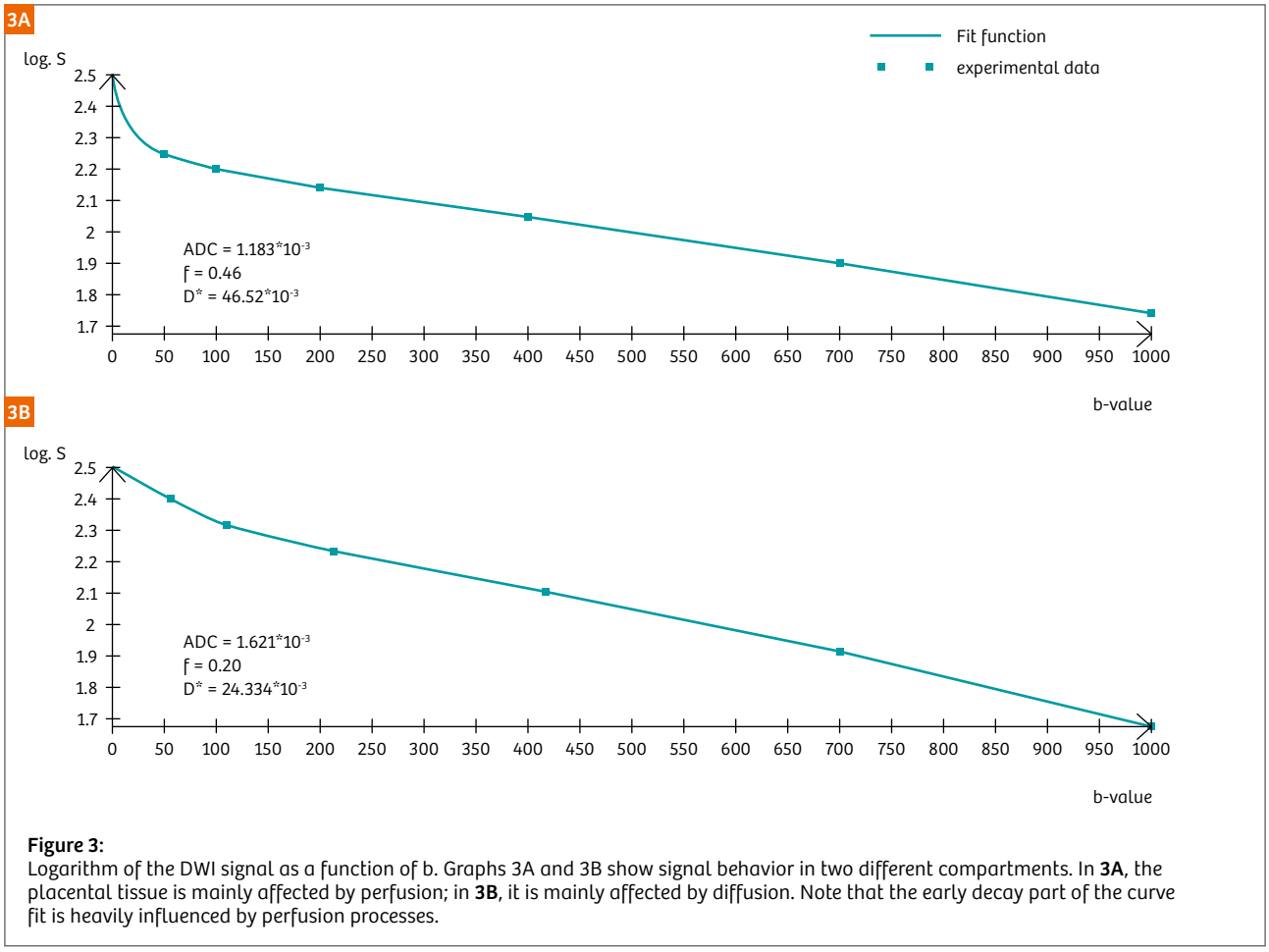

Figure 3:
Logarithm of the DWI signal as a function of b. Graphs 3A and 3B show signal behavior in two different compartments. In **3A**, the placental tissue is mainly affected by perfusion; in **3B**, it is mainly affected by diffusion. Note that the early decay part of the curve fit is heavily influenced by perfusion processes.

Anatomical visualizations of the uterus and the placental tissue were obtained in all cases by using T2-weighted MRI in coronal and transversal view with TE/TR 118/1100 ms and 149/1000 ms respectively.

DICOM images of DWI acquisitions were generated offline with applicable software, and homemade scripts in MATLAB (MathWorks 8.1, R2013a, 1994-2017, MathWorks, Natick, MA, USA) were used. Motion of the mother and fetus[1] is a limitation in placenta studies. Therefore, each diffusion image was reviewed by two radiologists for any evidence of motion in any direction.

The data was preprocessed with FMRIB Software Library, v5.0 (FSL, Oxford, UK). The DW images were realigned with respect to the b = 0 image using the FLIRT tool with six degrees of freedom. Even though FSL is optimized for the brain, good quality results were obtained. Since the low signal-to-noise ratio (SNR) of DW images is an obvious drawback for diffusion techniques, we assessed the SNR of DW images acquired at each b-value. In order to estimate the SNR, we selected an area in the placenta to calculate the signal, and an area placed outside the subject's body to calculate the background noise. We then took the ratio between the mean of the signal and the standard deviation (SD) of the noise, and multiplied it by 0.655. The 0.655 factor is due to the Rician distribution of the background noise in a magnitude MR image. We then calculated the average value of SNR across the cohort.

To investigate the biexponential model's potential for quantifying both water ADC and blood perfusion in the placenta, we investigated placental areas with different relative contributions of perfusion and diffusion (Fig. 1). Peripheral placentones are more clearly separated from each other. In the thicker, more central regions of the placenta, most villous trees overlap, which leads to less distinct differences between the maternal inflow and outflow areas in the placentone [17]. Therefore, we chose three regions of interest (ROIs) according to the lateral distance from the uterine wall. Specifically, three ROIs of about the same area were identified in each placenta by

[1] MR scanning has not been established as safe for imaging fetuses and infants less than two years of age. The responsible physician must evaluate the benefits of the MR examination compared to those of other imaging procedures.

4

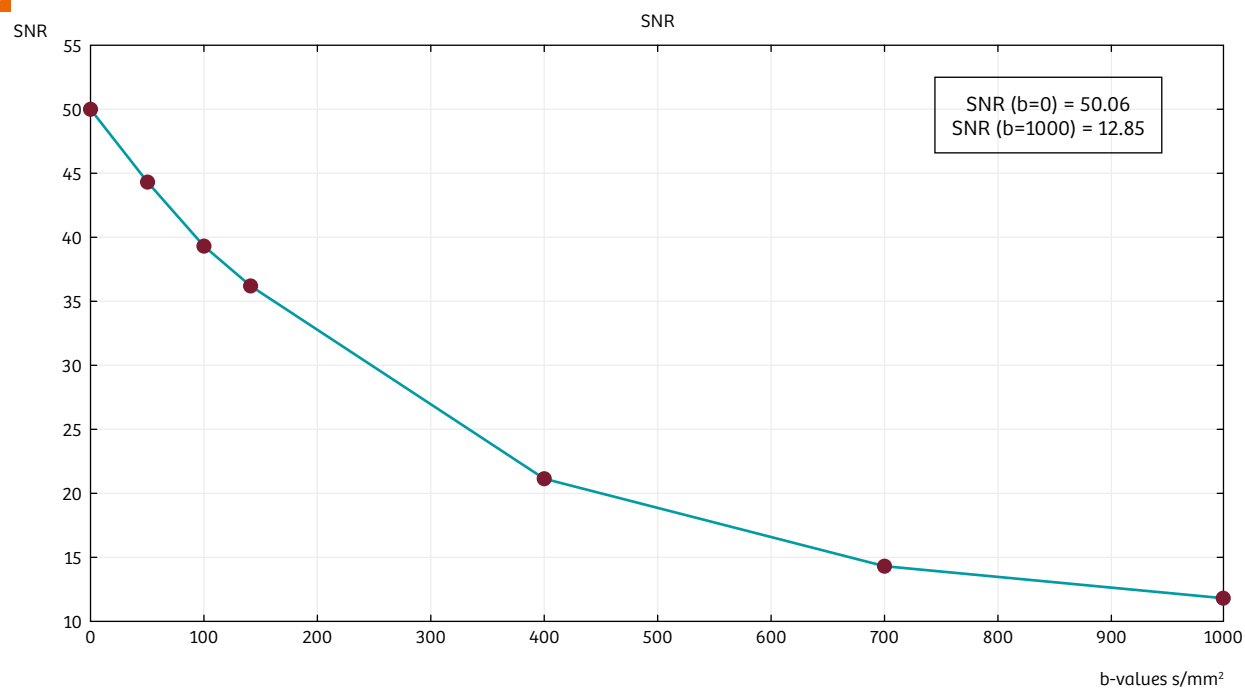

Figure 4:
SNR of DW images averaged over the cohort and the gradient directions, obtained at each b-value. The SNR values are well above the lowest acceptable value (SNR = 5) for considering diffusion data reliable.

an expert radiologist: The central ROI (C-ROI), peripheral ROI (P-ROI), and umbilical ROI (U-ROI) were outlined as shown in Figure 2A.

Data were spatially smoothed using a Gaussian filter with full-width-half-maximum of 3.2 mm. Signal intensity in each ROI was averaged, and data were fitted to the biexponential function [17–19]:

$$S(b)/S(0)=f\cdot\exp(-b\cdot D^*)+(1-f)\cdot\exp(-b\cdot ADC) \quad (1)$$

where S(b) is the attenuated signal, b is the b-value, S(0) is the signal amplitude in the absence of diffusion gradients, and ADC, D*, and f are the apparent diffusion coefficient, the pseudodiffusion coefficient, and the perfusion fraction respectively.

Figure 3 shows an example of the signal decay and the fitting procedure used to extract ADC, D*, and f in each ROI. The two graphs A and B in Figure 3 show the logarithm of the signal as a function of b in order to better highlight the deviation from the linear decay (typical of a signal affected only by diffusion) of the signal most affected by perfusion. The early decay part of the curve fit corresponds to a 'very fast diffusion' compartment, with a rate known as the pseudodiffusion coefficient (D*) that is strongly influenced by perfusion processes. Referring to Figure 1, this signal behavior can be most easily found in the placentones and umbilical cord, i.e., in vessel-rich tissues. The second part of the curve, which is linear in an Ln (S(b)) vs. b plot, corresponds to a compartment diffusing with the standard ADC. This signal behavior can be mainly found in the decidua basalis and placental septum (Fig. 1).

The fractional blood volume (f), or perfusion fraction, is the fraction of water molecules diffusing at the rate D*. Fitted values of f and ADC are usually reproducible and interpretable on the basis of tissue structure, whereas those for D* are less reliable [10].

Mean values and SD of ADC, D*, and f were obtained for each subject. The Pearson test with Bonferroni correction was performed to investigate the correlation between ADC, D*, f, and GA. In a first phase, we studied the correlations by considering the full GA range (19–37 weeks). We then studied the correlations in the third trimester of gestation (GA > 30 weeks).

Differences in ADC, D*, and f in the three investigated ROIs and in the second and third trimester were assessed using the analysis of variance (ANOVA) test. All analyses were performed using SPSS Statistics 17 (IBM SPSS Inc., Chicago, IL, USA).

Results

Two women did not meet the postdelivery criteria, and three subjects were eliminated due to low-quality MRI scans with image artifacts. We therefore investigated 33 placentas from normal singleton pregnancies.

The reliability of ADC, D*, and f measurements depends on the SNR of the DW images, which is displayed in Figure 4. We found that the SNR of the DW images ranges from approximately 50 (for the b = 0 image) to 12 (for DWI acquired at b = 1000 s/mm^2). These SNR values are well above the lowest acceptable value (SNR 5) for considering DW data reliable [20, 21].

The ADC and f maps of a subject's placenta are displayed in Figures 2B and C respectively.

The ADC map discriminates between fast diffusion of amniotic fluid (around 3*10^{-3} mm^2/s) and slow diffusion dynamics of biological water hindered and/or restricted in placental tissue (from approximately 1*10^{-3} mm^2/s to 2*10^{-3} mm^2/s). In the f map, the insertion of the umbilical cord in the placenta (between U-ROI and C-ROI) is clearly visible. Indeed, as expected, it is characterized by higher f values than those found in the placenta.

No significant difference was found between the mean values of ADC, D*, and f in the three selected placental ROIs, and between the mean values of ADC, D*, and f in the second and third trimester of gestation.

A positive linear correlation was found between f and GA in C-ROI ($r = 0.61$, $p < 0.03$) and between f and GA in P-ROI ($r = 0.59$, $p < 0.05$) for GA ≥ 30 weeks. A significant negative correlation was found between ADC and GA ($r = -0.76$, $p < 0.02$) for GA ≥ 30 weeks in P-ROI, while non-dependence of ADC on GA was observed in the GA range of 19–29 weeks (Fig. 5). Figure 5 shows ADC and f mean values as a function of GA in the central and peripheral ROIs.

Discussion

The human placenta is a rapidly developing organ that undergoes structural and functional changes throughout pregnancy. Our aim was to evaluate the potential of the parameters ADC, D*, and f, which were obtained with a biexponential diffusion model, to detect microstructural changes due to placenta development. The biexponential model assures the quantification of ADC without perfusion contamination. It also allows, via the f parameter, the quantification of the percentage of perfusing protons compared to the total volume of water. Finally, D* is strongly affected by perfusion, and is quantified as a pseudodiffusion parameter.

The mean ADC, D*, and f values are in general agreement with those found in the literature [10, 11, 13, 22, 23] and do not differ between the analyzed ROIs. In terms of the multi-compartmentalization of the placental tissue shown in Figure 1, the mean ADC values in our sample reflect a poor hindered water diffusion regime, which is consistent with placental histology that shows the intervillous space (where water randomly diffuses) measuring around 100 micrometers [2–4].

However, in contrast with previous studies performed in healthy placenta [13, 14] and in line with our recent paper [23], we found a significant decrease in ADC from the 30th gestational week (Fig. 5). The decrease in ADC with increasing GA is not a bias caused by an insufficient SNR, as we obtained SNR > 12 at b = 1000 s/mm^2. Instead, it may reflect and highlight physiological parenchymal changes that occur in late gestational age and are characterized by a more fibrotic environment [2]. In particular, calcium deposits develop that can cause small parts of the placenta to die, and may result in some parts being replaced with fibrous tissue. An abnormal growth of fibrous parenchymal tissue increases the barriers to diffusion and thus reduces ADC values [24]. Therefore, after the 30th gestational week, the increase in fibrotic tissue causes more slow dynamics in the placenta and leads to lower ADC values.

The differences between our results [23] and previous ADC results [13, 14] are due to the diffusion model used to estimate placental ADC. Unlike earlier works [13, 14], we used a biexponential model to eliminate perfusion contamination from ADC quantification.

Moreover, in contrast to previous studies in normal placenta performed with a biexponential model [10, 11, 15], and in agreement with our recent paper [23], we found a positive linear correlation between f and GA in the central placental region and in the peripheral placental region from the 30th week onwards. The f vs. GA behavior may reflect the increase in the volume, surface, and length of villi as the placental volume grows [2, 24]. In particular, the chorionic villi mature after the 30th week of gestation, increasing in size to maximize the contact/exchange between maternal and fetal placental substances, and to boost perfusion [24]. We estimated that D* is approximately one order of magnitude greater than ADC. However, its SD is almost 50% of the mean value. The SD of the mean values of ADC and f is roughly less than 12% and 20% respectively.

The b-values of a DWI acquisition should be chosen on the basis of the expected diffusion values and tissue features. In principle, the optimal b-value is roughly equal to the reciprocal of the ADC value that one is trying to estimate

5

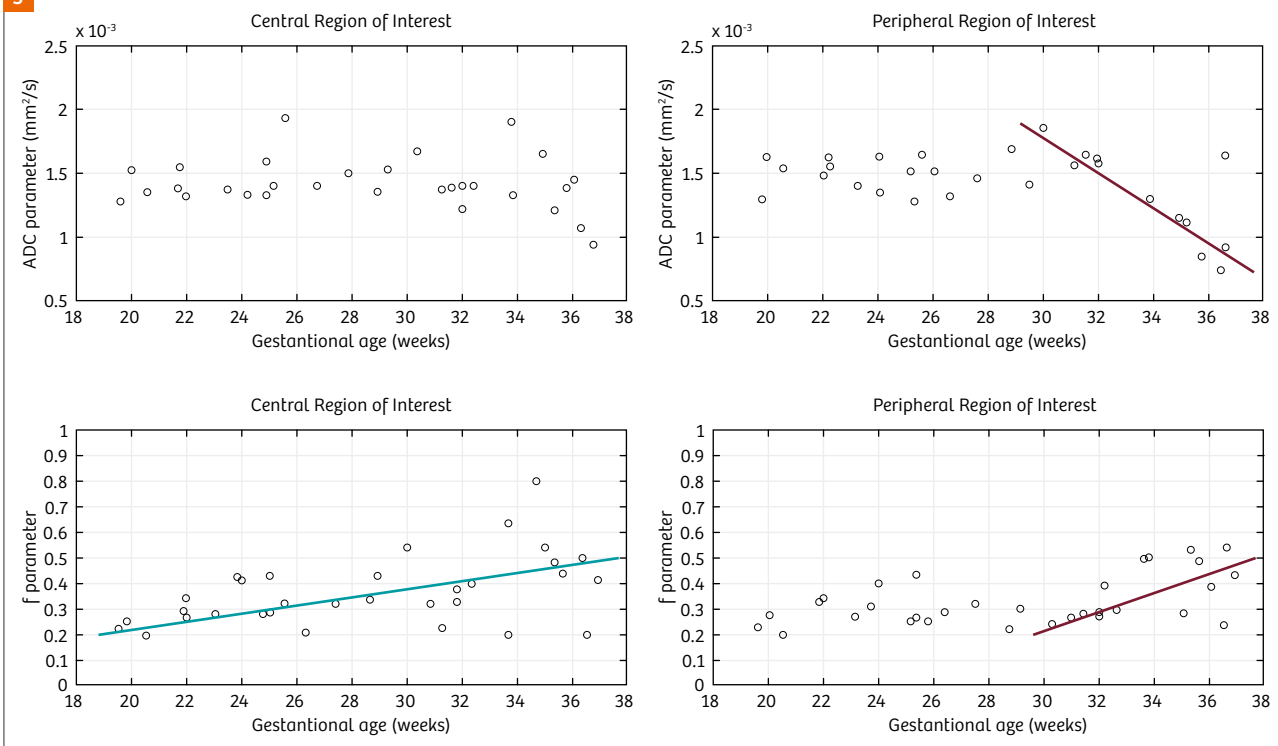

Figure 5:
Scatter plots of ADC and f values as a function of the gestational age (GA) in the central and peripheral placenta regions. The blue line indicates the statistically significant linear correlation found between f and GA ($r = 0.61$, $p < 0.03$) for all GA in the central ROI. The red line indicates the statistically significant linear correlation found between f and GA for GA > 30 weeks in the peripheral ROI ($r = 0.59$, $p < 0.05$), and between ADC and GA for GA > 30 weeks in the peripheral ROI ($r = -0.76$, $p < 0.02$). These data match our recent results [23].

[27]. In this work, we estimated an ADC value range of 0.7–1.7*10^{-3} mm^2/s that required b-values in the range of 600–1400 s/mm^2. Accordingly, we used b-values in the range of 400–1000 s/mm^2, which represents the best compromise between a sufficient SNR and a sufficient diffusion weight. While we can claim to have correctly estimated the ADC value of placental water, we cannot say the same for the perfusion parameters, which show a high variability (especially the D* parameter). To estimate perfusion parameters, we used b-values of 0, 50, 100, and 150 s/mm^2. However, to obtain D* and f parameters with a certain degree of reliability, some data must be acquired at very low b-values, especially in the range b = 0 and b = 50 s/mm^2 [22, 28]. Finally, it is important to emphasize that the biexponential model does not accurately reflect the characteristics of the complex placental tissue. According to recent results obtained in animal models, a diffusion model based on three different diffusion compartments would be more appropriate for modeling placental tissue [25, 26].

In conclusion, in line with our previous work [23], this study shows that ADC measurements performed in the peripheral placenta of 33 normal pregnancies using a biexponential diffusion model detect tissue changes occurring in the third trimester of gestation. In particular, ADC decreases as gestational age increases. Conversely, the fraction f, which represents water molecules affected by perfusion, increases with gestational age in the central placental region during the pregnancy and in the peripheral region during the third trimester. However, although the correlations between ADC, f, and GA are significant, a remarkable spread of data in the graphs of ADC and f vs. GA is observable. Moreover, f and D* show both a standard deviation and a variability that are too high to be considered as potential markers of microstructural changes caused by placental development.

In the light of these results, we have planned further studies to better estimate the perfusion parameters f and D* by acquiring more DW data in the b-value range of b = 0 and b = 150 s/mm^2. In addition, due to the complexity and heterogeneity of the placental tissue, we will choose ROIs with closer links to compartments that are more diffusive or more perfusive.

References

1 Regnault TR, Galan HL, Parker TA, Anthony RV. Placental development in normal and compromised pregnancies—a review. Placenta. 2002; 23 Suppl A:S119-29.
2 Benirschke K, Burton GJ, Baergen RN. Pathology of the Human Placenta. 6th ed. Springer; 2012.
3 Serov AS, Salafia CM, Filoche M, Grebenkov DS. Analytical theory of oxygen transport in the human placenta. J Theor Biol. 2015; 368:133-44.
4 Broses I, Pijnenborg R, Vercruysse L, Romero R. The "Great Obstetrical Syndromes" are associated with disorders of deep placentation. Am J Obstet Gynecol. 2011; 204(3):193-201.
5 Baschat AA, Hecher K. Fetal growth restriction due to placental disease. Semin Perinatol. 2004; 28(1):67-80.
6 Serov AS, Salafia C, Grebenkov DS, Filoche M. The role of morphology in mathematical models of placental gas exchange. J Appl Physiol. 2016; 120:17-28.
7 Siauve N, Chalouhi GE, Deloison B, Alison M, Clement O, Ville Y, Salomon LJ. Functional imaging of the human placenta with magnetic resonance. Am J Obstet Gynecol. 2015; 213 Suppl 4:S103-14
8 Blaicher W, Brugger PC, Mittermayer C, Schwindt J, Deutinger J, Bernaschek G, Prayer D. Magnetic resonance imaging of the normal placenta. Eur J Radiol. 2006; 57(2):256-60.
9 Basser JP. Inferring microstructural features and the physiological state of tissues from diffusion-weighted images. NMR Biomed. 1995; 8(7-8):333-44.
10 Moore R, Issa B, Tokarczuk P, Duncan KR, Boulby P, Baker PN, Bowtell RW, Worthington BS, Johnson IR, Gowland PA. In vivo intravoxel incoherent motion measurements in the human placenta using echo-planar imaging at 0.5T. Magn Reson Med. 2000; 43(2):295-302.
11 Moore RJ, Strachan BK, Tyler DJ, Duncan KR, Boulby P, Baker PN, Worthington BS, Johnson IR, Gowland PA. In utero Perfusing Fraction Maps in Normal and Growth Restricted Pregnancy Measured Using IVIM Echo-Planar MRI. Placenta. 2000; 21:726-32.
12 Linduska N, Dekan S, Messerschmidt A, Kasprian G, Brugger PC, Chalubinski K, Weber M, Prayer D. Placental pathologies in fetal MRI with pathohistological correlation. Placenta. 2009; 30(6):555-9.
13 Manganaro L, Fierro F, Tomei A, La Barbera L, Savelli S, Sollazzo P, Sergi ME, Vinci V, Ballesio L, Marini M. MRI and DWI: feasibility of DWI and ADC maps in the evaluation of placental changes during gestation. Prenat Diagn. 2010; 30(12-13):1178-84.
14 Sivrioğlu AK, Özcan ÜA, Türk A, Ulus S, Yıldız ME, Sönmez G, Mutlu. Evaluation of the placenta with relative apparent diffusion coefficient and T2 signal intensity analysis. Diagn Interv Radiol. 2013; 19:495-500.
15 Sohlberg S, Mulic-Lutvica A, Lindgren P, Ortiz-Nieto F, Wikström AK, Wikström J. Placental perfusion in normal pregnancy and early and late preeclampsia: a magnetic resonance imaging study. Placenta. 2014; 35(3):202-6.
16 Villar J, Ismail LC, Victora CG, Ohuma EO, Bertino E, Altman DG, Lambert A, Papageorghiou AT, Carvalho M, Jaffer YA, Gravett MG, Purwar M, Frederick IO, Noble AJ, Pang R, Barros FC, Chumlea C, Bhutta ZA, Kennedy SH; International Fetal and Newborn Growth Consortium for the 21st Century (INTERGROWTH-21st). International standards for newborn weight, length, and head circumference by gestational age and sex: the Newborn Cross-Sectional Study of the INTERGROWTH-21st Project. Lancet. 2014; 384(9946):857-68.
17 Niendorf T, Dijkhuizen RM, Norris DG, Van Lookeren Campagne M, Nicolay K. Biexponential diffusion attenuation in various states of brain tissue: implications for diffusion-weighted imaging. Magn Reson Med.1996; 36(6):847-57.
18 Mulkern RV, Gudbjartsson H, Westin CF, Zengingonul HP, Gartner W, Guttmann CR, Holtzman D, Kyriakos W, Jolesz FA, Maier SE. Multi-component apparent diffusion coefficients in human brain. NMR Biomed. 1999; 12:51-62.
19 De Santis S, Gabrielli A, Palombo M, Maraviglia B, Capuani S. Non-Gaussian diffusion imaging: a brief practical review. Magn Reson Imaging. 2011; 29(10):1410-6.
20 Nair G, Hu XP. Manifestation and Post-hoc Correction of Gradient Cross-term Artifacts in DTI. Magn Reson Imaging. 2012; 30(6):764-73.
21 Rossi C, Boss A, Martirosian P, Steidle G, Capuani S, Claussen CD, Maraviglia B, Schick F. Influence of steady background gradients on the accuracy of molecular diffusion anisotropy measurements. Magn Reson Imaging 2008; 26:1250-8.
22 De Santis S, Rebuzzi M, Di Pietro G, Fasano F, Maraviglia B, Capuani S. In vitro and in vivo MR evaluation of internal gradient to assess trabecular bone density. Phys Med Biol. 2010; 55(19):5767.
23 Capuani S, Guerreri M, Antonelli A, Bernardo S, Porpora MG, Giancotti A, Catalano C, Manganaro L. Diffusion and perfusion quantified by Magnetic Resonance Imaging are markers of human placenta development in normal pregnancy. Placenta. 2017; 58:33-9.
24 Baergen RN. Manual of Pathology of the Human Placenta. 2nd ed. Springer; 2011.
25 Avni R, Neeman M, Garbow JR. Functional MRI of the placenta – From rodents to humans. Placenta. 2015; 36(6):615-22.
26 Solomon E, Avni R, Hadas R, Raz T, Garbow JR, Bendel P, Frydman L. Major mouse placental compartments revealed by diffusion-weighted MRI, contrast-enhanced MRI, and fluorescence imaging. Proc Natl Acad Sci U S A. 2014; 111(28):10353-8.
27 Capuani S, Manenti G, Iundusi R, Tarantino U. Focus on Diffusion MR Investigations of Musculoskeletal Tissue to Improve Osteoporosis Diagnosis: A Brief Practical Review. BioMed Res Int. 2015; 2015:948610.
28 Le Bihan D, Breton E, Lallemand D, Aubin ML, Vignaud J, Laval-Jeantet M, Separation of diffusion and perfusion in intravoxel incoherent motion MR imaging. Radiology. 1988; 168(2):497-505.

Contact

Lucia Manganaro, M.D.
Department of Radiological, Oncological and Pathological Sciences
Sapienza University of Rome

Vle Regina Elena 324
00161 Roma
Italy
Phone +39 06 49972639
lucia.manganaro@uniroma1.it

High Resolution Breast Imaging using StarVIBE on 3T MAGNETOM Skyra^fit

Maria L. Carr[1]; Ioannis Koktzoglou[1]; Shivraman Giri[2]; Wei Li[1]; Georgia Spear[1]; Robert R. Edelman[1]

[1] NorthShore University HealthSystem, Evanston, IL, USA
[2] Siemens Healthineers, Chicago, IL, USA

New prospects for MRI breast imaging

Breast cancer is the most commonly diagnosed malignancy in women, with more than 40,000 deaths annually in the United States [1]. Magnetic resonance imaging (MRI) has become a key diagnostic tool in this disorder, and is essential for the evaluation of high-risk patients. The standard protocol relies on a dynamic contrast-enhanced 3D volume-interpolated breath-hold examination (VIBE) using a Cartesian *k*-space trajectory. However, use of a Cartesian *k*-space trajectory limits the flexibility of the technique resulting in an undesirable trade-off between temporal and spatial resolution. High spatial resolution is required to detect small lesions. However, this comes at the expense of acquisition speed and can result in suboptimal depiction of contrast agent kinetics (needed for lesion characterization). Recently, we have begun using an alternative technique, called StarVIBE, that uses radial *k*-space trajectory. StarVIBE provides some significant advantages over the conventional Cartesian-based VIBE approach, including:

1. reduced motion-sensitivity;
2. better image quality when using high scan acceleration factors; and
3. ability to acquire images with high temporal resolution that also provide high spatial resolution.

How to build your protocol on *syngo*.MR E11C 3T MAGNETOM Skyra/Skyra^fit system?

StarVIBE is an optional package on *syngo*.MR E11A or later software versions. It requires FREEZEit license. For high-resoluton breast imaging using StarVIBE, we used one of the existing StarVIBE protocols from SIEMENS tree, and modified some parameters. One can start with any of the protocols from SIEMENS tree; in our case, we started with the one in:

SIEMENS → Thorax → library →3D (protocol name: t1_starvibe_fs_tra_ISO). The changes required to adapt this protocol for high-resolution breast imaging are described in Table 1.

Parameter name	Tab combination	Breast StarVIBE
Orientation	Routine	axial
Slice thickness	Routine	0.8 mm
Slice oversampling	Routine	6.7%
Slice per slab	Routine	240
TR	Contrast/Common	5.45 ms
TE	Contrast/Common	2.46 ms
Flip angle	Contrast/Common	11°
Fat suppression	Contrast/Common	Q-fat sat
Table position mode	System/ Miscellaneous	ISO
Radial views	Resolution/Common	213
FOV read	Resolution/Common	280 mm
Base resolution	Resolution/Common	416
Slice resolution	Resolution/Common	50%
Slice partial Fourier	Resolution/Common	Off
Optimization	Sequence/Part1	In phase
Bandwidth	Sequence/Part1	430 hz/px
RF Pulse type	Sequence/Part2	Normal
Incr. Gradient spoiling	Sequence/Part2	Yes
Scan Time	Routine	2:35 min

Table 1:
Protocol adaptations required for StarVIBE sequence for breast imaging. Please start with the protocol that can be found on the scanner at: SIEMENS → Thorax → library → 3D. Protocol name: t1_starvibe_fs_tra_ISO. Invivo Sentinelle Breast coil used.

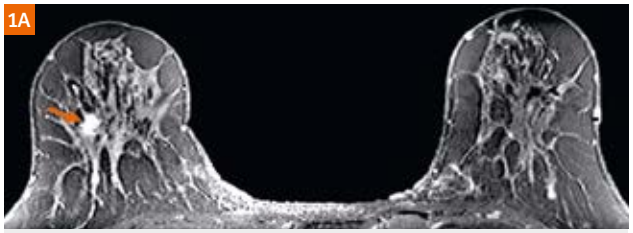

StarVIBE acquisition
Resolution: 0.67 x 0.67 x 0.8 mm³
Scan time: 2 min 35 sec

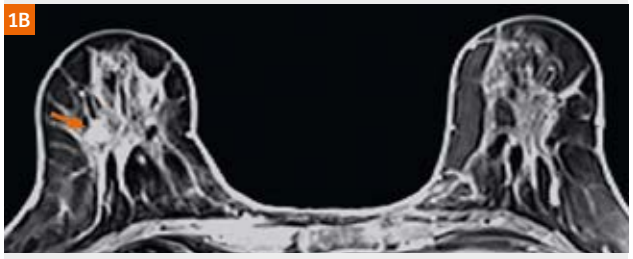

Conventional VIBE acquisition
Resolution: 1.02 x 0.82 x 1.60 mm³
Scan time: 2 min 49 sec

Figure 1:
Comparison of high-resolution StarVIBE **(1A)** with standard Cartesian VIBE **(1B)**, acquired in similar scan times. Due to superior spatial resolution, the enhancing mass (arrow) is much more sharply delineated using StarVIBE than with the standard imaging technique. (1A) Spatial resolution 0.67 x 0.67 x 0.80 mm³ (1B) 1.02 x 0.82 x 1.60 mm³.

Discussion

We showed that StarVIBE can be used for dynamic contrast-enhanced 3D imaging of the breast. In lieu of the standard Cartesian VIBE protocol, StarVIBE allows for reduced motion sensitivity, as well as the ability for high temporal resolution and spatial resolution, which increases the conspicuity of smaller lesions. Scan time with StarVIBE can be accelerated by reducing the number of acquired radial views, which comes at the expense of reduced signal-to-noise ratio and increased streak artifacts. Whereas accelerating Cartesian VIBE usually involves an increase in the iPAT factor, which can often result in strong ghost-like artifacts, the acquisition of fewer radial views with StarVIBE results in streaks artifacts which tend to be less pronounced.

Contact

Maria L. Carr R.T.R. (CT)(MR)
MRI Corporate Supervisor
NorthShore University HealthSystem

Walgreen Building, Suite G507
2650 Ridge Avenue
Evanston, IL 60201
USA
Phone: +1 847-570-4349
MCarr@northshore.org

Learn more!

Abbreviated Breast MRI

Professor Christiane Kuhl, M.D.
University of Aachen, RWTH Aachen, Germany

Don't miss the talks delivered by experienced and renowned experts at
www.siemens.com/magnetom-world

"Scars and stars" – MRI of Normal Findings and Complications After Cesarean Delivery

Malwina Kaniewska[1]; Michael Hohl[2]; Leonhard Schäffer[2]; Martin Heubner[2]; Rahel A. Kubik-Huch[1]

[1] Institute of Radiology, Kantonsspital Baden, Baden, Switzerland
[2] Department of Obstetrics and Gynaecology, Kantonsspital Baden, Baden, Switzerland

Abstract and key points

In the last two decades the number of deliveries by means of cesarean section (CS) has increased worldwide and, consequently, there is an increasing number of referrals to radiology departments.

Changes related to cesarean delivery (CD) are often detected as incidental findings in magnetic resonance (MR) examinations that are primarily performed for other indications.

Due to high-contrast and soft-tissue resolution, MR examinations deliver clinically important information on pelvis anatomy and postsurgical changes. T2-weighted sequences are essential in the assessment of morphology of the female pelvis. Postoperative artifacts with so-called "blooming effect" ("stars") are visible on gradient echo (GRE) and T2 star (T2*) sequences.

The main aim of our article is to familiarize radiologists with common MRI findings and characteristic imaging features after CS. Complications after CD, which may account for pelvic pain and deterioration of future reproductive health, are presented.

Given a global increase in the number of deliveries by CS, radiologists should be aware of common MRI findings and characteristic features of complications related to cesarean delivery.

Introduction

In the largest country of the world, China, the number of cesarean deliveries increased between 2008 and 2014 from 28.8% to 34.9% [1]. A similar tendency has been observed in Europe (from 7.4% in 1990 to 15.8% in 2008), and in the USA (from 21.2% in 1990 to 32.8% in 2011) [2, 3]. Changes related to the cesarean delivery (CD) are often detected as incidental findings in magnetic resonance (MR) examinations that are primarily performed for other indications (i.e. gastrointestinal, orthopedic). Moreover, acute and chronic postsurgical complications after a cesarean section (CS) are encountered with increasing frequency.

Clinical presentation

In the era of cesarean deliveries complications due to a previous CD, such as increased risk for implantation difficulties and further infertility or even uterine rupture,

Figure 1: "STARS" Postoperative susceptibility artifacts

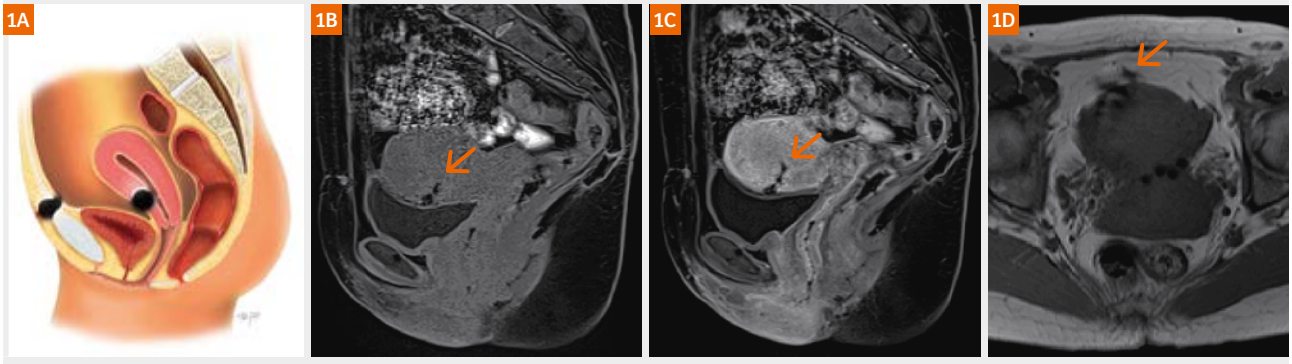

1A: Schematic image shows the so-called "blooming effect", which is usually visible on T2* and GRE MR sequences.
1B–1D: Susceptibility artifacts due to surgical sutures on MR images.
1B: Multi-phase dynamic contrast-enhanced T1-weighted sagittal images VIBE sequence, early phase.
1C: Multi-phase dynamic contrast-enhanced T1-weighted sagittal images VIBE sequence, late phase.
1D: T1-weighted axial FLASH 2D image. Artifacts are labelled with an arrow. Note that the cesarean section scar is located relatively high, above the lower anterior uterine segment.

are serious clinical considerations. Infection (wound infection and dehiscence, abscess and pelvic thrombophlebitis) is the most frequent complication after a CD/CS. The characteristic symptoms for acute/subacute complications after a CD/CS comprise excessive vaginal bleeding or hematuria, decreased hemoglobin level, postsurgical fever, and abdominal or pelvic pain. Postmenstrual spotting, urological problems, lower abdominal pain and infertility belong to the chronic complications after CD/CS. Chronic uterine alterations after CD are often discovered incidentally and may present without any symptoms. The increasing use of high-resolution ultrasound in daily routine check-ups in particular may lead to the detection of findings warranting further evaluation by MRI.

Following a CS, women are shown to be at higher risk for postpartal infection than those having had spontaneous or planned vaginal deliveries [4–6]. The impact of different surgical approaches (i.e. single- vs. double-layer closure of hysterotomy) on adverse outcomes and obstetric complications in future pregnancies has been examined, but there is still no consensus on best operation technique.

Role of magnetic resonance imaging (MRI)

Magnetic resonance imaging of the female pelvis with high-resolution T2-weighted images of the uterus is considered to be a reliable examination of patients with gynecological disorders, with 3 Tesla MRI scanners believed by some authors to provide even better image quality [7, 8]. Albeit MR examinations are not usually performed in acute setting, taking into account the increasing tendency of CD, MR imaging has become generally more frequent, even in case of (sub-)/acute complications.

The role of MR examinations has been demonstrated in pre- and postpartum conditions as a complimentary imaging technique to transvaginal ultrasound (TVUS) [9–13]. Although sonography is a first line imaging approach, it may be hampered by patient habitus and may be impaired by chronic complications after a CS like scarring tissue or adhesions between anterior uterine wall and posterior abdominal wall.

Acute/subacute complication	Chronic complications
Uterine rupture / Uterine dehiscence	Healed section scar / Adhesions
Bladder flap hematoma	Niche and related recurrent infections, vaginal spottig / Retained products of conception (RPOC)
Subfascial wound hematoma	Abdominal wall / Scar endometriosist
Superficial wound hematoma	Ectopic pregnancy in the ceasarean section scar
Infection / Abscess	Infertility

Table 1: Acute/subacute and chronic complications after Cesarean section.
Adapted from Rodgers et al. Radiographics doi: 10.1148/rg.326125516, PMID: 2306516.

MR examination delivers information on pelvis morphology and postsurgical changes and provides excellent soft-tissue contrast. Furthermore, contrary to US, it is an operator independent procedure and provides reproducible data.

Procedure details

High-resolution T2-weighted MRI sequences provide essential information on morphology of the female pelvis. They are normally performed in a sagittal plane and then angulated to the long axis of the uterus for further assessment. Contrast administration is usually not needed, but may be considered in case of a suspected infection. After a CS postoperative susceptibility artifacts in the section scar and in the abdominal wall are expected. A so-called "blooming effect" due to the susceptibility artifacts is visible on gradient echo (GRE) and T2 star (T2*) sequences and is depicted in Figures 1A–1D.

Complications after CD visible in the MR examinations

Acute/subacute and chronic complications after a CD are shown in Table 1.

Sudden pelvic pain, severe vaginal bleeding or hematuria and related laboratory results prompt immediate clinical investigation and a proper imaging. Presumed acute complications after a CD include uterine rupture, uterine dehiscence, bladder flap, superficial, and subfascial wound hematoma. In the acute setting fast and time-efficient examinations as ultrasound or computed tomography are preferably performed. However, in case of acute/subacute and chronic complications the MR examination can deliver information on the extension of pathology and involvement of the adjacent structures.

Acute/subacute complications

Uterine rupture and dehiscence

Uterine rupture is the most dangerous, yet underreported life-threatening complication after a CS [14]. Scarred uterus, often due to a previous cesarean delivery is considered to be a risk factor for a complete uterine rupture, especially in patients who choose a vaginal labor after a CS [15–18]. With increasing number of deliveries through cesarean section, higher incidence of uterine ruptures is expected. Schematic images with

uterine rupture and CT images are shown in Figures 2A–2C. Incomplete rupture of the uterine wall with an intact serosal layer characterizes the uterine dehiscence (Figs. 3A–3C). MRI is described as the most reliable modality for detection and evaluation of incomplete uterus rupture, which may be a challenging imaging diagnosis [19].

Bladder flap hematoma

Bladder flap hematoma is a less dramatic complication after a CS and is located between the anterior wall of lower uterine segment and the posterior wall of urinary bladder. This finding can occur after low incision surgery as for instance the Pfannenstiel or Joel-Cohen method, but is considered normal if the hematoma measures less than 4 cm on the axial images [20, 21].

Subfascial and superficial wound hematomas

Subfascial hematoma is an extraperitoneal blood collection located posteriorly to the abdominal musculature. It is a possible consequence after a sutured parietal peritoneum method, resulting from inadequate hemostasis of vessels of the parietal peritoneum and

Figure 2: Uterine rupture

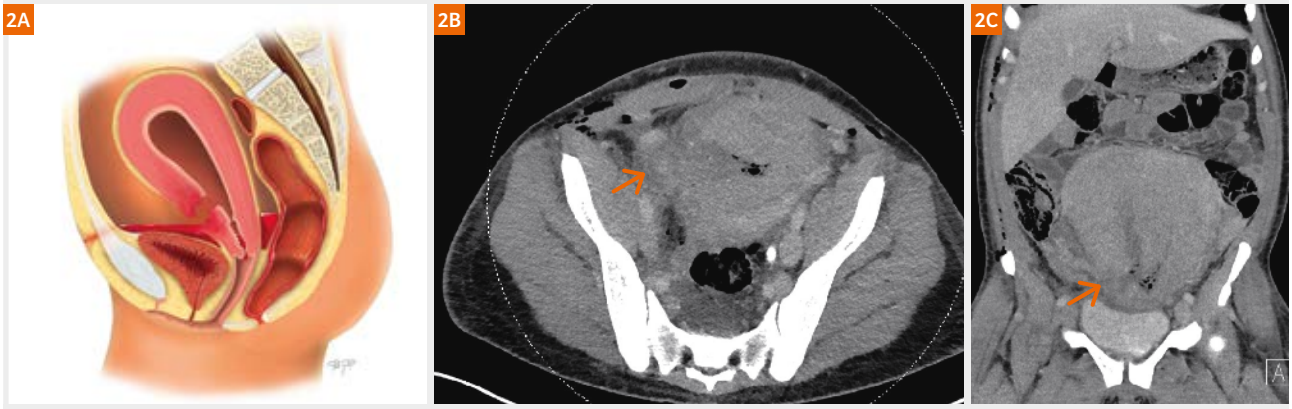

2A: Illustration shows a complete uterine rupture with separation of all layers of the uterine wall. Consecutive communication between the uterine cavity and the peritoneal cavity causes a free blood distribution in the pelvis with blood in the excavatio rectouterine, known as a Douglas space.
2B, C: Axial and coronal contrast-enhanced CT images show the uterine defect due to uterine rupture (arrow). Note increased uterine volume in the postpartal phase (2 days after cesarean. delivery).

In acute setting CT is a method of choice, especially when a uterine rupture is suspected.

Figure 3: Uterine dehiscence

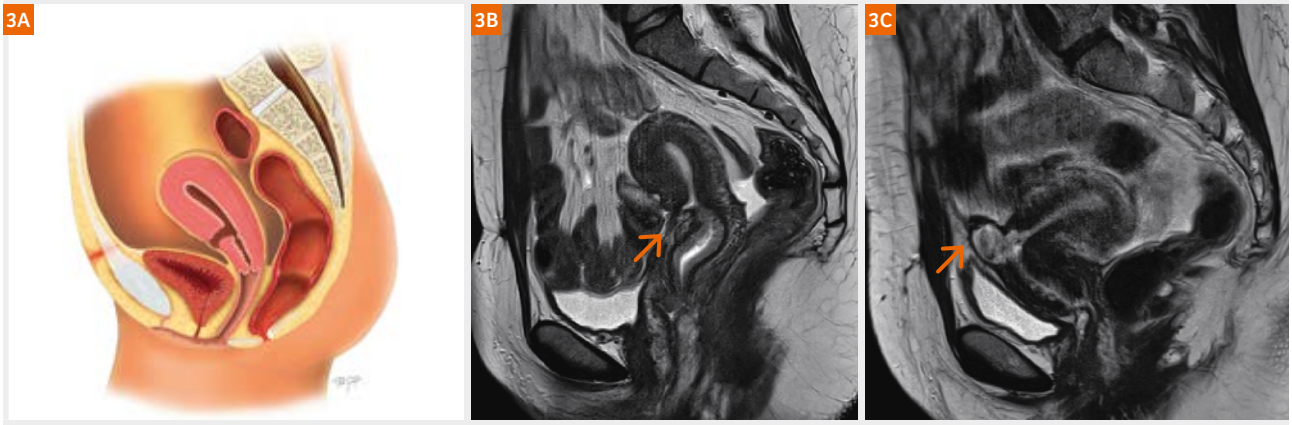

3A: Illustration presents a ruptured uterine wall with an intact, slightly thinned serosal layer.
3B: Sagittal T2-weighted MR exam shows the uterine dehiscence (arrow).
3C: Sagittal T2-weighted MR image depicts uterine dehiscence with isthmocele/hematoma. Note intact serosal layer (arrow).

surface of the fascia [22]. Superficial wound hematoma results from a direct injury of the rectus abdominis muscle due to the operation.

Bladder flap hematoma, subfascial and superficial wound hematomas are shown in Figure 4.

Chronic complications

Healed section scar/ Adhesions

The normal MR findings after a CS show a scar, located in the lower anterior uterine segment and a postsurgical scar in the abdominal wall slightly above the symphysis. The schematic illustration is depicted in Figure 5A. Related MRI examinations are found in Figures 5B, C.

Niche

A niche is a reservoir that forms in the region of the previous section scar, where blood and other products like retained products of conception (RPOC) may accumulate. As a result it may lead to an infection or be a source of the abnormal vaginal discharge and spotting. Niches have been described in a large variety concerning their shape

Figure 4: Schematic illustrations with:

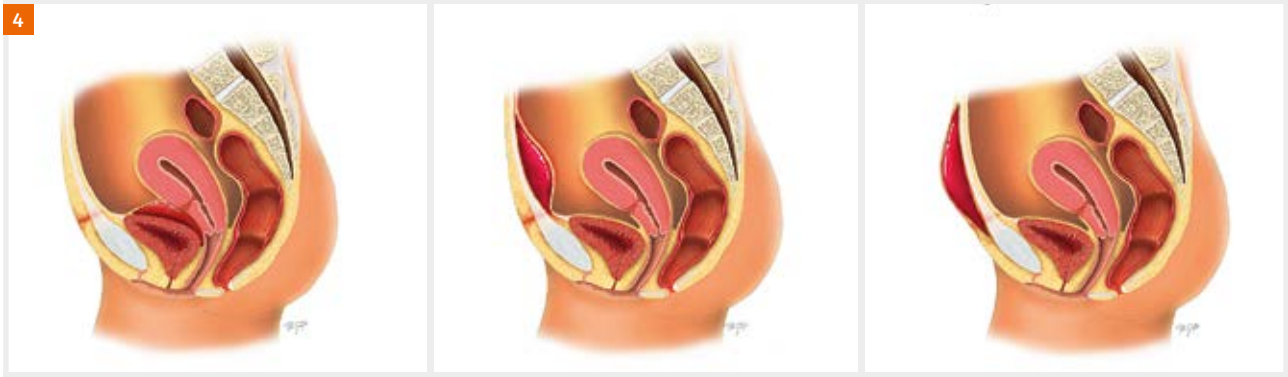

Bladder flap hematoma – Blood collection between the anterior wall of lower uterine segment and posterior wall of the urinary bladder.

Subfascial hematoma – Extraperitoneal blood collection located posteriorly to the rectus abdominal muscle.

Superficial wound hematoma – Surgical wound complication with a hematoma anterior to the rectus abdominis muscle.

The rectus abdominis muscle is an important anatomic landmark in differentiation between subfascial and superficial wound hematoma-subfascial hematoma is located posteriorly and superficial hematoma anteriorly to the muscle.

Figure 5: SCARS – Cesarean section scars.

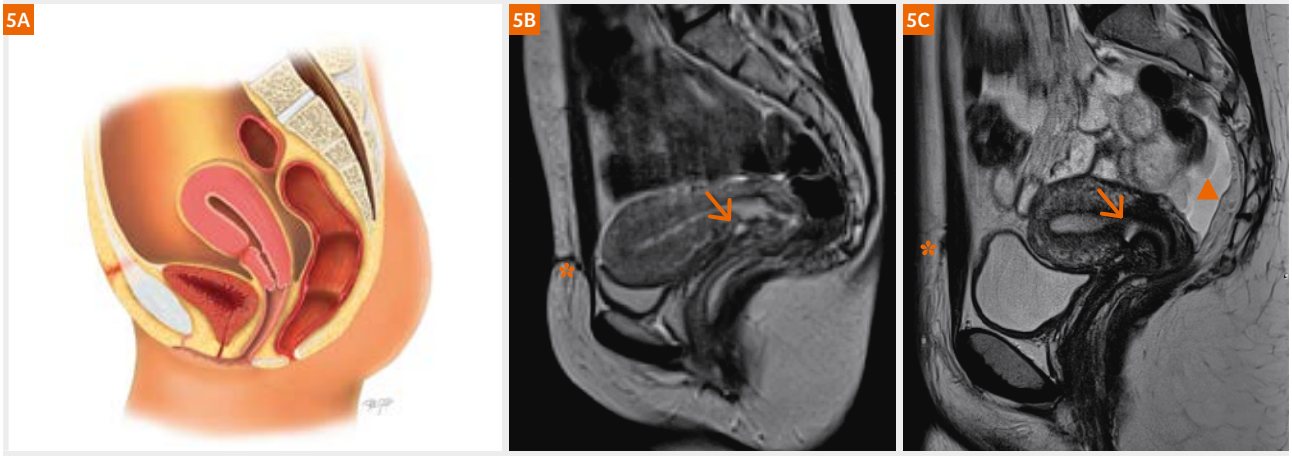

5A: Schematic illustration shows post-operative changes of the female pelvis with a CS scar and a scar in the abdominal wall.
5B, C: T2-weighted sagittal MR images with section scar located cranially to the transition zone between isthmus and cervix uteri (arrow). Note the postsurgical scar in the abdominal wall (asterisk) and free liquid in the excavatio rectouterina (Douglas pouch) (triangle).

and their extent. Currently, there is no widely accepted classification. Niches can lead to substantial defects of the uterine wall and therefore are associated with a high risk for uterine rupture in consecutive pregnancies. They can cause difficulties with implantation in subsequent pregnancies or even account for ectopic pregnancy. MRI may serve as a complimentary examination and accelerates the diagnosis when abnormal bleeding cannot be explained by means of the TVUS/US. An illustration of niche with retained products of conception is shown in Figure 6.

Abdominal wall / Scar endometriosis (Fig. 7)
Endometriosis of abdominal wall occurs approximately in 0.03–1% of patients after CS [23]. MRI can help in differentiating abdominal wall endometriosis from other entities and in assessing of the extent of disease. According to the ESUR recommendations, in the assessment of pelvic endometriosis MRI should be considered as a second-line modality after US. Better image quality can be achieved through proper patient preparation with bowel preparation and emptying of urinary bladder [24]. T2-weighted sequences without fat-suppression are considered the best sequences for detecting pelvic endometriosis, while T1-weighted fat-suppressed sequences help in identification of small endometriomas in the ovary and in their differentiation from other lesions. These sequences help in further classification and differentiation of ovarian lesions (i.e. teratomas) and allow better depiction of peritoneal implants [24, 25].

Conclusion

Increase of deliveries by means of cesarean section is a recent trend in gynecological departments worldwide. Radiologists should be aware of common MRI findings related to the cesarean delivery like cesarean section scar and postoperative susceptibility artifacts. Since the higher number of CS is expected, a simultaneous increase of postsurgical complications may occur. Radiologists should be familiar with complications after a CD and should be able to recognise briefly described MRI findings.

Figure 6: Niche with retained products of conception (RPOC)

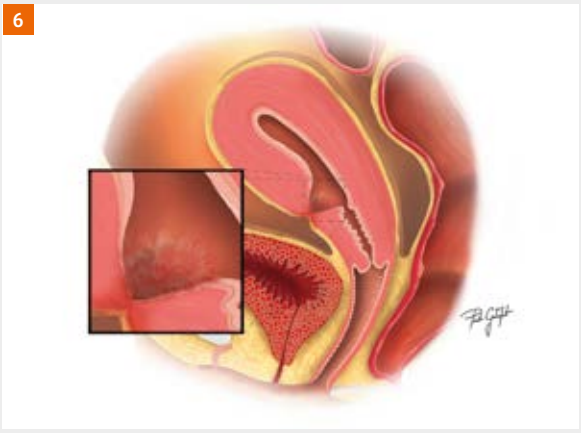

Figure 7: Abdominal wall / Scar endometriosis

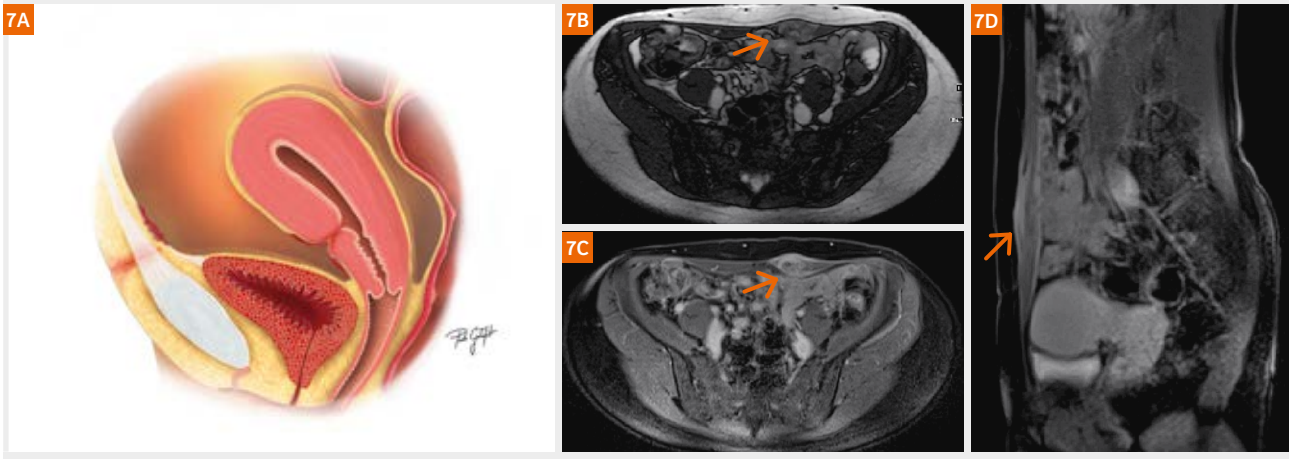

7A: Schematic illustration depicts implants in the abdominal wall and in the uterine scar.
7B–D: MR examinations depict abdominal wall endometriosis.
7B Axial non-enhanced T2-weighted TrueFISP sequence.
7C: Axial contrast-enhanced T2-weighted TrueFISP sequence.
7D: Sagittal contrast-enhanced VIBE sequence with fat suppression. The lesion was histologically confirmed to be abdominal wall endometrioma after CS.

References

1 Li HT, Luo S, Trasande L, Hellerstein S, Kang C, Li JX, et al. Geographic Variations and Temporal Trends in Cesarean Delivery Rates in China, 2008-2014. Jama. 2017;317(1):69-76. Epub 2016/12/29. doi: 10.1001/jama.2016.18663. PubMed PMID: 28030701.
2 Stichting Perinatale Registratie Nederland. Perinatale zorg in Nederland 2008. Utrecht: Stichting Perinatale Registratie Nederland. 2011. www.perinatreg.nl: 2013 25 April 2013. Report No.
3 http://www.cdc.gov/nchs/data/nvsr/nvsr61/nvsr61_05.pdf: 29 April 2013. Report No.
4 Allen VM, O'Connell CM, Liston RM, Baskett TF. Maternal morbidity associated with cesarean delivery without labor compared with spontaneous onset of labor at term. Obstetrics and gynecology. 2003;102(3):477-82. Epub 2003/09/10. PubMed PMID: 12962927.
5 Burrows LJ, Meyn LA, Weber AM. Maternal morbidity associated with vaginal versus cesarean delivery. Obstetrics and gynecology. 2004;103(5 Pt 1):907-12. Epub 2004/05/04. doi: 10.1097/01.AOG.0000124568.71597.ce. PubMed PMID: 15121564.
6 Liu S, Liston RM, Joseph KS, Heaman M, Sauve R, Kramer MS, et al. Maternal mortality and severe morbidity associated with low-risk planned cesarean delivery versus planned vaginal delivery at term. CMAJ : Canadian Medical Association Journal. 2007;176(4):455-60. doi: 10.1503/cmaj.060870. PubMed PMID: PMC1800583.
7 Kataoka M, Kido A, Koyama T, Isoda H, Umeoka S, Tamai K, et al. MRI of the female pelvis at 3T compared to 1.5T: evaluation on high-resolution T2-weighted and HASTE images. Journal of magnetic resonance imaging : JMRI. 2007;25(3):527-34. Epub 2007/02/28. doi: 10.1002/jmri.20842. PubMed PMID: 17326081.
8 Kılıçkesmez Ö, Fırat Z, Oygen A, Bozkurt DK, Güzelbey T, Gürses B, et al. Diffusion Tensor Imaging of the Uterine Zones Related to the Menstrual Cycle and Menopausal Status at 3 Tesla MRI. Balkan Medical Journal. 2016;33(6):607-13. doi: 10.5152/balkanmedj.2016.151638. PubMed PMID: PMC5156455.
9 Derman AY, Nikac V, Haberman S, Zelenko N, Opsha O, Flyer M. MRI of placenta accreta: a new imaging perspective. AJR American journal of roentgenology. 2011;197(6):1514-21. Epub 2011/11/24. doi: 10.2214/ajr.10.5443. PubMed PMID: 22109310.
10 Dicle O, Kucukler C, Pirnar T, Erata Y, Posaci C. Magnetic resonance imaging evaluation of incision healing after cesarean sections. European radiology. 1997;7(1):31-4. Epub 1997/01/01. doi: 10.1007/s003300050103. PubMed PMID: 9000391.
11 Lax A, Prince MR, Mennitt KW, Schwebach JR, Budorick NE. The value of specific MRI features in the evaluation of suspected placental invasion. Magnetic resonance imaging. 2007;25(1):87-93. Epub 2007/01/16. doi: 10.1016/j.mri.2006.10.007. PubMed PMID: 17222719.
12 Leyendecker JR, DuBose M, Hosseinzadeh K, Stone R, Gianini J, Childs DD, et al. MRI of pregnancy-related issues: abnormal placentation. AJR American journal of roentgenology. 2012;198(2):311-20. Epub 2012/01/24. doi: 10.2214/ajr.11.7957. PubMed PMID: 22268173.
13 Si MJ, Gui S, Fan Q, Han HX, Zhao QQ, Li ZX, et al. Role of MRI in the early diagnosis of tubal ectopic pregnancy. European radiology. 2016;26(7):1971-80. Epub 2015/09/17. doi: 10.1007/s00330-015-3987-6. PubMed PMID: 26373758.
14 Fogelberg M, Baranov A, Herbst A, Vikhareva O. Underreporting of complete uterine rupture and uterine dehiscence in women with previous cesarean section. The journal of maternal-fetal & neonatal medicine: the official journal of the European Association of Perinatal Medicine, the Federation of Asia and Oceania Perinatal Societies, the International Society of Perinatal Obstet. 2016:1-4. Epub 2016/12/03. doi: 10.1080/14767058.2016.1236249. PubMed PMID: 27899049.
15 Al-Zirqi I, Daltveit AK, Forsén L, Stray-Pedersen B, Vangen S. Risk factors for complete uterine rupture. American Journal of Obstetrics and Gynecology. doi: http://dx.doi.org/10.1016/j.ajog.2016.10.017.
16 Ofir K, Sheiner E, Levy A, Katz M, Mazor M. Uterine rupture: risk factors and pregnancy outcome. American Journal of Obstetrics and Gynecology. 2003;189(4):1042-6. doi: http://dx.doi.org/10.1067/S0002-9378(03)01052-4.
17 Smith JG, Mertz HL, Merrill DC. Identifying Risk Factors for Uterine Rupture. Clinics in Perinatology. 2008;35(1):85-99. doi: http://dx.doi.org/10.1016/j.clp.2007.11.008.
18 Ho S-Y, Chang S-D, Liang C-C. Simultaneous Uterine and Urinary Bladder Rupture in an Otherwise Successful Vaginal Birth After Cesarean Delivery. Journal of the Chinese Medical Association. 2010;73(12):655-9. doi: http://dx.doi.org/10.1016/S1726-4901(10)70143-X.
19 Maldjian C, Milestone B, Schnall M, Smith R. MR appearance of uterine dehiscence in the post-cesarean section patient. Journal of computer assisted tomography. 1998;22(5):738-41. Epub 1998/10/01. PubMed PMID: 9754109.
20 Gui B, Danza FM, Valentini AL, Laino ME, Caruso A, Carducci B, et al. Multidetector CT appearance of the pelvis after cesarean delivery: normal and abnormal acute findings. Diagnostic and interventional radiology (Ankara, Turkey). 2016;22(6):534-41. Epub 2016/10/21. doi: 10.5152/dir.2016.15593. PubMed PMID: 27756714; PubMed Central PMCID: PMCPMC5098948.
21 Rodgers SK, Kirby CL, Smith RJ, Horrow MM. Imaging after cesarean delivery: acute and chronic complications. Radiographics: a review publication of the Radiological Society of North America, Inc. 2012;32(6):1693-712. Epub 2012/10/16. doi: 10.1148/rg.326125516. PubMed PMID: 23065165.
22 Malvasi A, Tinelli A, Tinelli R, Serio G, Pellegrino M, Mettler L. Subfascial hematomas and hemoperitoneum after cesarean section: prevalence according to closure and non-closure of the parietal peritoneum. Gynecologic and obstetric investigation. 2008;66(3):162-8. Epub 2008/06/20. doi: 10.1159/000140512. PubMed PMID: 18562796.
23 Hensen JH, Van Breda Vriesman AC, Puylaert JB. Abdominal wall endometriosis: clinical presentation and imaging features with emphasis on sonography. AJR American journal of roentgenology. 2006;186(3):616-20. Epub 2006/02/25. doi: 10.2214/ajr.04.1619. PubMed PMID: 16498086.
24 Bazot M, Bharwani N, Huchon C, Kinkel K, Cunha TM, Guerra A, et al. European society of urogenital radiology (ESUR) guidelines: MR imaging of pelvic endometriosis. European radiology. 2016. Epub 2016/12/07. doi: 10.1007/s00330-016-4673-z. PubMed PMID: 27921160.
25 Siegelman ES, Oliver ER. MR Imaging of Endometriosis: Ten Imaging Pearls. Radiographics : a review publication of the Radiological Society of North America, Inc. 2012;32(6):1675-91. doi: doi:10.1148/rg.326125518. PubMed PMID: 23065164.

Contact

Professor Rahel A. Kubik-Huch, M.D., M.P.H.
Head of Department
Institute of Radiology
Kantonsspital Baden
Im Ergel 1
5404 Baden
Switzerland
Phone +41 56 486 38 02
Fax +41 56 486 38 09
rahel.kubik@ksb.ch

Malwina Kaniewska, M.D.
Institute of Radiology
Kantonsspital Baden
Im Ergel 1
5404 Baden
Switzerland
malwina.kaniewska@ksb.ch

FLAWS and MP2RAGE Sequence at 3T for Surgical Localization in Pre Deep Brain Stimulator Patients

David Shipp[1]; **Tobias Kober, Ph.D.**[2]

[1] Monash Medical Centre, Clayton, Victoria, Australia
[2] Advanced Clinical Imaging Technology, Siemens Medical Solutions-CIBM, Lausanne, Switzerland

Introduction

3D MRI sequences for pre-surgical planning are in everyday use. The newer Siemens Healthineers 3D sequences MP2RAGE[1] (Magnetisation Prepared 2 Rapidly Acquired Gradient Echo) and FLAWS[1] (FLuid And White matter Suppression) have allowed us to better visualize the deep grey matter structures required for accurate Deep Brain Stimulator (DBS) insertion in a cohort of neurology and neurosurgical patients.

Clinical applications, surgery approaches and indications

The patient cohort requiring DBS treatment contains three sub-groups of patients with movement disorders, either (1) Parkinson's disease, (2) Parkinson's patients with severe dyskinesia, and (3) essential tremors or dystonia.

In Parkinson's disease, most patients have been on medication for many years, mainly L-DOPA ($_L$-3,4-dihydroxyphenylalanine), and perhaps dopamine agonists activating signalling pathways through the dopamine receptor. The efficacy of the administered medications may however reduce after 5 to 10 years; at this stage, a patient may become a surgical candidate. The associated side effects of these drugs (dyskinesia being involuntary muscle movements, or neuropsychiatric side effects) may also have become intolerable for the patient and family by this time. Also, some form of tremor-dominant Parkinson's disease is refractory to such treatments. DBS surgery is then an option.

The anatomical area needing accurate visualisation for these patients is the **Sub-Thalamic Nucleus (STN)**. See Figures 1A (coronal anatomical view) and 1B (coronal FLAIR MPR).

[1] WIP, the product is currently under development and is not for sale in the US and in other countries. Its future availability cannot be ensured.

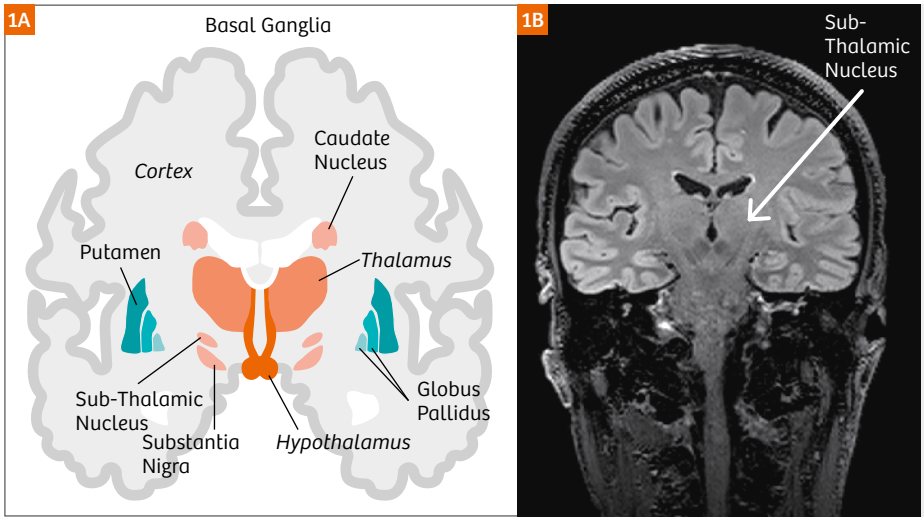

Figure 1:
Sub-Thalamic Nucleus (STN).
(1A) Coronal anatomical view and **(1B)** coronal FLAIR MPR.

For other Parkinson's patients with substantial cognitive or psychiatric co-morbidity, or with very severe dyskinesia, the anatomical area needing accurate visualization is the **Internal segment of the Globus Pallidus (GPi)**. See Figures 2A (coronal anatomical view) and 2B (coronal FLAWS MPR).

If the treatment for essential tremor and dystonia – mainly being mysoline, beta blockers and botulin toxin – have proven no longer successful, DBS surgical intervention is an option. The anatomical area needing accurate visualization for these patients is the **Ventral Intermediate Thalamus Nucleus (VIM)**, see Figures 3A (coronal anatomical view) and 3B (coronal FLAWS MPR).

Anatomical dimensions

These three deep grey matter structures, the Sub-Thalamic Nucleus (STN), the Internal segment of the Globus Pallidus (GPi) and the Ventral Intermediate Thalamus Nucleus (VIM) are typically less than 10 mm x 5 mm in dimension. See Figure 4. A dataset acquired with 0.9 mm isotropic resolution is used stereotactically to precisely ascertain the positioning of the stimulating electrodes. No fiducials are required, as facial landmarks suffice. The probes used at Monash Health are Medtronic 3389 or 3387 quadripolar electrode (Medtronic plc, Dublin, Ireland), with an electrode total diameter of 1.27 mm and total longitudinal length of 10.5 mm. They can deliver stimulation using either one polar electrode or a combination of polar electrodes along their length. So ≤ 1 mm isotropic voxel size should be the target resolution of any acquisition.

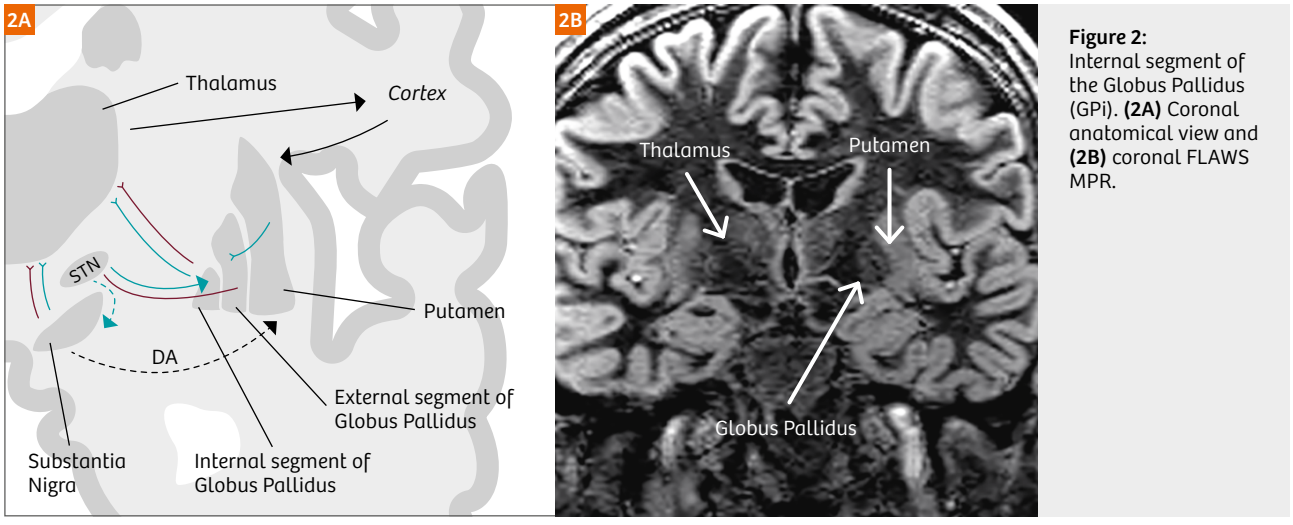

Figure 2: Internal segment of the Globus Pallidus (GPi). **(2A)** Coronal anatomical view and **(2B)** coronal FLAWS MPR.

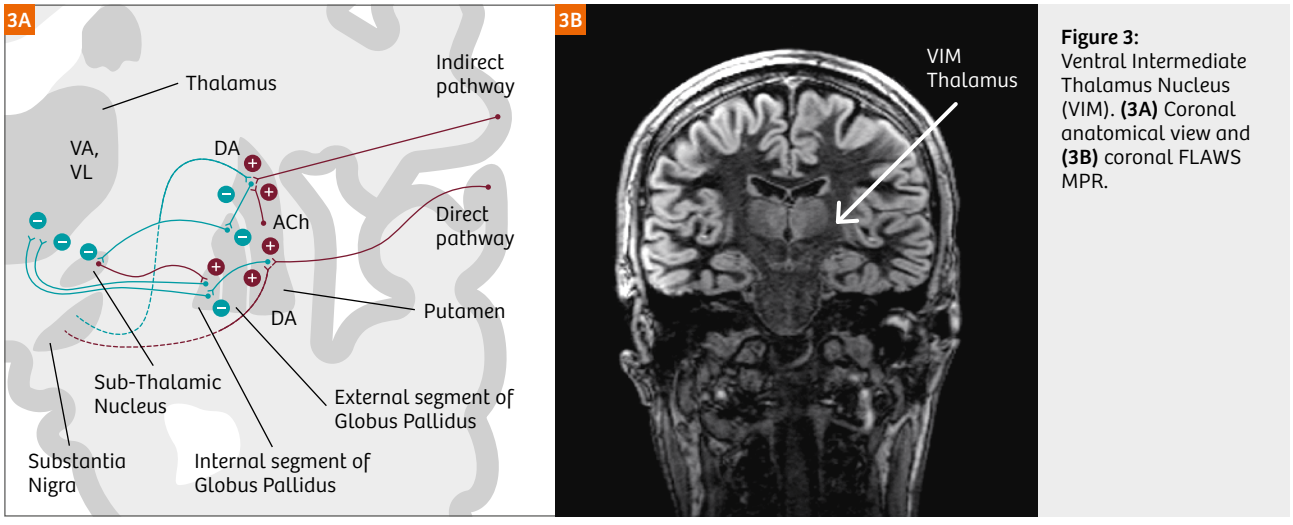

Figure 3: Ventral Intermediate Thalamus Nucleus (VIM). **(3A)** Coronal anatomical view and **(3B)** coronal FLAWS MPR.

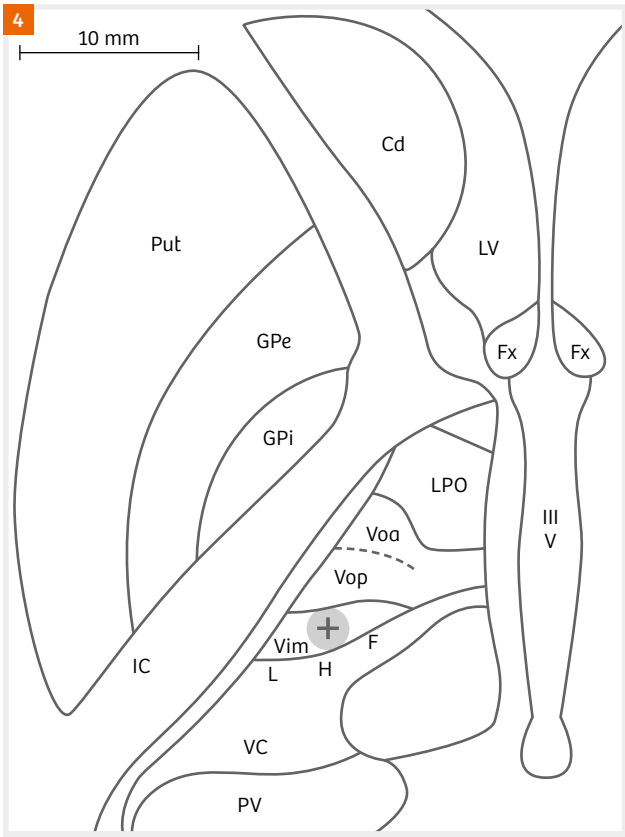

Figure 4:
Axial view of the three deep grey matter structures Sub-Thalamic Nucleus (STN), the Internal segment of the Globus Pallidus (GPi) and the Ventral Intermediate Thalamus Nucleus (Vim).

Imaging sequences

The Siemens Healthineers MP2RAGE sequence [1], featuring two gradient echo readout trains after each inversion pulse which are defined by two different inversion times ($TI_1$and TI_2), yields a significant increase in grey/white matter contrast as compared to a normal MPRAGE. At Monash Health we use a TI_1 = 700 ms and TI_2 = 2200 ms. An example of a MP2RAGE contrast can be seen in Figure 5.

However, the standard protocol of the MP2RAGE sequence is optimized for highest WM/GM contrast in the cortex. By altering the two inversion times, an increased contrast between deep grey and white matter structures can be achieved. In a special MP2RAGE variant called FLAWS [2], the TI_1 is chosen so that the WM signal decay after the inversion is around zero when the first image is sampled, i.e. at the WM null point. The second TI_2 can then be adjusted to obtain a 'normal' MPRAGE contrast, yielding two complementary contrasts from a single acquisition. At Monash Health, we use a first inversion time of 409 ms and a second inversion time of 1330 ms. An example of the two obtained image contrasts can be seen in Figure 6.

In a simple post-processing step which is performed directly during the image reconstruction on the scanner, a minimum-intensity projection (MIP) between the two contrasts (WM-nulled and MPRAGE) results in the so-called FLAWS contrast. An example can be seen in Figures 7A–C. (Axial FLAWS MPR) 7B (Cor FLAWS MPR) and 7C (Sag FLAWS acquisition).

Scan parameters

Protocol

- MP2RAGE with embedded FLAWS with 0.9 mm isotropic voxels
- 3D FLAIR, with 0.9 mm isotropic voxels

All sequences were acquired on a 3T MAGNETOM Verio, with a 32-channel head coil.

The referring neurosurgeon and neurologist both request the 3D FLAIR sequence as well as the 3D FLAWS / MP2RAGE sequence, as they believe the STN is still best displayed on the FLAIR acquisition. The other areas are best delineated on the FLAWS.

Even an acquisition time of 5 mins 30 secs can sometimes be problematic for this cohort of patients, with their tremors leading to motion artifacts. Preparation includes the patient taking their medication in the early morning as usual, and scheduling their MRI examination mid-morning. Intravenous Midazolam can be an option. As a final option to obtain diagnostic images free of motion artifacts, a general anesthetic may be rarely required.

Acknowledgements

Professor Stephen Stuckey (Director Monash Imaging and Head of MRI Monash Health), Associate Professor Andrew Danks (Head of Neurosurgery, Monash Health), Professor Dominic Thyagarajan (Director of Neurology, Monash Health), Sonal Josan (Senior Scientist MRI, Siemens Healthcare Australia).

References

1 Marques JP, Kober T, Krueger G, van der Zwaag W, Van de Moortele PF, Gruetter R. „MP2RAGE, a self bias-field corrected sequence for improved segmentation and T1-mapping at high field", Neuroimage. 2010 Jan 15;49(2):1271-81.
2 Tanner M, Gambarota G, Kober T, Krueger G, Erritzoe D, Marques J, Newbould R, "Fluid and White Matter Suppression with the MP2RAGE Sequence", JMRI 35:1063-1070 (2012).

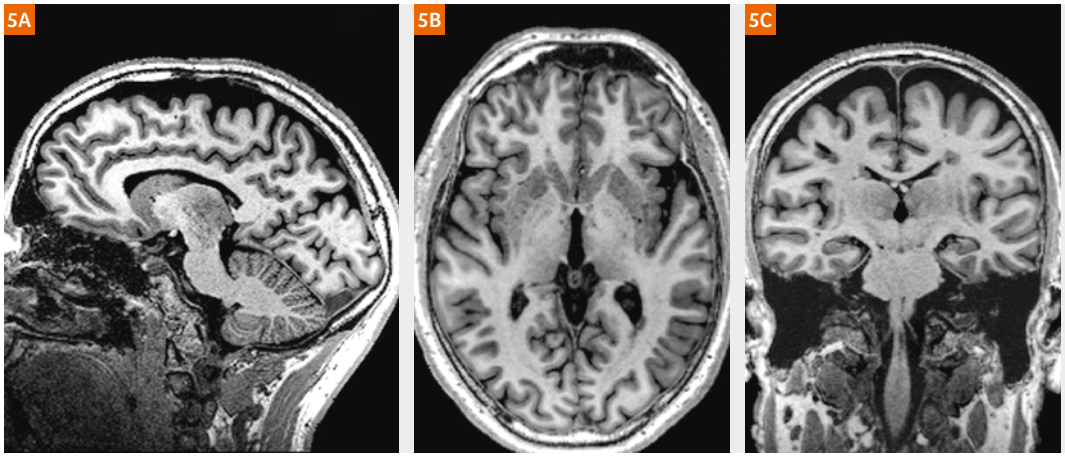

Figure 5:
Examples of the MP2RAGE contrast. **(5A)** sagittal, **(5B)** axial, **(5C)** coronal.

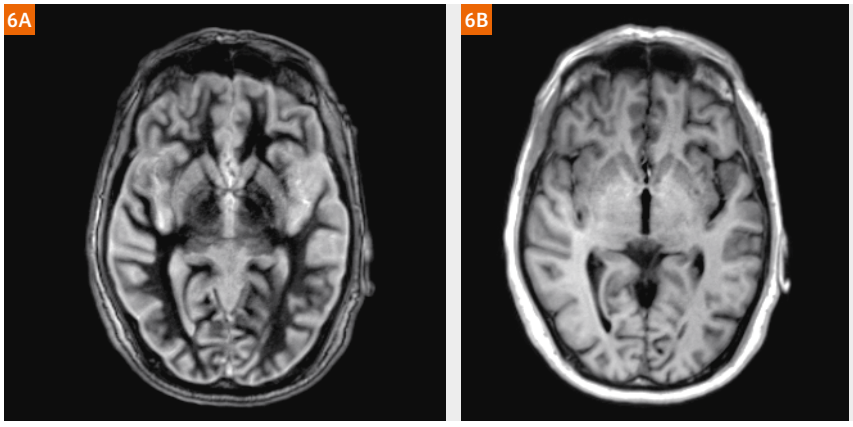

Figure 6:
Image contrasts obtained using a first inversion time of 409 ms **(6A)** and a second inversion time of 1330 ms **(6B)**.

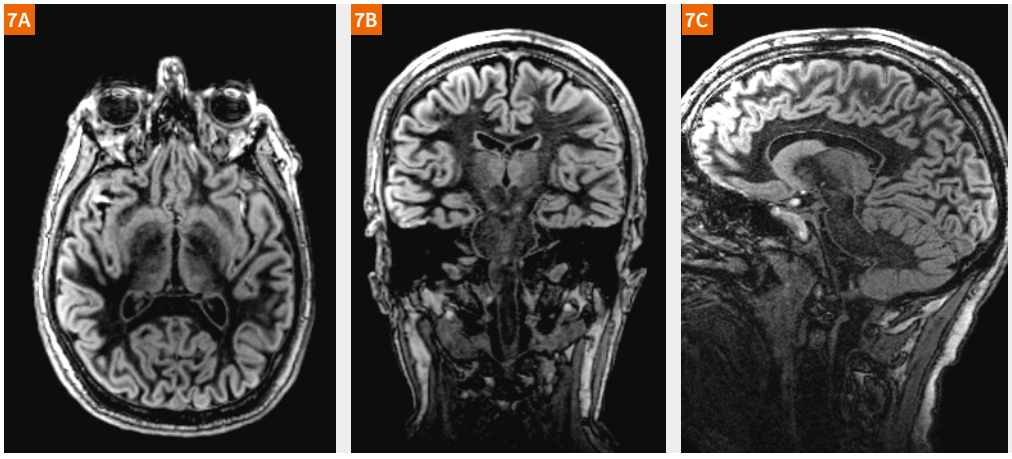

Figure 7:
A minimum-intensity projection (MIP) between the two contrasts (WM-nulled and MPRAGE) results in the so-called FLAWS contrast. **(7A)** Axial, **(7B)** coronal, **(7C)** sagittal.

Contact

David Shipp
Monash Medical Centre

246 Clayton Rd
Clayton VIC 3168
Australia
david.shipp@monashhealth.org

Meet Siemens Healthineers

Siemens Healthineers: Our brand name embodies the pioneering spirit and engineering expertise that is unique in the healthcare industry. The people working for Siemens Healthineers are totally committed to the company they work for, and are passionate about their technology. In this section we introduce you to colleagues from all over the world – people who put their hearts into what they do.

Santiago, Chile

Miguel Contreras

was born and raised in the city of Maracaibo, Venezuela, where he graduated from Dr. Rafael Belloso Chacín University in Electronics Engineering in 2008. He began working at Siemens in Venezuela in July 2010. In March 2014 Siemens offered him the opportunity to relocate to Santiago, Chile, where he has settled with his wife. It's been a very interesting challenge, to say the least. Chile gave him the chance of professional growth outside of training, e.g. participation in Gradient Coil replacements and two Thermal Cycles, as well as the opportunity to work with colleagues from Siemens Magnet Technologies in Oxford, UK in advanced procedures – rare opportunities in Chile. Today Miguel works as a Customer Service Engineer focused on MR Systems and Magnets.

What was your first experience with MRI?
My first experience with MRI was a visit to a 0.35T MAGNETOM C! system in a small town about 80 minutes' travel from Caracas. The system had been badly damaged after a broken pipe flooded the magnet room. It was only my second week working at Siemens Venezuela.

What fascinates you most about MRI?
The magnets themselves. From the construction of the vessels to servicing at field it's a really interesting area. There's nothing quite like performing a critical procedure on a valve that's venting cryogenic gasses below -70° Celsius and still manage to break a sweat.

How do you use the Siemens Customer Service remote capabilities of our equipment in your daily job?
Siemens Remote Service (SRS) and a phone call are the very first tools I use when troubleshooting. I can get the customer's feedback while I'm looking at the event logs or test tools trying to discover what caused the error to show up and even make a judgment of what tools I'll need for any necessary troubleshooting on site.

How do the remote capabilities benefit the MAGNETOM user?
There's the possibility of fixing the problem remotely if no parts are damaged, which saves a lot of time. I think it also gives the user some peace of mind that we're working on their case as soon as possible and they don't have to wait at least an hour to get some news on what's happening to their systems. Even small things like updating the clock at the start and end of daylight savings time, or adding a new DICOM node, are resolved faster since they won't have to wait for a Customer Service Engineer (CSE) to get there.

What part of your job motivates you the most?
There's always something new. From exciting new systems and upgrades for older systems to new software versions, there's always something changing within the work environment. This pushes me to learn new things about our systems every day.

If you were free to do anything for one month, what would it be?
I would definitely use that time to travel and photograph all the natural landscapes I could. Starting from Chile, in which I still have a lot to see. My hobbies of travelling and photography really complement each other well. This line of work also gives me good opportunities to carry on with my hobbies, as I always pack my camera every time I have to travel somewhere for work or training.

Craig Haker

became interested in Biomedical Engineering while attending an open house at British Columbia Institute of Technology (BCIT), Vancouver, Canada. An introduction to some smaller equipment found around hospitals, the responsibilities of a Biomed, and the opportunities in that working environment inspired him with this combination of technology and dedication to improving people's lives.

At the end of the Biomedical Engineering program Craig was lucky enough to be chosen for a five-week placement program within the Richmond/Vancouver branch of Siemens. He shadowed the Field Service Representatives (FSR) from that office, learning about the imaging equipment Siemens offered. Finishing the practicum and BCIT program, an opportunity with Siemens awaited in Saskatoon, Saskatchewan, Canada, where he has lived and worked for the last 9 years. When not working, Craig enjoys outdoor activity during the summer months. He plays soccer, ultimate Frisbee, and enjoys biking. During winters, he is more likely to be found staying warm watching hockey, indoor sports, or visiting family in British Columbia, trying to avoid the -40° C weather in Saskatchewan.

What was your first experience with MRI?
My first experience with MRI would have been an introduction to the 1T MAGNETOM Harmony and 1.5T MAGNETOM Symphony systems in our local hospital in Saskatoon when I first began working with Siemens in July of 2008. It was in the basement of our hospital, and felt a little secluded. It was here that I began to learn the basics of our systems. Shortly after came trips to our training centers for the basics and system courses from Siemens.

What fascinates you most about MRI?
What fascinates me the most is the use of magnetic fields in the equipment. It is a force that we seldom get to experience to the degree that MRIs produce in our daily lives. Magnets were fun toys for children, and can have practical purposes around the house as tools or holders, but in MRI they are at the heart of the equipment, they are a fundamental component.

What is your role in Siemens Customer Service?
My primary role in Siemens Customer Service is to provide field service to our customers. Over the last two years that role has expanded to include Technical Service Representative (TSR) roles, where I am the first technical point of contact for MAGNETOM users to clarify their problem, to resolve the problem if possible, or to determine that an onsite service call is required.

How do the remote capabilities benefit the MAGNETOM user?
In my daily duties, the Siemens Remote Service platform allows me to monitor our customers' systems without impacting their workflow. I am also able to respond to problems or questions that arise quickly and with more accuracy than would be possible if my information was limited to what the customer was able to describe over the phone. With SRS, I am able to check event logs, system status, trends, etc. to gain a much better understanding of a system's situation.

What part of your job motivates you the most?
I am most motivated by the variety in my daily work routine, the ability to see a job through completion, and the challenging field of maintaining modern medical equipment.

If you were free to do anything for one month, what would it be?
I would be torn between taking a vacation overseas with my girlfriend, as she has never had the opportunity yet to travel, and using the time to work on my home. I recently became a home owner and have many small projects around the house to tackle!

PI-RADS 2
Standardized Prostate MRI Reporting

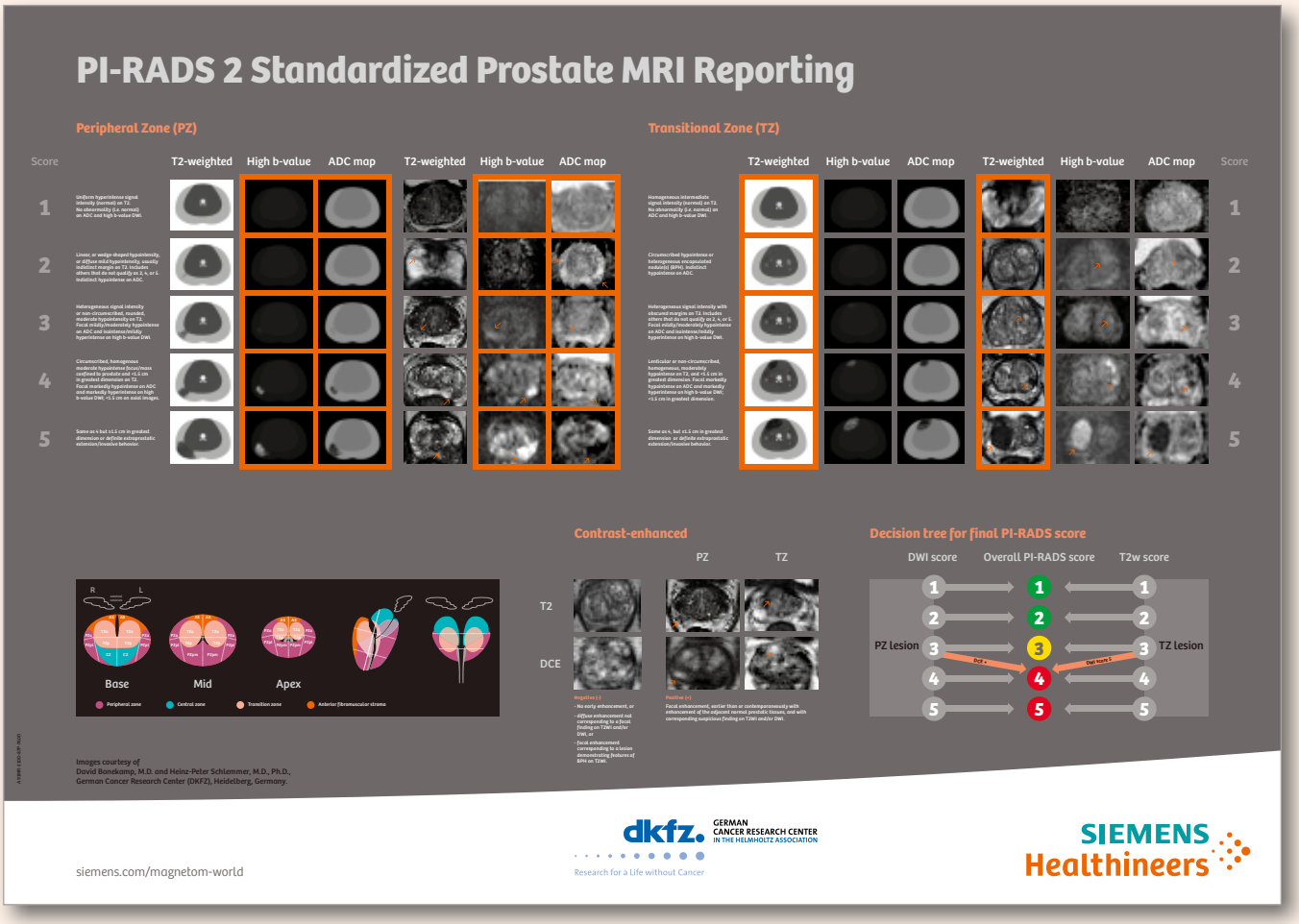

Visit us at **www.siemens.com/magnetom-world**

Go to > Publications > Subscriptions > **MRI Poster**

Get your free copy of the PI-RADS 2 poster

MAGNETOM Flash – Imprint

Publisher:
Siemens Healthcare GmbH
Magnetic Resonance,
Karl-Schall-Str. 6, D-91052 Erlangen, Germany

Editor-in-chief:
Antje Hellwich
(antje.hellwich@siemens-healthineers.com)

Guest editor:
Steven L. Mendelsohn, M.D.
Chief Executive Officer
Zwanger-Pesiri Radiology
Lindenhurst, NY, USA

Editorial Board:
Reto Merges; Wellesley Were;
Sunil Kumar S.L., Ph.D.;
Gary R. McNeal, MS (BME)

Review Board:
Lisa Chuah, Ph.D.; Daniel Fischer;
Christian Geppert, Ph.D.; Berthold Kiefer, Ph.D.;
Heiko Meyer, Ph.D.; Gregor Thörmer, Ph.D.

Copy Editing:
Sheila Regan, Jen Metcalf, UNIWORKS,
www.uni-works.org
(with special thanks to Kylie Martin)

Layout:
Agentur Baumgärtner,
Friedrichstr. 4, D-90762 Fürth, Germany

Production:
Norbert Moser,
Siemens Healthcare GmbH

Printer:
Schmidl & Rotaplan Druck GmbH,
Hofer Str. 1, D-93057 Regensburg, Germany

Note in accordance with § 33 Para.1 of the German Federal Data Protection Law: Despatch is made using an address file which is maintained with the aid of an automated data processing system.

MAGNETOM Flash is sent free of charge to Siemens MR customers, qualified physicians, technologists, physicists and radiology departments throughout the world. It includes reports in the English language on magnetic resonance: diagnostic and therapeutic methods and their application as well as results and experience gained with corresponding systems and solutions. It introduces from case to case new principles and procedures and discusses their clinical potential. The statements and views of the authors in the individual contributions do not necessarily reflect the opinion of the publisher.

The information presented in these articles and case reports is for illustration only and is not intended to be relied upon by the reader for instruction as to the practice of medicine. Any health care practitioner reading this information is reminded that they must use their own learning, training and expertise in dealing with their individual patients. This material does not substitute for that duty and is not intended by Siemens Healthcare to be used for any purpose in that regard. The drugs and doses mentioned herein are consistent with the approval labeling for uses and/or indications of the drug. The treating physician bears the sole responsibility for the diagnosis and treatment of patients, including drugs and doses prescribed in connection with such use. The Operating Instructions must always be strictly followed when operating the MR system. The sources for the technical data are the corresponding data sheets. Results may vary.

Partial reproduction in printed form of individual contributions is permitted, provided the customary bibliographical data such as author's name and title of the contribution as well as year, issue number and pages of MAGNETOM Flash are named, but the editors request that two copies be sent to them. The written consent of the authors and publisher is required for the complete reprinting of an article.

We welcome your questions and comments about the editorial content of MAGNETOM Flash. Please contact us at magnetomworld.med@siemens.com.

Manuscripts as well as suggestions, proposals and information are always welcome; they are carefully examined and submitted to the editorial board for attention. MAGNETOM Flash is not responsible for loss, damage, or any other injury to unsolicited manuscripts or other materials. We reserve the right to edit for clarity, accuracy, and space. Include your name, address, and phone number and send to the editors, address above.

MAGNETOM Flash is also available online:

www.siemens.com/magnetom-world

MAGNETOM Flash

Issue Number 69 · 3/2017
RSNA Edition

Not for distribution in the US

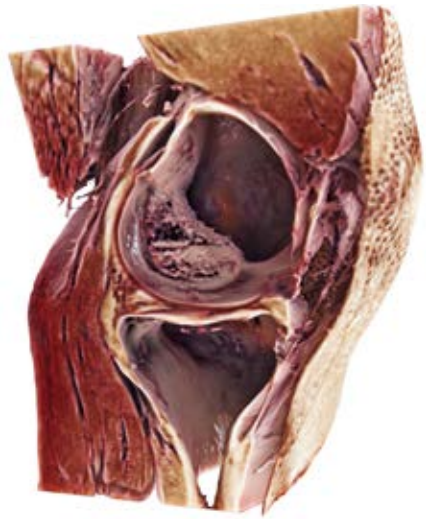

SIEMENS Healthineers

siemens.com/magnetom-world

Please enter your business address

Institution

Department

Function

Title

Name

Street

Postal Code

City

State

Country

MR system used

Please include me in your mailing list for the following Siemens Healthcare customer magazine(s):

☐ MAGNETOM Flash

☐ SOMATOM Sessions

☐ Imaging Life

☐ AXIOM Innovations

☐ Go HYBRID!

Stay up to date with the latest information

Register for:

E-mail

☐ Yes, I consent to the above information being used for future contact regarding product updates and other important news from Siemens.

☐ unsubscribe from info service

Please print clearly!

→ Visit www.siemens.com/magnetom-world for case reports, clinical methods, application tips, talks and much more clinical information.

Subscribe now!

– and get your free copy of future MAGNETOM Flash!

Relevant information from the world of magnetic resonance – gratis to your desk. Send us this postcard, or subscribe online at

www.siemens.com/magnetom-world

Siemens Healthcare GmbH
Antje Hellwich
HC DI MR CRM SCI
Karl-Schall-Str. 6
91052 Erlangen
Germany

MAGNETOM Flash

On account of certain regional limitations of sales rights and service availability, we cannot guarantee that all products included in this brochure are available through the Siemens sales organization worldwide. Availability and packaging may vary by country and is subject to change without prior notice. Some/All of the features and products described herein may not be available in the United States.

The information in this document contains general technical descriptions of specifications and options as well as standard and optional features which do not always have to be present in individual cases, and which may not be commercially available in all countries. Due to regulatory reasons their future availability cannot be guaranteed. Please contact your local Siemens organization for further details.

Siemens reserves the right to modify the design, packaging, specifications, and options described herein without prior notice. Please contact your local Siemens sales representative for the most current information.

Note: Any technical data contained in this document may vary within defined tolerances. Original images always lose a certain amount of detail when reproduced.

Siemens Healthineers Headquarters
Siemens Healthcare GmbH
Henkestr. 127
91052 Erlangen
Germany
Phone: +49 9131 84-0
siemens.com/healthineers

Published by Siemens Healthcare GmbH · Order No. A91MR-1000-127M-7600 · Printed in Germany · 4740 111711. ·